

INFORMATION TO USERS

This manuscript has been reproduced from the microfilm master. UMI films the text directly from the original or copy submitted. Thus, some thesis and dissertation copies are in typewriter face, while others may be from any type of computer printer.

The quality of this reproduction is dependent upon the quality of the copy submitted. Broken or indistinct print, colored or poor quality illustrations and photographs, print bleedthrough, substandard margins, and improper alignment can adversely affect reproduction.

In the unlikely event that the author did not send UMI a complete manuscript and there are missing pages, these will be noted. Also, if unauthorized copyright material had to be removed, a note will indicate the deletion.

Oversize materials (e.g., maps, drawings, charts) are reproduced by sectioning the original, beginning at the upper left-hand corner and continuing from left to right in equal sections with small overlaps.

ProQuest Information and Learning
300 North Zeeb Road, Ann Arbor, MI 48106-1346 USA
800-521-0600

UMI[®]

University of Alberta

**The Effect of Surfactants on Microscale Wave Breaking and
the Aqueous Boundary Layer**

by

Mohamed Khairy Mohamed El Kamash



A thesis submitted to the Faculty of Graduate Studies and Research in partial
fulfillment of the requirements for the degree of Doctor of Philosophy

in

Water Resources Engineering

Department of Civil and Environmental Engineering

Edmonton, Alberta

Spring 2005



Library and
Archives Canada

Bibliothèque et
Archives Canada

0-494-08229-1

Published Heritage
Branch

Direction du
Patrimoine de l'édition

395 Wellington Street
Ottawa ON K1A 0N4
Canada

395, rue Wellington
Ottawa ON K1A 0N4
Canada

Your file *Votre référence*

ISBN:

Our file *Notre référence*

ISBN:

NOTICE:

The author has granted a non-exclusive license allowing Library and Archives Canada to reproduce, publish, archive, preserve, conserve, communicate to the public by telecommunication or on the Internet, loan, distribute and sell theses worldwide, for commercial or non-commercial purposes, in microform, paper, electronic and/or any other formats.

The author retains copyright ownership and moral rights in this thesis. Neither the thesis nor substantial extracts from it may be printed or otherwise reproduced without the author's permission.

AVIS:

L'auteur a accordé une licence non exclusive permettant à la Bibliothèque et Archives Canada de reproduire, publier, archiver, sauvegarder, conserver, transmettre au public par télécommunication ou par l'Internet, prêter, distribuer et vendre des thèses partout dans le monde, à des fins commerciales ou autres, sur support microforme, papier, électronique et/ou autres formats.

L'auteur conserve la propriété du droit d'auteur et des droits moraux qui protègent cette thèse. Ni la thèse ni des extraits substantiels de celle-ci ne doivent être imprimés ou autrement reproduits sans son autorisation.

In compliance with the Canadian Privacy Act some supporting forms may have been removed from this thesis.

Conformément à la loi canadienne sur la protection de la vie privée, quelques formulaires secondaires ont été enlevés de cette thèse.

While these forms may be included in the document page count, their removal does not represent any loss of content from the thesis.

Bien que ces formulaires aient inclus dans la pagination, il n'y aura aucun contenu manquant.


Canada

Abstract

This study reports on a laboratory investigation of the effect of surfactants on the properties of the aqueous boundary layer, the properties of microscale-breaking waves, the characteristics of coherent structures and the air-water gas transfer rate. Digital particle image velocimetry and surface wave profile measurements were gathered for clean and surfactant-influenced water surfaces. At all wind speeds (3.8 to 9.8 m·s⁻¹) the flow in the aqueous boundary layer was found to be in the transition regime for both water surface conditions.

The fraction of the total vertical momentum transferred to the aqueous boundary layer decreased from 0.8 to 0.2 for clean water surfaces and from 0.9 to 0.3 for surfactant-influenced water surfaces as the wind speed increased from 3.8 to 9.8 m·s⁻¹. A strong negative correlation was observed between the fraction of the total momentum transferred to the aqueous boundary layer and the mean square wave slope irrespective of water surface condition.

The ratio of the rate of dissipation of turbulent kinetic energy in surfactant-influenced water, to that in clean water decreased from 1.0 to 0.70 as the wind speed increased from 3.8 to 9.6 m·s⁻¹. A surfactant reduced the thickness of the enhanced layer of near-surface turbulence on average by 35%. The surfactant reduced the percentage of wave breaking by approximately one third and reduced the wave amplitude and the maximum wave slope on the forward face of the waves by an average factor of 25% and 28%, respectively for breaking waves and 22% and 19%, respectively for non-breaking waves. A strong correlation was observed between the fraction of the total momentum

transferred to the wave field and the percentage of breaking waves irrespective of the water surface cleanliness.

The frequency of occurrence of coherent structures increased by a factor of ~ 10 for both clean and surfactant-influenced water surfaces as the wind speed increased from 3.8 to 9.6 $\text{m}\cdot\text{s}^{-1}$. The surfactant reduced the frequency of occurrence of coherent structures by approximately 20% and the measured bulk gas transfer velocities by approximately 55%.

Acknowledgements

I am grateful to my supervisor Professor Mark R. Loewen for his great support and help. He started me off on the right way, provided academic guidance and encouragement, introduced me to much of the materials in the thesis, offered his time to discuss the development and progress of the thesis and learned me a lot throughout the course of my research. He also supported me financially, supported my conference presentations and my visit to the University of Washington to carry out my experimental work.

During my PhD program, many people have helped me. Dr. Kamran Siddiqui provided me with a lot of his experience in the field of my work as well as computer algorithms related to much of the materials in the thesis. Dr. William Asher and Dr. Andrew Jessup at the University of Washington allowed me to carry out my experiments, helped and guided me as well. Dr. Mohamed Atmane assisted me with the IR measurements, provided me with the bulk gas transfer results and offered his time to discuss some of my results.

I gratefully acknowledge the excellent atmosphere surrounded my research by all the staff, colleagues and friends in the water resources group. My heartfelt thanks are also extended to my parents, family and friends for their continued encouragement and support. And last but not least, thanks to my wife for her never-ending support, confidence and love.

I gratefully acknowledge the support of the University of Alberta, National Science and Engineering Research Council (NSERC) and Alberta Informatics Circle of Research Excellence (icore) in the form of postgraduate scholarships.

Table of Contents

1 Introduction	1
2 Aqueous Boundary Layer and Momentum Transfer	
2.1 Introduction.....	6
2.2 Experimental Setup.....	10
2.2.1 Instrumentation and Methods.....	10
2.2.2 Experimental Procedures.....	15
2.3 Results.....	20
2.3.1 Wave Properties.....	20
2.3.2 Surface Drift Velocity.....	21
2.3.3 Airside Friction Velocity.....	22
2.3.4 Aqueous Boundary Layer.....	23
2.3.4.1 Mean Velocity Profiles.....	23
2.3.4.2 Velocity Defect Law.....	25
2.4 Discussion.....	28
2.5 Conclusion.....	41
3 Near-Surface Turbulence and Microscale-Breaking Waves	
3.1 Introduction.....	64
3.2 Bulk Gas Transfer Velocities.....	72
3.3 Rate of dissipation of Turbulent Kinetic Energy.....	73
3.3.1 Spectral Analysis.....	73
3.3.2 Turbulent Kinetic Energy Dissipation Calculations.....	74
3.4 Discussion: Turbulent Kinetic Energy Dissipation.....	79
3.5 Microscale-Breaking Waves.....	83
3.5.1 Detection Scheme.....	83
3.5.2 Microscale-Breaking Wave Characteristics.....	88
3.6 Discussion: Microscale-Breaking Waves.....	91
3.7 Conclusions.....	100
4 Coherent Structures and Air-water Gas Transfer	
4.1 Introduction.....	133

4.2 Near surface vorticity.....	138
4.3 Coherent Structures Identification Technique.....	139
4.4 Characteristics of Coherent Structures.....	143
4.5 Air-Water Gas Transfer.....	149
4.5.1 Surface renewal model.....	149
4.5.2 Air-Water Gas Transfer Results.....	155
4.6 Conclusions.....	160
5 Conclusions and recommendations	
5.1 Summary and Conclusions.....	180
5.2 Recommendations for Future Work.....	183
References.....	186
Appendix A.....	196
Appendix B.....	204

List of Tables

Table 2.1: Summary of environmental parameters for both water surface conditions.....	44
Table 2.2: Summary of velocity measurements for different experimental runs for both water surface conditions.....	45
Table 2.3: Summary of velocity defect law results for both water surface conditions.	46
Table 3.1: Comparison between the rates of turbulent kinetic energy dissipation computed using three different methods for clean water surface runs.....	102
Table 3.2: Depth-averaged rate of energy dissipation values for the top 2 cm water for both water surface conditions.....	103
Table 3.3: Values of the vorticity variance threshold and numbers of detected microscale-breaking waves from different methods.....	104
Table 4.1: Summary of the characteristics of coherent structures for both water surface conditions.....	163
Table 4.2: Summary of air-water gas transfer velocity results for both water surfaces conditions.....	164

List of Figures

FIGURE 1.1: Sketch illustrating the conceptual model of a microscale-breaking wave	5
FIGURE 2.1: Schematic of the experimental setup illustrating the instrumentation used in the wind wave tank.....	47
FIGURE 2.2: A flow chart showing the synchronization of the IR, profile and DPIV cameras and the laser.....	48
FIGURE 2.3: A typical profile image obtained from the profile camera at a wind speed of $9.6 \text{ m}\cdot\text{s}^{-1}$ with the computed water surface profile plotted on top of it as a white line.....	49
FIGURE 2.4: A typical DPIV image with the water surface profile plotted on top of it as a white line.....	50
FIGURE 2.5: The two-dimensional instantaneous velocity field.....	51
FIGURE 2.6: Infrared image showing a heated patch generated by the CO_2 laser.....	52
FIGURE 2.7: Plot of the ratio of the surface velocity U_s to the wind friction velocity u_{*a} for various wind speeds.....	53
FIGURE 2.8: Vertical profiles of the stream wise component of the mean velocity. (a) Clean water surfaces, (b) Surfactant-influenced water surfaces.....	54
FIGURE 2.9: Vertical profiles of the stream wise component of the mean velocity for clean and surfactant-influenced water surfaces.....	55
FIGURE 2.10: The mean streamwise velocity plotted in the form of a velocity defect law in wall coordinates. (a) Clean water surfaces, (b) Surfactant-influenced water surfaces.....	56
FIGURE 2.11: Plots of the shear stresses for various wind speeds.....	58
FIGURE 2.12: Plot of the ratio of the waterside shear stress to the airside shear stress at various wind speeds.....	59
FIGURE 2.13: Plot of the ratio of the waterside shear stress to the airside shear stress versus the mean square wave slope of the waves.....	60

FIGURE 2.14: Plot of the ratio of the shear stress ratio versus the wind speed. Different sets of data were compiled from the literature as labeled in the figure.....	61
FIGURE 2.15: Plot of the ratio of the shear stress versus the steepness.....	62
FIGURE 2.16: Plot of 1- the ratio of the waterside shear stress to the airside shear stress versus the mean square wave slope of the waves.....	63
FIGURE 3.1: Plot of the bulk gas transfer velocity for various wind speeds.....	105
FIGURE 3.2: Plot of the bulk gas transfer velocity versus the mean square wave slope.....	106
FIGURE 3.3: Longitudinal wave number spectra of the streamwise instantaneous velocity component, at five wind speeds for clean water surface runs.....	107
FIGURE 3.4: Comparison of the longitudinal wave number spectra of the streamwise instantaneous velocity component for clean and surfactant influenced water surfaces.....	108
FIGURE 3.5: Vertical profiles of the rate of energy dissipation at different wind speeds (a) Clean water surfaces, (b) Surfactant-influenced water surfaces.....	109
FIGURE 3.6: Vertical profiles of the rate of energy dissipation, ϵ , for clean and surfactant influenced water surfaces.....	110
FIGURE 3.7: Plot of the dimensionless rate of energy dissipation versus the dimensionless depth for both water surface conditions.....	111
FIGURE 3.8: Plot of the dimensionless rate of energy dissipation versus the dimensionless depth using wall layer scaling (a) Clean water surfaces, (b) Surfactant-influenced water surfaces.....	112
FIGURE 3.9: Plot of the mean square wave slope versus the depth averaged rate of energy dissipation over top 2-cm layer.....	113
FIGURE 3.10: (a-c) A sequence of paired plots of an instantaneous vorticity field (top) and IR image (bottom) showing a non-breaking waves at a wind speed of $9.6 \text{ m}\cdot\text{s}^{-1}$	114
FIGURE 3.11: (a-c) A sequence of paired plots of an instantaneous vorticity field (top) and IR image (bottom) showing a microscale-breaking waves at a wind speed of $9.6 \text{ m}\cdot\text{s}^{-1}$	117

FIGURE 3.12: Plot showing the instantaneous vorticity field beneath a wave crest at wind speed of $9.6 \text{ m}\cdot\text{s}^{-1}$. The region of interest (ROI) is marked with dashed-lines.....	120
FIGURE 3.13: The percentage of microscale breaking waves P_b versus wind speed.....	121
FIGURE 3.14: Plot of the maximum wave slope on the downwind face of the wave versus wind speed for clean and surfactant influenced water surfaces. (a) Microscale breaking waves, (b) Non-breaking waves.....	122
FIGURE 3.15: Plot of the maximum wave amplitude versus wind speed for clean and surfactant influenced water surfaces. (a) Microscale breaking waves, (b) Non-breaking waves.....	123
FIGURE 3.16: PDF's of the maximum wave slope on the downwind face of the waves at a wind speed of $9.6 \text{ m}\cdot\text{s}^{-1}$ for a clean water surface for microscale breaking waves and non-breaking waves.....	124
FIGURE 3.17: PDF's of the maximum wave amplitude at a wind speed of $9.6 \text{ m}\cdot\text{s}^{-1}$ for a clean water surface for microscale breaking waves and non-breaking waves.....	125
FIGURE 3.18: PDF's of the maximum wave slope on the downwind face of the waves at a wind speed of $9.6 \text{ m}\cdot\text{s}^{-1}$ for microscale breaking waves for clean and surfactant influenced water surfaces.....	126
FIGURE 3.19: PDF's of the maximum wave amplitude at a wind speed of $9.6 \text{ m}\cdot\text{s}^{-1}$ for microscale breaking waves for clean and surfactant influenced water surfaces.....	127
FIGURE 3.20: Vertical profile of the rate of energy dissipation at a wind speed of $9.6 \text{ m}\cdot\text{s}^{-1}$ under non-breaking waves, microscale-breaking waves, entire flow field and background flow field. (a) Clean water surface, (b) Surfactant influenced water surface.....	128
FIGURE 3.21: Vertical profiles of the rate of energy dissipation beneath microscale-breaking waves. (a) Clean water surface, (b) Surfactant influenced water surface.....	129

FIGURE 3.22: Plot of the mean square of the maximum wave slope on the downwind face of the waves versus the rate of energy dissipation averaged over top 2-cm layer for clean and surfactant influenced water surfaces.....	130
FIGURE 3.23: Plot of the fraction of the total momentum transferred to wave drag versus the percentage of microscale breaking waves P_b , for clean and surfactant-influenced water surfaces.....	131
FIGURE 3.24: Plot of the bulk gas transfer velocity, k_G versus the percentage of microscale breaking waves P_b , for clean and surfactant-influenced water surfaces.....	132
FIGURE 4.1(a-d): A sequence of four DPIV instantaneous vorticity contour plots at a wind speed of $9.6 \text{ m}\cdot\text{s}^{-1}$	165
FIGURE 4.2: Plot showing the coherent structures identified by applying the vorticity threshold to the raw instantaneous vorticity field (i.e. no interpolation) at a wind speed of $9.6 \text{ m}\cdot\text{s}^{-1}$	167
FIGURE 4.3: (a) Contours of the instantaneous vorticity beneath the crest of a microscale-breaking wave at a wind speed of $9.6 \text{ m}\cdot\text{s}^{-1}$. (b) Plot showing the coherent structures identified by applying the vorticity threshold on the instantaneous vorticity field shown in panel (a). Vorticity data was interpolated by a factor of 4.....	168
FIGURE 4.4: Probability density function (PDF) of λ , the nominal size of the coherent structures at wind speed of $3.8 \text{ m}\cdot\text{s}^{-1}$, (a) no interpolation and interpolating by a factor of 4. (b) interpolating by a factor of 24 and a factor of 4.....	169
FIGURE 4.5: Probability density function (PDF) of λ , the nominal size of the coherent structures for different wind speeds. (a) clean water surfaces, (b) surfactant-influenced water surfaces.....	170
FIGURE 4.6: Probability density function (PDF) of the maximum vorticity of the coherent structures at different wind speeds, positive values are the counter clockwise vortices and negative values are the clockwise vortices. (a) Clean water surfaces, (b) surfactant-influenced water surfaces.	171

FIGURE 4.7: The total kinetic energy of coherent structures versus wavenumber ($k=2\pi/\lambda$) at different wind speeds. (a) For clean water surfaces, (b) for surfactant-influenced water surfaces.....172

FIGURE 4.8: Comparison between the total kinetic energy of coherent structures versus wavenumber at a wind speed of 9.6 m.s^{-1} for clean and surfactant-influenced water surfaces.....173

FIGURE 4.9: Plot of the average length scale of the coherent structures as a function of wind speed for clean and surfactant-influenced water surfaces.....174

FIGURE 4.10: Plot of the average maximum vorticity of the coherent structures versus wind speed for clean and surfactant-influenced water surfaces.....175

FIGURE 4.11: The frequency of occurrence of coherent structures versus wind speed for clean and surfactant-influenced water surfaces.....176

FIGURE 4.12: The total air-water gas transfer velocity normalized to a Schmidt number of 600, versus wind speed for clean and surfactant-influenced water surfaces.....177

FIGURE 4.13: Measured bulk gas transfer velocity normalized to a Schmidt number of 600 versus the fraction of the surface area renewed by eddies for clean and surfactant-influenced water surfaces.....178

FIGURE 4.14: The percentage of microscale-breaking waves versus the fraction of the surface area renewed by eddies for clean and surfactant-influenced water surfaces.....179

List of Symbols

a	Wave amplitude.
a_1	Constant.
C_1	Constant.
C_2	Constant.
C_r	Roughness constant.
D	Molecular diffusivity of the gas in the liquid.
$D(k)$	Dissipation spectrum.
f_{CO_2}	Frequency of CO ₂ pulses.
f_{CS}	Frequency of occurrence of coherent structures.
f_d	Dominant intrinsic wave frequency.
$F(\omega)$	Energy spectrum of the wave amplitude time series.
g	Gravitational acceleration.
H_{rms}	Root mean square (RMS) wave height.
H_s	Significant wave height.
k	Wavenumber.
k_e	Gas transfer velocity inside the energetic areas.
k_G	Gas transfer velocity.
k_{me}	Wavenumber of the most energetic coherent structures.
k_q	Gas transfer velocity inside the quiescent areas.
KE	Kinetic energy of coherent structures.
n	Constant.
N	Constant (threshold factor).
N_{DS}	Number of microscale-breaking waves identified by the detection scheme.
N_{FN}	Number of falling negative waves.
N_{FP}	Number of falling positive waves.
N_V	Number of microscale-breaking waves identified by IR visual inspection.
N_c	Number of microscale-breaking waves identified by both schemes.
P	Probability density function.
P_b	Percentage of breaking waves.

R	Longitudinal spatial correlation.
Re_*	Roughness Reynolds number.
S	Wave slope.
S_c	Schmidt number.
S_M	Maximum mean shear.
S_{max}	Maximum wave slope.
S_{rms}	Root mean square (RMS) wave slope.
T	Top width of coherent structures.
T_m	Mean top width of coherent structures.
T_{skin}	Water skin temperature.
T_{thres}	Threshold temperature.
u	Instantaneous stream wise velocity.
\bar{u}	Mean stream wise velocity.
u'	Turbulent stream wise velocity.
u_*^a	Friction velocity in the air.
u_*^w	Friction velocity in the water.
u^+	Non-dimensional stream wise velocity in the universal wall coordinates.
\tilde{u}	Wave-induced velocity component.
U_∞	Wind speed.
U_s	Surface velocity.
U_{SL}	Lagrangian surface drift velocity.
U_{stokes}	Stokes drift velocity.
$U(z)$	Mean wind velocity.
w'	Vertical turbulent velocity component.
X	Horizontal coordinate.
Y	Longitudinal coordinate.
z	Vertical height above the interface.
z_{oa}	Roughness length in the air.
z_{ow}	Roughness length in the water.
α	Constant.
Δy	Difference in the y coordinate.

Δt	Time interval between the images.
η	Kolmogorov length scale.
η_{max}	Maximum wave amplitude.
ε	Rate of turbulent kinetic energy dissipation.
ε_{av}	Depth averaged rate of turbulent kinetic energy dissipation.
Φ	Fraction of the surface occupied by energetic areas.
Φ_u	Wave number spectrum of the stream wise velocity.
γ_i	Fraction of time.
κ	Von Karman constant.
λ	Nominal size of coherent structures.
λ_d	Dominant wavelength.
λ_{me}	Nominal size of the most energetic coherent structures.
μ	Dynamic viscosity.
ν	Kinematic viscosity.
ρ_a	Air density.
ρ_w	Water density.
σ_T	Standard deviation.
τ	Characteristic timescale.
τ_a	Shear stress in the air.
τ_w	Shear stress in the water.
τ_v	Viscous shear stress.
ω	Radian frequency.
ω_{max}	Maximum vorticity of coherent structures.
ω_b	Mean value of the background vorticity.
Ω	Angular velocity of an eddy.
Ω_{max}	Maximum vorticity variance.
ζ	Water depth in the wave-following coordinate system.
ζ^+	Non-dimensional water depth in the universal wall coordinates.

Chapter 1

Introduction

The topic of this study is in the area of environmental fluid mechanics, focusing on the study of the effect of surfactants on the flow beneath microscale-breaking waves. Microscale-breaking waves are small-scale breaking waves for which surface tension is sufficiently strong to prevent air entrainment. Microscale-breaking waves occur at low to moderate wind speeds (i.e. 4 to 12 m.s⁻¹) and they are in the order of (0.1-0.5) m in length, less than a centimeter in amplitude and have a bore-like crest directly preceded by parasitic capillary waves riding along the forward face (Figure 1.1). A typical microscale-breaking wave produces a high level of turbulence in its wake and turbulent region beneath its crest (Figure 1.1). In the field microscale breakers are far more wide spread than whitecaps and therefore, it has been speculated that microscale-breaking may be important in controlling the flux of heat, gas and momentum across the air-sea interface. Previous laboratory wind wave experiments have demonstrated the importance of microscale-breaking in controlling the flux of gas, heat and momentum. Zappa *et al.* (2001) showed that microscale wave breaking is the physical process that determines the gas transfer rate at low to moderate wind speeds. Siddiqui *et al.* (2001) found that the turbulent wakes produced by microscale-breaking waves lead to enhanced air-water heat transfer rates. Siddiqui and Loewen (2005) demonstrated that microscale-breaking waves generate strong near-surface turbulence and enhanced the rate of turbulent kinetic energy dissipation.

Recent observations suggest that surface-active materials present naturally in lakes and seas and also adventitiously in laboratory wind-wave tanks have a significant effect on free surface behavior and hence on the rate of gas transfer (Frew *et al.* 1995; 2004). The presence of surfactants cause the air-water interface to behave similar to a rigid surface, as the surface stress is too weak to overcome the restoring force of the surfactant monolayer. In addition, surfactants influence the propagation characteristics of waves and alter the near-surface turbulent length and velocity scales (Mass and Milgram 1998). These effects are thought to inhibit surface renewal and therefore reduce the rate of air-water gas and heat transfer Saylor *et al.* (2000). Recent laboratory experiments in a wind-wave tank have shown that the presence of a surfactant reduces the occurrence of microscale-breaking waves and that this was accompanied by a 60% reduction in the gas transfer rate (Zappa *et al.* 2001).

The next three chapters are in the form of three papers that present the main three objectives of this research, which are to:

1. Investigate the properties of the aqueous boundary layer beneath the air-water interface and how surfactants affect these properties.
2. Examine how surfactants change the kinematics, frequency and geometry of microscale-breaking waves and to determine the influence of surfactants on the near-surface turbulence generated by microscale-breaking waves.
3. Determine the characteristics of coherent structures generated beneath the interface by wind waves and to investigate the contribution of microscale-breaking waves to air-water gas transfer and how it is changed in the presence of a surfactant.

A series of experiments were conducted in August 2001 in a wind-wave flume at the University of Washington, Seattle, USA. Measurements were made at wind speeds from 4 to 10 m·s⁻¹ with clean and surfactant contaminated water. An infrared imager was used to detect microscale-breaking waves since the absence of air entrainment makes them very difficult to detect using conventional video. Digital Particle Image Velocimetry (DPIV) was used to measure the two dimensional turbulent velocity fields beneath the microscale-breaking waves. Circular heated patches generated at the water surface using a CO₂ laser were used in conjunction with the infrared imager to detect the surface drift velocity. Bulk gas transfer velocities were measured during these experiments for two gases, He and SF₆, by supersaturating the water with the gases and measuring the decrease in their concentration over time. These experiments were unique because they were the first to investigate the flow fields beneath microscale-breaking waves for clean and surfactant contaminated water surfaces.

The collected data were processed and analyzed in order to achieve the goals listed above. A description of the experimental setup, properties of the aqueous boundary layer and a detailed discussion of the momentum flux transfer across the air-water interface beneath clean and surfactant-influenced water surfaces are presented in Chapter 2. The rate of turbulent kinetic energy dissipation, an algorithm for detecting microscale-breaking waves, and the characteristics of microscale-breaking waves and non-breaking waves are presented in Chapter 3. Measured gas transfer velocities and the effect of surfactants and microscale-breaking waves are also discussed in Chapter 3. In Chapter 4, a scheme for detecting coherent structures

and the characteristics of coherent structures are presented. Measured gas transfer velocities are compared to values predicted using a surface renewal model in Chapter 4. Conclusions and recommendations for future work in this area are given in Chapter 5.

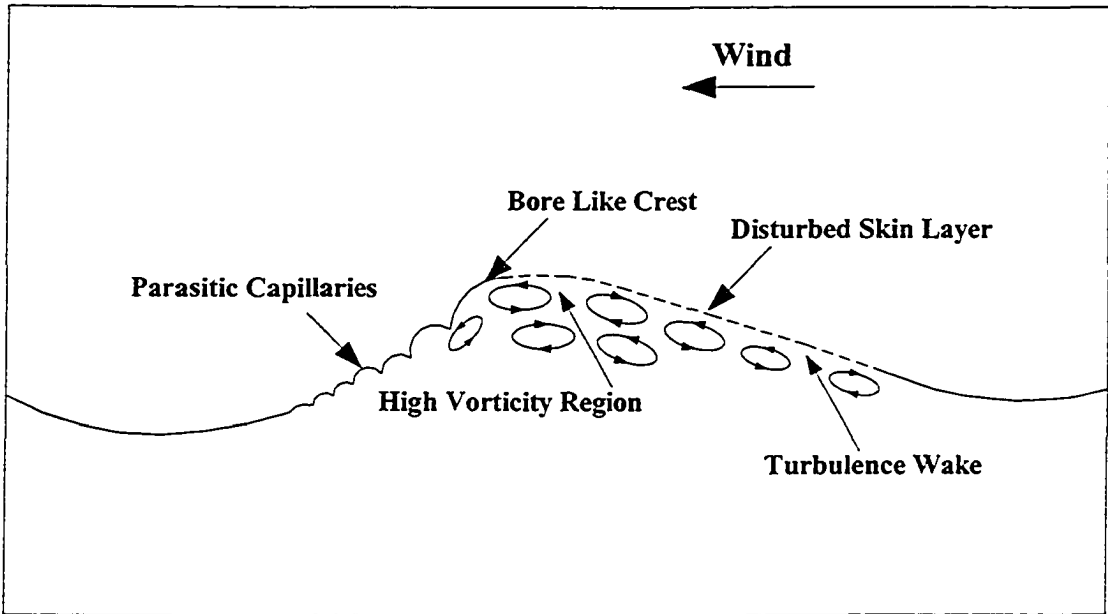


Figure 1.1: Sketch illustrating the conceptual model of a microscale-breaking wave. The significant characteristics are the bore-like crest directly preceded by parasitic capillary waves riding along the forward face and the generation of high vorticity and a turbulent wake. The dashed line represents the disturbed skin layer due to the near-surface turbulence below the air-water interface.

Chapter 2

Aqueous Boundary Layer and Momentum Transfer

2.1 Introduction

Understanding the fluid mechanics of air-water interfaces is crucial in a wide range of disciplines because the transfer of momentum, mass and energy across the interface is controlled by the near-surface flow. Wind is the primary source of energy and momentum for all open water bodies (oceans, seas, lakes, etc). The presence of wind waves makes the study of air-water interfaces complicated. Recent studies indicate that understanding the nature and key features of the near-surface flows associated with small waves is fundamental to explaining the dramatic enhancement of constituent exchange that occurs in their presence (Pierson and Banner 2003). Our understanding of the physics that dominate momentum transfer at the air-water interface lags behind that of most other regions of the ocean and lower atmosphere (Donelan 1990). Models of the tropical Pacific have shown that the feedbacks between wind stress, drift currents, sea surface temperature anomalies and CO₂ transfer may have a large impact on modeling the effects of El Nino Southern Oscillation (ENSO) and global warming (Cane *et al.* 1997). Accurate parameterization of the momentum transferred from the atmosphere to the ocean is important when modeling the speed of upper ocean currents, surface divergence and the rate of upwelling in coupled ocean-atmosphere climate models (Bourassa 2000).

Most recent studies have focused on the airside or marine boundary layer (e.g. Uz *et al.* 2002). However, the waterside boundary layer or the wind-induced drift current has not received as much attention from researchers even though it is an important

component of the coupled boundary layer system that exists at the air-sea interface. The transport of momentum, gas and heat across the air-sea interface is directly influenced by the properties of the aqueous boundary layer. Accurate predictions of these transport processes are essential in modelling global weather and ocean circulation. Furthermore, because the wind drift current has a steep gradient near the water surface it influences to a large extent the diffusion, dispersion and drift of foreign mass, such as pollutants, discharged into natural bodies of water (Wu 1975).

Several wave heights above the air-sea interface the total vertical momentum flux is completely due to the turbulent flux, that is, it is equal to the turbulent shear stress (Bourassa 2000; Uz *et al.* 2002). At the air-sea interface the total stress or momentum flux is comprised of two components, the form or wave drag and the viscous or tangential stress (Uz *et al.* 2002). The tangential stress is equal to the turbulent stress that occurs just outside the viscous sublayer and the wave drag is the horizontal component of the average pressure force acting on the waves (Uz *et al.* 2002). In the underlying water this momentum flux is redistributed among the wind drift current and wave motions; and ultimately turbulence via many mechanisms such as wave breaking (Cheung and Street 1988). Waves absorb much of the momentum transferred from the wind to the water and in the absence of wave breaking they transport it horizontally (Mitsuyasu 1985). The wave drag is the rate of direct momentum transfer from the wind to the waves (Wu 1975).

The partitioning of the stress in the aqueous boundary layer, into wave-induced stresses and tangential stresses, has been investigated experimentally by a number of researchers. Using wind wave tank experiments, Wu (1968; 1975) found that for wind

speeds greater than $4 \text{ m}\cdot\text{s}^{-1}$, the ratio of the wave-induced stress to the total stress varied from 0.2 to 0.3. Hsu *et al.* (1981; 1982) also conducted wind wave tank experiments and estimated that this ratio varied from 0.4 to 0.6. Snyder *et al.* (1981) found that this ratio was 0.57 from field data. Banner and Peirson (1998) used Particle Image Velocimetry (PIV) in a wind wave tank to make direct measurements of the tangential stress in the aqueous viscous sublayer. At a fetch of 0.13 m and wind speeds from $4.8 \text{ m}\cdot\text{s}^{-1}$ to $8.1 \text{ m}\cdot\text{s}^{-1}$ the ratio of the tangential stress to the total stress was found to be approximately 1.0 (i.e. the wave-induced stress was zero). However, at fetches of 2.45 m and 4.35 m they found that this ratio varied from 0.32 to 0.62 and decreased with increasing wind speed. Recently, Bourassa (2000) reanalyzed two sets of field data of mean velocities sampled in the aqueous boundary layer. At wind speeds from $6 \text{ m}\cdot\text{s}^{-1}$ to $10 \text{ m}\cdot\text{s}^{-1}$ he estimated that the average ratio of the tangential stress to the total stress was approximately 0.2.

The velocity in the aqueous boundary layer has been observed to vary logarithmically with depth in laboratory and field studies (Wu 1975; Cheung and Street 1988; Bourassa 2000; Siddiqui and Loewen 2005). Estimates of the friction velocity and roughness length are typically obtained by fitting the measured velocity profiles to a logarithmic relationship. A boundary layer over a solid wall is fully characterized by the friction velocity and roughness length. However, because the wind-driven water surface is moving, a third parameter is required to fully characterize the aqueous boundary layer, the surface velocity.

There is considerable uncertainty in the literature regarding the properties of the aqueous boundary layer investigated in wind wave tanks. At a fetch of 11 m, Wu (1975) found that for wind speeds up to $7 \text{ m}\cdot\text{s}^{-1}$ the flow was hydrodynamically smooth.

Siddiqui and Loewen (2005) observed that for wind speeds ranging between 4.5 and 11 $\text{m}\cdot\text{s}^{-1}$, the flow was hydrodynamically smooth at a fetch of 5.5 m. Conversely, Cheung and Street (1988) concluded that for wind speeds higher than 3.2 $\text{m}\cdot\text{s}^{-1}$ the flow was hydrodynamically rough at a fetch of 13 m.

Natural and anthropogenic surfactants are often found on the surface of lakes and oceans (Frew *et al.* 2004). Surfactants are known to dampen shorter surface waves and this introduces temporal and spatial variability into the wind forcing, especially in productive areas (Uz *et al.* 2002). Therefore, for studies of the aqueous boundary layer to be relevant to the field they should include the influence of surfactants within their scope. When surfactant molecules have sufficient surface density they form surface films over regions with a wide range of sizes on the ocean surface (Mass and Milgram 1998). Most natural sea surfactants have sufficient solubility for there to be exchanges of them between the surface and the underlying bulk fluid. In the open sea, the largest sources of surfactants are phytoplankton exudates and the chemical breakdown of dead organisms (Mass and Milgram 1998).

In the absence of wind the only surface stress acting at a clean air-water interface (i.e. free of surfactants) is surface tension. Surfactants typically reduce the surface tension in proportion to their concentration at the free surface. Thus when the surfactant concentration varies along a free surface, surface tension gradients occur and these produce shear stresses, thus altering the boundary condition (Lang and Gharib 2000). Surfactants are important to the dynamics of free-surface flows because their presence influences the behavior of the near-surface turbulence (Lang and Gharib 2000). Specifically, studies of turbulent processes have shown that surfactants affect near-

surface turbulence length and velocity scales and inhibit surface renewal (Frew *et al.* 1995). Surfactants affect not only the dissipation terms of the wave energy budget, but also the wind wave growth and mixing terms (Frew *et al.* 1995).

The objective of this study is to improve our understanding of the aqueous boundary layer beneath clean and surfactant-influenced water surfaces. Specifically, the focus of this chapter is on the properties of the mean flow in the aqueous boundary layer and the partitioning of the stress into tangential and wave-induced components. Results from a series experiments in a laboratory wind-wave tank are reported. Particle image velocimetry (PIV) and infrared imaging (IR) techniques were used to make measurements of the near-surface flow fields. In section 2 the experimental set-up and procedures are described; in section 3 the results and properties of the aqueous boundary layer beneath clean and surfactant-influenced water surfaces are presented; in section 4, the results are discussed and analyzed; and section 5 contains the summary and conclusions.

2.2 Experimental Setup

2.2.1 Instrumentation and Methods

A series of experiments were conducted in a wind-wave tank at Harris Hydraulics Laboratory, University of Washington, Seattle, USA. Figure 2.1 is a schematic of the experimental setup and instrumentation. The wave flume is 1.18-m wide, 9.2-m long and the total water depth was maintained at 87-cm during the experiments. The flume is equipped with a centrifugal fan that is installed on the upstream end of the tank to produce wind speeds up to $11 \text{ m}\cdot\text{s}^{-1}$. A wave absorbing “beach” made of rubberized

horsehair was placed at the downstream end and a water heater and circulation pump were used to vary the water temperature. Bulk air and water temperature, wind speed and relative humidity were measured during every run. These data were sampled at a rate of 100 Hz per channel using an eight-channel A/D board. A wind sensor (OMEGA FMA-905-V) with an output voltage range 0-5 Volts was used to measure the wind velocity profile above the interface. The output voltage values were converted to wind speed values according to the sensor's calibration equation. Table 2.1 provides a summary of the environmental conditions for these experiments. The water in the tank was filtered tap water, and the surface was vacuumed before each experiment to remove accumulated surface contaminants. For surfactant-influenced runs, $1 \text{ gm}\cdot\text{m}^{-3}$ (one part per million) of the soluble surfactant Triton X-100 was added to the water. Measurements were made at five wind speeds ranging from $3.5 \text{ m}\cdot\text{s}^{-1}$ to $10.0 \text{ m}\cdot\text{s}^{-1}$ at a fetch of 5.5 m for both clean water and surfactant-influenced runs.

The two-dimensional velocity field beneath the wind waves was measured using a Digital Particle Image Velocimetry (DPIV) technique. The two-dimensional velocity field was measured in a plane parallel to the wind and intersecting the water surface as shown in Figure 2.1. The DPIV laser used in this study was a dual-cavity Minilite PIV model Q-switched Nd:YAG laser (Continuum Electro-Optics, Santa Clara, California). The Nd:YAG laser produces a horizontally polarized beam of light at a visible wavelength of 532 nm and 3 mm nominal diameter. A plano-cylindrical glass lens (Melles-Griot, Nepean, Ontario) with a focal length of -12.7 mm , was mounted and aligned such that the beam passed through the lens center to produce a plane of light parallel to the flume bed. A flat surface mirror (Edmund Industrial Optics, Barrington,

New Jersey) 200 mm by 235 mm in size angled at 45 degrees was used to reflect plane of light vertically upwards through the glass bed and into the channel. This optical setup produced a pulsed 3 mm thick light sheet directed upwards, perpendicular to the tank bed, and positioned perfectly along the centerline of the channel illuminating a plane in the flow parallel to the wind direction.

The camera used for imaging the flow field was a model TM-1040 progressive scanning high-resolution monochrome CCD camera (Pulnix, Sunnyvale, California) with 30 frames per second output rate. It captures 8-bit grayscale images with a resolution of 1008 by 1008 pixels² in size. Equipped with a 25 mm 1:1.4 camera lens (Fujinon, Deerfield, Illinois) and set at an aperture of 2.8, the camera has minimum field of view (FOV) of 9 cm length. The camera was mounted below the mean water level looking up at an angle of 8° with respect to the horizontal (see Figure 2.1) and the field of view was set to 10.2 cm wide and 10.2 cm high.

Digital images were recorded using a 733 MHz Pentium III-class personal Computer running Windows NT 4, equipped with 256 MB of RAM memory and a striped-set array of four high-speed SCSI 9.1 GB hard drives. The frame-grabbing software package Video Savant (IO Industries, London, Ontario) and Road Runner digital camera interface hardware (BitFlow, Woburn, Massachusetts) permitted real-time image acquisition to the computer at a frame rate of 30 Hz and subsequent export of individual image frames in an 8-bit tagged image file format (TIFF) for further analysis.

The timing of the laser pulses must be accurately controlled in order to use the PIV technique and to synchronize the laser pulses with the imaging system. The pulse generator that was used as the main timing control component, was a model 500A

(Berkeley Nucleonics, San Rafael, California) pulse generator. This pulse generator is used to produce laser illumination pulses very close to the end of the first frame of an image pair and very close to the beginning of the second frame of the same pair.

Silver-coated glass spheres, with a mean diameter of 15- μm and a specific gravity of 1.65 (Potters Industries, Paoli, PA) were used as seed particles for the DPIV. When using DPIV to measure the near-surface velocity field, problems are often encountered locating the true position of the interface. The problem is that in many of the DPIV images the reflected seed particles appear above the air-water interface, which makes it impossible to locate the true position of the interface. This problem is serious because reliable estimation of the near-surface velocities requires that the interface be accurately located in the DPIV images. In order to locate the interface in the DPIV images, a technique based on the fact that the laser light sheet is visible only in the water because of the high reflectivity of the seed particles, was used to measure the surface wave profiles. The waterside is brighter due to the reflection of the seed particles and therefore the difference in the gray-scale values on the airside and the waterside was used to detect the water surface in the profile images (Banner & Peirson 1998). To image the surface wave profile, where the laser light sheet intersects the water surface, a second camera a TM-9701 progressive scanning full frame 8-bit CCD camera (Pulnix, Sunnyvale, California) with a 30 frame per second output rate was used. It captures 8-bit grayscale images with a resolution of 768×484 pixels². The camera was mounted above the mean water level looking down at an angle of 18° with respect to the horizontal (see Figure 2.1). The field of view was set at 14-cm wide and 8.8-cm high in these experiments.

In order to estimate the Lagrangian surface drift velocity (U_{SL}), circular heated patches generated at the water surface using a CO₂ laser (Synrad H48-2-28S 25 watt, 10 μm wavelength) were tracked. The heated patches were generated approximately 3 cm upwind of the DPIV field of view and tracked using an infrared (IR) imager (Radiance HS Raytheon TI Systems, Dallas, TX) with a resolution of 256×256 pixels². This IR imager is sensitive to radiation in the 3-5 μm wavelength band and therefore has an optical depth of approximately 10 μm . The IR imager was mounted on top of the tank looking down at an incidence angle of 20°, with a field of view of approximately 64.3 cm \times 64.3 cm (see Figure 2.1). The imager was connected to the same personal computer as the surface profile camera. This computer was equipped with Video Savant software (IO Industries, London, Ontario) and two Road Runner digital frame grabbers (Bitflow, Woburn, MA) that acquired the 12-bit digital IR images at a rate of 120 Hz and the surface profile images at 30 Hz.

Bock *et al.* (1999) skimmed the surface continuously during their wind wave tank experiment in order to keep the water surface free from contamination. They found that surface skimming effectively eliminated any surface films due to insoluble surfactants, which existed in the tank and concluded that only the soluble surfactant that they had added to the water (e.g. Triton X-100) was altering the surface rheology. Triton X-100 is a stable-soluble surfactant that dissolves completely in water. Many researchers have used Triton X-100 to model the effect of surface-active materials on the air-water interface (e.g. Bock *et al.* 1999). The Triton X-100 concentration used in this experiment (one part per million) has been used frequently in the past in similar experiments to mimic the effect of natural surfactants

The total number of experimental runs was 10; five runs each for clean and surfactant-influenced water surfaces at wind speeds 3.8, 4.9, 6.2, 8.1 and 9.6 m·s⁻¹. For each 10 minute experimental run, 72000, 12-bit digital IR images were acquired at a rate of 120 Hz, and 18000, 8-bit DPIV images and 18000, 8-bit surface profile images were acquired at a rate of 30 Hz. To achieve simultaneous sampling of the DPIV, profile and IR images, all three cameras were synchronized. The vertical sync signal of the profile camera was used to synchronize the DPIV camera and the IR imager and the delay generator was used to trigger the start of the data acquisition. The synchronization circuit diagram is shown in Figure 2.2.

2.2.2 Experimental Procedures

In order to measure and collocate the fields of view of the DPIV and profile cameras, a collocation frame (a rigid frame with horizontal and vertical scales mounted on it) was used. The collocation frame was mounted such that the horizontal and vertical scales were in the fields of view of the DPIV and profile cameras. Before each run, digital images of the collocation frame were captured from both cameras. These images were used to convert the horizontal and vertical pixel dimensions of each camera into actual distance, to collocate the fields of view of both cameras and to scale the wave profile data when it was imported into the DPIV images. The field of view of the profile camera was set 40 mm wider than the DPIV camera's field of view to avoid any possibility of missing wave profile information in the DPIV images. In order to locate the field of view of the DPIV camera in the IR imager's field of view, vertical metal bars were installed on the collocation frame. These metal bars protruded through the water

surface and appeared as dark points in the IR images, connecting these points by a line located the DPIV plane.

To detect the location of the water surface in the wave profile images, an algorithm based on a threshold gray scale value was used. This threshold is set based on the average gray scale below the water surface. Working column by column from the top down in each image, the vertical location of the water surface was identified as the first pixel above the threshold value. Lowering the threshold value will shift the computed profiles up and increasing it will shift them down. The final threshold value was set by plotting the computed profiles on top of the original profile images and visually determining when the match was optimal. The uncertainty in computing the wave profile was estimated to be ± 0.2 mm. Figure 2.3 shows a typical profile image with the computed surface wave profile placed on top of it. Siddiqui *et al.* (2001) computed the wave properties from water surface profiles obtained from profile images using a similar technique and then compared the results with surface displacement data obtained from co-located wave gauges. Their comparison of the wave properties computed from both data sets showed that the differences in the RMS wave slope were less than 8% and the differences in the RMS wave height were less than 3%, which are acceptably small differences.

The vertical offset and angular displacement between the profile and DPIV cameras fields of view must be taken into account to accurately locate the interface in the DPIV images. To facilitate collocation and orientation of the surface profile in the DPIV images, digital images of the still water surface were captured from both profile and DPIV cameras prior to each experimental run. The interfaces were clearly visible as

straight lines in both still water surface images so these were detected in order to determine the vertical offset and angular displacement. After determining the vertical offset and angular displacement, the surface wave profile data was then scaled, collocated and imported into the corresponding DPIV images. The total error in locating the water surface in the DPIV images was estimated to be ± 0.2 mm. To estimate this error, the wave surface profiles were plotted on top of a number of DPIV images in which the interface was clearly visible. The vertical offset and angular displacement were varied by 0-3 pixels to achieve the minimum difference between the profiles. Figure 2.4 shows a typical DPIV image that has the corresponding profile computed from the image shown in Figure 2.3 plotted on it. Reflected seed particles and bright regions are clearly visible above the air-water interface in the DPIV image. This illustrates that it could be difficult to accurately locate the true position of the interface without the surface profile data.

The velocity field was estimated by computing a cross correlation between an interrogation window (48×48 pixels²) in the first image and a corresponding search window (96×96 pixels²) in the second image. A 50% window overlap was used resulting in a nominal resolution of the velocity field of 2.6 mm. With this resolution, the closest velocity measurements relative to the water surface were, on average, 1.3 mm below the surface. In most of the DPIV images, seed particles were reflected above the interface causing bright regions as mentioned earlier. If the interrogation window straddles the interface, the reflected particles will cause errors in the computation of the velocity vectors. To minimize these errors, the DPIV were preprocessed before performing the velocity field computations. The surface wave profile data was used to determine the location of the interface, then the gray scale values of all the bright regions

above the interface were set equal to the median gray scale of the image (i.e., equal to the background gray scale value) (Dabiri and Gharib 1997). The interface that was used when computing the velocity vectors was set two pixels below the true interface position to ensure that all reflected particles were excluded.

There are two main contributors to the uncertainties in DPIV measurements; the experimental conditions (which include image quality, flow field characteristics and seed particle properties) and the accuracy of the computing algorithm (Cowen and Monismith 1997). The experimental conditions were designed to minimize the uncertainty in the DPIV measurements, as will be explained later. These conditions were: the dynamic range was 8 bits, i.e., gray scale ranged from 0 for black pixels to 255 for white pixels and the average background grayscale value was 50; seed density was 15 particles per 32 by 32 pixels² interrogation window; time difference between paired DPIV images ranged from 20 milliseconds at the lowest wind speed to 6 milliseconds at the highest wind speed to detect all the velocity vectors correctly and the field of view was 10.2 by 10.2 cm². There are bias errors that occur when the estimated location of the correlation peak is shifted towards the nearest integer value and this is referred to peak locking (Fincham and Spedding 1997). In any type of image velocimetry technique where sub-pixel determination of the correlation peak is attempted, peak locking occurs. Fincham and Delerce (2000) developed a method to calculate the peak locking error (i.e., the percentage of vectors affected by peak locking error) based on the histogram of the computed velocity vectors. We used this scheme to calculate the peak locking errors and found that from 6% to 10% of the vectors were affected by peak locking. Siddiqui *et al.* (2001) and Fincham and Spedding (1997) reported that typically 15 % of velocity vectors

are affected by peak locking when using a sub-pixel fit cross correlation DPIV algorithm. Therefore, peak locking errors of 6% to 10% are acceptable.

An algorithm adapted from Siddiqui *et al.* (2001) was used to identify spurious vectors and then correct them. The cross-correlation algorithm computes a displacement vector within every interrogation region including the regions that are above the air-water interface. These vectors are meaningless and the spurious vector scheme simply discards them. Below the interface the algorithm uses the local median value of eight or fewer neighboring velocity vectors depending on the location of the given vector with reference to the water surface. Vectors are identified as spurious based on two criteria. First if the magnitude of the raw vector was less than 0.75 or larger than 1.25 times the local median value. Second if the angular difference between the raw vector and the local median value is larger than 15 degrees. We found that on average less than 2% of the velocity vectors were spurious. After correcting the spurious velocity vectors, using an adaptive Gaussian window (AGW) interpolator (Agüi and Jiménez 1987), the velocity vectors were interpolated onto a rectangular grid. The vorticity was then computed using a central difference scheme. Figure 2.5 shows a plot of the corrected and interpolated velocity field that corresponds to the DPIV image shown in Figure 2.4.

Cowen and Monismith (1997) reported that the total error in the PIV measurements is the sum of the errors due to particle diameter, dynamic range, particle density, out of plane motion, gradient, dynamic range, peak locking and AGW interpolation. We found that the velocity gradients are the largest in the top 1 cm layer at the highest wind speed, so we expect the largest error to occur there. We used the results of Cowen and Monismith (1997) to estimate the error in our PIV data since they used a

similar cross correlation algorithm and the same AGW interpolator in their analysis. We estimated the maximum percentage errors in the velocity and vorticity measurements to be 7% and 14% respectively in the near-surface layer. These errors are comparable to others; for example Siddiqui *et al.* (2001) reported errors of 7% and 14% in the velocity and vorticity measurements and Pierson (1997) reported errors of 6% in the instantaneous velocity measurements beneath wind waves, using PIV. Therefore we can conclude that the errors associated with our PIV measurements are within the acceptable range for instantaneous measurements of the velocity field.

2.3 Results

2.3.1 Wave Properties

The surface wave profile data were used to compute the root mean square (RMS) wave height (H_{rms}), significant wave height (H_s), dominant intrinsic wave frequency (f_d) and the RMS wave slope (S_{rms}). The deep-water dispersion relationship was used to estimate the dominant wavelength (λ_d) and these data are presented in table 2.1 for clean and surfactant-influenced water surfaces. The RMS wave slope was computed from the surface wave profiles that had been smoothed with a low-pass filter with a cut-off wavelength of 4.4 mm. From the wave properties shown in table 2.1, it is clear that the wave height, slope and length for surfactant-influenced water surface are less than the corresponding values for clean water surface. The waves were smaller in amplitude, shorter in length and less steep in the presence of the surfactant, as expected. For example, the RMS wave height and wave slope were reduced on average by 23% and 16%, respectively in the presence of the surfactant.

2.3.2 Surface Drift Velocity

As described earlier, heated patches generated at the water surface by a CO₂ laser and recorded with an IR imager were used to estimate the Lagrangian surface drift velocity (U_{SL}). The laser was pulsed for 40 ms and produced a 2 cm diameter heated circular patch on the water surface. The CO₂ laser pulse rate, f_{CO_2} was 0.5, 1 and 2 Hz depending on the wind speed. Table 2.2 lists the pulse rates for every experimental run. Figure 2.6 shows a typical IR image with a heated patch that appears as a bright circle. Each heated patch was separately tracked by applying an image-processing algorithm developed by Atmane *et al.* (2004) to the IR image sequences. The algorithm segments each IR image by applying a temperature threshold. The threshold temperature T_{thresh} was computed as,

$$T_{thresh} = T_{skin} + N \sigma_T \quad [2.1]$$

Where, T_{skin} is the water skin temperature (defined as the average temperature of the coldest 0.5% pixels in a given IR image), N is a threshold factor and σ_T is the standard deviation of the temperature in a given IR image (Atmane *et al.* 2004). Atmane *et al.* (2004) set N equal to 5 based on a sensitivity analysis that showed that varying this factor over a range of 3.5 to 6 had a negligible effect. The segmented image is then processed to remove bright pixels that are not linked to the heated patches. First a region of interest (ROI) is defined around the heated patch, and all the bright pixels outside the ROI are set to zero. Erosion and dilation operations are then performed within the ROI to remove bright pixels that are not connected to the heated patch. The area, and the centroid of each patch are then computed. The Lagrangian surface drift velocity is then computed using; $U_{SL} = \Delta y / \Delta t$, where Δy is the change in the y coordinate of the patch centroid in

two successive images and Δt is the time interval between the images. The average value of U_{SL} for a given run was computed by tracking 150 to 600 heated patches (see table 2.2). The standard error of the mean value of U_{SL} was less than 1.7% at all wind speeds. The values of U_{SL} for surfactant-influenced water surfaces are on average 10 % larger than for clean water surfaces. Values of U_{SL} ranged from 2.5% to 2.7 % and 2.6% to 3.0 % of the wind speed for clean and surfactant-influenced water surfaces, respectively.

The Stokes drift velocity, U_{stokes} can be estimated using,

$$U_{stokes} = \int \frac{2\omega^3 F(\omega)}{g} d\omega \quad [2.2]$$

where, ω is the radian frequency, $F(\omega)$ is the energy spectrum of the wave amplitude time series and g is the gravitational acceleration (Bye 1967). At each wind speed, the surface velocity (U_s) was computed by subtracting the Stokes drift velocity U_{stokes} from the Lagrangian surface drift velocity U_{SL} . The values of U_{stokes} and U_s are also listed in table 2.2.

2.3.3 Airside Friction Velocity

Vertical velocity profiles of the mean horizontal wind speed were used to compute the airside friction velocities. All of the profiles followed a semi-logarithmic velocity distribution expressed as,

$$U(z) = \frac{u_{*a}}{\kappa} \ln\left(\frac{z}{z_{oa}}\right) \quad [2.3]$$

where $U(z)$ is the mean wind velocity, u_{*a} is the airside friction velocity, κ is the Von Karman constant ($\kappa = 0.4$), z is the vertical height above the interface (positive upwards) and z_{oa} is the airside roughness length. The airside friction velocity, u_{*a} and the

roughness length, z_{oa} were obtained by performing a linear regression between $U(z)$ and $\ln(z)$. The correlation coefficient between the measured velocity profiles and equation [2.3] had an average value of 0.98, which confirms that the wind velocity profiles were semi-logarithmic. In table 2.2 values of u_{*a} and z_{oa} at each wind speed for clean and surfactant-influenced water surfaces are tabulated. Values of u_{*a} and z_{oa} for the surfactant-influenced water surface were on average 15% and 30% less respectively, than the corresponding values for the clean water surface. This was expected since the presence of a surfactant makes the water surface smoother. In Figure 2.7, the ratio of the surface velocity to the wind friction velocity, U_s/u_{*a} is plotted versus the wind speed for both water surface conditions. The average values of U_s/u_{*a} were 0.41 and 0.51 for clean and surfactant-influenced water surfaces, respectively.

2.3.4 Aqueous Boundary Layer

2.3.4.1 Mean Velocity Profiles

The instantaneous velocity fields in a fixed Eulerian coordinate system were obtained from the DPIV measurements. This velocity data was transformed to a wave-following Eulerian coordinate system, in which the air-water interface is the origin (Hsu *et al.* 1981). In this wave-following coordinate system, the vertical coordinate $\zeta = 0$ is at the interface and the negative ζ axis points downwards parallel to the gravity vector. The horizontal and vertical spacing between velocity grid points was 2.6 mm. Therefore, the instantaneous free surface was located anywhere from 0 mm to 2.6 mm above the closest grid point to the interface. Therefore, the first grid point below the interface was located on average at $\zeta = -1.3$ mm.

The deepest possible velocity measurements in the wave-following coordinate system were 5.9 cm below the interface at the highest wind speed ($9.6 \text{ m}\cdot\text{s}^{-1}$) and 7.5 cm below the interface at the lowest wind speed ($3.8 \text{ m}\cdot\text{s}^{-1}$) for the clean water surface runs. Depths larger than these were located below the field of view of the DPIV camera, which was approximately 10 cm by 10 cm. Therefore the velocity data were transformed into the wave-following coordinate system only to a maximum depths of $\zeta = -5.9 \text{ cm}$ to $\zeta = -7.5 \text{ cm}$ for the clean water surface runs. The corresponding maximum depths for the surfactant-influenced runs were $\zeta = -6.7 \text{ cm}$ and $\zeta = -8.07 \text{ cm}$ at the highest and lowest wind speeds, respectively.

The mean velocity components were obtained by time-averaging 10 minutes of instantaneous velocity measurements at a given grid point in the wave-following coordinate system. The standard error of the mean of the time-averaged velocities was 0.1% at the first grid point at the highest wind speed and this was the maximum error. The standard errors of the mean velocities were extremely small because there were 9000 samples to average at each grid point (i.e. sample rate of 15 Hz for 10 minutes). Vertical profiles of the mean stream wise velocity are shown plotted at five wind speeds in Figure 2.8(a) for clean water surfaces and in Figure 2.8(b) for surfactant-influenced water surfaces. In all cases, the mean vertical velocity component had a magnitude less than $0.4 \text{ cm}\cdot\text{s}^{-1}$, which indicates that there is no significant systematic error in the velocity measurements. As shown in Figures 2.8(a)&(b), the mean horizontal velocity increases with wind speed and decreases monotonically with depth.

Figure 2.9 shows a comparison of the vertical profiles of the mean stream wise velocity for clean and surfactant-influenced water surfaces at the wind speeds 6.3 and 9.6

m·s⁻¹, respectively. It can be seen that the magnitudes of the mean stream wise velocities beneath the surfactant-influenced water surface were typically smaller than beneath the clean water surface. It is evident from Figure 2.9 that the near-surface velocity gradients are greater beneath the surfactant-influenced water surface at both wind speeds. When the mean streamwise velocity profiles shown in Figure 2.8 are plotted on a semi-logarithmic scale, the profiles were found to be linear. Therefore, a semi-logarithmic equation will be a good approximation to the mean stream wise velocity profiles.

2.3.4.2 Velocity Defect Law

The mean stream wise velocity profile in a neutral aqueous boundary layer can typically be expressed as a velocity defect law,

$$\frac{U_s - \bar{u}(\zeta)}{u_{*w}} = \frac{1}{\kappa} \ln\left(\frac{\zeta}{z_{ow}}\right) + C_r \quad [2.4]$$

where U_s is the surface velocity, $\bar{u}(\zeta)$ is the mean stream wise velocity, u_{*w} is the friction velocity on the waterside, κ is the Von Karman constant ($\kappa=0.4$), ζ is the water depth in the wave-following coordinate system, z_{ow} is the waterside roughness length and C_r is a roughness constant (Schlichting and Gersten 2000). The roughness Reynolds number Re_* is defined as,

$$Re_* = \frac{u_{*w} z_{ow}}{\nu} \quad [2.5]$$

where, ν is the kinematic viscosity of water. For a boundary layer over a solid wall if Re_* is less than 5, the flow is hydraulically smooth and equation [2.4] can be written in the following form,

$$\frac{U_s - \bar{u}(\zeta)}{u_{*w}} = \frac{1}{\kappa} \ln \left[\frac{\zeta u_{*w}}{\nu} \right] + 5. \quad [2.6]$$

If Re_* is larger than 70, the flow is hydraulically rough and $C_r = 8$ in equation [2.4] (Schlichting and Gersten 2000). If the value of Re_* is between 5 and 70 then the flow is in the transitional regime. The value of the constant C_r in equation [2.4] varies from 8 to 9.6 depending on the value of the roughness Reynolds number Re_* in the transitional flow regime (Schlichting and Gersten 2000, p528).

The mean stream wise velocity profiles can be plotted in the form of a velocity defect law in universal wall coordinates, that is u^+ versus $\ln(\zeta^+)$ where u^+ is defined as,

$$u^+ = [U_s - \bar{u}(\zeta)] / u_{*w} \quad [2.7]$$

and ζ^+ is defined as,

$$\zeta^+ = \zeta u_{*w} / \nu \quad [2.8]$$

Three layers are typically defined for a boundary layer over a smooth solid wall. A viscous sublayer exists adjacent to the wall at $\zeta^+ < 5$ and in this layer $u^+ = \zeta^+$. A logarithmic layer, in which the velocity varies logarithmically with depth, typically exists at $\zeta^+ > 30$. The buffer layer is found at $5 < \zeta^+ < 30$ and in this layer the velocity profile is neither linear nor logarithmic.

U_s and $\bar{u}(\zeta)$ were measured as described previously leaving three unknowns in equation [2.4], u_{*w} , z_{ow} and C_r . The mean velocity profiles were observed to be logarithmic and therefore, u_{*w} and z_{ow} can be determined at each wind speed by performing a least squares fit of the mean velocity data to equation [2.4]. The average value of the correlation coefficient was 0.99 confirming that the mean velocity profiles were logarithmic. However, the slope and intercept of the logarithmic equation can only be used to solve for two unknowns. Estimates of u_{*w} are obtained directly from the slope of $\bar{u}(\zeta)$ versus $\ln(\zeta)$. Values of C_r were obtained from Schlichting and Gersten (2000,

Figure 17.8, p528) and estimates of z_{ow} from the intercept of $\bar{u}(\zeta)$ versus $\ln(\zeta)$. However, C_r is a function of Re_* which is proportional to z_{ow} and therefore, an iterative scheme was required. It normally took 10 iterations to obtain accurate values of C_r and z_{ow} for each experimental run. It should be noted that estimates of z_{ow} are very sensitive to variations in U_s and u_{*w} . For example, a 5% variation in the value of U_s may cause up to a 100% variation in z_{ow} .

The values of u_{*w} , z_{ow} , C_r and Re_* obtained using this scheme are listed in table 2.3. The values of z_{ow} for the surfactant-influenced water surfaces are on average 20% smaller than the values for the clean water surface at the same wind speed. This is evidence that the surfactant made the aqueous boundary layer smoother. At the same wind speed the values of u_{*w} were on average 20% larger for the surfactant-influenced water surface compared to the clean surface. The values of Re_* ranged from approximately 10 to 30 for both clean and surfactant-influenced water surfaces at all wind speeds. This indicates that the aqueous boundary layer was in the transitional flow regime for all conditions in these experiments.

Plots of u^+ versus $\ln(\zeta^+)$ for clean and surfactant-influenced water surfaces are shown in Figures 2.10(a)&(b), respectively. The dotted lines represent the law of the wall for a turbulent boundary layer with a zero pressure gradient over smooth and rough walls (Schlichting and Gersten 2000). The measured velocity profiles all lie between the smooth and rough wall curves, confirming that under all conditions the aqueous boundary layer was in the transitional regime, between hydrodynamically smooth and rough. A comparison between Figures 2.10(a)&(b) indicates that the surfactant-influenced water

surface profiles were slightly smoother than the clean water surface profiles at the same wind speed.

In Figure 2.11(a) the shear stress in the air or the total stress, τ_a , is plotted versus wind speed for clean and surfactant-influenced water surfaces. At the lowest wind speed the total stress is approximately equal but on average the values of τ_a were 22% lower in the presence of a surfactant. This is consistent with Uz et al. (2002) who reported that τ_a decreased by 20-30% at a given wind speed in the presence of a surfactant. In Figure 2.11(b) the shear stress in the water or the tangential stress, τ_w is plotted versus the wind speed for clean and surfactant-influenced water surfaces. The surfactant produced an increase in the waterside shear stress that varied from 10% to 60% with an average increase of 36%.

2.4 Discussion

Bourassa (2000) stated that most previous observations of currents in the aqueous boundary layer in the field or laboratory were limited to the upper few centimeters of the flow. He found that estimates of u_{*w} and z_{ow} were inaccurate if the logarithmic equation was fitted to mean velocity data located too close to the water surface. His reasoning was that a roughness sublayer typically exists near the water surface and velocity data within this layer do not follow a logarithmic equation. Bourassa (2000) also noted that the uncertainties in calculating u_{*w} and z_{ow} are highly dependent on the number of observation depths within the logarithmic layer and that the minimum number is three.

Therefore, in order to obtain accurate estimates of u_{*w} and z_{ow} , the mean velocity data were fitted to equation [2.4] for non-dimensional depths $\zeta^+ > 100$. This limit on ζ^+ was

selected after examining plots of $\bar{u}(\zeta)$ versus $\ln(\zeta)$ and noting that a change in slope occurred in the range $100 < \zeta^+ < 200$ in most cases (see Figure 2.10). This change in slope was interpreted as an indication that a buffer layer or a roughness sublayer existed at smaller values of ζ^+ depending on wind speed and surface condition. This assumption was supported by the fact that the average value of the correlation coefficient for the least squares fit to equation [2.4] was 0.99 indicating that the velocity profiles were clearly logarithmic. The minimum number of velocity data points used to fit equation [2.4] within the logarithmic layer (i.e. $\zeta^+ > 100$) was 22.

Values of u_{*w} can also be estimated from,

$$u_{*w} = \sqrt{\frac{\tau_v}{\rho_w}} \quad [2.9]$$

where, ρ_w is the water density and τ_v is the shear stress just below the interface and it is given by,

$$\tau_v = \mu \frac{d\bar{u}}{d\zeta} = \mu \frac{(U_s - \bar{u}_1)}{\Delta\zeta} \quad [2.10]$$

where, μ is the dynamic viscosity of the water, U_s is the surface velocity, \bar{u}_1 is the mean stream wise velocity at the first grid point, and $\Delta\zeta = 1.3$ mm. Table 2.3 compares values of u_{*w} computed from equation [2.4] and equation [2.9] and the percentage differences were found to be less than 10% in all cases. This close agreement confirms that fitting equation [2.4] as described above produced accurate estimates of u_{*w} . The fact that equation [2.9] is valid between the water surface and the first grid point indicates that a viscous sublayer existed in this region.

There have been numerous studies of the effect of surfactants on free surface flows (e.g. Lang and Gharib 2000) and on their influence on air-water gas transfer (e.g. Frew *et al.* 1995). However, to our knowledge, this study is the first to examine the properties of the wind drift turbulent layer beneath clean and surfactant-influenced water surfaces. Wu (1975), Cheung and Street (1988), Thais and Magnaudet (1996) and Siddiqui and Loewen (2005) reported results from similar experiments but for clean water surfaces only. We will first compare our clean water surface results to theirs and then discuss the effect of the surfactants on the aqueous boundary layer.

Figure 2.10(a) shows the mean velocity profiles plotted in the form of a velocity defect law in wall coordinates for clean water surfaces. All the profiles indicate that the aqueous boundary layer is hydrodynamically transitional between the smooth and rough regimes for wind speeds ranging between 3.8 and 9.6 m·s⁻¹. There is considerable uncertainty in the literature regarding the properties of aqueous boundary layers. Studying the aqueous boundary layer at a fetch of 11m, Wu (1975) found that the roughness Reynolds number, Re^* was in the range of 5 to 10 for wind speeds up to 7 m·s⁻¹ and concluded that the flow was hydrodynamically smooth. Siddiqui and Loewen (2005) found that for wind speeds ranging between 4.5 and 11 m·s⁻¹, the flow is hydrodynamically smooth at a fetch of 5.5 m. However, Cheung and Street (1988) studied the aqueous boundary layer at a fetch of 13 m and concluded that for wind speeds higher than 3.2 m·s⁻¹ the flow was hydrodynamically rough. These inconsistent results are most likely caused by uncertainties in estimating u_{*w} and z_{0w} .

Siddiqui and Loewen's (2005) measurements were similar to this study. They were carried out in the same wind wave tank, at the same fetch and over a similar range of

wind speeds but only for clean water surfaces. The most significant difference between the two data sets was that in this study the velocity measurements extended significantly deeper into the water column. The maximum depth of their mean velocity profiles were limited to 2.5 cm because of the limited vertical field of view of their PIV camera. In this study a higher resolution PIV camera was used and this allowed the maximum depth of the velocity profiles to be increased up to 8 cm. As discussed previously, if equation [2.4] is fitted to velocity data at values of $\zeta^+ < 100$ (i.e. too close to the interface) the estimated values of u_{*w} and z_{ow} may be inaccurate. The maximum non-dimensional depths of Siddiqui and Loewen's (2005) velocity profiles ranged from $\zeta^+ = 100$ to 200. Consequently, their estimates of u_{*w} and z_{ow} were computed by fitting the velocity defect law to profiles that probably included data points within the buffer or roughness sublayer. At comparable wind speeds their estimates of u_{*w} are approximately two-thirds of the values presented in table 2.3 for clean water surfaces. Estimates of z_{ow} are very sensitive to changes in u_{*w} and as a result their estimates of z_{ow} are several orders of magnitude smaller than the values presented in table 2.3. This explains why their values of the roughness Reynolds number were all less than one and why they reported that the velocity profiles were all in the smooth flow regime.

Wu (1975) measured the drift current below the water surface by timing the passage of submerged floats of various sizes between two stations. Subsequently friction velocities u_{*w} were obtained from the slope of the observed logarithmic velocity profiles. The surface drift velocities were estimated by extrapolating the logarithmic velocity profiles to the water surface. Wu (1975) then used the rough wall velocity defect law (i.e. equation [2.4] with $C_r = 8.5$) to estimate values of z_{ow} . His estimates of u_{*w} ranged

from 0.6 to $2 \text{ cm}\cdot\text{s}^{-1}$ over a wind speed range of 4 to $10 \text{ m}\cdot\text{s}^{-1}$ which is approximately two times larger than the values presented in table 2.3. As the wind speed increased from 4 to $10 \text{ m}\cdot\text{s}^{-1}$ his estimates of z_{ow} decreased from approximately 0.05 cm to 0.01 cm . These values are approximately one order of magnitude smaller than the z_{ow} values presented in table 2.3. The increase in u_{*w} with wind speed was offset by the decrease in z_{ow} and as a result Re_* remained approximately constant in the range 5 to 10 . The fact that Wu (1975) found that z_{ow} decreased by approximately a factor of five as the wind speed increased from 4 to $10 \text{ m}\cdot\text{s}^{-1}$ suggests that there may have been systematic errors in his estimates of u_{*w} or U_s . This is perhaps not surprising given the fact that submerged wooden floats were used to measure the mean velocity profiles.

Cheung and Street (1988) measured the wind drift current below the wave troughs using a laser Doppler anemometer for depths from 0.3 to 30 cm . Their friction velocities were determined by extrapolating Reynolds stress measurements to the mean water level and their estimates of u_{*w} were approximately 60% larger than our values. These larger friction velocities may be due to the fact that Cheung and Street (1988) made measurements at a fetch of 13 m compared to 5.5 m in this study. However, it should be noted that the accuracy of their u_{*w} estimates relies on the accurate decomposition of the turbulent and wave velocity components. If the turbulent velocity component is contaminated by even a small fraction of the wave velocity component, the magnitude of the Reynolds stresses may be overestimated by a large percentage.

Thais and Magnaudet (1996) measured the instantaneous velocity field beneath wind waves using a two-component LDV system at a fetch of 26 m . They measured the mean streamwise air velocity profile with a static Pitot tube and then computed the airside

friction velocity, u_{*a} by fitting the velocity data to a logarithmic equation. The waterside friction velocity u_{*w} , was calculated by assuming that the airside and waterside shear stresses were equal at the interface (i.e. $\rho_a u_a^2 = \rho_w u_w^2$). Thais and Magnaudet's (1996) values of u_{*w} are larger than ours by a factor of 20%, 50% and 80% at wind speeds of 4.5 $\text{m}\cdot\text{s}^{-1}$, 6 $\text{m}\cdot\text{s}^{-1}$ and 7.8 $\text{m}\cdot\text{s}^{-1}$ respectively. It will be shown later in this section that the assumption that the shear stresses are equal at the interface is incorrect.

In the velocity defect law (equation [2.4]) the value of the von Karman constant, κ was assumed to be 0.40. This value was determined from experimental data gathered in solid wall boundary layers. Consequently, using equation [2.4] with $\kappa = 0.40$ implicitly assumes that the aqueous boundary layer is completely analogous to a solid wall boundary layer. However, Cheung and Street (1988) found that the value of κ was not always 0.40 beneath wind waves in their experiments. They argued that it was the influence of the waves on the mean flow that caused κ to depart from this standard value. In this study we showed that friction velocities, estimated from the slope of the logarithmic velocity profiles, agreed closely with estimates computed from the viscous shear stress. This is convincing evidence that the correct value for κ is 0.40 in the aqueous boundary layer flows in this study.

The ocean surface roughness length, z_{ow} arises as an important scaling length for defining the depth of the wave-affected layer, profiles shapes for turbulent kinetic energy, velocity and other parameters (Craig and Banner 1994). However, at the present time there is no reliable method for predicting values of z_{ow} in the ocean. This is in large part due to the fact that accurate measurements of z_{ow} either from the laboratory or the field

are scarce. For example as was stated earlier, a 5% error in the value of U_s may cause up to a 100% error in z_{ow} .

Craig and Banner (1994) estimated that the roughness length is the same order as the wave amplitude and that it is several orders of magnitude larger than the roughness length in the atmosphere. Craig (1996) used Cheung and Street's (1988) experimental data in a turbulence model to predict z_{ow} values beneath laboratory wind waves. These z_{ow} values ranged from 0.2 to 1.4 cm over a wind speed range of 3.2 to 9.9 m·s⁻¹. From these estimates he concluded that the aqueous boundary layer roughness length is approximately one sixth the dominant wavelength. In this study z_{ow} varied from 0.21 to 0.35 cm and the R.M.S. wave amplitude from 0.07 to 0.42 cm over a comparable range of wind speeds. These z_{ow} values are the same order of magnitude as Craig's (1996) estimates and the difference may be due to the difference in fetch in the two experiments, 5.5 m compared to 13 m.

In these experiments the ratio of the roughness height to the R.M.S. wave amplitude varied from 3.0 to 0.8 as the wind speed increased from 3.8 to 9.5 m·s⁻¹ with an average value of 1.6. The ratio of z_{ow} to the dominant wavelength (c.f. data in tables 1 & 3) varied from 1/20 to 1/40 and had an average value of approximately 1/30. Bye (1988) proposed using Charnock's (1955) atmospheric formula,

$$z_{ow} = \frac{a_1 u_{*w}^2}{g} \quad [2.11]$$

to predict values of z_{ow} where a_1 is a constant of order 1400. Using the values of z_{ow} and u_{*w} measured beneath clean water surfaces from table 2.3, values of a_1 computed using equation [2.11] ranged from 460 to 760 with an average value of 650. Using equation

[2.11] with $a = 650$ gives z_{ow} values that are on average within 15% of the measured values beneath clean water surfaces.

The results shown previously demonstrated that the surfactants altered the properties of the boundary layers in both the air and the water. The waves had lower heights, shorter wavelengths and smaller slopes in the presence of a surfactant. This produced a smoother interface and hence smaller friction velocities and roughness heights in the air. In the aqueous boundary layer the friction velocities were approximately 20% larger with a surfactant and at the same time the roughness lengths were approximately 20% smaller. This resulted in roughness Reynolds numbers that were approximately the same beneath clean and surfactant-influenced water surfaces at the same wind speed. However, the plots of the velocity defect law in wall coordinates in Figure 2.10(a)&(b) show that the mean velocity profiles beneath the surfactant-influenced water surfaces are shifted up compared to the clean water surface profiles, closer to the smooth wall equation. This shift is due to the fact that the surface drift velocities were approximately 10% larger in the presence of a surfactant. If the aqueous boundary layer flows are completely analogous to a solid wall boundary layer the shift in the profiles would indicate that the surfactant caused the flow to be hydrodynamically smoother. However, the fact that the roughness Reynolds numbers are approximately equal at the same wind speed, for both water surface conditions, indicates that the flow regimes are very similar despite the fact that the velocity profiles are shifted.

In Figure 2.7 values of the ratio U_s/u_{*a} are shown plotted as a function of wind speed. One notable feature of this plot is the fact that the presence of a surfactant caused this ratio to increase on average by 0.1. This shift is caused by the fact that the tangential

shear stress τ_w is larger at a given wind speed when a surfactant is present (see Figure 2.11(b)). This is reasonable because the surface drift velocity is controlled by the magnitude of the tangential stress not the total stress. A number of previous laboratory investigations have provided estimates of U_s/u_{*a} that can be compared to the results in Figure 2.7. Wu (1975) found that the average value of U_s/u_{*a} was 0.55 and Cheng and Mitsuyasu (1992) reported an average value of \bar{U}_s/u_{*a} of 0.52. Peirson and Banner (2003) stated that this ratio varied from 0.23 to 0.30 between the wave trough and the crest of wind waves. Zhang and Harrison (2004) measured the surface drift using PIV applied to IR images and reported that U_s/u_{*a} was approximately 0.30. These results can be reconciled with the data in Figure 2.7 in the following way.

First, it should be noted that in Figure 2.7 the ratio U_s/u_{*a} varies from approximately 0.3 to 0.6 depending on wind speed and surface cleanliness. This range encompasses all of the previous results with the exception of Peirson and Banner's (2003) measurements beneath the troughs of laboratory wind waves. In other words the variations in previous measurements of U_s/u_{*a} may be explained by changes in surface cleanliness and wind speed that cause the tangential stress to increase. The trend in the values of U_s/u_{*a} is similar in Figure 2.7 for both clean and surfactant-influenced water surfaces. As the wind speed increased from 3.8 to 6 m·s⁻¹ the decrease in U_s/u_{*a} was caused by the fact that the total stress, τ_a increased by a factor of approximately 4.6 while the tangential stress, τ_w only increased by a factor of approximately 1.6. However, as the wind speed increased from 6 to 10 m·s⁻¹ the total stress and the tangential stress both increased by approximately a factor of two. This is reflected by the fact that the ratio

U_s/u_{*a} is approximately constant over this wind speed range for both water surface conditions.

The fact that the surface drift velocities and the aqueous friction velocities were both larger implies that a greater fraction of the total vertical momentum flux is transferred to the near-surface current in the presence of a surfactant. The total stress or total vertical momentum flux is equal to the sum of the tangential and wave induced components when the wave field is locally uniform (Melville 1996). Accordingly, the ratio of the tangential stress to the total stress (i.e. τ_w/τ_a) quantifies the partitioning of the total stress into wave-induced stress and tangential stress in the aqueous boundary layer. In Figure 2.12 the ratio of τ_w/τ_a is plotted versus the wind speed for clean and surfactant-influenced water surfaces. It can be seen that this ratio decreases from approximately 0.8 to 0.2 for clean water surfaces and from 0.9 to 0.3 for surfactant-influenced water surfaces as the wind speed increases. The values of τ_w/τ_a for the surfactant-influenced water surfaces are larger than the clean water surface values, at the same wind speed, because the tangential stress values are higher and the total stress values are lower when a surfactant is present (see Figure 2.11).

It was shown in Figure 2.11(a) that the presence of a surfactant reduced the total stress τ_a , above the air-water interface because the water surface became smoother, that is, the waves became smaller and less steep. At the same time, the surfactant caused the tangential stress in the water τ_w , to increase as was shown in Figure 2.11(b). Consequently, the fraction of the total momentum transferred from the wind to the drift current is larger in the presence of a surfactant. In other words the fraction of the total momentum transferred to the waves is smaller. Hence, it can be concluded that the

fraction of the momentum transferred to the aqueous boundary layer is increased when either the wind speed is significantly decreased or if a surfactant is present.

The trend in stress ratios plotted in Figure 2.12 can also be explained in terms of the wave slope. As the wind speed increased the wave slope increased monotonically for a given surface condition (see table 2.1). The addition of a surfactant reduced the R.M.S. wave slope by 16% at a given wind speed. The wave slope is a measure of the physical roughness of the water surface and therefore, it should have a direct influence on the partitioning of the total stress. When the wave slope increases the water surface becomes physically rougher and it follows that the wave drag increases and the tangential drag decreases. This hypothesis is supported by the plot of τ_w/τ_a versus the mean square wave slope, $\langle S^2 \rangle$ shown in Figure 2.13. This plot indicates that there is a strong negative correlation between τ_w/τ_a and $\langle S^2 \rangle$ regardless of the cleanliness of the water surface. The trend in the data in Figure 2.13 suggests that when the mean square wave slope is less than 0.01 the ratio τ_w/τ_a is approximately 1.0, or that the wave drag is zero. When the mean square wave slope reaches 0.04 approximately 85% of the total stress is supported by the waves.

There have been a number of previous studies in the laboratory and field that reported the ratio of the tangential or wave induced stresses to the total stress. Bourassa (2000) found that the ratio of τ_w/τ_a was approximately one at a wind speed of $5 \text{ m}\cdot\text{s}^{-1}$ and that it decreased rapidly and in the wind speed range 6 to $10 \text{ m}\cdot\text{s}^{-1}$ had an average value of approximately 0.2. The magnitude and trend of his estimates of τ_w/τ_a produced using field data (see Figure 5 in Bourassa 2000) are very similar to the trend in our estimates shown in Figure 2.12. Hsu *et al.* (1981; 1982) and Snyder *et al.* (1981)

estimated the ratio of the wave induced stress to the total stress or the fraction of the momentum flux that went into the wave field (i.e. the fraction of the wave induced stress) in the laboratory and field, respectively. Banner and Peirson (1998) directly measured the ratio of the tangential stress to the total stress in a laboratory wave tank. The data from all of these studies was compiled and is plotted in Figure 2.14 as a function of the wind speed.

The trend in the data from all of the studies is similar. As the wind speed increases the fraction of the momentum flux transferred to the current or mean shear flow decreases. This consistent trend in data gathered under such diverse conditions is remarkable. The laboratory data was gathered in three different wind wave tanks at fetches from 2.45 m to 15.66 m and the field data was sampled in a lake and coastal waters. The trend is consistent but there is considerable scatter in the data. Estimating or measuring this ratio is challenging and therefore, some of this scatter may be due to errors associated with measurements or approximations. However, it is worth noting that the estimates made using data at the two shortest fetches, 2.45 m and 3.46 m, are significantly larger than the other values at comparable wind speeds. Excluding these short fetch results a large portion of the scatter can be explained by variations in the cleanliness of the water surface. That is, approximately two thirds of the data points from the other studies (excluding the short fetch results) lie in the band between our clean and surfactant data points.

Mitsuyasa (1985) derived an equation to estimate the ratio of the wave induced stress to the total stress in terms of the wave steepness ak where a is the wave amplitude

and k is the wavenumber. This equation can be rewritten to calculate the ratio of the tangential stress to the total stress τ_w/τ_a as follows,

$$\tau_w/\tau_a = 1 - 22(ak)^2 \quad [2.12]$$

In Figure 2.15 values of τ_w/τ_a predicted using equation [2.12] are compared to the experimental data. It can be seen that equation [2.12] predicts the trend of the data reasonably well and that this trend is very similar to the trend observed in Figure 2.13 since the mean square slope and wave steepness are obviously closely related. Compared to the experimental data equation [2.12] underestimates τ_w/τ_a at smaller steepnesses and overestimates it at higher steepnesses. The comparison in Figure 2.15 demonstrates that Mitsuyasu's equation is a realistic approach for predicting the partitioning of the stress for these laboratory wind waves.

The mean square slope, $\langle S^2 \rangle$ is a better integrated measure of wave slope because it includes the contributions from all wavelengths whereas, $(ak)^2$ is the steepness of the dominant waves. Therefore, it is logical to investigate how well τ_w/τ_a scales with $\langle S^2 \rangle$. A least square fit of the data plotted in Figure 2.13, τ_w/τ_a versus $\langle S^2 \rangle$, gives the following relationship,

$$\tau_w/\tau_a = 1.26 - 27.5 \langle S^2 \rangle \quad [2.13]$$

with a correlation coefficient of 0.92. This equation predicts similar values of τ_w/τ_a as Mitsuyasu's equation for corresponding values of $\langle S^2 \rangle$ and $(ak)^2$. However, equation [2.13] predicts that $\tau_w/\tau_a = 1.0$ for $\langle S^2 \rangle$ less than 0.01, whereas Mitsuyasu's equation predicts that $\tau_w/\tau_a = 1.0$ for $(ak)^2 = 0$. Physically, it is more logical that the water surface becomes smooth enough for the drag to be completely tangential at a small but non-zero

wave slope. Equation [2.13] accounts for changes in τ_w / τ_a that occur when either the wind speed or the cleanliness of the water surface changes. Equation [2.13] was obtained using data gathered at a fetch of only 5.5 m however; it may be applicable at longer fetches if it is the small scale or shorter wavelength waves that dominate the stress partitioning.

It is evident from the data presented in Figures 2.13 and 2.14 that it would be incorrect to assume that $\tau_w = \tau_a$ in most cases. If this assumption is ever accurate it will only be when the wave slope is small. The data in Figure 2.14 suggest that the wave slope becomes this small in both the laboratory and field when the wind speed is less than 3 to 4 $\text{m}\cdot\text{s}^{-1}$. For example, at wind speeds greater than 6 $\text{m}\cdot\text{s}^{-1}$ the data in Figure 2.14 shows that assuming that $\tau_w = \tau_a$ would overestimate u_{*w} by a factor of two for clean water surfaces.

2.5 Conclusion

The results from a series of experiments using DPIV to investigate the aqueous boundary layer beneath clean and surfactant-influenced water surfaces have been reported. The presence of a surfactant caused the boundary layer on both sides of the air-water interface to be smoother. That is, in the airside boundary layer the friction velocity and roughness length were reduced on average by 15% and 30%, respectively. In the aqueous boundary layer the surfactant caused the roughness length to be reduced on average by 20% but the friction velocity increased on average by 20%. At all wind speeds (3.8 to 9.8 $\text{m}\cdot\text{s}^{-1}$) the flow in the aqueous boundary layer was found to be in the transition regime for both water surface conditions.

The surfactant reduced the airside shear stress on average by 22% and increased the waterside shear stress on average by 36%. The total stress or airside shear stress is a measure of the total vertical momentum flux from the air to the water. As this total momentum flux is transferred to the water it is partitioned into the wave field and the mean flow in the aqueous boundary layer. This can be thought of as a partitioning of the total stress into tangential and wave components. It was shown that the fraction of the momentum transferred to the aqueous boundary layer, τ_w / τ_a is increased when the wind speed is significantly decreased or if a surfactant is present. As the wind speed increased from 3.8 to 9.8 m·s⁻¹ τ_w / τ_a decreased from approximately 0.8 to 0.2 for clean water surfaces and from 0.9 to 0.3 for surfactant-influenced water surfaces. The trend and magnitudes of τ_w / τ_a measured in this laboratory study were found to agree reasonably well with previous field and laboratory measurements reported in the literature.

A strong negative correlation was observed between τ_w / τ_a and the mean square wave slope irrespective of the water surface cleanliness, which is consistent with Mitsuyasu's (1985) theoretical analysis. This correlation indicates that any factor that increases or decreases the wave slope will result in a decrease or increase in the fraction of the momentum transferred to the aqueous boundary layer. Accordingly, when the mean square wave slope is less than 0.01 it was predicted that all of the momentum is transferred to the aqueous boundary layer.

Csanady (2001) described the pathways of the airside momentum flux at the air-water interface. He argued that the momentum is transferred into three paths; viscous shear stress that is quantified as τ_w / τ_a , momentum transferred into long waves that correspond to less than 6% approximately of the total momentum flux and short wave

breaking. Wave breaking generates patches of turbulence and this is the main dissipative mechanism (Csanady 2001). Assuming that the momentum flux transferred into long waves is negligible, at low wind speeds the ratio τ_w/τ_a is close to 1 and correspondingly the fraction of the momentum flux that is transferred to short waves that break is small. At high wind speeds, the ratio of τ_w/τ_a is small (e.g. 0.2 to 0.3) and the fraction of the momentum flux that is transferred to short waves that break is expected to be large.

The fraction of the momentum flux that is transferred to short waves can be expressed as $(1-\tau_w/\tau_a)$ and in Figure 2.16 this fraction is plotted versus the mean square wave slope plotted. As expected, Figure 2.16 shows that the fraction of the momentum flux transferred to waves is strongly correlated with the mean square wave slope irrespective of the water surface cleanliness. This means that as the wind speed increases, the fraction of the momentum flux transferred to the wave field increases and the waves become steeper.

From the previous discussion it can be concluded that the presence of a surfactant would reduce the occurrence of breaking waves and possibly reduce the near-surface turbulence. In the next chapter, an investigation of the effect of surfactants on breaking waves, near-surface turbulence and the rate of turbulent kinetic energy dissipation is presented.

Clean water surfaces					
U_{∞} (m.s ⁻¹)	3.79	4.89	6.23	7.99	9.53
f_d (Hz)	4.73	3.91	3.30	2.79	2.46
λ_d (cm)	6.99	10.19	14.30	20.07	25.85
H_{rms} (cm)	0.14	0.26	0.41	0.65	0.83
H_s (cm)	0.21	0.39	0.61	0.97	1.23
S_{rms}	0.14	0.18	0.19	0.20	0.21

Surfactant influenced water surfaces					
U_{∞} (m.s ⁻¹)	3.87	4.91	6.21	8.15	9.75
f_d (Hz)	5.03	3.96	3.37	2.84	2.48
λ_d (cm)	6.17	9.95	13.74	19.32	25.50
H_{rms} (cm)	0.12	0.21	0.31	0.50	0.64
H_s (cm)	0.18	0.32	0.46	0.74	0.96
S_{rms}	0.13	0.15	0.16	0.17	0.18

Table 2.1: Summary of environmental parameters for clean and surfactant-influenced water surfaces. U_{∞} is the wind speed; f_d is the dominant wave intrinsic frequency; λ_d is the dominant wavelength; H_{rms} is the root mean square wave height; H_s is the significant wave height; and S_{rms} is the root mean square wave slope. H_{rms} and H_s were computed from the surface wave profile data. The dominant wavelength was computed from the linear dispersion relationship.

Clean water surfaces					
U_{∞} (m.s ⁻¹)	3.79	4.89	6.23	7.99	9.53
f_{CO_2} (Hz)	0.50	1.00	1.00	1.00	2.00
Number of patches	150	300	300	300	600
U_{SL} (cm.s ⁻¹)	10.33	12.87	15.72	20.21	23.64
U_{stokes} (cm.s ⁻¹)	0.24	0.53	0.87	1.34	1.59
U_s (cm.s ⁻¹)	10.09	12.34	14.84	18.87	22.05
u_{*a} (cm.s ⁻¹)	18.57	27.76	41.46	60.80	63.45
z_{oa} (cm)	0.00525	0.01275	0.02764	0.06352	0.06743

Surfactant influenced water surfaces					
U_{∞} (m.s ⁻¹)	3.87	4.91	6.21	8.15	9.75
f_{CO_2} (Hz)	0.50	1.00	1.00	1.00	1.00
Number of patches	150	300	300	300	300
U_{SL} (cm.s ⁻¹)	11.49	14.97	17.05	21.67	25.48
U_{stokes} (cm.s ⁻¹)	0.17	0.37	0.51	0.75	0.86
U_s (cm.s ⁻¹)	11.32	14.60	16.54	20.92	24.62
u_{*a} (cm.s ⁻¹)	18.46	25.53	37.83	48.05	51.49
z_{oa} (cm)	0.00415	0.00909	0.02315	0.03433	0.03832

Table 2.2: Summary of velocity measurements for different experimental runs for clean and surfactant-influenced water surfaces. U_{∞} is the wind speed; f_{CO_2} is the frequency by which the CO₂ pulses used to generate the heated patch; U_{SL} is the Lagrangian surface drift velocity; U_{stokes} is the Stokes drift velocity; $U_s = U_{SL} - U_{stokes}$ is the surface velocity; u_{*a} is the wind friction velocity and z_{oa} is the roughness length in the air.

Clean water surfaces					
U_{∞} (m.s ⁻¹)	3.79	4.89	6.23	7.99	9.53
u_{*w} profile (cm.s ⁻¹)	0.52	0.58	0.60	0.71	0.86
u_{*w} vel. gradient (cm.s ⁻¹)	0.56	0.62	0.64	0.72	0.77
z_{ow} (cm)	0.21	0.23	0.27	0.31	0.35
Re_*	12.07	15.04	17.87	27.09	33.49
C_r	9.55	9.47	9.41	9.13	9.00

Surfactant influenced water surfaces					
U_{∞} (m.s ⁻¹)	3.87	4.91	6.21	8.15	9.75
u_{*w} profile (cm.s ⁻¹)	0.55	0.73	0.75	0.88	0.95
u_{*w} vel. gradient (cm.s ⁻¹)	0.55	0.70	0.75	0.82	0.90
z_{ow} (cm)	0.15	0.18	0.22	0.25	0.30
Re_*	10.51	14.19	18.90	24.81	29.22
C_r	9.66	9.50	9.40	9.24	9.06

Table 2.3: Summary of velocity defect law results for clean and surfactant-influenced water surfaces. U_{∞} is the wind speed; u_{*w} profile is the water friction velocity calculated from the mean velocity profiles using the velocity defect law equation; u_{*w} velocity gradient is the water friction velocity below the interface calculated from the shear stress using the velocity gradient at the interface; z_{ow} is the roughness length in the water; Re_* is the roughness Reynolds number and C_r is the roughness coefficient in the velocity defect law equation for transitional flow.

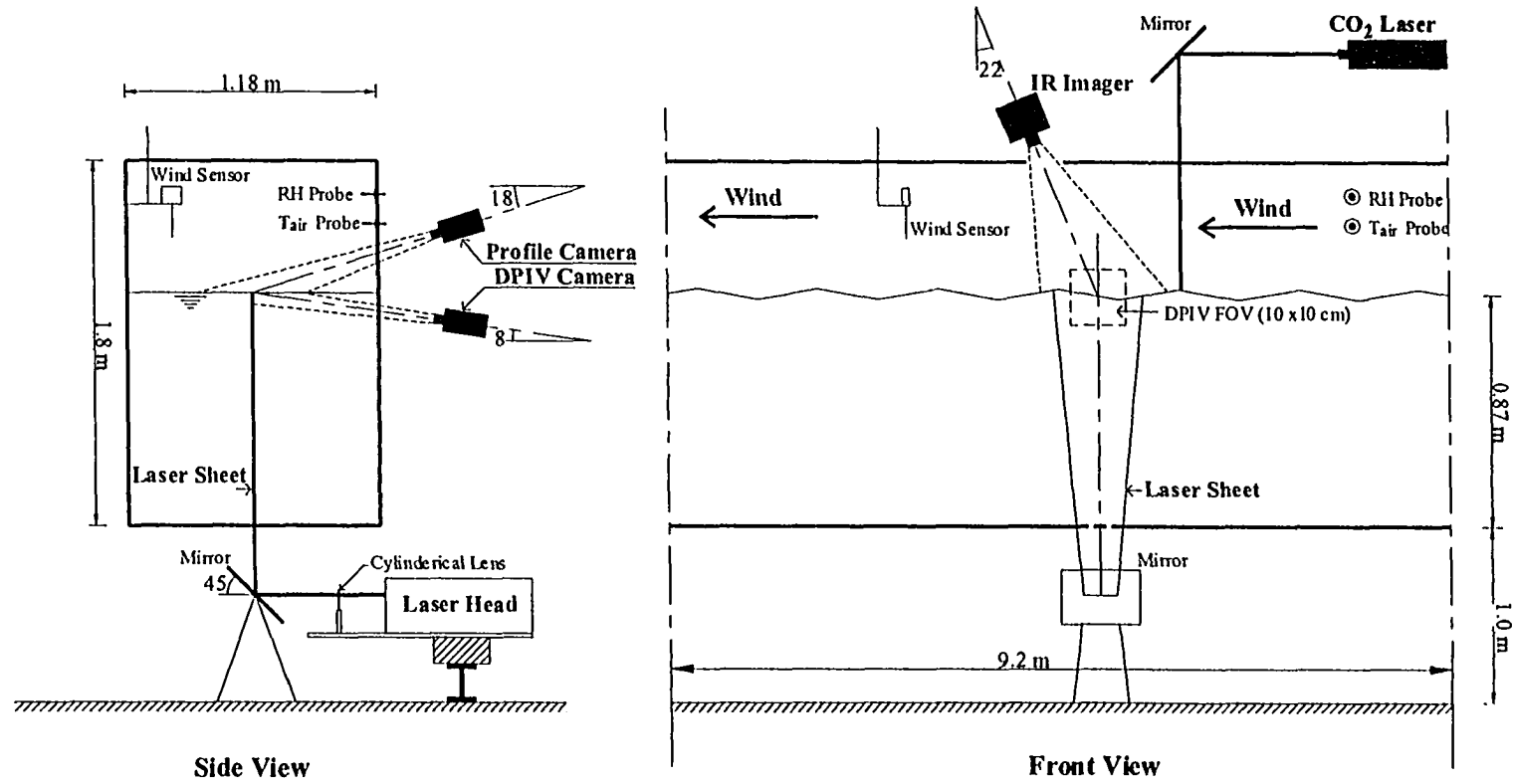


FIGURE 2.1: Schematic of the experimental setup illustrating the instrumentation used in the wind wave tank (not to scale).

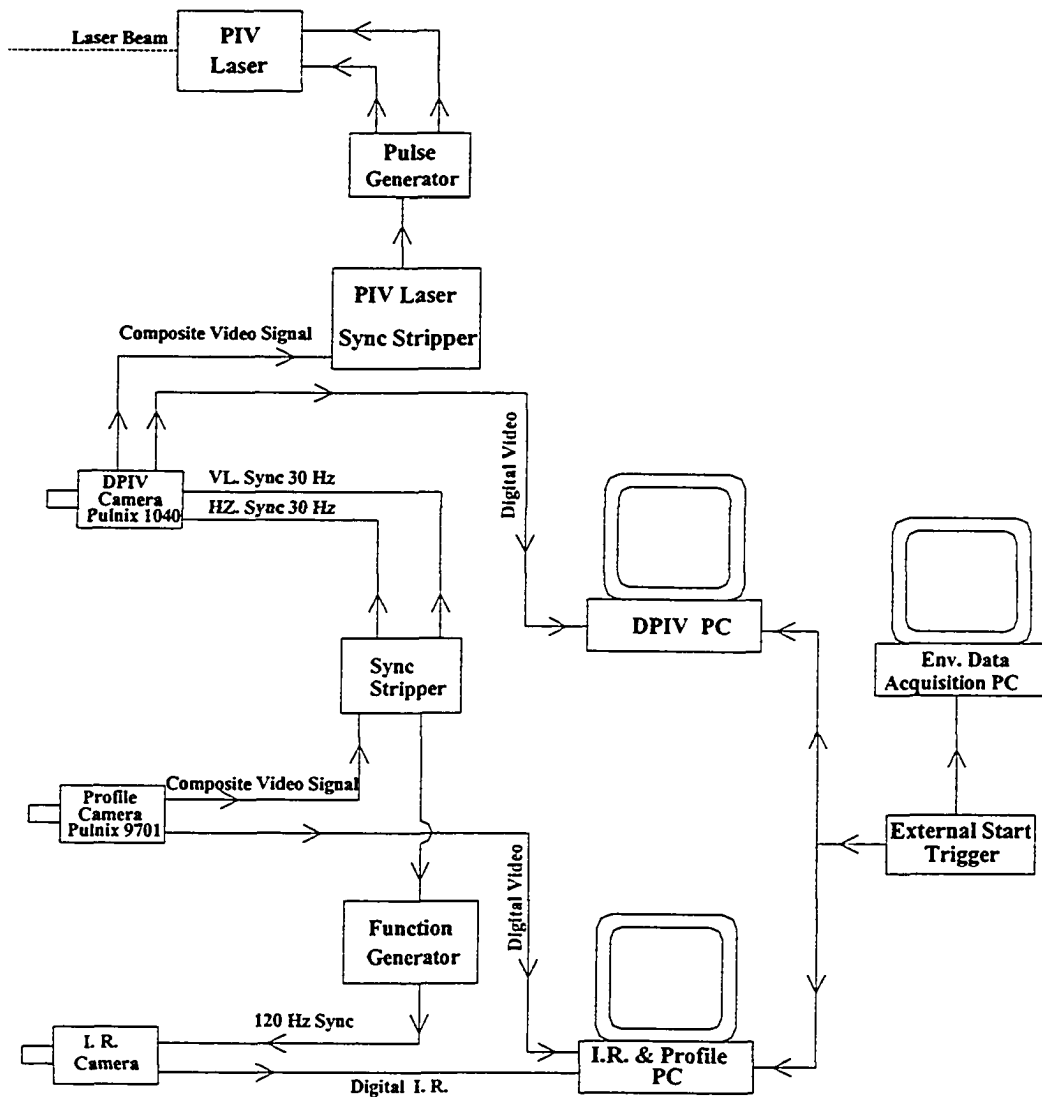


FIGURE 2.2: A flow chart showing the synchronization of the IR, profile and DPIV cameras and the laser. The vertical sync signal obtained from the profile camera was used to synchronize the DPIV and IR cameras. The vertical sync signal obtained from the DPIV camera was used to synchronize the laser.

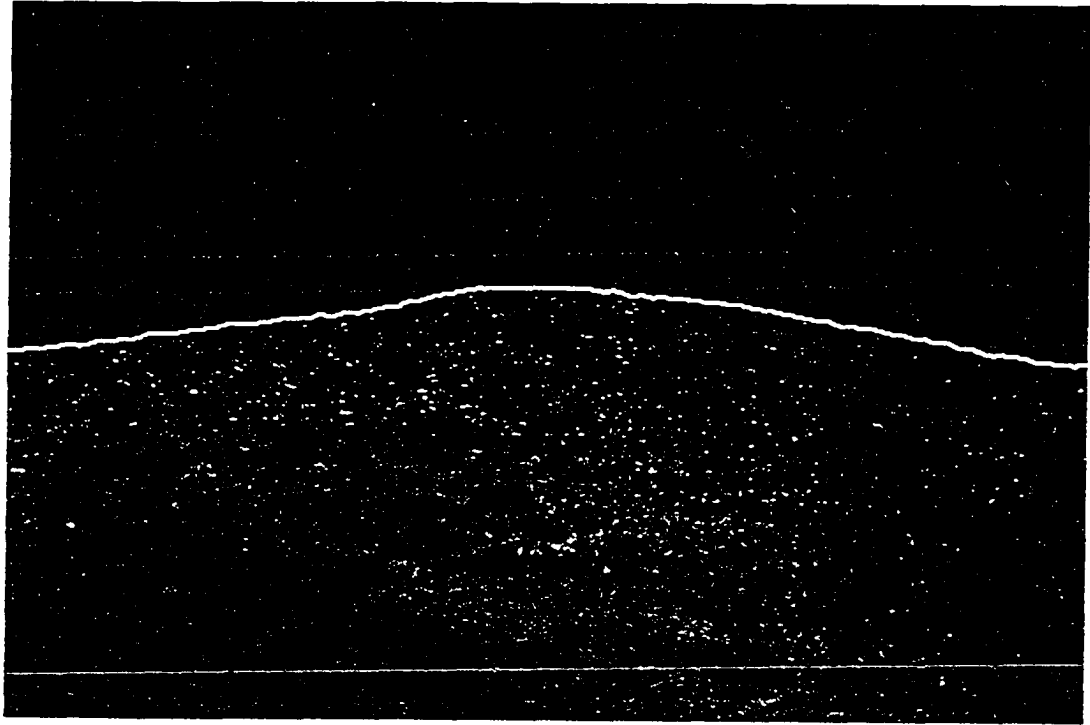


FIGURE 2.3: A typical profile image obtained from the profile camera at a wind speed of $9.6 \text{ m}\cdot\text{s}^{-1}$ with the computed water surface profile plotted on top of it as a white line.

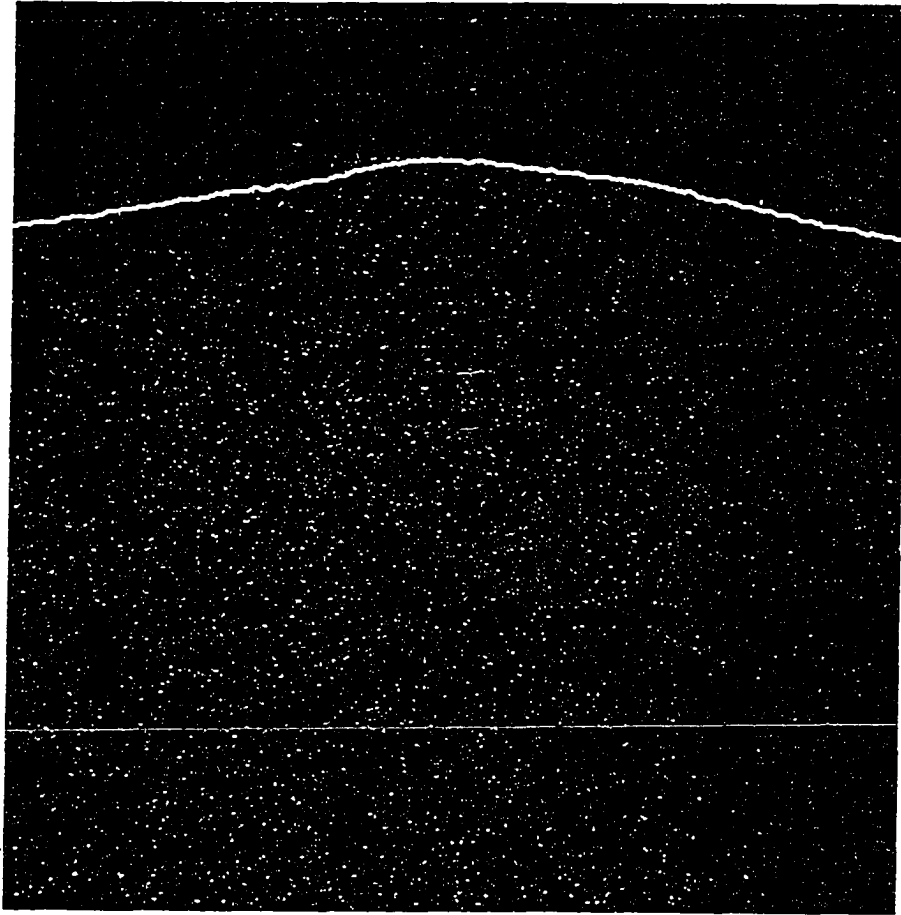


FIGURE 2.4: A typical DPTV image that corresponds to the profile image shown in Figure 2.3 with the water surface profile plotted on top of it as a white line.

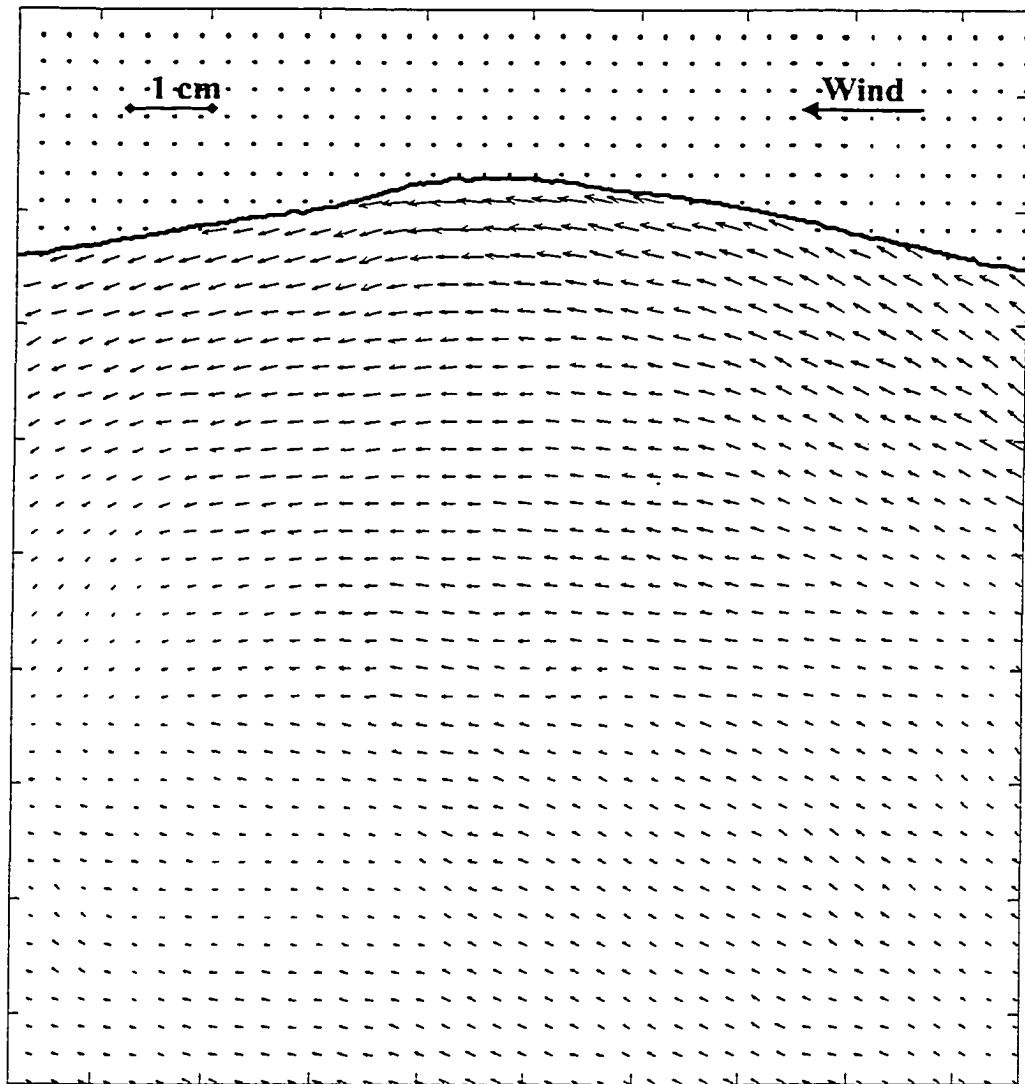


FIGURE 2.5: The two-dimensional instantaneous velocity field obtained by processing the DPIV image pair from Figure 2.4. The closest velocity vector is within 1.3 mm from the water surface and the spatial resolution of the velocity vector is 2.6 mm.

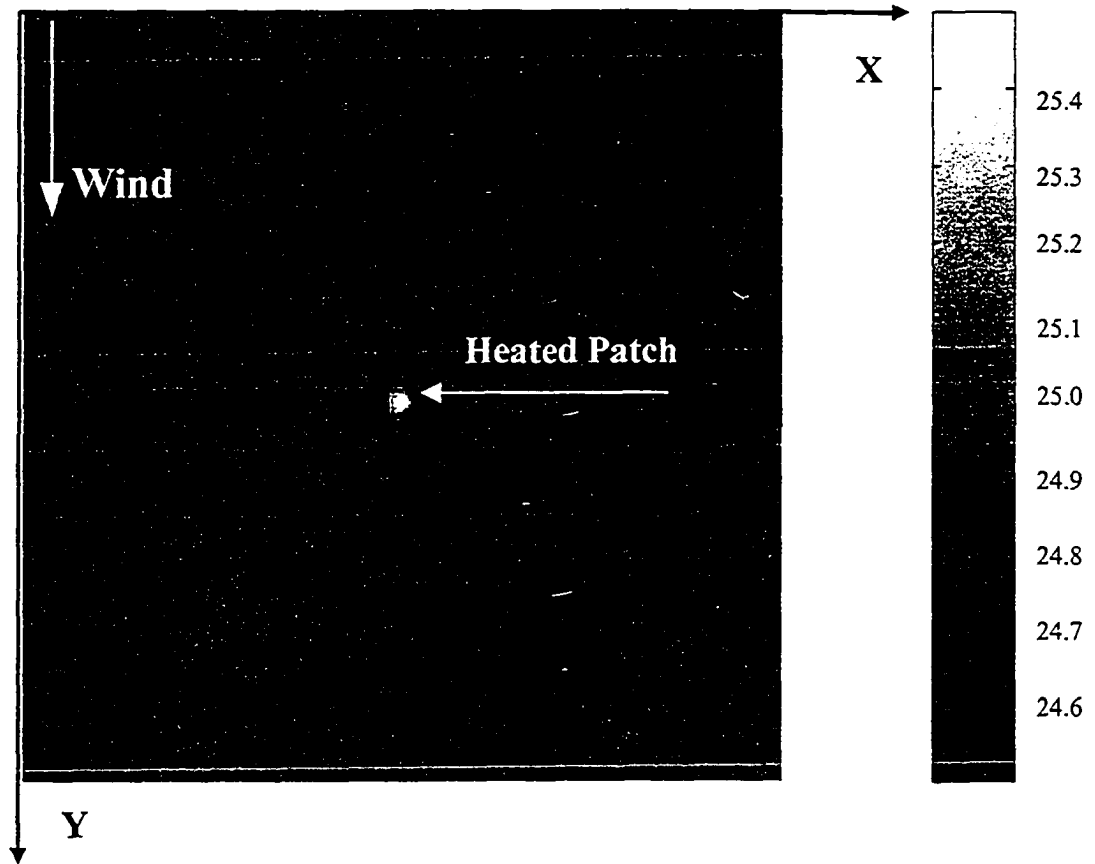


FIGURE 2.6: Infrared image showing a heated patch generated by the CO₂ laser.

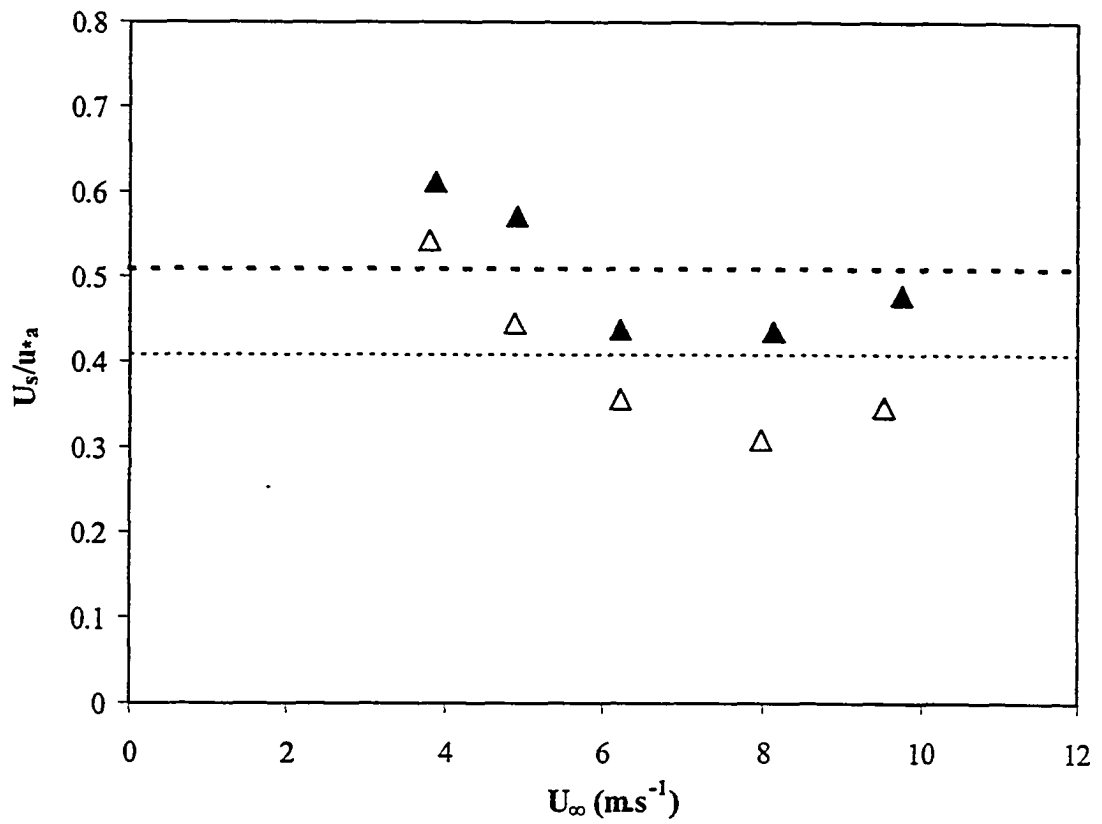


FIGURE 2.7: Plot of the ratio of the surface velocity U_s to the wind friction velocity u_{*a} for various wind speeds. Values are averaged over 10 minutes of data. \triangle , = Clean water surface; \blacktriangle , = surfactant-influenced water surface.

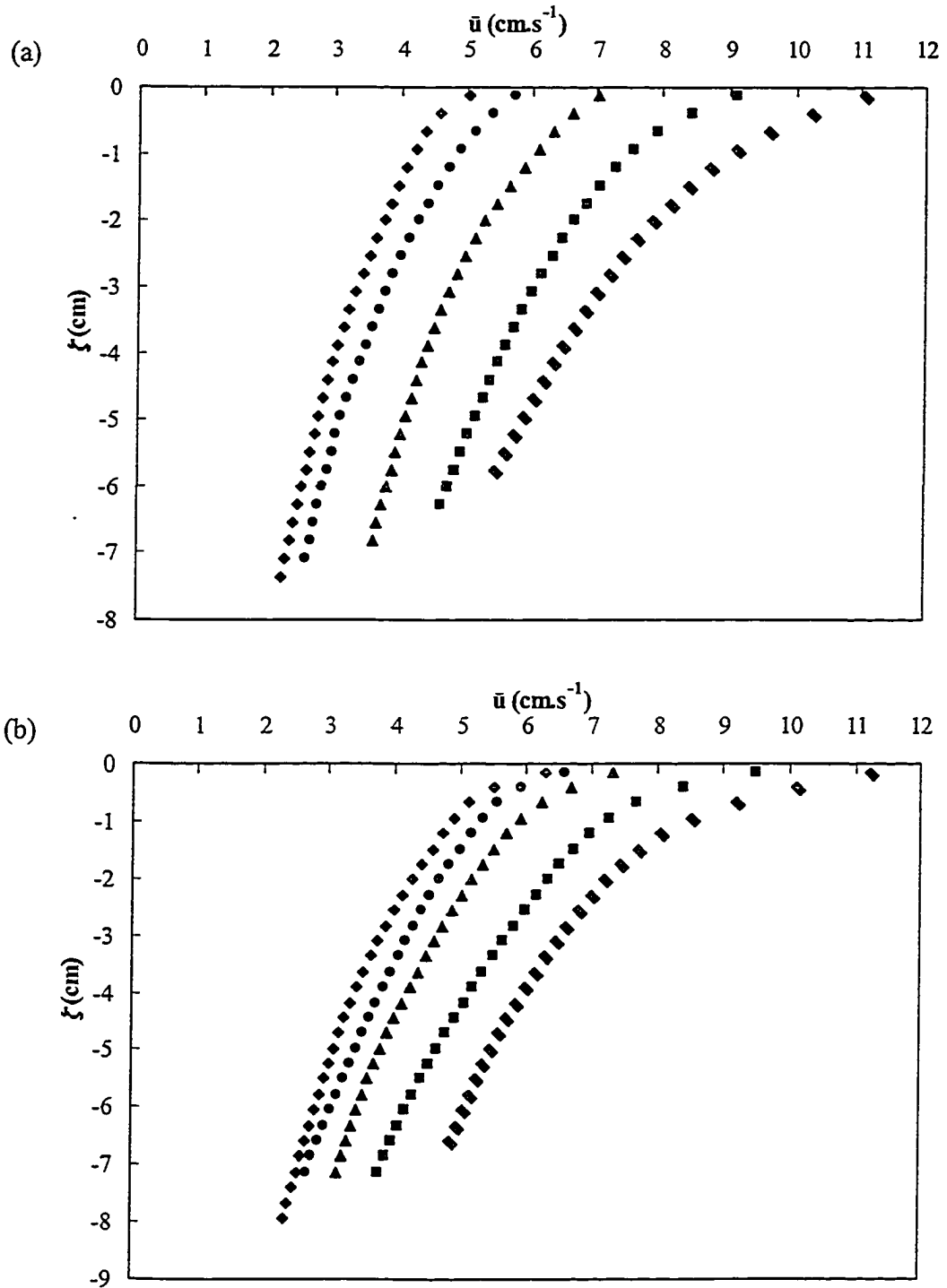


FIGURE 2.8: Vertical profiles of the stream wise component of the mean velocity, \bar{u} . ζ is the vertical coordinate in the wave following system. Values are averaged over 10 minutes of data. (a) Clean water surface, (b) Surfactant-influenced water surface, \diamond , = 3.8 m.s⁻¹; \bullet , = 4.9 m.s⁻¹; \blacktriangle , = 6.2 m.s⁻¹; \blacksquare , = 8.0 m.s⁻¹; \blacktriangledown , = 9.6 m.s⁻¹.

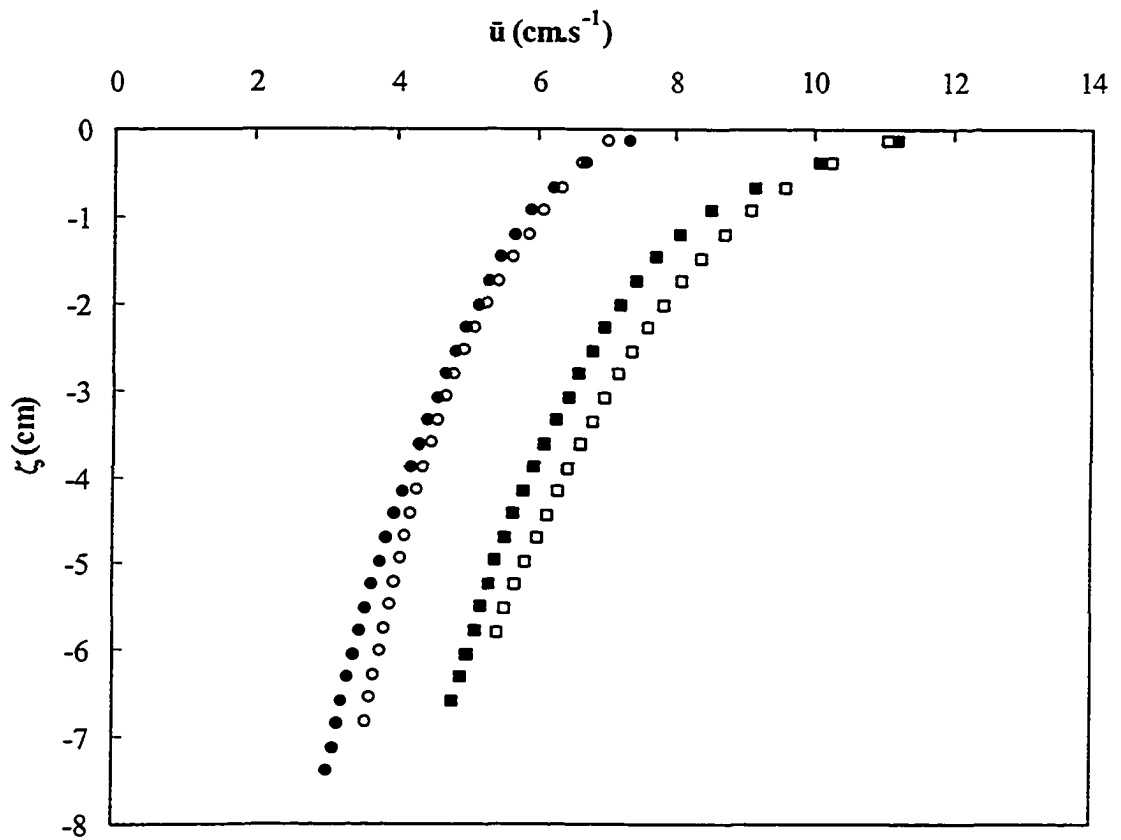


FIGURE 2.9: Vertical profiles of the stream wise component of the mean velocity, \bar{u} , for clean and surfactant-influenced water surfaces. ζ is the vertical coordinate in the wave following system. Values are averaged over 10 minutes of data. \circ , = clean 6.2 m s^{-1} ; \bullet , = surfactant 6.2 m s^{-1} ; \square , = clean $9.6 \text{ m}\cdot\text{s}^{-1}$; \blacksquare , = surfactant $9.6 \text{ m}\cdot\text{s}^{-1}$.

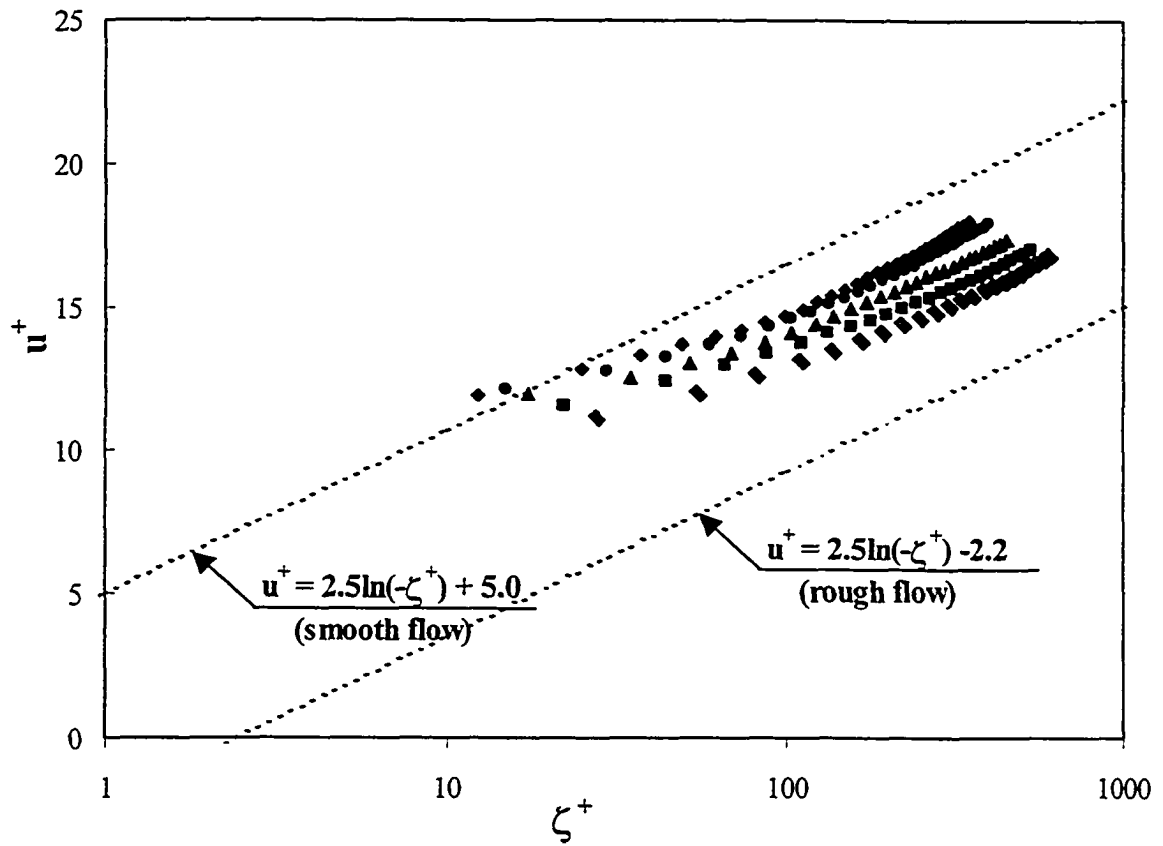


FIGURE 2.10(a): The mean streamwise velocity plotted in the form of a velocity defect law in wall coordinates for clean water surfaces. $u^+ = [U_s - \bar{u}(\zeta)] / u_{*w}$ and $\zeta^+ = \zeta u_{*w} / \nu$. \blacklozenge , = $3.8 \text{ m}\cdot\text{s}^{-1}$; \bullet , = $4.9 \text{ m}\cdot\text{s}^{-1}$; \blacktriangle , = $6.2 \text{ m}\cdot\text{s}^{-1}$; \blacksquare , = $8.0 \text{ m}\cdot\text{s}^{-1}$; \blacktriangledown , = $9.6 \text{ m}\cdot\text{s}^{-1}$.

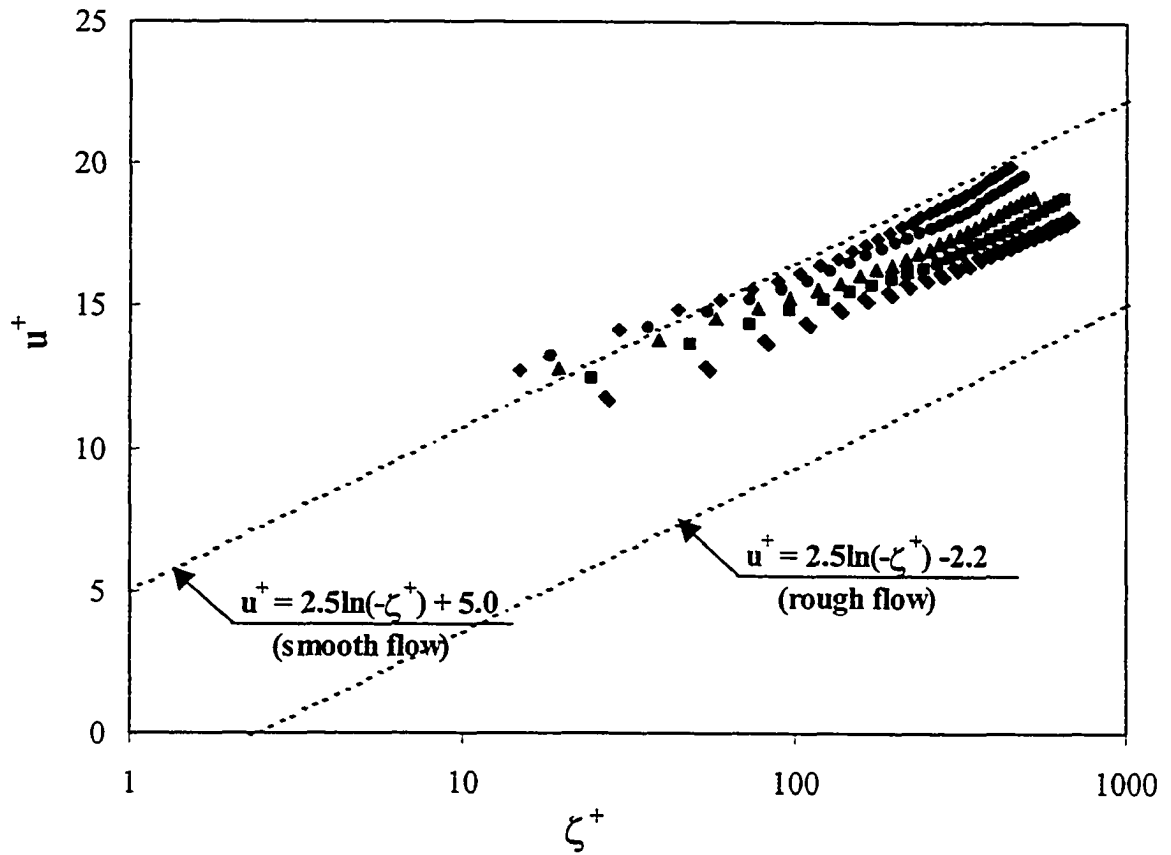


FIGURE 2.10(b): The mean streamwise velocity plotted in the form of a velocity defect law in wall coordinates for surfactant-influenced water surfaces. $u^+ = [U_s - \bar{u}(\zeta)] / u_{*w}$ and $\zeta^+ = \zeta u_{*w} / \nu$. \blacklozenge , = 3.8 m·s⁻¹; \bullet , = 4.9 m·s⁻¹; \blacktriangle , = 6.2 m·s⁻¹; \blacksquare , = 8.1 m·s⁻¹; \blacktriangledown , = 9.6 m·s⁻¹.

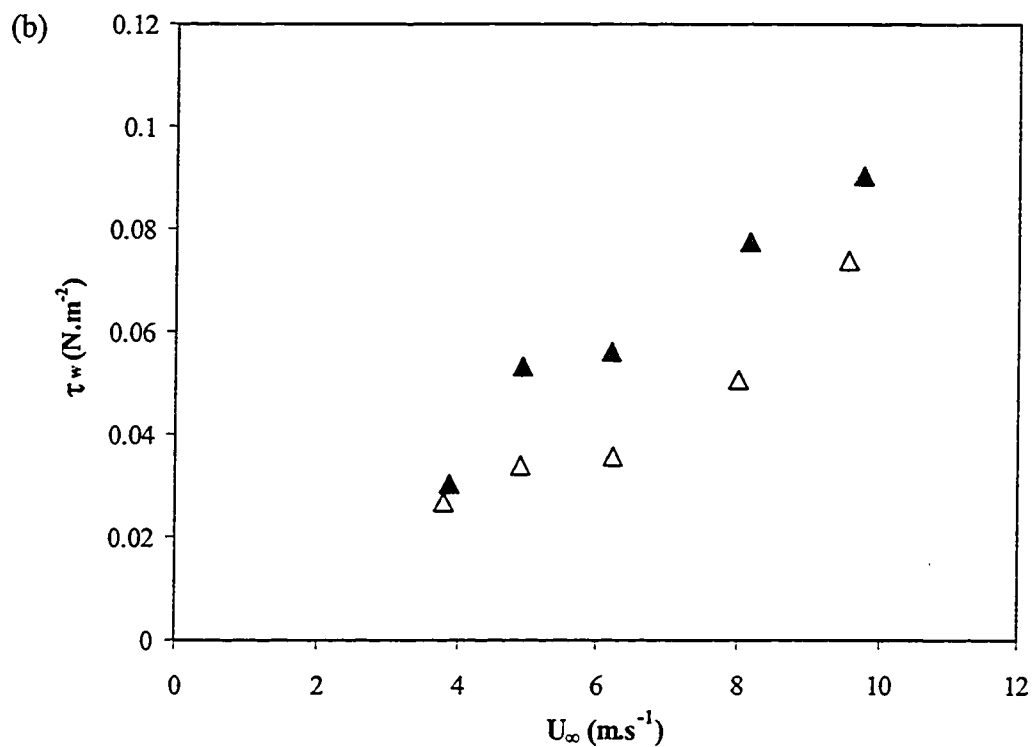
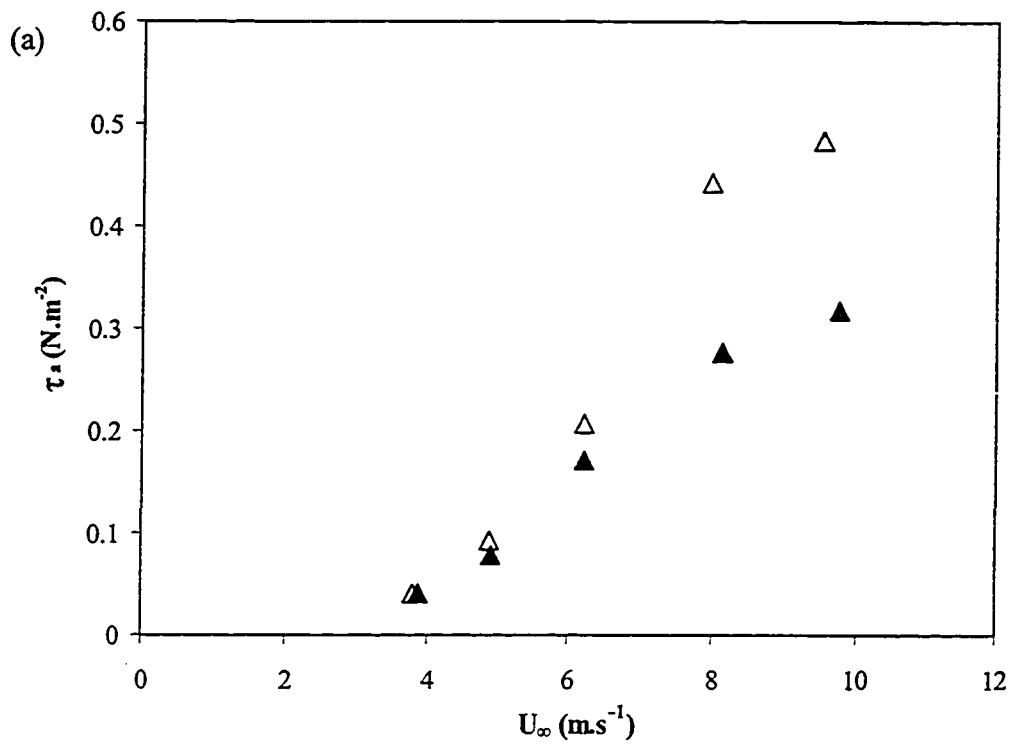


FIGURE 2.11: Plots of the shear stresses for various wind speeds. (a) Shear stress in the air $\tau_a = \rho_a u_a^2$; (b) shear stress in the water $\tau_w = \rho_w u_w^2$. Δ , = Clean water surface; \blacktriangle , = surfactant-influenced water surface.

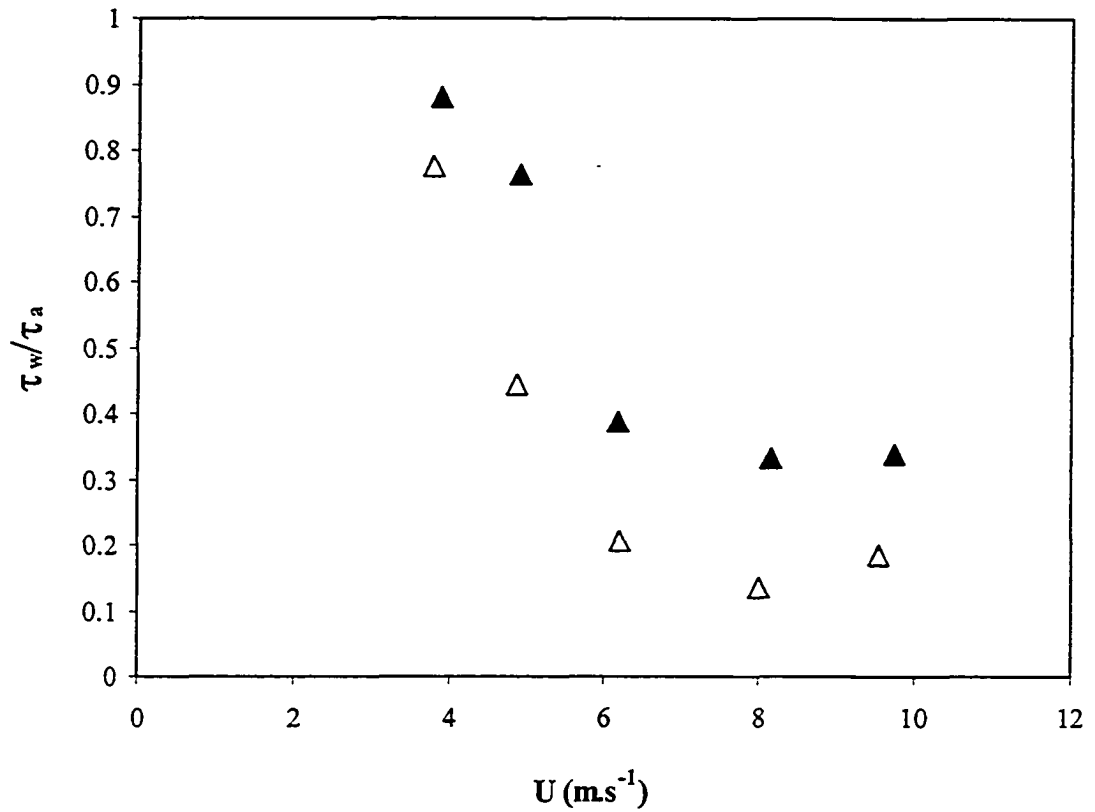


FIGURE 2.12: Plot of the ratio of the waterside shear stress $\tau_w = \rho_w u_{*w}^2$ to the airside shear stress $\tau_a = \rho_a u_{*a}^2$ at various wind speeds. Δ , = Clean water surface; \blacktriangle , = surfactant-influenced water surface.

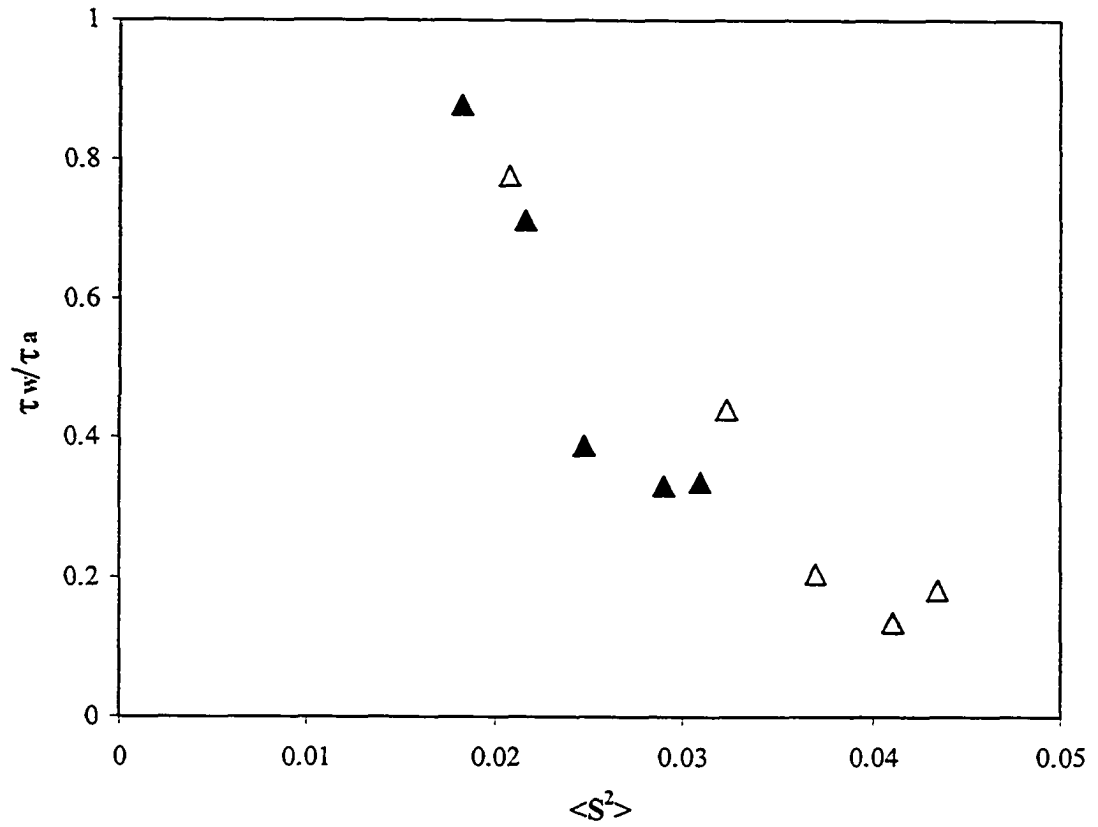


FIGURE 2.13: Plot of the ratio of the waterside shear stress $\tau_w = \rho_w u_{*w}^2$ to the airside shear stress $\tau_a = \rho_a u_{*a}^2$ versus the mean square wave slope of the waves, $\langle S^2 \rangle$. Δ , = Clean water surface; \blacktriangle , = surfactant-influenced water surface.

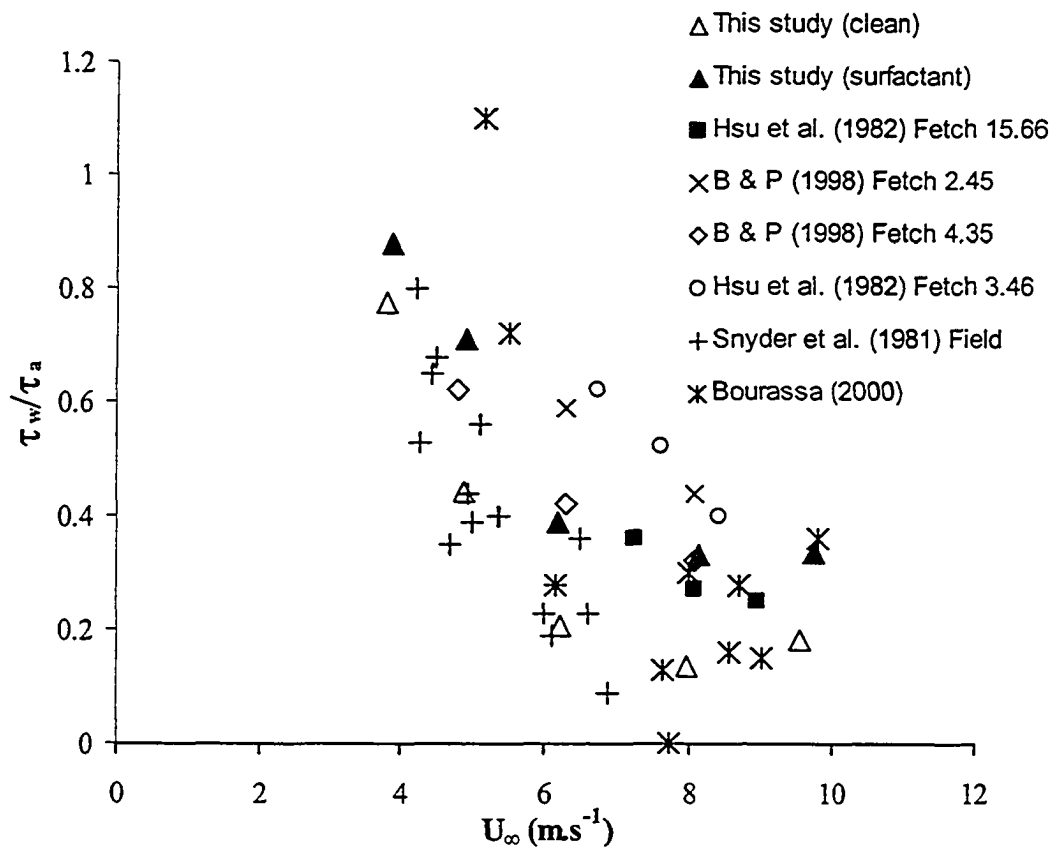


FIGURE 2.14: Plot of the ratio of the shear stress ratio τ_w/τ_a versus the wind speed. Different sets of data were compiled from the literature as labeled in the figure.

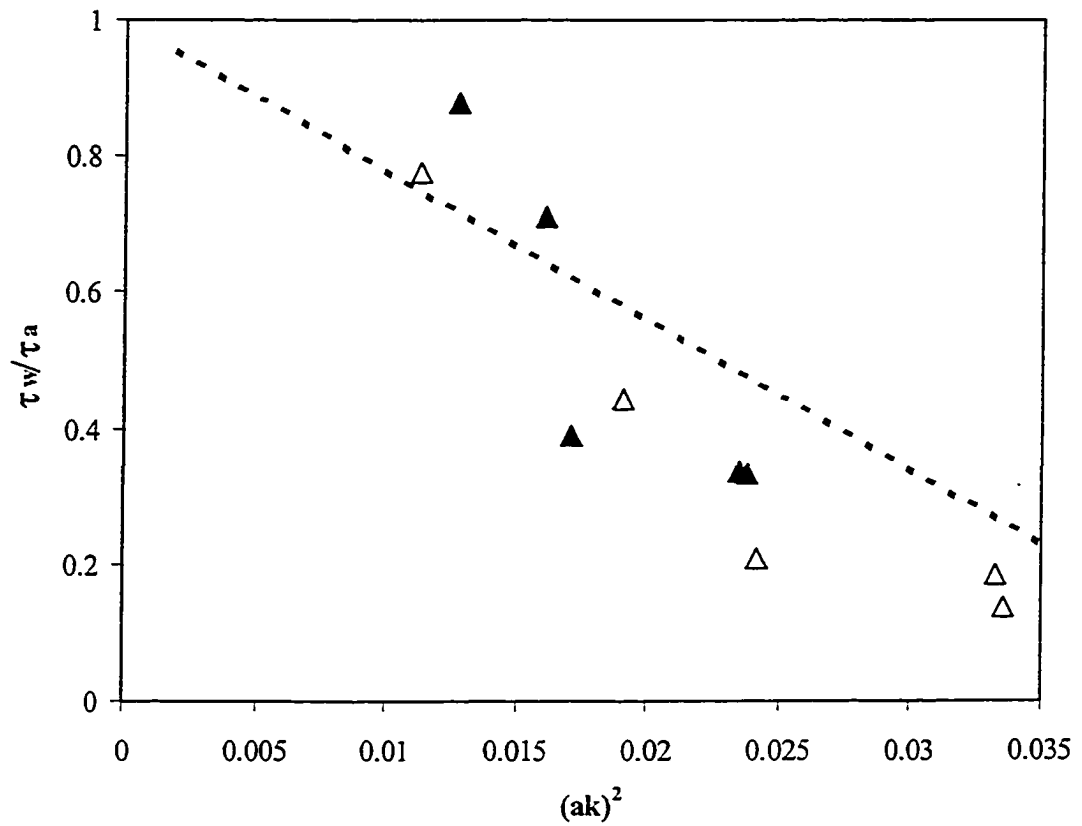


FIGURE 2.15: Plot of the ratio of the shear stress τ_w/τ_a versus the steepness ak where a is the RMS wave amplitude (cm) and k is the wavenumber (rad.cm^{-1}). Δ , = Clean water surface; \blacktriangle , = surfactant-influenced water surface. The dashed line represents Mitsuyasa's (1985) equation, which is, $\tau_w/\tau_a = 1 - 22(ak)^2$.

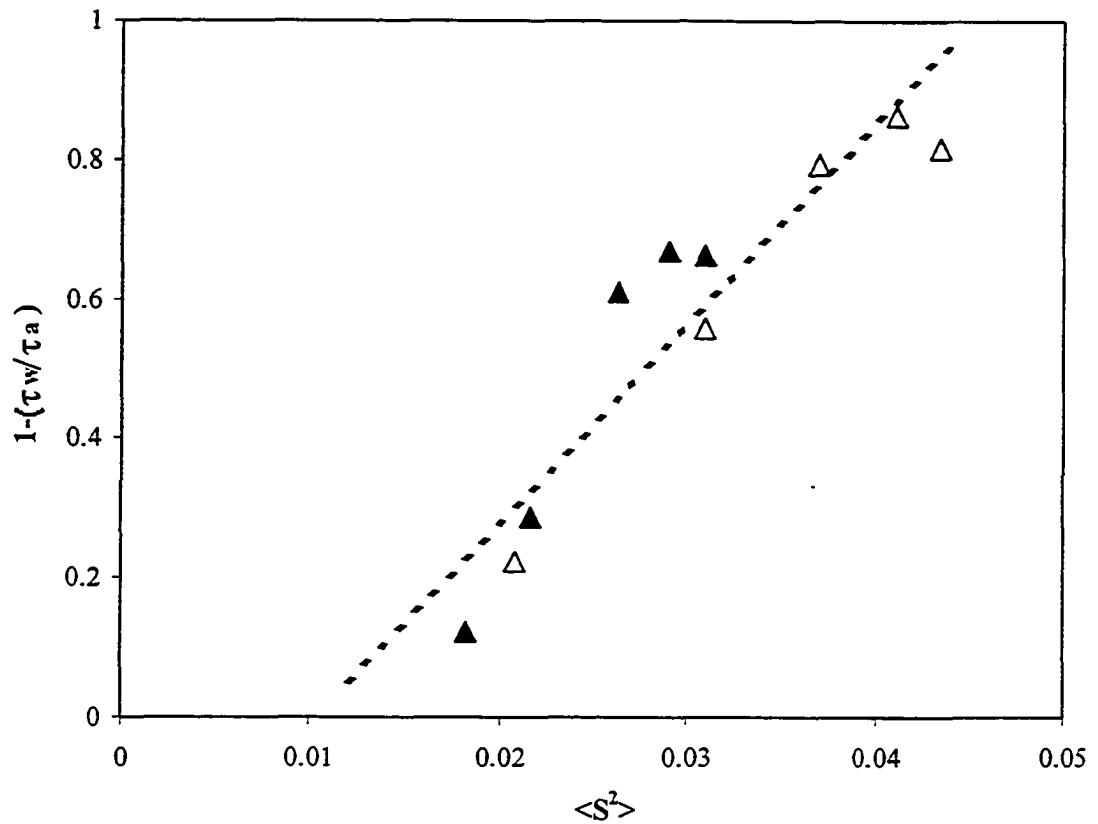


FIGURE 2.16: Plot of $1 - \tau_w / \tau_a$ versus the mean square wave slope of the waves, $\langle S^2 \rangle$, whereas τ_w / τ_a is the ratio of the waterside shear stress to the airside shear stress. Δ , = Clean water surface; \blacktriangle , = surfactant-influenced water surface. The dashed line represents the best-fit line for all the shown data points at both water surface conditions.

Chapter 3

Near-Surface Turbulence and Microscale-Breaking Waves

3.1 Introduction

The wind wave is a surface water wave that is created by the action of wind at the air-water interface. Most recent studies of wavy air-water interfaces have been principally concerned with two essential aspects; the mechanism of generation and the dynamics of small-scale features of the interface (Brocchini *et al.* 2001a). It is well known that waves break when the fluid particles near the wave crest travel faster than the wave and overtake it. According to this kinematic criterion, during the breaking process, the wave crest becomes turbulent and spills down the forward slope losing its potential energy and in this manner it leaves behind a decaying turbulent wake. The most familiar expression of breaking is the formation of a whitecap due to air entrainment. Whitecaps occur for large scale breaking waves (lengths of order 1 to 100m), but breaking may occur without air entrainment down to a scale of centimeters (Melville 1996), which is defined as micro breaking.

A number of areas in air sea interaction research would benefit from a better understanding of turbulence and mixing due to wave breaking. Breaking is generally known to be a sink of energy for surface waves and a source of energy for near-surface turbulence. Moreover, when momentum is preserved, breaking as a dissipative mechanism leads to the generation of currents (Melville *et al.* 2002). Accurate estimates of the flux of gas and heat across the air-water interface are essential for weather and climate modeling up to global scales (Cane *et al.* 1997). These fluxes depend on the

levels of near-surface turbulence, which in turn is directly related to wave breaking. In addition, breaking waves are important factors when considering convection and diffusion processes undergone by passive tracers at an air-water interface (Brocchini *et al.* 2001a).

Gas exchange through the air-water interface is a significant pathway for many gases in the environment. Quantifying air-water gas fluxes is crucial in understanding biological process in the upper ocean. For example, accurate estimates of oxygen fluxes at the air-water interface are important in water quality modeling (Chu and Jirka 1995) and accurate estimates of CO₂ fluxes at the interface are crucial for global warming predictions (Banner and Peregrine 1993). Hence, better understanding of the processes that govern air-water gas transfer, such as near-surface turbulence, are needed in order to obtain more accurate estimates of gas fluxes.

Near-surface turbulence produced by breaking waves has been suggested as a mechanism that controls air-water gas transfer rates (Jähne *et al.* 1987). Consequently, studying breaking waves and their role in generating near-surface turbulence should lead to improved understanding of air-water gas transfer. Wave parameters such as the mean square wave slope have become the focus of research aimed at explaining the observed discrepancies in gas transfer rates at similar wind speeds (Jähne *et al.* 1987). Jähne *et al.* (1987) argued that the mean-square wave slope is directly related to the near-surface turbulence generated by waves. This was based on their observations that the air-water gas transfer velocity was strongly correlated with the mean square slope of the waves. Moreover, they suggested that waves at all scales contribute to an energy cascade that eventually produces near-surface turbulence, hence enhancing gas transfer rates.

Csanady (1990) argued that air-water gas transfer rates are controlled by small scale breaking waves. He hypothesized that regions of intense surface divergence were generated during the breaking process, which reduced the thickness of the concentration boundary layer and hence enhances air-water gas transfer.

Wave breaking is an irregular or random process in space and time and it is a highly nonlinear phenomenon (Chen *et al.* 1999). Banner & Peregrine (1993) argued that while linear wave theory is a good approximation for waves with gentle slopes it is not accurate for steep waves or breaking waves. There has been some recent progress in numerical modeling for the breaking phenomenon. However, these models still have to include a number approximations and simplifications due to the complexity of the breaking process. Brocchini *et al.* (2001b) discussed some of the complexities that needed to be simplified in these numerical models of breaking waves; accounting for two phase flow (air and water) in the modeling of the turbulence, specifying the boundary conditions for the flow of mass and momentum for both air and water and tracking the exceptionally complex interface between the two phases of flow. Therefore, most of the research related to breaking waves and its influence on air-water interactions has been carried out experimentally either in the laboratory or in the field. Conducting experiments in the field is difficult because of the lack of control on many constraints such as wind speed and the difficulty in positioning the measuring equipment. As a result much of the progress that has been made in understanding breaking waves have been achieved in laboratory wave channels (e.g. Rapp and Melville 1990).

In laboratory wind wave studies, Okuda (1982) identified a high vorticity region near the crests of gravity waves with capillary ripples generated ahead of the crests. The

origin of vorticity within the surface roller has been identified by Longuet-Higgins (1992) as the accompanying parasitic capillary waves which generate fluid rotations and vortices via the surface tension effect (Yeh 1995). Rollers identified by Longuet-Higgins (1992), breaking wavelets identified by Csanady (1990), and steep wind waves accompanied by a high vorticity layer near the crest identified by Okuda (1982) are all descriptions of phenomena which are associated with the micro breaking first described by Banner and Phillips (1974). For consistency and convenience, the general description of breaking offered above is adopted and the term microscale-breaking waves is used to describe very short, wind generated gravity waves that break without air entrainment. Microscale-breaking waves typically occur at low to moderate wind speeds (i.e. 4 to 11 m·s⁻¹). In microscale-breaking waves, the effect of surface tension is strong enough to maintain the structure of the surface but gravity fails to keep it (Brocchini et al. 2001a), thus breaking occurs with no air entrainment.

Normally, microscale-breaking waves are of the order of (0.1-0.3) m in length, a few centimeters in amplitude, and have a bore-like crest preceded by parasitic capillary waves carried along the forward face (Jessup *et al.* 1997). Veron and Melville (2001) noted that the air-water interface represents approximately 70% of the Earth's surface and that the globally averaged wind speed is in the range of 6 to 8 m·s⁻¹, which means that the global air-sea interface is on average in a low-wind regime. Accordingly, microscale-breaking waves occur much more frequently than large-scale breaking waves which lead some researchers to propose that perhaps microscale wave breaking are important in governing the flux of heat, gas and momentum across the interface (Banner & Peregrine 1993; Melville 1996).

It is difficult to identify microscale-breaking waves using standard optical techniques due to the lack of air entrainment. The surface of the ocean is typically a few tenths of a degree Celsius cooler than the bulk water temperature immediately below. Microscale-breaking waves disrupt this cool surface skin layer via turbulent mixing and the resulting water surface temperature rises to the bulk water temperature. Hence, microscale-breaking waves produce thermal signatures of the turbulent wakes generated when the cool skin layer is disrupted. Accordingly, Jessup *et al.* (1997) have used infrared (IR) imagers to measure the temperature changes in the skin layer and by this means detect microscale-breaking waves.

Zappa *et al.* (2001) examined the influence of microscale-breaking waves on air-water gas and heat transfer using infrared and wave slope imaging techniques. They found that the fraction of the area occupied by the thermal signatures of the turbulent wakes generated by microscale-breaking waves was correlated with the gas and heat transfer velocities. They observed that the disruption of the skin layer coincides with waves that have a dimpled bore-like crest and steep forward face. More recently, Zappa *et al.* (2004) measured the local heat transfer velocities inside and outside these wakes generated by microscale breaking waves. They found that on average the heat transfer rate was enhanced by a factor of 3.5 inside the wakes and that microscale wave breaking was responsible for up to 75% of the transfer across the air-water interface. Based on that, they concluded that microscale wave breaking is the physical process that determines the gas transfer rate at low to moderate wind speeds.

Peirson and Banner (2003) examined the flow underneath microscale-breaking waves using high-resolution digital particle image velocimetry (DPIV). They detected

microscale-breaking waves by using a method based on the local wave slope. Microscale-breaking waves were identified if the local slope on the leeward face of the wave was greater than 0.5. At the leading edge of the spilling area, they observed high values of vorticity and surface convergence. They declared that these regions of localized convergence were produced by subduction of the fluid beneath the spilling area.

Siddiqui *et al.* (2001) measured the flow beneath microscale-breaking waves using infrared imagery and digital particle image velocimetry (DPIV). They found that a series of vortices that form behind the leading edge of the breaker typically produce the thermal wakes generated by microscale-breaking waves. They observed good correlations between the near-surface vorticity and both the fraction of the area occupied by the thermal wakes and the local heat transfer velocity. Further, they showed that the regions of high near-surface vorticity are the thermal wakes produced by microscale-breaking waves. In addition, these wakes comprised of high vorticity and they are responsible for enhancing air-water heat transfer rates.

Siddiqui and Loewen (2005) carried out an earlier wind wave tank experiment that is similar to the one conducted in this study for clean water surfaces. They proposed and validated a vorticity threshold technique that is based on the variance of the vorticity in the crest region to detect microscale-breaking waves from the DPIV data. Using that technique, they were able to compare the characteristics of breaking and non-breaking waves. They showed that breaking waves enhance the rate of dissipation of turbulent kinetic energy by a factor of two and that the rate of energy dissipation beneath breaking waves is on average 2.5 times larger than non breaking waves. In addition, they found that as the wind speed reached $11 \text{ m}\cdot\text{s}^{-1}$, 90% of the waves are microscale-breaking

waves. However, at a wind speed of $4.8 \text{ m}\cdot\text{s}^{-1}$, 11% of the waves were breaking and they found that as the wind speed increases the number of breaking waves increases rapidly. Moreover, they declared that microscale-breaking waves were on average 65% larger in height and 50% steeper than non-breaking waves. They concluded that, microscale-breaking waves produce coherent structures upwind of the leading edge of the breaker and that these structures created well-mixed areas up to a depth of approximately 1 cm. Siddiqui *et al.* (2004) estimated that 60% of the total air-water gas flux was due to the surface renewal produced by the observed near-surface coherent structures generated by microscale breaking waves.

Natural and anthropogenic surfactants are often found on the surface of lakes and oceans (Frew *et al.* 2004). Surfactants are known to dampen shorter surface waves and this introduces temporal and spatial variability into the wind forcing, especially in productive areas (Uz at al. 2002). Jähne and Haußecker (1998) stated that the presence of surfactants damp the capillary waves while the dominant gravity waves survive. Cenicerous (2003) studied the effect of surfactants on the formation of short capillary waves numerically. He found that surfactants affected capillary waves dramatically and that the capillary region is regularly marked by accumulation of surfactant concentration. He concluded also that the size of the roller decreases and both the amplitude and wavelength of the capillary ripples are also reduced by surfactants.

Therefore, for studies of breaking waves to be relevant to the field they should include the influence of surfactants within their scope. When surfactant molecules have sufficient surface density they form surface films over regions with a wide range of sizes on the ocean surface (Mass and Milgram 1998). Most natural sea surfactants have

sufficient solubility for there to be exchanges of them between the surface and the underlying bulk fluid. In the open sea, the largest sources of surfactants are phytoplankton exudates and the chemical breakdown of dead organisms (Mass and Milgram 1998).

Surfactants not only affect the wave field through damping but also modify the surface boundary conditions. In the absence of wind the only surface stress acting at a clean air-water interface (i.e. free of surfactants) is surface tension. Surfactants typically reduce the surface tension in proportion to their concentration at the free surface. Thus when the surfactant concentration varies along a free surface, surface tension gradients occur and these produce shear stresses, thus altering the boundary condition (Lang and Gharib 2000). Surfactants are important to the dynamics of free-surface flows because their presence influences the behavior of the near-surface turbulence (Lang and Gharib 2000). Specifically, studies of turbulent processes have shown that surfactants affect near-surface turbulence length and velocity scales and inhibit surface renewal (Frew *et al.* 1995). Surfactants affect not only the dissipation terms of the wave energy budget, but also the wind wave growth and mixing terms (Frew *et al.* 1995). Jähne *et al.* (1987) showed that the gas transfer velocity correlated with the mean square slope of the waves irrespective of the surface cleanliness (i.e. clean or surfactant-influenced) suggesting that waves are able to integrate the effect of surfactants on gas transfer.

The objective of this study is to improve our understanding of the near-surface turbulence generated by microscale-breaking waves beneath clean and surfactant-influenced water surfaces. The specific focus of this chapter is on how the properties of microscale-breaking waves and the near-surface turbulence change due to the presence of

a surfactant. In section 3.2 the bulk gas transfer velocity results for clean and surfactant-influenced water surfaces are presented; in section 3.3, the properties of the near-surface turbulence and rates of turbulent kinetic energy dissipation are presented; in section 3.4 the results of the turbulent kinetic energy dissipation are discussed; in section 3.5 a scheme for detecting microscale-breaking waves is described and the characteristics of microscale-breaking and non-breaking waves are compared for both water surface conditions; in section 3.6 a discussion about microscale-breaking waves results and their contribution to the near-surface turbulence are discussed; and section 3.7 contains the summary and conclusions.

3.2 Bulk Gas Transfer Velocities

In Figure 3.1 the values of the bulk gas transfer velocity, k_G , measured by Atmane *et al.* (2004) during the same experiments for this study are plotted as a function of wind speed for clean and surfactant-influenced water surfaces. It can be seen that as the wind speed increases, k_G increases for both water surface conditions. It is noteworthy that k_G is strongly correlated with wind speed for both water surface conditions as shown in Figure 3.1. Specifically, as the wind speed increased from 3.8 to 9.6 m·s⁻¹, k_G increased by approximately a factor of 4 from 7.5 to 29.9 cm·hr⁻¹ for clean water surfaces and by approximately a factor of 3.1 from 4.6 to 14.3 cm·hr⁻¹ for surfactant-influenced water surfaces. It is also evident from Figure 3.1 that the presence of the surfactant reduced k_G significantly; the average reduction factor was 55%. This was expected since previous studies had shown that surfactants inhibit surface renewal and damp capillary gravity waves (Saylor *et al.* 2000). Figure 3.2 shows the relationship between the mean square

wave slope $\langle S^2 \rangle$ and k_G for both water surface conditions. It can be seen that $\langle S^2 \rangle$ and k_G are strongly correlated with each other irrespective of the water surface condition. This supports the hypothesis that the mean square wave slope best parameterizes k_G because it is sensitive to the presence of a surfactant (Jähne *et al.* 1987; Zappa *et al.* 2001; Frew *et al.* 2004).

3.3 Rate of Dissipation of Turbulent Kinetic Energy

3.3.1 Spectral Analysis

The one-dimensional wavenumber spectrum is defined as,

$$\Phi(k,t) = \frac{1}{2\pi} \int_{-\infty}^{+\infty} R(r,t) e^{-ikr} dr \quad [3.1]$$

where, $R(r,t)$ is the longitudinal spatial correlation given by

$$R(r,t) = \overline{u_1(x_1,t)u_1(x_1+r,t)} \quad [3.2]$$

where, $u_1(x_1,t)$ is the instantaneous stream wise component of the velocity and the over bar denotes spatial averaging. One-dimensional longitudinal wavenumber spectra were computed at different wind speeds and depths for clean and surfactant-influenced water surfaces in the wave-following coordinate system. One-dimensional transverse wavenumber spectra were computed by replacing the stream wise component of the velocity with the vertical component in equations [3.1] and [3.2]. Average longitudinal and transverse wavenumber spectra were computed by time averaging 9000 instantaneous wavenumber spectra at each depth in the wave-following coordinate system for depths from 0.13 cm to 6.0 cm.

In Figure 3.3, the time averaged longitudinal wavenumber spectra computed at a depth of 0.9 cm for five wind speeds and clean water surfaces are shown plotted. At this depth the wavenumber spectra have a well-defined inertial subrange, that is, they have a slope of approximately $-5/3$. In the longitudinal and transverse wavenumber spectra that had a well-defined inertial subrange it typically existed over a range of wavenumbers from approximately $250 \text{ rad}\cdot\text{m}^{-1}$ to the Nyquist wavenumber for both clean and surfactant-influenced water surfaces. The magnitudes of the wavenumber spectra increased monotonically with wind speed and decreased monotonically with increasing depths. In Figure 3.4, time averaged longitudinal wavenumber spectra for clean and surfactant-influenced water surfaces at a depth of 0.9 cm are compared at three wind speeds. At all but the lowest wind speed we found that the magnitudes of all wavenumber spectra for clean water surface runs were larger than for the corresponding surfactant-influenced water surface runs. This indicates that there was more turbulent kinetic energy generated beneath clean water surfaces at the four highest wind speeds.

3.3.2 Turbulent Kinetic Energy Dissipation Calculations

Study of the rate of dissipation of turbulent kinetic energy will contribute to a better understanding of turbulence near free surfaces and has a practical importance for the transport of gas and heat across the air-water interface in turbulent flows (Teixeira and Belcher 2000). Doron *et al.* (2001) showed that the “direct” method was the most accurate method of estimating the rate of turbulent kinetic energy dissipation compared to four other methods. The direct method uses the velocity gradients computed from the DPIV data as follows,

$$\varepsilon = 3\nu \left\{ \overline{\left(\frac{\partial u'}{\partial x} \right)^2} + \overline{\left(\frac{\partial w'}{\partial z} \right)^2} + \overline{\left(\frac{\partial u'}{\partial z} \right)^2} + \overline{\left(\frac{\partial w'}{\partial x} \right)^2} + 2 \overline{\left(\frac{\partial u'}{\partial z} \frac{\partial w'}{\partial x} \right)} + \frac{2}{3} \overline{\left(\frac{\partial u'}{\partial x} \frac{\partial w'}{\partial z} \right)} \right\} \quad [3.3]$$

where u' and w' are the stream wise and vertical turbulent velocities and ν is the kinematic viscosity of water (Doron *et al.* 2001).

Benilov *et al.* (1974) decomposed the instantaneous velocity field created beneath wind waves into three components, the mean, wave-induced and turbulent using the following equation,

$$u(x,t) = \bar{u} + \tilde{u}(x,t) + u'(x,t) \quad [3.4]$$

where \bar{u} , \tilde{u} and u' are the mean, wave-induced and turbulent components of the instantaneous velocity u , respectively. Instantaneous velocity fields were obtained from the DPIV measurements and the mean velocity components were obtained by time averaging the instantaneous velocity over 10 minutes. Subtracting the mean velocity components from the instantaneous velocities, gives velocity components designated as u_{wt} and w_{wt} , which are comprised of wave and turbulent velocities. Wave component velocity gradients are typically considerably smaller in magnitude than the corresponding turbulent velocity gradients. Siddiqui and Loewen (2005) found that the magnitudes of the wave velocity gradients were approximately 2.5 times smaller than the corresponding gradients in the turbulent velocities. Therefore, it should be possible to obtain accurate estimates of ε using u_{wt} and w_{wt} in equation [3.3]. To test whether u_{wt} and w_{wt} could be used in equation [3.3] to provide accurate estimates of ε , we compared these estimates to values computed using two other methods.

The first method estimates ε by fitting a $k^{-5/3}$ constant slope curve to the portion of the longitudinal wavenumber spectrum of the stream wise instantaneous velocity

component that corresponds to the inertial subrange. The one-dimensional wavenumber spectrum in the inertial subrange is given by,

$$\Phi_u(k) = \frac{18}{55} \left(\frac{8}{9\alpha} \right)^{2/3} \varepsilon^{2/3} k^{-5/3} \quad [3.5]$$

where, Φ_u is the wavenumber spectrum of the stream wise velocity, k is the wavenumber within the inertial subrange, α is a constant equal to 0.4 and ε is the rate of energy dissipation (Hinze 1975). Equation [3.5] is the simple relationship between the wavenumber spectra and the rate of energy dissipation through the inertial subrange part of the wavenumber spectrum. The presence of a $-5/3$ slope in a measured wavenumber spectrum is clear evidence that the inertial subrange is present in the turbulence (Hinze 1975).

The second method is based on the dissipation spectrum $D(k)$ defined as,

$$D(k) = 2\nu k^2 \Phi_u(k) \quad [3.6]$$

where Φ_u is the wavenumber spectrum of the stream wise velocity, ν is the kinematic viscosity and k is the wavenumber (Tennekes and Lumely 1972). The dissipation is proportional to the square of the velocity gradients (see equation [3.3]) and the factor k^2 in equation [3.6] arises because differentiation corresponds to multiplication by wavenumber. The rate of energy dissipation ε is estimated by integrating the dissipation spectrum over the entire range of wavenumbers as follows,

$$\varepsilon = \int_0^{\infty} D(k) dk . \quad [3.7]$$

Table 3.1 shows a comparison between rates of energy dissipation computed by the three different methods at depths at which the wavenumber spectra of the

instantaneous stream wise velocity had well defined inertial subrange, i.e. $-5/3$ slope. The average percentage difference between values of ε estimated using the first and second methods is 10% and between the first and third methods the average percentage difference is 7%. The comparison shown in table 3.1 provides convincing evidence that using velocities u_{wr} and w_{wr} in the direct method (i.e. equation [3.3]) provides accurate estimates of ε . Therefore, the direct method was used in all subsequent analyses to estimate values of ε .

In Figures 3.5(a)&(b), vertical profiles of ε are plotted at five wind speeds for both clean and surfactant-influenced water surfaces, respectively. As the wind speed increased from 3.8 to 9.6 $\text{m}\cdot\text{s}^{-1}$, the rate of energy dissipation increased on average by a factor of 5 and 3.5 for clean and surfactant-influenced water surfaces, respectively. The profiles in Figure 3.5 show that ε decreased rapidly from the water surface down to a depth of approximately 3.0 cm and beneath this layer ε decreased much more slowly with depth. Figure 3.6 directly compares profiles of ε for clean and surfactant-influenced water surfaces at the lowest and highest wind speeds. At the lowest wind speed, the presence of a surfactant did not significantly affect the values of ε . At the highest wind speed, however the profiles have the same trend, but it is apparent that surfactants not only reduced ε values but also decreased the decaying of ε with depth. For example, at the higher wind speed, at depths of 20 mm and 27 mm, the value of ε decreased by a factor of 10 relative to its values at the uppermost grid point for clean and surfactant-influenced water surfaces, respectively.

In table 3.2, values of the depth averaged rate of energy dissipation, ε_{av} are compared for clean and surfactant-influenced water surfaces. At the lowest wind speed, ε_{av} was found to be the same for both surface conditions. At wind speeds of 4.9 and 6.2 $\text{m}\cdot\text{s}^{-1}$, the presence of the surfactant reduced ε_{av} on average by 15% and for wind speeds of 8.1 and 9.6 $\text{m}\cdot\text{s}^{-1}$, the values of ε_{av} were reduced by approximately 30%. The data in table 3.2 demonstrate that the surfactant reduced the rate of energy dissipation and as the wind speed increases, the magnitude of this reduction increases.

The Kolmogorov length scale η can be computed from the rate of energy dissipation ε using the following equation,

$$\eta = (\nu^3 / \varepsilon)^{1/4} \quad [3.8]$$

where ν is the kinematic viscosity of the water (Tennekes & Lumley 1972). It was found that η decreased as the wind speed increased and that the presence of a surfactant increased the value of η slightly. For example at a depth of 0.13 cm, η decreased from 271 μm to 180 μm for clean water surfaces and from 276 μm to 192 μm for surfactant-influenced water surfaces as the wind speed increases from 3.8 $\text{m}\cdot\text{s}^{-1}$ to 9.6 $\text{m}\cdot\text{s}^{-1}$. In addition, on average η increased by a factor of 2.3 going from a depth of 0.13 cm to 6.0 cm for both water surfaces conditions. Surfactants increased η by an average factor of 10% at the highest wind speed.

In the upper ocean, Soloviev *et al.* (1988) argued that ε should be scaled with the waterside friction velocity, u_{*w} , the depth below the interface, ζ , and the gravitational acceleration, g . Using dimensional analysis with g and u_{*w} chosen as the repeating variables, the dimensionless dissipation is, ε / gu_{*w} and the dimensionless depth is

$g\zeta / u_w^2$. In Figure 3.7, the dimensionless dissipation is plotted versus the dimensionless depth for both water surface conditions and all wind speeds. Figure 3.7 shows that the data beneath clean and surfactant-influenced water surfaces collapses onto separate curves for values of ε / gu_w greater than 0.0005. It is clear that the difference between the two data sets is due to the effect of the surfactant. It is also evident from Figure 3.7 that for both clean and surfactant-influenced water surfaces ε is approximately proportional to ζ^{-1} .

3.4 Discussion: Turbulent Kinetic Energy Dissipation

It has been reported that the rate of turbulent kinetic energy dissipation, ε was enhanced by up to several orders of magnitude at depths greater than the wave amplitude relative to a wall layer (i.e below the troughs of the waves) in both the laboratory and field (Agrawal *et al.* 1992; Thais and Magnaudet 1996). Comparing the magnitudes of ε observed in our study with previous measurements, Thais and Magnaudet (1996) measured values of ε of approximately $7 \text{ cm}^2\cdot\text{s}^{-3}$ below the troughs of laboratory wind waves. Siddiqui and Loewen (2005) measured values of ε in the range of 0.5 to $8 \text{ cm}^2\cdot\text{s}^{-3}$ in the top 2.5 cm below the troughs of laboratory wind waves at comparable wind speeds to this study. Terray *et al.* (1996) conducted field experiments and their measured values of ε were in the range of 1 to $5 \text{ cm}^2\cdot\text{s}^{-3}$ within the top meter. In this study the measured values of ε in the top 6 cm were in the range of 0.4 to $7 \text{ cm}^2\cdot\text{s}^{-3}$ for clean water surfaces and 0.26 to $5.4 \text{ cm}^2\cdot\text{s}^{-3}$ for surfactant-influenced water surfaces at the highest wind speed (see Figure 3.5). These results are comparable with previous field and laboratory results.

Figure 3.7 shows that ε is proportional to ζ^{-1} and this agrees with the classical law of the wall description of the surface layer (Melville 1996) and is a strong indication that the turbulent wind drift layer behaved similar to a wall layer. Siddiqui and Loewen (2005) also observed logarithmic velocity profiles but found that ε was proportional to $\zeta^{-0.55}$. In their experiments the average air-water temperature difference was 8 °C (the water was heated) but they argued that the existence of logarithmic velocity profiles was proof that buoyant production of turbulence was negligible compared to mechanically generated turbulence. However, it is possible that the large air-water temperature difference changed the dependence of ε with depth slightly. It is worth noting that small changes in ζ^{-n} are exaggerated when using wall layer scaling where n is the power of the water depth.

A number of previous investigations have shown that ε can be significantly enhanced relative to a wall layer (Veron and Melville 1999). For example, Drennan et al. (1992) found that ε was proportional to ζ^{-2} and that ε was enhanced by up to two orders of magnitude compared to a wall layer. In Figures 3.8(a)&(b), the dissipation is shown plotted using wall layer scaling for clean and surfactant-influenced water surfaces, respectively. Using wall layer scaling the dimensionless dissipation is given by $\varepsilon \cdot k \cdot \zeta / u_{*w}^3$ and the dimensionless depth is given by $g\zeta / u_{*w}^2$. The dimensionless dissipation is $O(1)$ which is consistent with our previous conclusion that in these experiments the turbulent wind drift layer was behaving similar to a wall layer. The dimensionless dissipation $\varepsilon \cdot k \cdot \zeta / u_{*w}^3$ represents the ratio of the rate of energy dissipation to the production of turbulence by the mean shear. When this term is $O(1)$

this implies that the turbulent transport and turbulent diffusion terms in the turbulent kinetic energy equation are relatively small (Kundu and Cohen 2002). Figure 3.8 shows that the value of $\varepsilon \cdot k \cdot \zeta / u_w^3$ increased as the wind speed increased, which means that as the wind speed increased the rate of energy dissipation increased slightly more than the rate of production. Figure 3.8(b) shows that beneath a surfactant-influenced water surface the dimensionless dissipation, $\varepsilon \cdot k \cdot \zeta / u_w^3$, increased as the wind speed increased (same trend as for clean water surfaces) and that it was also $O(1)$. Comparing Figure 3.8(a) with Figure 3.8(b) it is evident that $\varepsilon \cdot k \cdot \zeta / u_w^3$ was always less beneath surfactant-influenced water surfaces at the same wind speed. The dimensionless dissipation rate is smaller for surfactant-influenced water surfaces because the rate of energy dissipation ε is always less and the production by the mean shear, which is proportional to u_w^3 , is always larger in the presence of a surfactant.

In Figure 3.2, it was shown that there is a strong correlation between the air-water gas transfer velocity k_G and the mean-square wave slope $\langle S^2 \rangle$. Jähne *et al.* (1987) suggested that waves at all scales contribute to an energy cascade that eventually produces near-surface turbulence, thus enhancing the gas transfer velocity, k_G . They also argued that the observed correlation between k_G and $\langle S^2 \rangle$ was due to the fact that the mean-square wave slope is correlated with the near-surface turbulence generated by breaking waves. In Figure 3.9 the mean square wave slope, $\langle S^2 \rangle$, is plotted versus the rate of turbulent kinetic energy dissipation ε_{av} , depth averaged over the upper 2 cm for both clean and surfactant-influenced water surfaces. The plot shows that there is a correlation between ε_{av} and $\langle S^2 \rangle$ for both water surface conditions. These results agree

with Jähne's *et al.* (1987) hypothesis that the mean square waves slope is a measure of near-surface turbulence generated by waves. This is consistent with Siddiqui and Loewen (2005) who demonstrated that steeper waves on average generate stronger near-surface turbulence.

In Figure 3.9, the data points corresponding to the surfactant-influenced water surface are shifted to the left, indicating that at the same wind speed both ε and $\langle S^2 \rangle$ are smaller compared to a clean water surface. Both Figure 3.2 in this chapter and Figure 2.13 in the previous chapter show that the mean square wave slope is strongly correlated with the gas transfer velocity and the fraction of the momentum transferred to the aqueous boundary layer, irrespective of the surface cleanliness. However, Figure 3.9 shows that the correlation between ε_{av} and $\langle S^2 \rangle$ changes with the surface cleanliness. For example, Figure 3.9 shows that at $\langle S^2 \rangle = 0.032$, the value of ε_{av} for a surfactant-influenced water surface is 2.5 times larger than the corresponding value for a clean water surface. This mean square slope corresponds to wind speeds of 4.9 and 9.8 $\text{m}\cdot\text{s}^{-1}$ for clean and surfactant-influenced water surfaces, respectively. To achieve the same mean square wave slope when the surfactant was present requires twice the wind speed. This comparison has demonstrated that in order to obtain approximately the same gas transfer velocity and the same fraction of the momentum transferred to the aqueous boundary layer the wind speed must be doubled over a surfactant-influenced water surface. However, in this case the rate of turbulent kinetic energy dissipation will be much larger beneath the surfactant-influenced water surface than under a clean water surface at the same $\langle S^2 \rangle$.

3.5 Microscale-Breaking Waves

3.5.1 Detection Scheme

Siddiqui *et al.* 2001 were the first to show that strong near-surface vortices occurred in the crests of microscale-breaking waves and that they disrupt the skin layer and produce thermal wakes. Jessup *et al.* (1997) found that IR imagery is capable of detecting these thermal wakes and they demonstrated that IR imagery is an effective technique for studying microscale-breaking waves. Figure 3.10 shows a series of three IR images and the corresponding turbulent vorticity fields obtained from the DPIV data at a wind speed of $9.6 \text{ m}\cdot\text{s}^{-1}$. Positive vorticity values correspond to counter clockwise vortices and negative vorticity values correspond to clockwise vortices. The time difference between these three images is 1/15 sec. The thick black line represents the DPIV field of view in the IR images. In Figure 3.10(a), a wave crest that has traveled approximately one-third of the distance across the DPIV field of view is visible in the vorticity contour plot. This wave is identified as a non-breaking wave because in the corresponding IR image there is no disruption of the skin layer by this wave over top of the DPIV field of view. In Figure 3.10(b), the wave has traveled more than half of the distance across the DPIV field of view and in the corresponding IR image no thermal wake is visible. The vorticity reached a maximum value of approximately 20 s^{-1} in the crest region, which is above the background vorticity level, but still there is no disruption of the skin layer. In Figure 3.10(c), the wave has just passed the downwind end of the DPIV field of view and the vorticity has returned to the background level. It can be noticed in these figures that there are two thermal wakes generated by a microscale-

breaking waves that are clearly visible in the IR images to the left of the DPIV field of view.

In Figure 3.11, another series of three IR images and the corresponding turbulent vorticity fields are shown but for a typical microscale-breaking wave at a wind speed of $9.6 \text{ m}\cdot\text{s}^{-1}$. In Figure 3.11(a), the crest of a microscale-breaking wave has travelled approximately one-third of the distance across the DPIV field of view. A warm thermal wake is visible in the IR image due to the disruption in the cool skin layer and vorticity values up to 60 s^{-1} are visible under the crest and near the leading edge of this breaking wave in the vorticity contour plot. In the IR image in Figure 3.11(b), the leading edge of the breaker passed the middle of the DPIV field of view. The warm thermal wake is visible and strong vorticity, up to 80 s^{-1} , can be observed along the windward face of the wave in the corresponding vorticity contour plot. The leading edge of the breaker has just passed the downwind end of the DPIV field of view in Figure 3.11(c). Strong vortices in the wake of the wave can still be observed in the vorticity contour plot and the warm thermal wake is still visible.

Figure 3.11 demonstrates that a typical microscale-breaking wave generates strong vortices in its crest that disrupt the cool skin layer and create a wake that is visible in an IR image. Non-breaking waves do not generate vortices that are strong enough to disrupt the skin layer. After examining sequences of 9,000 vorticity fields at all five wind speeds at both water surface conditions it was concluded that the characteristic signature of a microscale-breaking wave is the appearance of strong vortices in the crest region. Therefore, following Siddiqui and Loewen (2005) a technique for detecting microscale-

breaking waves based on the statistical properties of the vorticity in the crest region was used.

The scheme for detecting microscale-breaking waves was based on the variance of the vorticity in the wave crest, computed from the instantaneous velocity fields. An algorithm developed by Siddiqui and Loewen (2005) was adapted for this study. Using the surface profile data any portion of a wave that appeared in the DPIV field of view that had a surface displacement greater than one-quarter the RMS wave amplitude was defined as a wave crest. If a wave crest was located within the DPIV field of view, a region-of-interest (ROI) was defined in the corresponding velocity field. The depth of the ROI was set equal to 1 cm in the wave-following coordinate system and its length was set equal to one-quarter of the dominant wavelength, λ_d . Siddiqui *et al.* (2001) showed that the size of the strong near-surface vortices generated beneath microscale-breaking waves were of the order of 1 cm and that is why the depth of the ROI was set equal to 1 cm. The location of the maximum surface displacement, η_{\max} was chosen as the center of the ROI. However, when η_{\max} was located closer than one-eighth of a wavelength to either side of the field of view, the ROI was placed at the edge of the velocity field. In Figure 3.12, the vorticity field beneath a wave crest at a wind speed of $9.6 \text{ m}\cdot\text{s}^{-1}$ is shown plotted with the ROI outlined in the figure with a dashed line. The criterion for the detection of microscale-breaking waves was if the variance of the vorticity exceeded a threshold value within the ROI.

The value of the vorticity threshold was set by comparing microscale-breaking waves detected visually in the sequences of IR images and those detected by the algorithm. Visually detecting microscale-breaking waves in the IR images is relatively

simple as was shown in Figure 3.11 where the leading edge of the breaker can be seen crossing the DPIV field of view. Normally, a wave appeared in three to four successive vorticity fields and IR images. A total of 1800 simultaneous IR images and DPIV vorticity fields (i.e. 120 sec of data at 15 Hz) at the two highest wind speeds were analyzed to select the vorticity threshold. Data at lower wind speeds was not used because it becomes more difficult to distinguish the thermal wakes generated by microscale-breaking waves visually from the background temperature field in the IR images at lower wind speeds. The detection algorithm was used to detect microscale-breaking waves in 1800 DPIV velocity fields at the highest two wind speeds for vorticity threshold values of 50, 60, 70 and 80 s^{-2} . Then the microscale-breaking waves were detected visually in the simultaneously sampled IR image sequences.

The results of this analysis are presented in table 3.3 for the highest wind speed. Table 3.3 shows the number of microscale-breaking waves identified using the detection algorithm, detected visually in the IR images and the number detected simultaneously by both methods. For example, 102 microscale-breaking waves were detected visually in the IR images and the detection algorithm detected 159 waves using a vorticity threshold of 50 s^{-2} . There were 98 breaking waves detected by both methods. That is, 61 of the waves detected by the algorithm using this vorticity threshold were not detected visually in the IR images. These are referred to as false positives because the algorithm falsely identified them as breaking waves when they did not generate a thermal wake in the IR images. The algorithm did not detect four of the 102 visually detected waves and these waves are referred to as false negatives. At this low value for the vorticity threshold there is a large number of false positives, 61, and a relatively small number of false

negatives, 4. Therefore, using this low threshold value will clearly lead to an over-estimation of the number of microscale breaking waves.

As the vorticity threshold is increased the number of false positives decreases but the number of false negatives increases. At the highest threshold value, 80 s^{-2} , the number of false positives decreased to 9 and the number of false negatives increased to 26. The optimum value for the vorticity variance threshold is the value that gives the minimum total number of false positives and false negatives. As shown in table 3.3, the optimum threshold value is 70 s^{-2} because at this value the total number of false positives and false negatives is 32. At this threshold value the false positives approximately cancel the false negatives. At the second highest wind speed the optimum vorticity threshold was also found to be 70 s^{-2} . In this case the number of false positives was 13 and the number of false negatives was 15. Siddiqui & Loewen (2005) also found that the optimum vorticity threshold was 70 s^{-2} . Accordingly, the vorticity threshold was set to 70 s^{-2} .

The detection algorithm was then used to analyze all of the DPIV data, that is, 9000 velocity fields and their corresponding surface profiles (10 minutes of data at 15 Hz) at each wind speed for both clean and surfactant-influenced water surfaces. If a wave has a surface displacement greater than one-quarter the RMS wave amplitude, it is identified as a wave crest and it may be a breaking or non-breaking wave. Accordingly, velocity fields associated with small waves (i.e. surface displacement less than one-quarter the RMS wave amplitude) were not included when calculating the characteristics of breaking and non-breaking waves.

A wave crest typically appeared in two to four velocity fields and surface profiles, depending on its phase speed for both breaking and non-breaking waves. For each field that the wave crest appeared in, the variance of the vorticity within the ROI, the wave amplitude and the wave slope on the downwind face of the wave were computed. The maximum values of the variance of the vorticity (Ω_{max}), amplitude (η_{max}) and wave slope (S_{max}) were computed in all fields that a particular wave crest appeared in. The wave was identified as a microscale-breaking wave if Ω_{max} exceeded 70 s^{-2} in any velocity field in which it appeared. If Ω_{max} never exceeded 70 s^{-2} then the wave was identified as a non-breaking wave. Normally, Ω_{max} , η_{max} and S_{max} occurred in the same field but not always. The velocity fields associated with breaking waves were then conditionally sampled. The one velocity field in which Ω_{max} occurred was selected for each wave. Conditionally sampling the velocity data in this manner selects all of the velocity fields in which the signature of a particular microscale-breaking wave was the strongest. Another advantage of this conditional sampling is that these velocity fields occur at approximately the same phase in the breaking process. Non-breaking velocity fields were conditionally sampled in the same way as well to be consistent. Once the velocity fields are identified as breaking and non-breaking then comparisons can be made between microscale breaking waves, and non-breaking waves.

3.5.2 Microscale-Breaking Wave Characteristics

Using the detection algorithm it was possible to detect the percentage of microscale-breaking waves at each wind speed. The percentage of breaking waves, P_b is defined as the number of breaking waves divided by the total number of identified wave crests as a percentage. In other words, it is the number of breaking waves divided by summing up

the number of breaking and non-breaking waves. In Figure 3.13, the breaking percentages detected by the algorithm are plotted as a function of wind speed for clean and surfactant-influenced water surfaces. It can be seen that at the lowest wind speed ($3.8 \text{ m}\cdot\text{s}^{-1}$), the breaking percentage is 9% for a clean water surface and 7% for a surfactant-influenced water surface. As expected, the breaking percentage increases as the wind speed increases and it reached a maximum value of 55% for a clean water surface and 35% for a surfactant-influenced water surface. Surfactants reduced the percentage of microscale-breaking waves by a factor of approximately one third on average.

The average values of the maximum wave slope, $\langle S_{max} \rangle$, and maximum wave amplitude, $\langle \eta_{max} \rangle$, were computed at each wind speed for breaking and non-breaking waves for both water surface conditions. In Figures 3.14(a)&(b), $\langle S_{max} \rangle$ of microscale breaking and non-breaking waves is plotted versus the wind speed for both clean and surfactant-influenced water surfaces. As the wind speed increased from 3.8 to $9.6 \text{ m}\cdot\text{s}^{-1}$ the average maximum slope of breaking waves increased from 0.16 to 0.61 and from 0.16 to 0.38 for clean and surfactant-influenced water surfaces respectively. For non-breaking waves, $\langle S_{max} \rangle$ increased from 0.13 to 0.43 and from 0.13 to 0.29 for clean and surfactant-influenced water surfaces, respectively over the same range of wind speeds. These data show that breaking waves are on average 42% and 34% steeper than non-breaking waves and on clean and surfactant-influenced water surfaces, respectively. At the lowest wind speed $\langle S_{max} \rangle$ is approximately equal for both water surface conditions but as the wind speed increases the slopes of both breaking and non-breaking were reduced by the presence of the surfactant. For example, at the highest wind speed the surfactant reduced

the average slope of the microscale-breaking waves by 30%. The average reduction in $\langle S_{max} \rangle$ due to the presence of a surfactant is 28% for breaking waves and 22% for non-breaking waves.

The average maximum wave amplitude, $\langle \eta_{max} \rangle$, of microscale breaking and non-breaking waves is plotted in Figures 3.15(a)&(b) as a function of wind speed for clean and surfactant-influenced water surfaces. As the wind speed increased from 3.8 to 9.6 $\text{m}\cdot\text{s}^{-1}$, $\langle \eta_{max} \rangle$ of the breaking waves increased from 0.19 cm to 1.0 cm for clean water surfaces and from 0.15 to 0.7 cm for surfactant-influenced water surfaces. For non-breaking waves, $\langle \eta_{max} \rangle$ increased from 0.15 to 0.72 cm and from 0.13 to 0.59 cm for clean and surfactant-influenced water surfaces respectively over the same range of wind speeds. Microscale-breaking waves were on average 33% and 25% higher than non-breaking waves for clean and surfactant-influenced water surfaces, respectively. The data in Figure 3.15 indicates that surfactants lowered the average height of both breaking and non-breaking waves and as the wind speed increased, the reductions in height become more pronounced. The surfactant reduced the height of breaking and non-breaking waves on average by 25 % and 19 %, respectively.

The data in Figures 3.14 and 3.15 imply that microscale-breaking waves could be detected using a technique based on the wave slope and/or wave amplitude. To investigate if this idea has merit probability distribution functions (PDF) of S_{max} and η_{max} were compared for breaking and non-breaking waves. In Figures 3.16 and 3.17, PDF's of S_{max} and η_{max} for breaking and non-breaking waves, respectively, on a clean water surface at a wind speed of 9.6 $\text{m}\cdot\text{s}^{-1}$ are compared. As expected the PDF's of both S_{max} and η_{max} for breaking waves are shifted to the right of the PDF's for the non-breaking waves. It is

evident from these figures that there is a large overlap between the PDF's of slope and amplitude for breaking and non-breaking waves. This overlap also occurred at all wind speeds and for both clean and surfactant-influenced water surfaces as well. Holthuijsen and Herbers (1986) compared the PDF's of wave slope and amplitude for large-scale breaking and non-breaking waves in the ocean and they also observed significant overlap similar to our results.

In Figures 3.18 and 3.19, the PDF's of S_{max} and η_{max} for breaking waves on clean and surfactant-influenced water surfaces are compared. The PDF's of both S_{max} and η_{max} on the surfactant-influenced water surfaces are shifted to the left since the average slope and magnitude of all waves including breaking ones are reduced by the surfactant. However, there is still considerable overlap of the slope and amplitude PDF's of breaking waves on the clean and surfactant-influenced water surfaces.

3.6 Discussion: Microscale-Breaking Waves

It is challenging to detect large or small-scale breaking waves reliably. Large-scale breaking waves entrain air that can be detected successfully using a number of different methods. Some of these methods depend on the visual signature created by the whitecap and some are acoustic methods that rely on the underwater sound produced by the air entrainment process. These methods are obviously not applicable to microscale breaking waves. Alternatively, methods based on wave slope, IR imagery and the turbulent flow field generated beneath the waves can be used to detect microscale-breaking waves. Loewen and Siddiqui (2005) compared three methods for detecting microscale-breaking waves. They concluded that a vorticity threshold detection algorithm identical to the one

described above was the most accurate. The other two methods that were included in their comparison were a method that used a local wave slope threshold and one that applied a temperature threshold to the IR image sequences.

Melville (1996) discussed previous efforts to detect breaking waves based on point measurements of wave properties. He wrote that point measurements are problematic because they may catch breaking waves at any phase in the breaking process. Hence, the measured wave parameters may not necessarily be the same as those at the onset of breaking. Specifically, he noted that using point measurements of the surface displacement or its derivative in time as an indicator of breaking has a lot of inherent difficulties.

Jessup *et al.* (1997) computed the frequency spectrum of the time series of the fractional area covered by the thermal wakes generated by microscale-breaking waves at a wind speed of $5.0 \text{ m}\cdot\text{s}^{-1}$ and a fetch of 5 m. They found that the peak of this spectrum was located at approximately one-third of the dominant wave frequency and accordingly they estimated that the breaking percentage was approximately 33%. In this study at a wind speed of $5.0 \text{ m}\cdot\text{s}^{-1}$ and a fetch of 5.5 m the breaking percentage was 30% (see Figure 3.13), which is in a reasonable agreement with the value observed by Jessup *et al.* (1997).

Siddiqui and Loewen (2005) conducted an earlier set of experiments in the same wind wave tank at the same fetch of 5.5 m and with a clean water surface. They reported breaking percentages of 11%, 45% and 77% at wind speeds of 4.5, 6.1 and $7.4 \text{ m}\cdot\text{s}^{-1}$. The corresponding breaking percentages on a clean water surface at the same wind speeds determined in this study were 19%, 38% and 50%. The trends are similar but the breaking percentages were considerably smaller in this study at all wind speeds. The

most likely explanation for these differences is that a vane that had directed the airflow towards the water surface at the upwind end of the wind wave tank was removed for this study. In addition, Siddiqui and Loewen (2005) heated the water and maintained an average air-water temperature difference of approximately 8°C. The combination of these two factors could explain the higher breaking percentages.

Banner and Peirson (1998) measured the local wave steepness at a point using a wire wave gauge. They defined a microscale-breaking wave as any wave that exceeded a slope threshold of 0.5 on its downwind face. Using this detection method they estimated that 53%, 70% and 89% of the waves break at wind speeds of 4.8, 6.3 and 8.1 m·s⁻¹, respectively at a fetch of 4.35 m. These values are considerably higher than the breaking percentages estimated in this study. In Figure 3.16 it was demonstrated that there is a significant overlap between the PDF's of the slope for breaking and non-breaking waves. The PDF in Figure 3.16 shows that approximately 40% of the non-breaking waves have a local slope greater than 0.5 or that 40% of the detected waves would be false positives. This might explain why Banner and Peirson's (1998) breaking percentages are so high.

The rate of turbulent kinetic energy dissipation ε was computed under the conditionally sampled velocity fields using the direct method. This produced estimates of dissipation rate that fall into three categories. The first is the dissipation rate beneath the ROI of microscale breaking waves, the second is the rate beneath the ROI of non-breaking waves and the third is the rate beneath the remaining velocity fields corresponding to small waves (surface displacement less than one-quarter the RMS wave amplitude). The third category will be referred to in the following discussion as the background velocity fields.

In Figures 3.20 (a)&(b), four profiles of ε at the highest wind speed are plotted for clean and surfactant-influenced water surfaces, respectively. Describing the four profiles starting from the profile with the highest to the lowest dissipation rates; the first is the average ε vertical profile directly under crests (i.e. ROI) of microscale-breaking waves; the second is the average ε profile for all the velocity fields (as reported in Figure 3.5); the third is the average ε profile beneath the background velocity fields and; the fourth is the average ε profile beneath the crests (i.e. ROI) of non breaking waves. The fact that the dissipation rate is the highest beneath the crests of microscale-breaking waves is evidence that the most intense near-surface turbulence occurred in these regions.

An additional finding from Figures 3.20(a)&(b) is that ε beneath the crests of non-breaking waves is smaller than the background ε . This means that the near-surface turbulence beneath non-breaking waves, is weaker than the background turbulence occurred from the regular flow (excluding breaking waves). This may be explained by the fact that the turbulent wake produced by microscale-breaking waves usually extended outside the ROI on the windward side of the waves. An example of this can be seen in Figure 3.11(c) where the leading edge of the breaker has just passed downwind end of the DPIV field of view but the region of high vorticity region extends across the entire field of view. Therefore, including these extended wakes with the background likely produces considerably larger rates of turbulent kinetic energy dissipation values than beneath the crests of non-breaking waves.

The profiles in Figure 3.20 (a) indicate that most of the changes and differences in the ε profiles occurred near the water surface. For example, ε decreased by approximately a

factor of 15 from a depth of 0.12 cm to 3.5 cm beneath the crests of breaking waves in clean water. Similarly, in Figure 3.20(b) ε decreased by approximately a factor of 15 from a depth of 0.12 cm to 2.5 cm depth beneath the crests of breaking waves in surfactant-influenced water surface. At depths larger than 3.5 cm for clean and 2.5 cm for surfactant-influenced, the ε profiles collapsed into a single curve. In clean water surface, the ratio of ε beneath breaking waves to ε beneath non-breaking waves was 2.3 at a depth of 0.12 cm and it decreased to 1.1 at a depth of 3.5 cm. Below 3.5 cm, this ratio was approximately constant and equal to 1.05. A similar result was obtained for the surfactant-influenced water surface; that is, this ratio was 2.5 at a depth of 0.12 cm and decreased to 1.1 at a depth of 2.5 cm. Below that depth the ratio was on average 1.05. Consequently, at depths greater than 3.5 cm and 2.5 cm the depth averaged values of ε were found to be approximately equal for all four profiles plotted in Figures 3.20 (a)&(b) for clean and surfactant-influenced water surfaces, respectively.

These findings lead to the conclusion that, at this wind speed, microscale wave breaking generates near-surface turbulence to depths of approximately 3.5 cm and 2.5 cm for clean and surfactant-influenced water surfaces, respectively. At greater depths the turbulence or the rate of turbulent kinetic energy dissipation are dependent only on the mean shear flow. An interesting conclusion is that not only did the surfactant reduce the number of breaking waves and the rate of energy dissipation but it also reduced the thickness of the layer of enhanced near-surface turbulence. Interestingly, the depths 3.5 cm and 2.5 cm are 4.2 and 3.9 times the RMS wave height for clean and surfactant-influenced water surfaces, respectively. Hence, it is logical to conclude that the thickness of the layer of the enhanced near-surface turbulence is proportional to the wave height,

whether or not surfactant is present. The trends of the four ε profiles in Figure 3.20 are similar at the other four wind speeds in both clean and surfactant-influenced water.

Figures 3.21(a)&(b) show vertical profiles of ε beneath the crests of microscale-breaking at all five wind speeds for clean and surfactant-influenced water surfaces, respectively. Comparing the profiles in Figures 3.21 with the profiles in Figure 3.5, it can be seen that the values of ε are larger beneath microscale-breaking waves than non-breaking waves for both water surface conditions at all wind speeds. It is evident in Figure 3.21 that ε decreases rapidly with depth by approximately a factor of 15 at depths from 1.5 to 3.5 cm for clean water surfaces and from 1.2 to 2.5 cm for surfactant-influenced water surfaces according to the wind speed. Using the data from Figures 3.21(a)&(b), it was found that the surfactant reduced the rate of energy dissipation beneath microscale-breaking waves on average by 20%. Moreover, the surfactant reduced the depth of the influence of microscale wave breaking on the near-surface turbulence at all wind speeds by an average factor of 35%. The value of ε averaged over the top 2 cm depth under microscale-breaking waves was on average 1.9 and 1.7 larger than under non-breaking waves for clean and surfactant influences water surfaces, respectively. This is comparable with Siddiqui and Loewen (2005) who reported that the rate of energy dissipation beneath breaking waves is on average 2.5 times larger than beneath non-breaking waves.

In Figure 3.22 the average maximum mean square wave slope on the downwind face of the waves, $\langle S_{max}^2 \rangle$ is plotted versus the rate of energy dissipation, ε , averaged over top 2 cm for clean and surfactant-influenced water surfaces. This plot demonstrates

that there is a strong linear correlation between the two parameters for both water surface conditions. Conditionally sampling the microscale-breaking waves illustrates the direct relation between the mean square slope of breaking waves and the near-surface turbulence as this linear correlation was not observed in Figure 3.9. It also shows that ε , beneath a microscale-breaking wave in surfactant-influenced water surface is much higher at the same $\langle S_{max}^2 \rangle$. The plot shows that there is more turbulence when the waves are steeper. These results support the hypothesis that microscale-breaking waves are the main source of the near-surface turbulence, because waves that have steeper forward faces are associated with enhanced rates of turbulent kinetic energy dissipation. Moreover, this agrees with the previously mentioned hypothesis that the slope of the waves is the most important parameter that is relating the near-surface turbulence to gas transfer and energy dissipation.

The effect of the surfactant is obvious in Figure 3.22. At the lowest wind speed the dissipation rate and average maximum mean square slope are the same for clean and surfactant-influenced water surfaces. This is because the near-surface turbulence at this low wind speed is produced primarily via shear production. This follows from the fact that in Figure 2.8 it was shown that for both water surface conditions that 80% to 90% of the total drag was tangential, that is, the wave drag was only 10% to 20% at the lowest wind speed. As the wind speed increased the wave drag increased and the tangential drag decreased but at all wind speeds the fraction of the total drag supported by the waves was greater for clean water surfaces. The mean square slope is smaller in the presence of surfactant because surfactants damped the capillary waves and hence the near-surface turbulence and rates of energy dissipation were reduced.

Csanady (2001) described in detail the pathways of momentum transfer at the air-water interface. He stated that the momentum flux at the airside is transferred through three processes; breaking of short waves or the micro breaking of waves in the shallow surface layer; momentum transferred into shear flow; and momentum transferred to long waves. In the absence of large scale breaking waves (i.e. whitecaps), the portion of momentum transferred to long waves is small, which is the case in this study. The ratio τ_w/τ_a , represents the portion of the momentum flux that is transferred to the shear flow (see chapter 2). Csanady (2001) stated that wave breaking transfers a large fraction of the momentum downward; thus the dominant loss mechanism is wave breaking. He also pointed out that wave breaking injects significant amounts of turbulent kinetic energy into the water layer to a depth of the order of the wave height.

The results presented in this chapter on the percentage of microscale breaking waves, P_b , and the rate of dissipation of turbulent kinetic energy, ε are consistent with Csanady's (2001) description of the pathways of momentum transfer across the air-water interface. In Figure 2.12, the ratio τ_w/τ_a was shown plotted versus the wind speed for clean and surfactant-influenced water surfaces. As the wind speed increased, the ratio τ_w/τ_a decreased for both water surface conditions and at wind speeds greater than $7 \text{ m}\cdot\text{s}^{-1}$ the wave drag comprised 60% to 80% of the total drag. In Figure 3.23 the ratio $(1 - \tau_w/\tau_a)$ that represents the portion of the momentum flux that is transferred to the wave field, is plotted versus the percentage of microscale-breaking waves, P_b . The correlation coefficient between these two parameters was found to be 0.94. This means that the percentage of microscale-breaking waves increased proportionally with the fraction of the momentum transferred to the wave field regardless of the water surface condition. This

is consistent with the increase in the depth-averaged values of ε listed in table 3.1. That is, as the wind speed increased the wave drag became dominant and this led to more microscale wave breaking and more intense near-surface turbulence. At low wind speeds the tangential drag dominates and there is less microscale wave breaking and weaker near-surface turbulence.

Jähne *et al.* (1987) argued that air-water gas transfer velocity is strongly correlated with the mean square slope of the waves as it is directly related to the near-surface turbulence generated by waves. Figure 3.24 shows the relation between the measured bulk gas transfer velocity, k_G , and the percentage of microscale-breaking waves, P_b . The magnitude of the correlation coefficient for the data in Figure 3.24 is 0.96 indicating that there is a strong linear correlation between k_G and P_b . This explains the observed correlation between the air-water gas transfer velocity and the mean square wave slope. That is, as the wind speed increases, the fraction of the momentum transferred to the wave field increases, waves become steeper, the number of microscale-breaking waves increases, near-surface turbulence becomes more intense and hence the gas transfer velocity increases.

The effect of the surfactant on the partitioning of the stress was to increase the value of τ_w / τ_a by 0.1 to 0.2 at a given wind speed compared to the clean water surface. As was discussed in chapter 2 this is due to the fact that the waves are smaller in amplitude and less steep, producing a smoother water surface, when a surfactant is present. This results in significantly less microscale wave breaking (see Figure 3.13) and weaker near-surface turbulence (see table 3.1). Moreover, the depth of the layer of enhanced near-surface turbulence is reduced by the surfactant.

3.7 Conclusions

The properties of the near-surface turbulence generated beneath wind waves in clean and surfactant-influenced water were reported in this study. The presence of a surfactant caused the rate of dissipation of turbulent kinetic energy to decrease but only for wind speeds larger than $4.0 \text{ m}\cdot\text{s}^{-1}$. The ratio of the energy dissipation rate in surfactant-influenced water, to that in clean water decreased from 1.0 to 0.70 as the wind speed increased from 3.8 to $9.6 \text{ m}\cdot\text{s}^{-1}$. The rate of energy dissipation was found to be proportional to ζ^{-1} and this agrees with the classical law of the wall description of the surface layer. An enhanced layer of turbulence was observed in which the rate of energy dissipation decreased rapidly to 7% of its original value just below the interface. The thickness of this layer varied from 1.5 to 3.5 cm and from 1.2 to 2.5 cm for clean and surfactant-influenced water surfaces, respectively as the wind speed increased from 3.8 to $9.6 \text{ m}\cdot\text{s}^{-1}$. Surfactants reduced the thickness of the enhanced layer of turbulence on average by 35%.

Microscale-breaking waves were detected by applying a threshold to the vorticity in the wave crest. As the wind speed increased from 3.8 to $9.6 \text{ m}\cdot\text{s}^{-1}$, the percentage of breaking waves increases from 9% to 55% and from 7% to 35% for clean and surfactant-influenced water surfaces, respectively. Surfactants reduced the percentage of wave breaking by approximately one third. Furthermore, the presence of surfactants changed the geometric properties of microscale-breaking waves and non-breaking waves. They reduced the wave amplitude by an average factor of 28% for breaking waves and 22% for non-breaking waves and reduced the maximum wave slope on the forward face of the waves by an average factor of 25% for breaking waves and 19% for non-breaking waves.

A strong linear correlation was observed between the maximum mean square wave slope on the downwind face of the breaking waves and the depth averaged rate of energy dissipation beneath the crest of the breaking waves. The fraction of the total momentum transferred to the wave field was found to be strongly correlated with the percentage of breaking waves irrespective of the water surface cleanliness. In addition, it was found that the bulk gas transfer velocity is strongly correlated with the percentage of breaking waves are irrespective of the water surface cleanliness.

U_∞ (m.s ⁻¹)	ζ (mm)	ε_1 (cm ² .s ⁻³)	ε_2 (cm ² .s ⁻³)	ε_3 (cm ² .s ⁻³)
3.79	6.50	0.36	0.28	0.25
4.89	6.50	0.82	0.70	0.53
4.89	9.10	0.56	0.44	0.39
6.23	9.10	0.89	0.80	0.68
6.23	11.70	0.67	0.70	0.57
7.99	6.50	1.89	1.96	1.69
7.99	9.10	1.41	1.41	1.33
7.99	11.70	1.12	1.07	0.97
9.53	6.50	2.80	3.01	2.83
9.53	9.10	2.01	2.23	1.93
9.53	11.70	1.58	1.82	1.48

Table 3.1: Comparison between the rates of turbulent kinetic energy dissipation computed using three different methods for clean water surface runs. U_∞ is the wind speed; ζ is the water depth in the wave-following coordinate system; ε_1 is the rate of energy dissipation calculated by the direct method; ε_2 is the rate of energy dissipation calculated by fitting a $k^{-5/3}$ line in the inertial subrange of the wavenumber spectrum; ε_3 is the rate of energy dissipation calculated by integrating the dissipation spectrum.

Clean water surfaces					
U_{∞} (m.s ⁻¹)	3.79	4.89	6.23	7.99	9.53
ϵ_{av} (cm ² .s ⁻³)	0.37	0.77	1.14	1.81	2.57

Surfactant influenced water surfaces					
U_{∞} (m.s ⁻¹)	3.87	4.91	6.21	8.15	9.75
ϵ_{av} (cm ² .s ⁻³)	0.38	0.66	0.95	1.24	1.82
Ratio	1.02	0.86	0.84	0.68	0.71

Table 3.2: Depth-averaged rate of energy dissipation values for the top 2 cm of water, ϵ_{av} , for clean and surfactant-influenced water surfaces runs. The ratio of ϵ_{av} for surfactant-influenced water surface runs to the ϵ_{av} for clean water surface runs is shown in the last row.

$\Omega \text{ s}^{-2}$	50	60	70	80
N_{DS}	159	125	104	85
N_V	102	102	102	102
N_C	98	93	87	76
N_{FP}	61	32	17	9
N_{FN}	-4	-9	-15	-26
$N_{FP}+N_{FN}$	57	23	2	-17

Table 3.3: Values of Ω , the vorticity variance threshold; N_{DS} , the number of microscale-breaking waves identified by the detection scheme; N_V , the number of microscale-breaking waves identified by visual inspection of the IR images; N_C , the number of microscale-breaking waves identified as such by both methods; N_{FP} , the number of false positive waves = $N_{DS} - N_C$ and N_{FN} , the number of false negative waves = $N_C - N_V$. The results are based on 1800 IR images and DPIV vorticity fields at the highest wind speed.

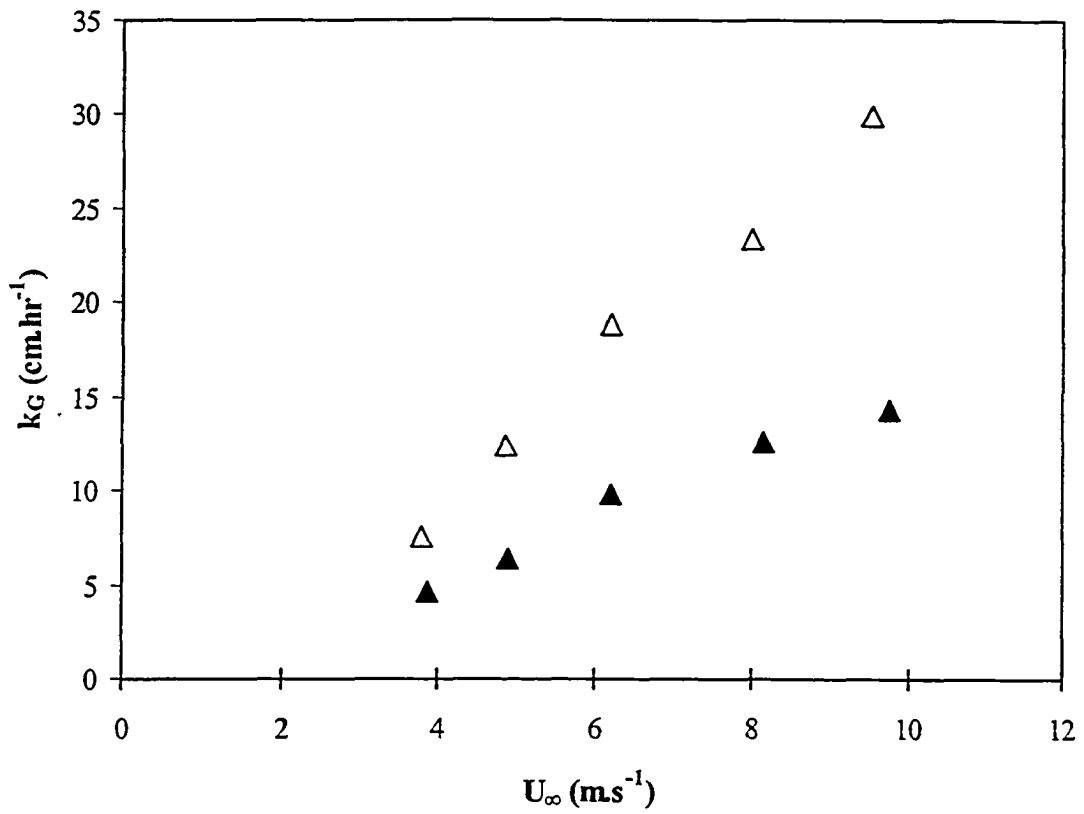


FIGURE 3.1: Plot of the bulk gas transfer velocity, k_G for various wind speeds. Δ , = Clean water surface; \blacktriangle , = surfactant-influenced water surface (Atmane *et al.* 2004).

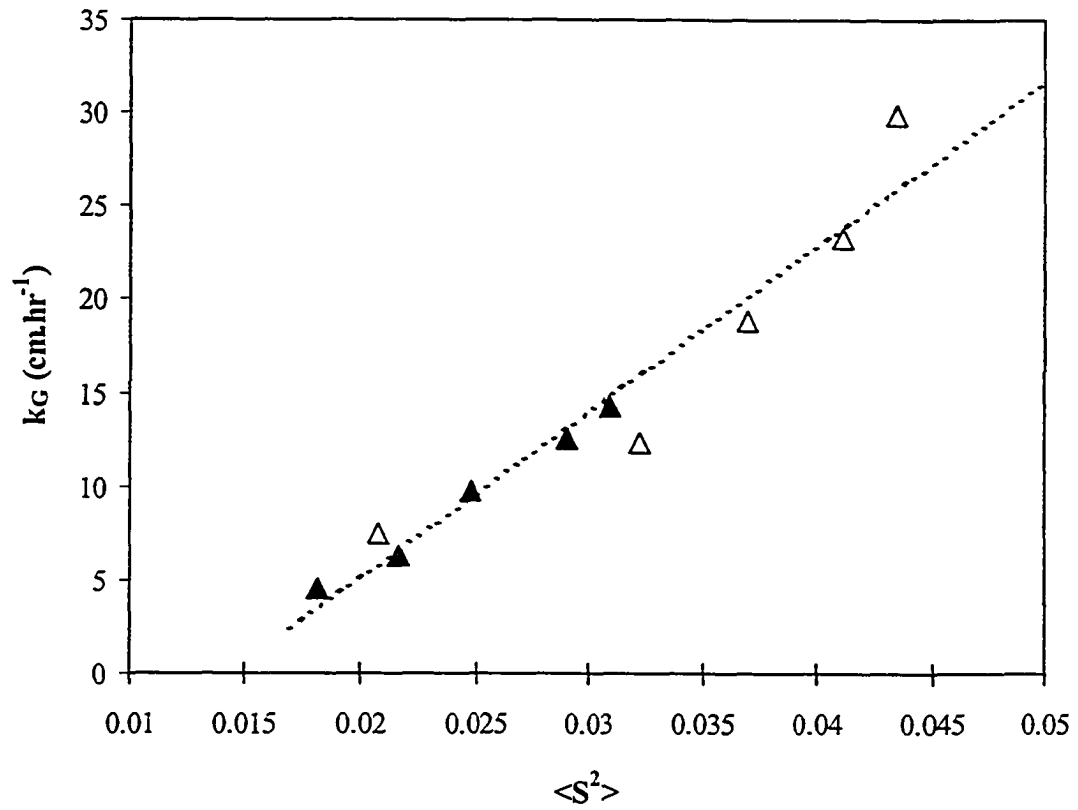


FIGURE 3.2: Plot of the bulk gas transfer velocity, k_G versus the mean square wave slope. Δ , = Clean water surface; \blacktriangle , = surfactant-influenced water surface.

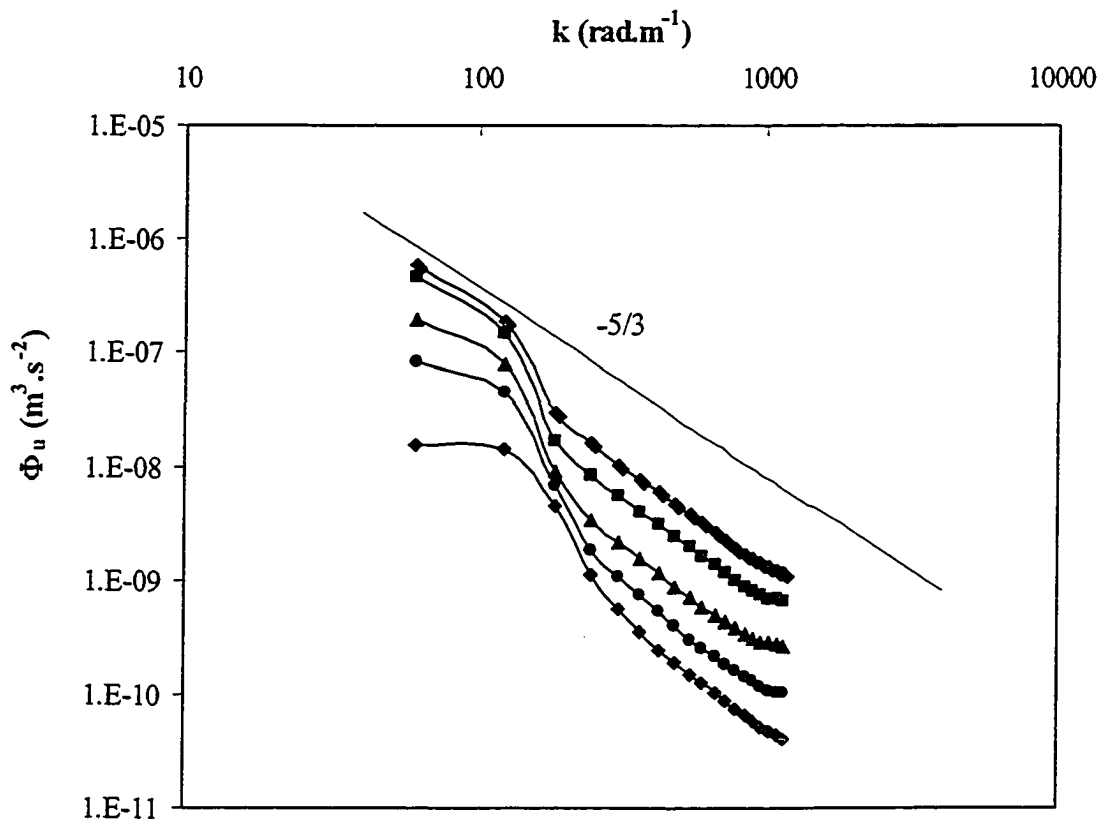


FIGURE 3.3: Longitudinal wavenumber spectra $\Phi_u(k)$ of the streamwise instantaneous velocity component, at five wind speeds for clean water surface runs computed using 10 minutes of data at a depth of 9.0 mm. \blacklozenge , = $3.8 \text{ m} \cdot \text{s}^{-1}$; \bullet , = $4.9 \text{ m} \cdot \text{s}^{-1}$; \blacktriangle , = $6.2 \text{ m} \cdot \text{s}^{-1}$; \blacksquare , = $8.0 \text{ m} \cdot \text{s}^{-1}$; \blacktriangledown , = $9.5 \text{ m} \cdot \text{s}^{-1}$.

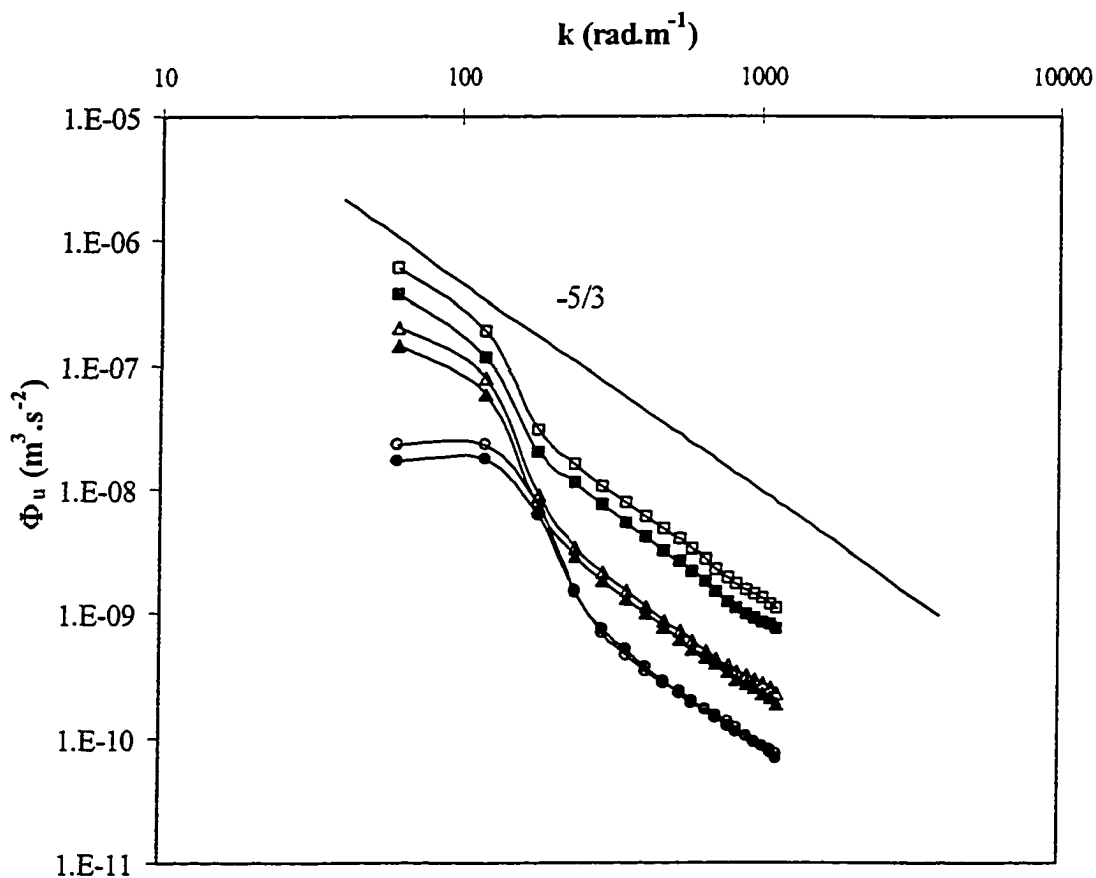


FIGURE 3.4: Comparison of the longitudinal wavenumber spectra $\Phi_u(k)$ of the streamwise instantaneous velocity component for clean and surfactant-influenced water surfaces computed using 10 minutes of data at a depth of 9 mm. \circ , = clean $3.8 \text{ m} \cdot \text{s}^{-1}$; \bullet , = surfactant $3.8 \text{ m} \cdot \text{s}^{-1}$; Δ , = clean $6.2 \text{ m} \cdot \text{s}^{-1}$; \blacktriangle , = surfactant $6.2 \text{ m} \cdot \text{s}^{-1}$; \square , = clean $9.6 \text{ m} \cdot \text{s}^{-1}$; \blacksquare , = surfactant $9.6 \text{ m} \cdot \text{s}^{-1}$.

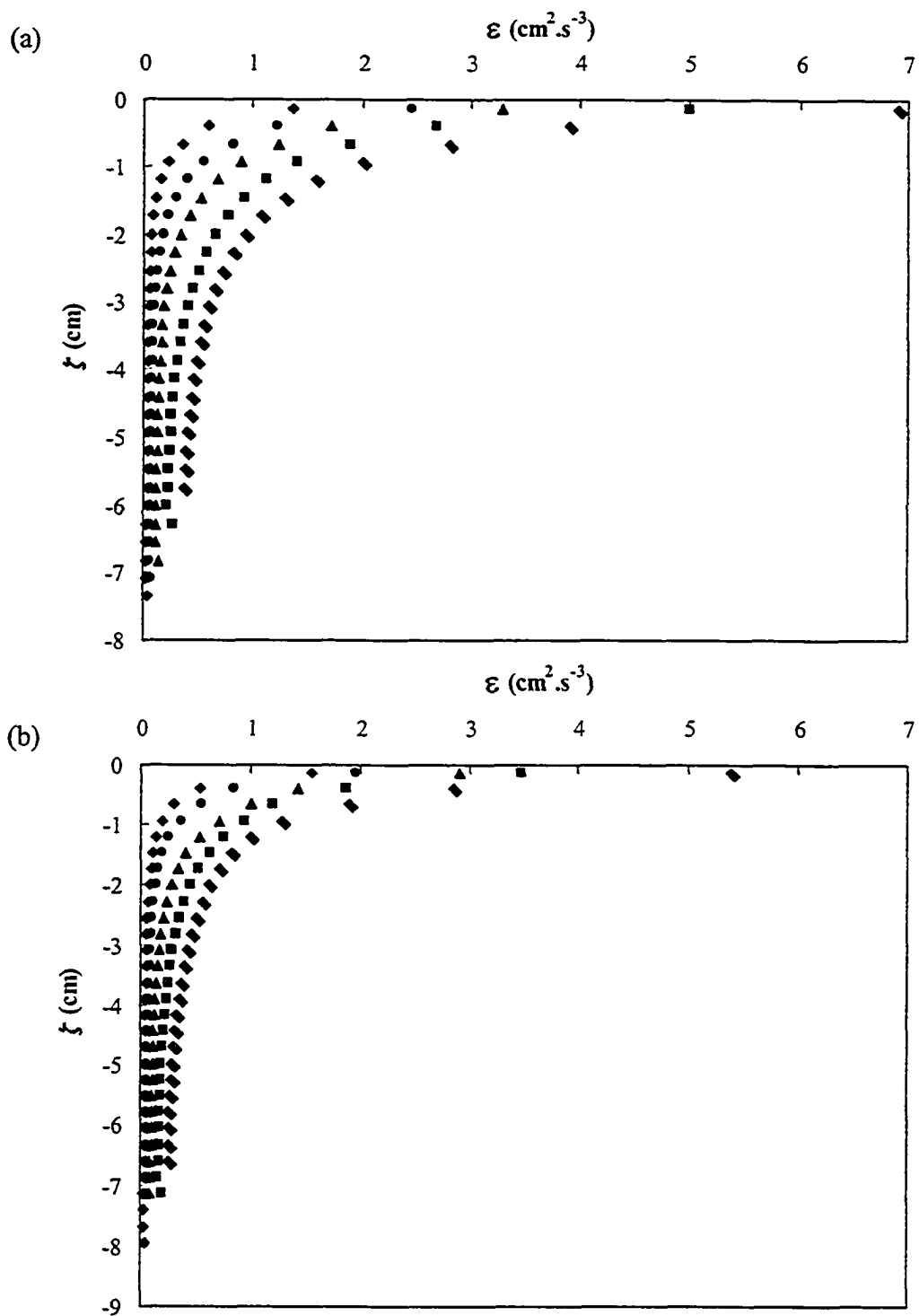


FIGURE 3.5: Vertical profiles of the rate of energy dissipation ε , and the vertical coordinate in the wave following system is ζ . Values are averaged over 10 minutes of data. (a) Clean water surface, (b) Surfactant-influenced water surface. \blacklozenge , = $3.8 \text{ m}\cdot\text{s}^{-1}$; \bullet , = $4.9 \text{ m}\cdot\text{s}^{-1}$; \blacktriangle , = $6.2 \text{ m}\cdot\text{s}^{-1}$; \blacksquare , = $8.0 \text{ m}\cdot\text{s}^{-1}$; \blacktriangledown , = $9.6 \text{ m}\cdot\text{s}^{-1}$.

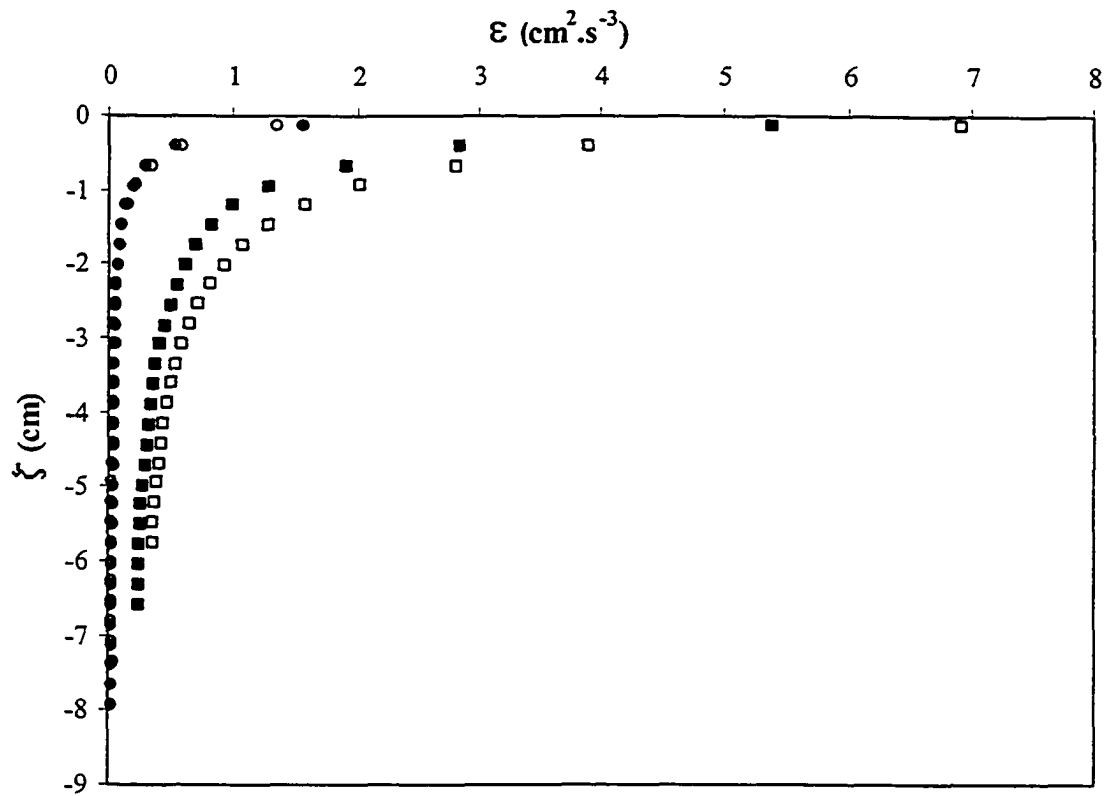


FIGURE 3.6: Vertical profiles of the rate of energy dissipation, ϵ , for clean and surfactant-influenced water surfaces. ζ is the vertical coordinate in the wave following system. Values are averaged over 10 minutes of data. ○, = clean $3.8 \text{ m} \cdot \text{s}^{-1}$; ●, = surfactant $3.8 \text{ m} \cdot \text{s}^{-1}$; □, = clean $9.5 \text{ m} \cdot \text{s}^{-1}$; ■, = surfactant $9.7 \text{ m} \cdot \text{s}^{-1}$.

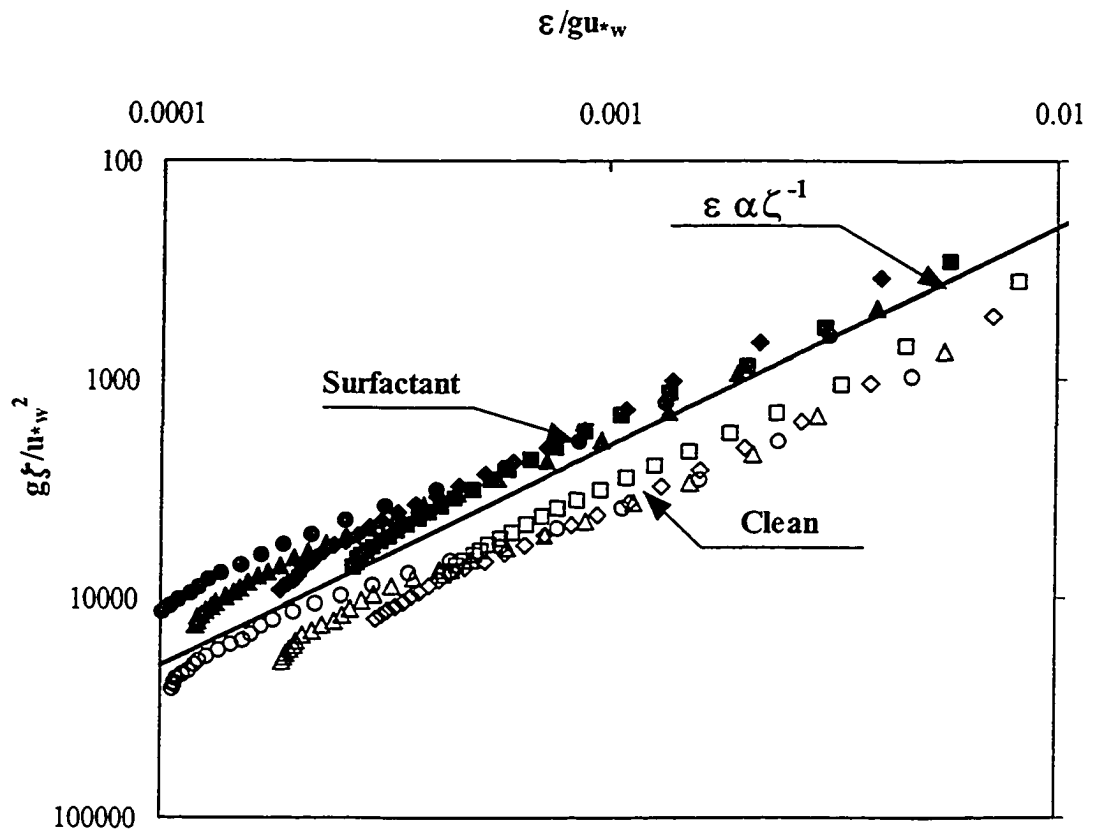


FIGURE 3.7: Plot of the dimensionless rate of energy dissipation, ϵ/gu_{*w} , versus the dimensionless depth, $g\zeta/u_{*w}^2$. Open symbols are for clean water surface runs and dark symbols are for surfactant-influenced water surface runs.

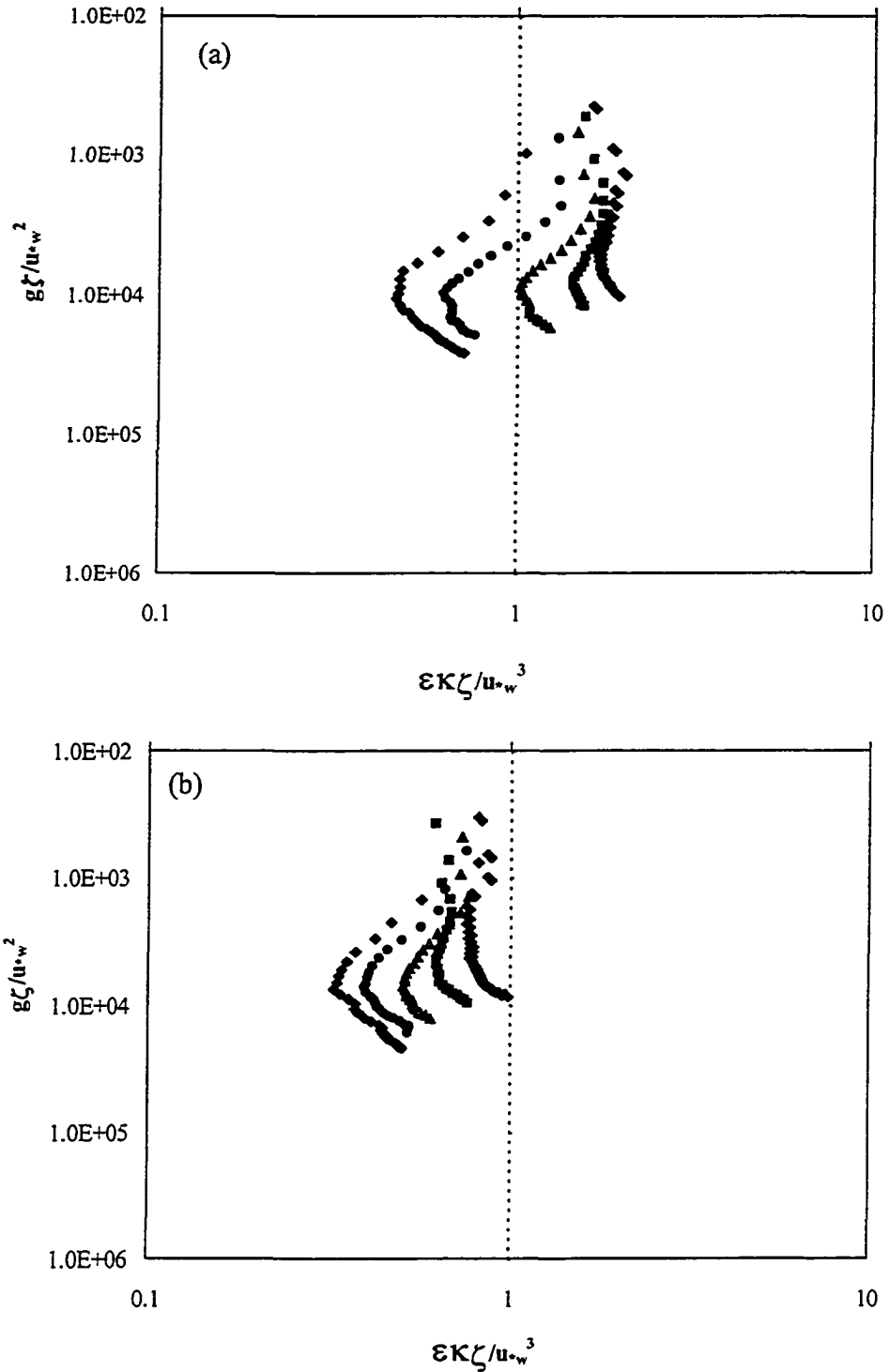


FIGURE 3.8: Plot of the dimensionless rate of energy dissipation, versus the dimensionless depth using wall layer scaling. (a) Clean water surface, (b) Surfactant-influenced water surface. \blacklozenge , = $3.8 \text{ m}\cdot\text{s}^{-1}$; \bullet , = $4.9 \text{ m}\cdot\text{s}^{-1}$; \blacktriangle , = $6.2 \text{ m}\cdot\text{s}^{-1}$; \blacksquare , = $8.0 \text{ m}\cdot\text{s}^{-1}$; \blacktriangledown , = $9.6 \text{ m}\cdot\text{s}^{-1}$.

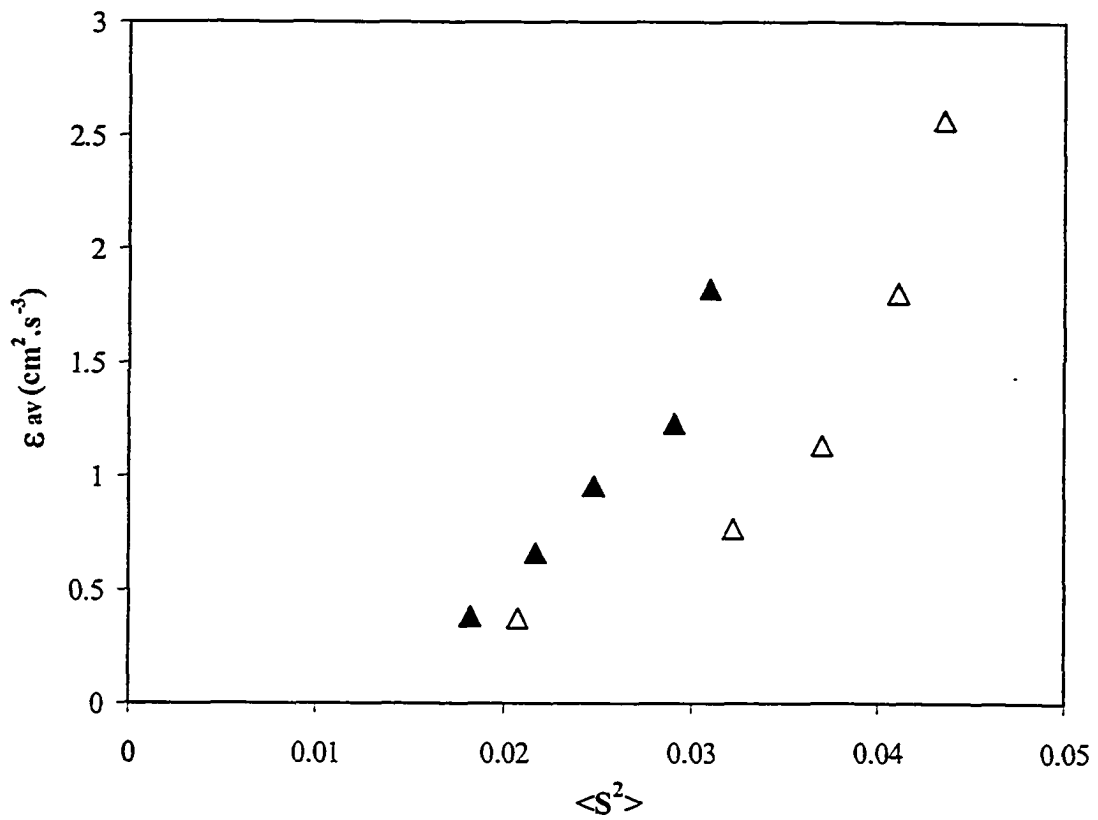


FIGURE 3.9: Plot of the mean square wave slope, $\langle S^2 \rangle$, versus the rate of energy dissipation, ϵ_{av} , averaged over top 2-cm layer. Values are averaged over 10 minutes of data. Δ , = Clean water surface; \blacktriangle , = surfactant-influenced water surface.

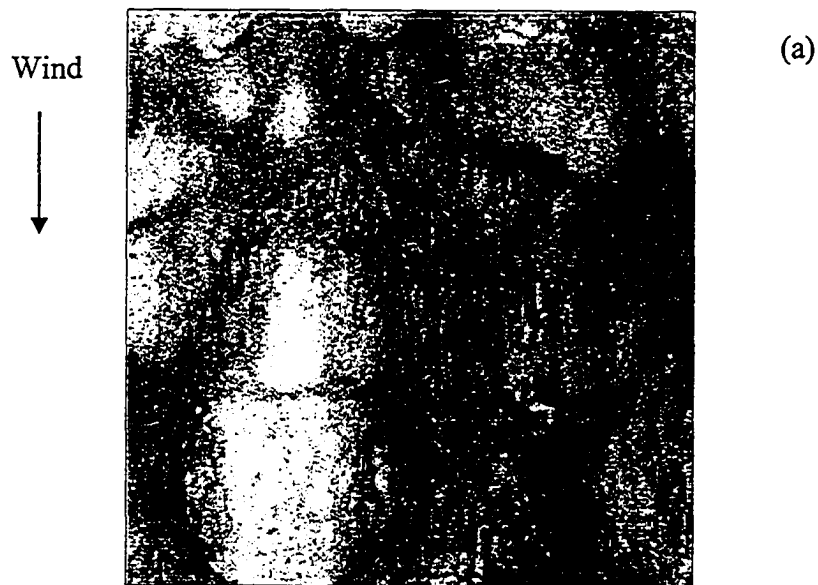
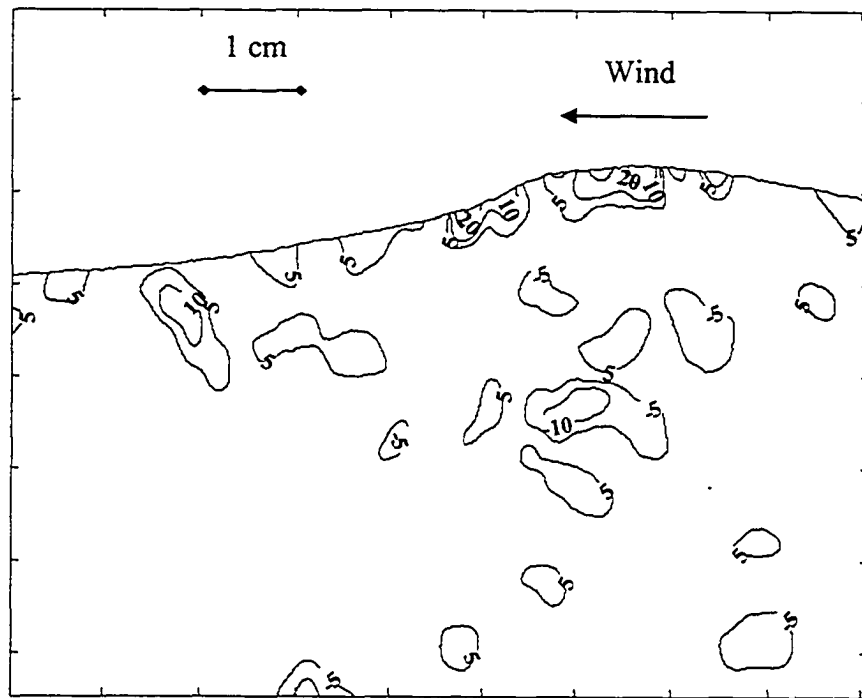
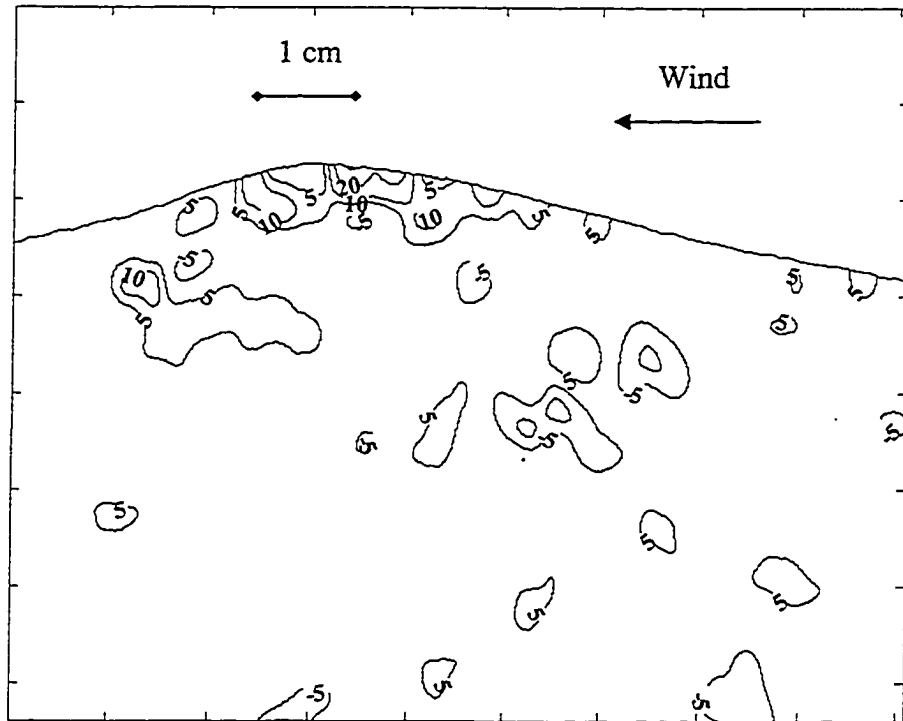


FIGURE 3.10: (a-c) A sequence of paired plots of an instantaneous vorticity field (top) and IR image (bottom) showing a non-breaking wave at a wind speed of $9.6 \text{ m}\cdot\text{s}^{-1}$. The sample rate for both the IR images and the DPIV fields was 15 Hz. The dimensions of the IR image are $64.3 \text{ cm} \times 64.3 \text{ cm}$. The location of the DPIV field of view is marked with a vertical black line in the IR images.



(b)

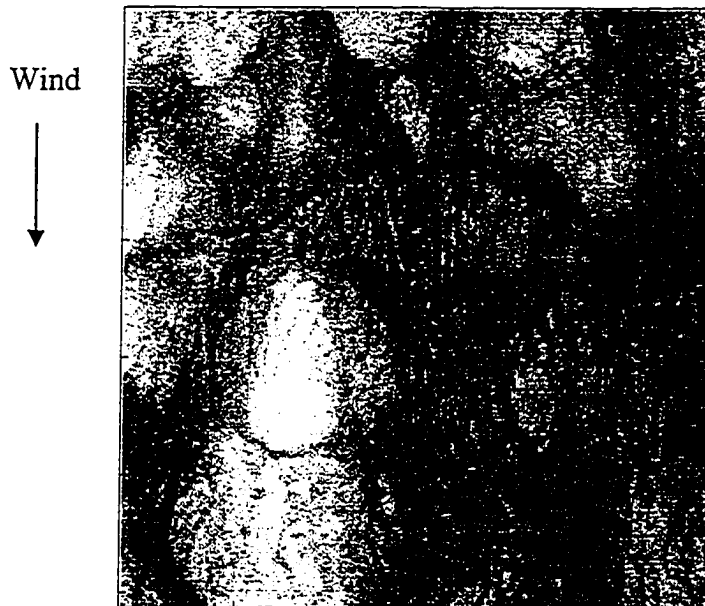


FIGURE 3.10: (Continued)

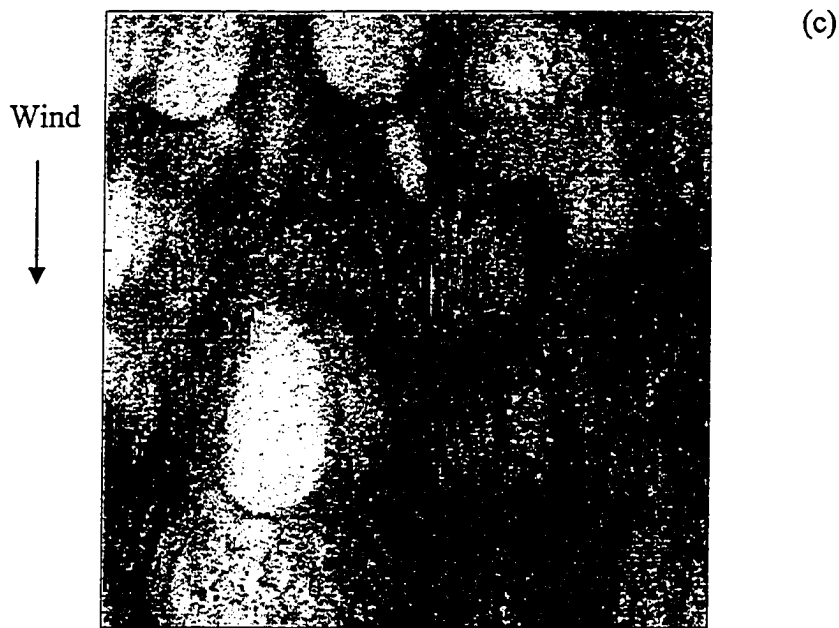
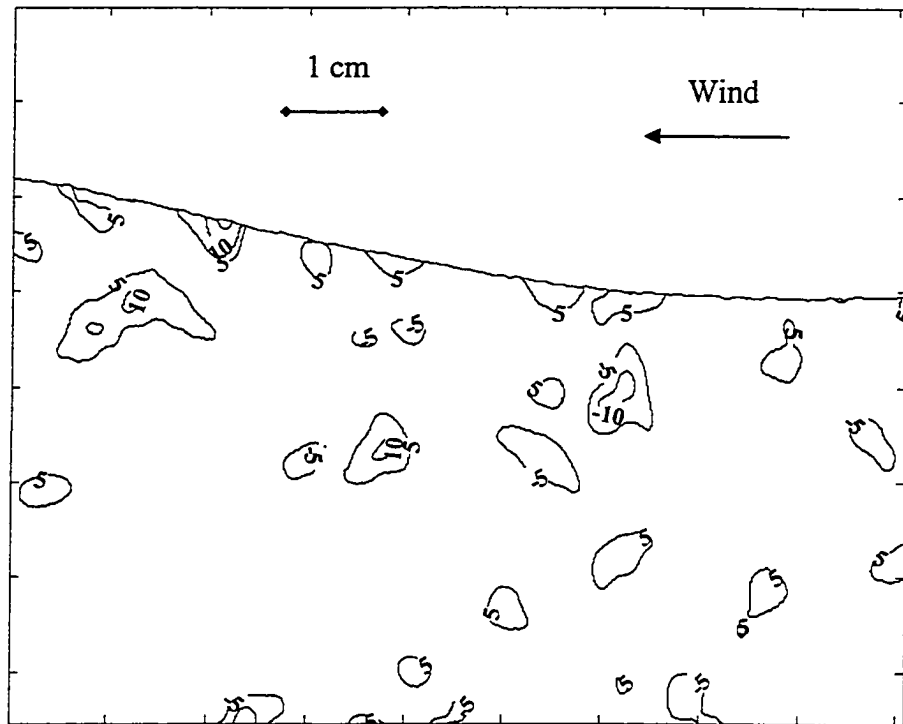


FIGURE 3.10: (Continued)

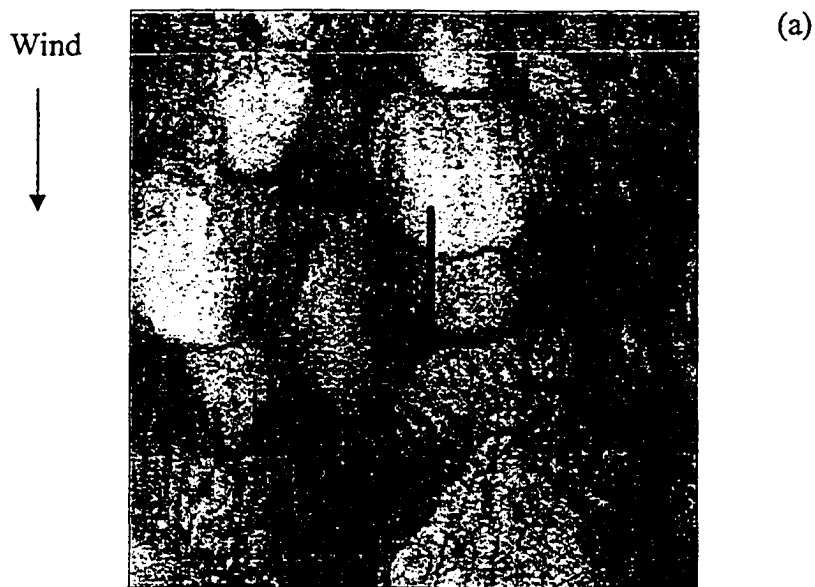
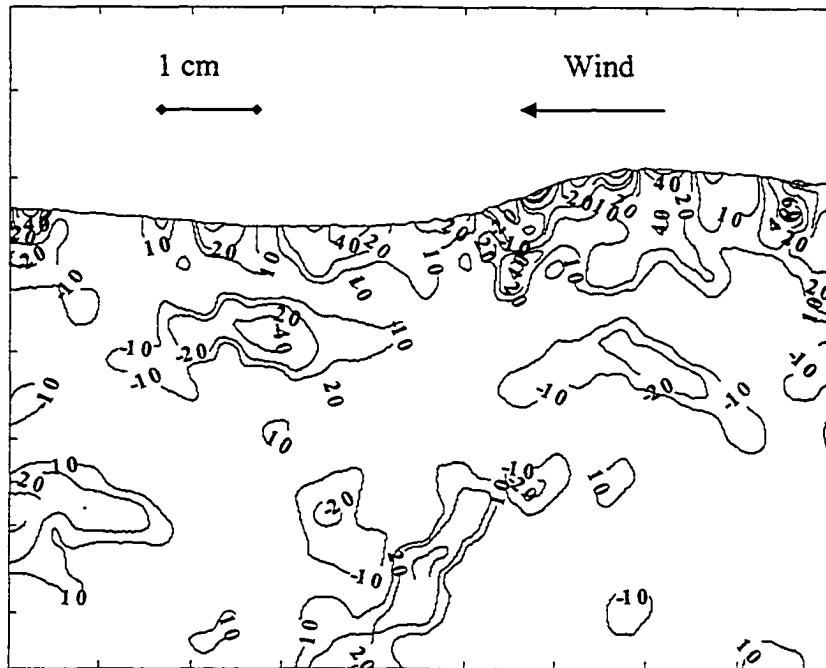
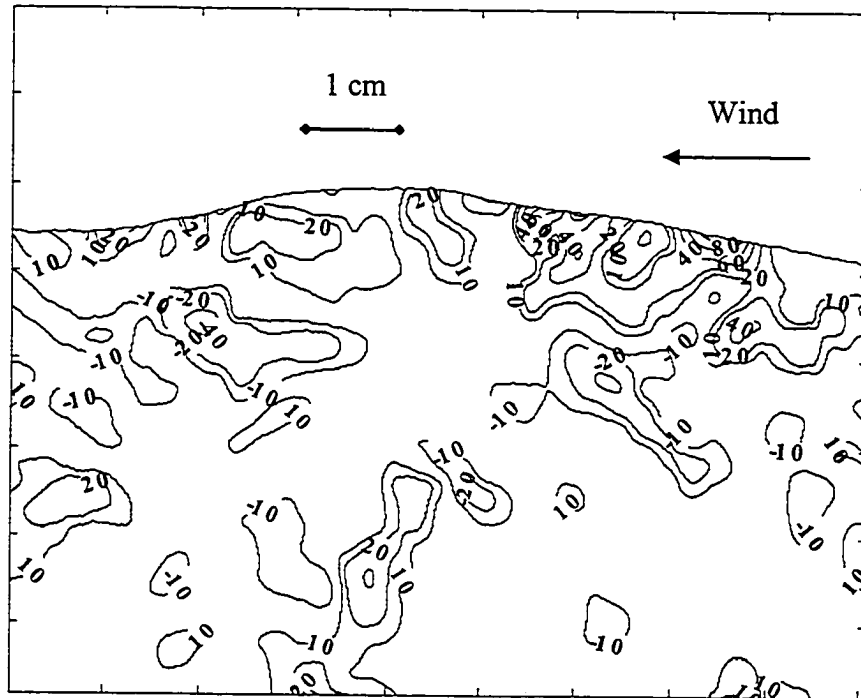


FIGURE 3.11: (a-c) A sequence of paired plots of an instantaneous vorticity field (top) and IR image (bottom) showing a microscale-breaking wave at a wind speed of $9.6 \text{ m}\cdot\text{s}^{-1}$. The sample rate for both the IR images and the DPIV fields was 15 Hz. The dimensions of the IR image are $64.3 \text{ cm} \times 64.3 \text{ cm}$. The location of the DPIV field of view is marked with a vertical black line in the IR images.



(b)

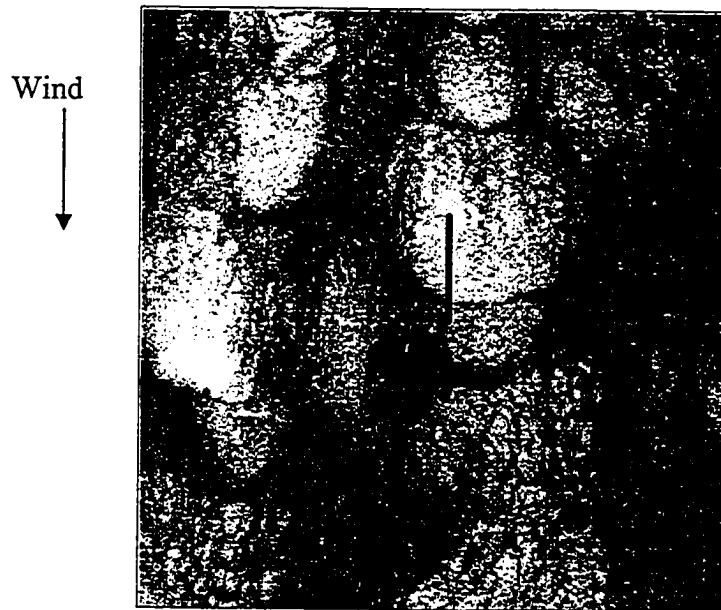
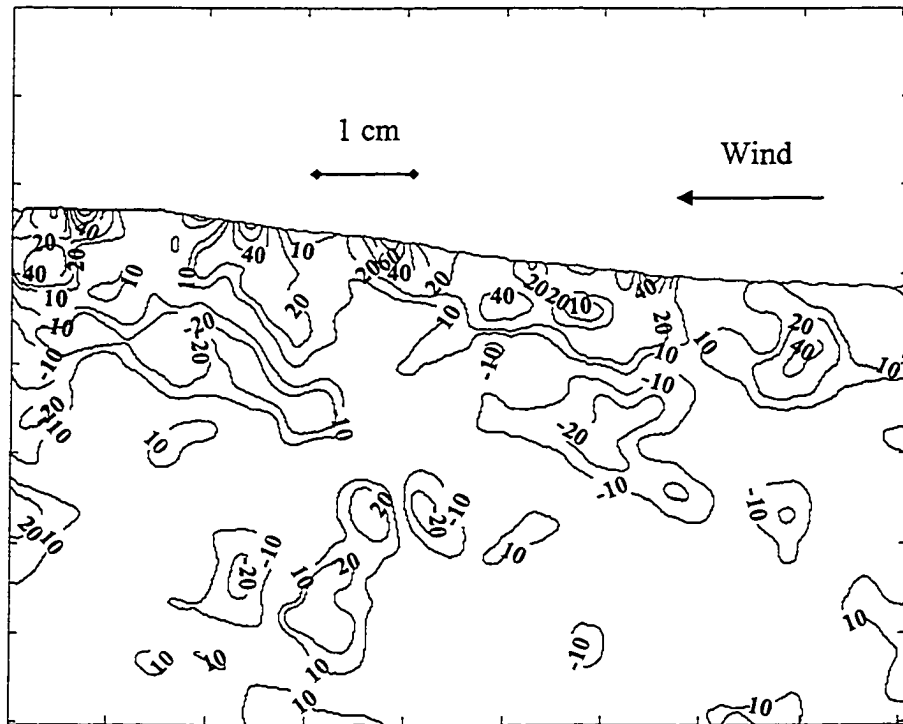


FIGURE 3.11: (Continued)



(c)

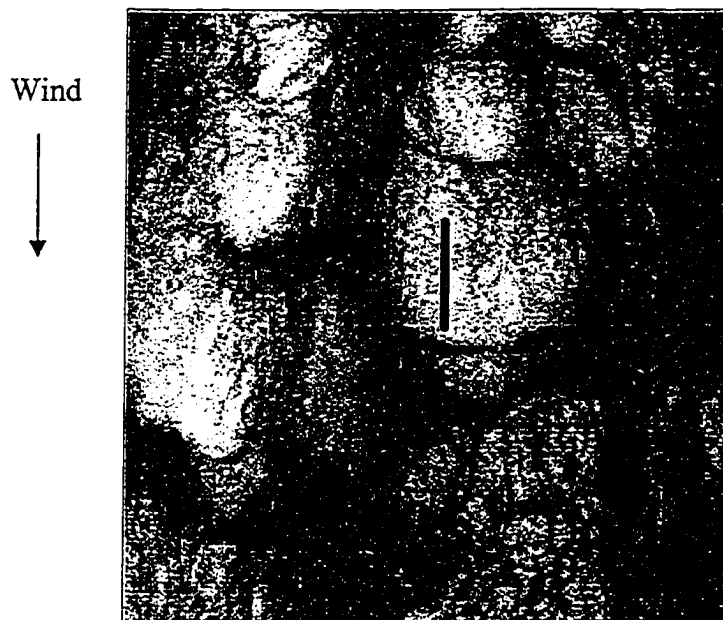


FIGURE 3.11: (Continued)

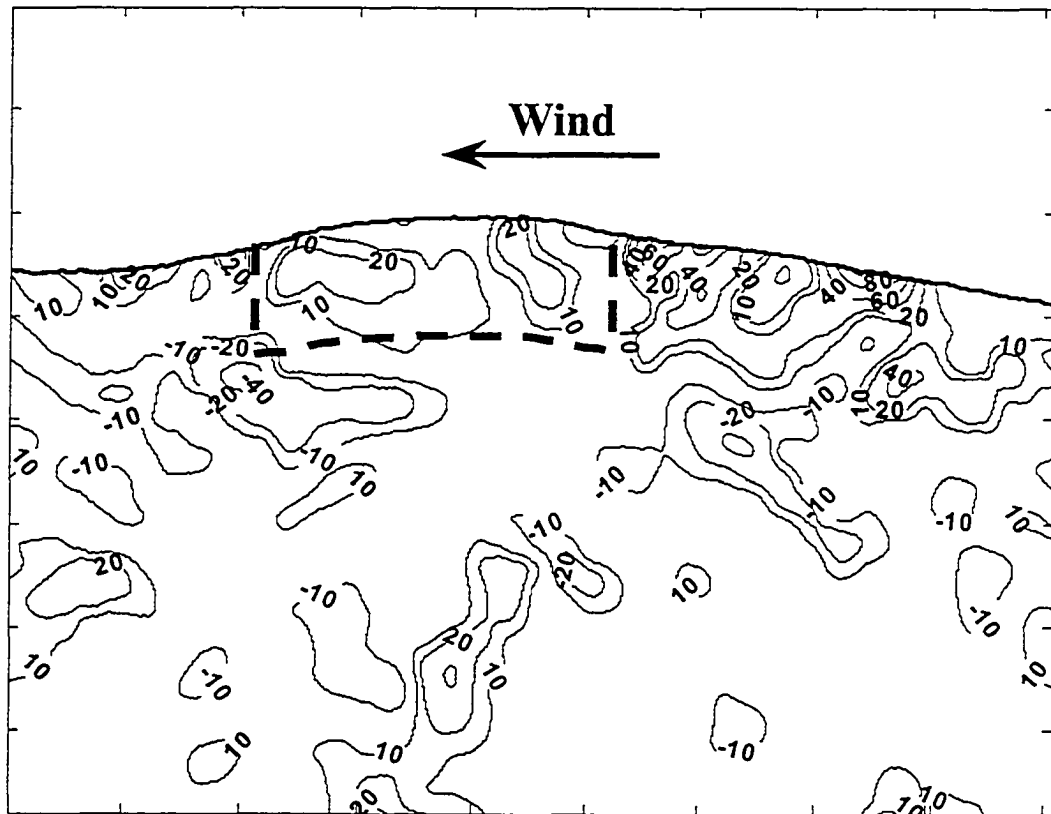


FIGURE 3.12: Plot showing the instantaneous vorticity field beneath a wave crest at wind speed of $9.6 \text{ m}\cdot\text{s}^{-1}$. The region of interest (ROI) is marked with dashed-lines. Positive vorticity ($\text{rad}\cdot\text{s}^{-1}$) contours correspond to counter clockwise vorticity and negative contours correspond to clockwise vorticity.

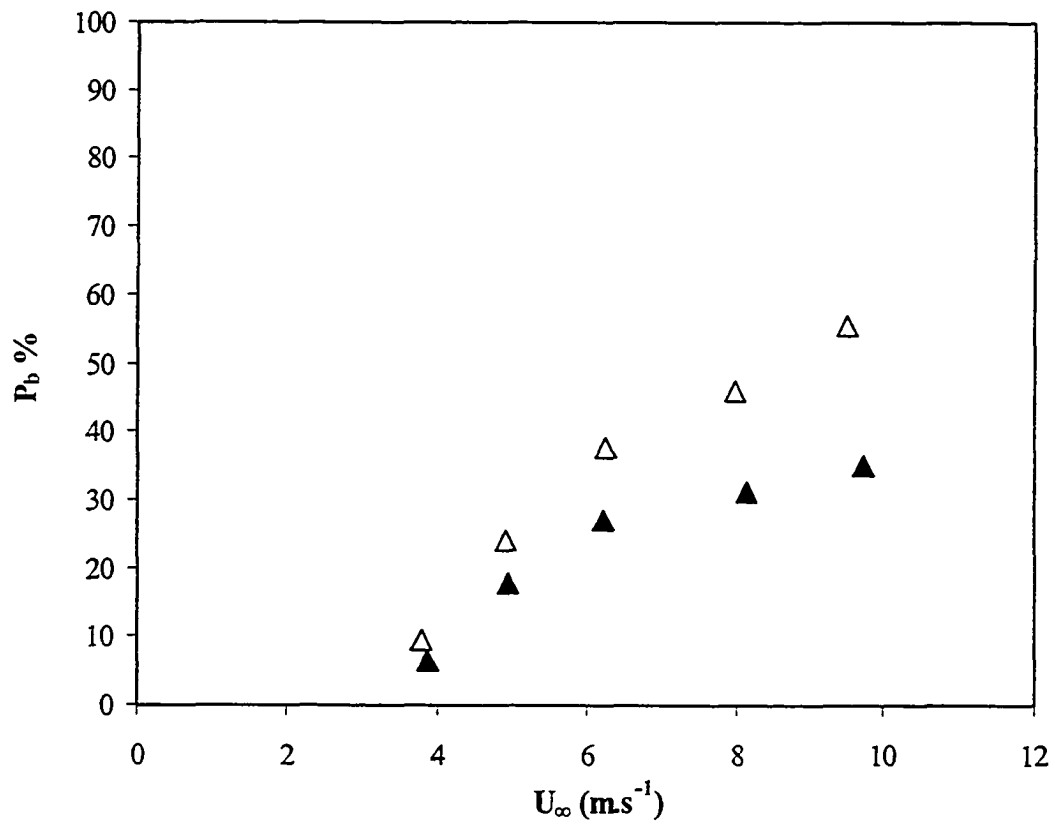


FIGURE 3.13: The percentage of microscale breaking waves P_b versus wind speed. Δ , = Clean water surface; \blacktriangle , = surfactant-influenced water surface.

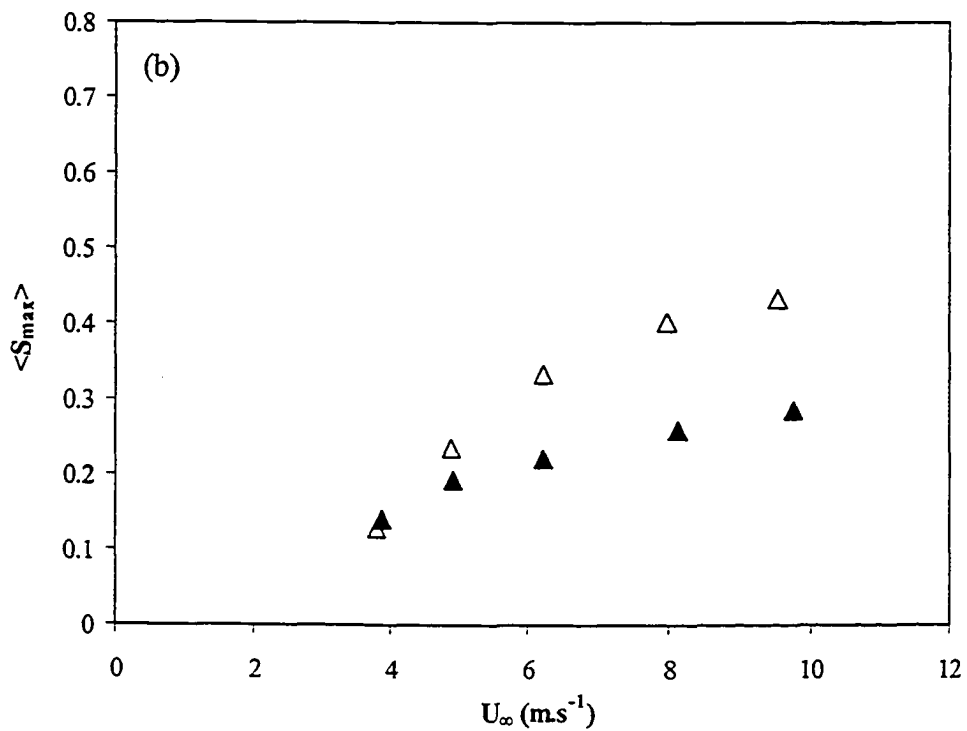
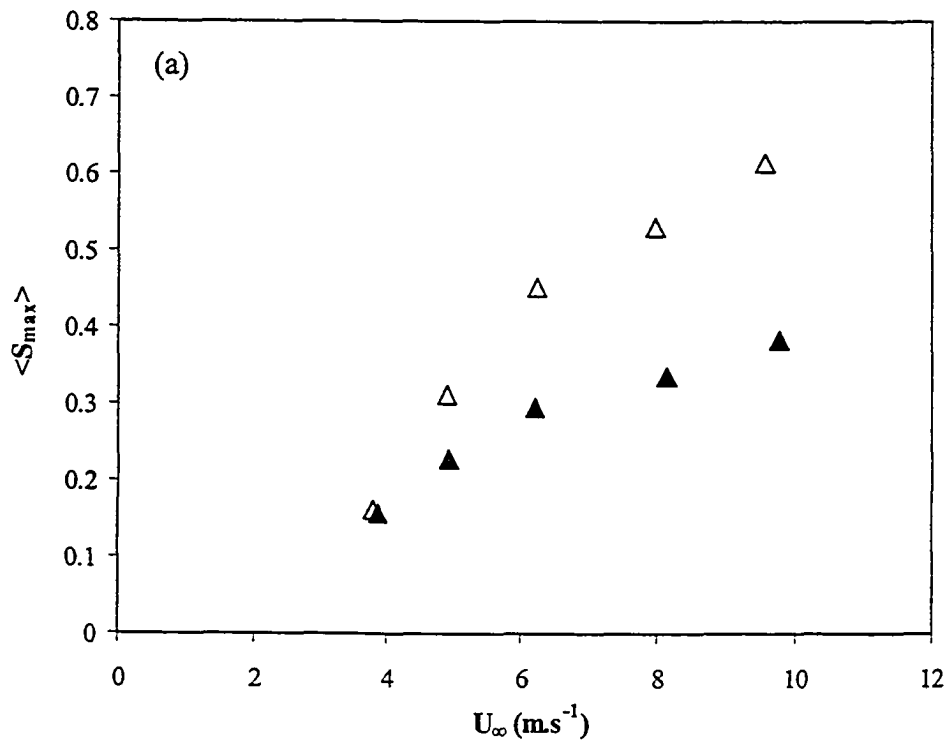


FIGURE 3.14: Plot of the maximum wave slope (S_{max}) on the downwind face of the wave versus wind speed. Δ , = Clean water surface; \blacktriangle , = surfactant-influenced water surface. (a) Microscale breaking waves. (b) Non-breaking waves

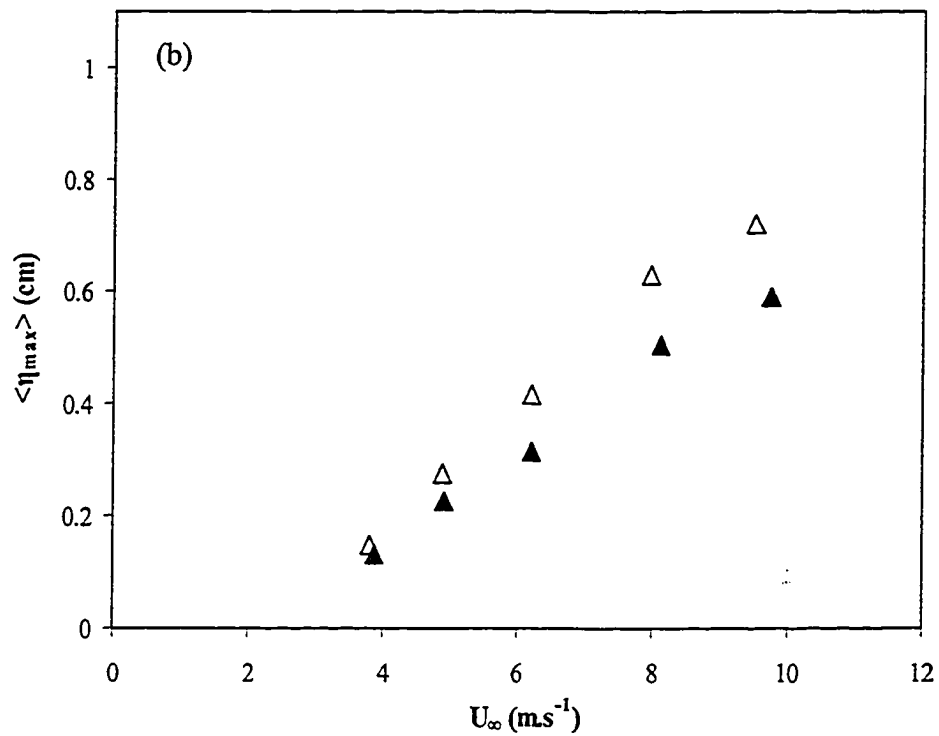
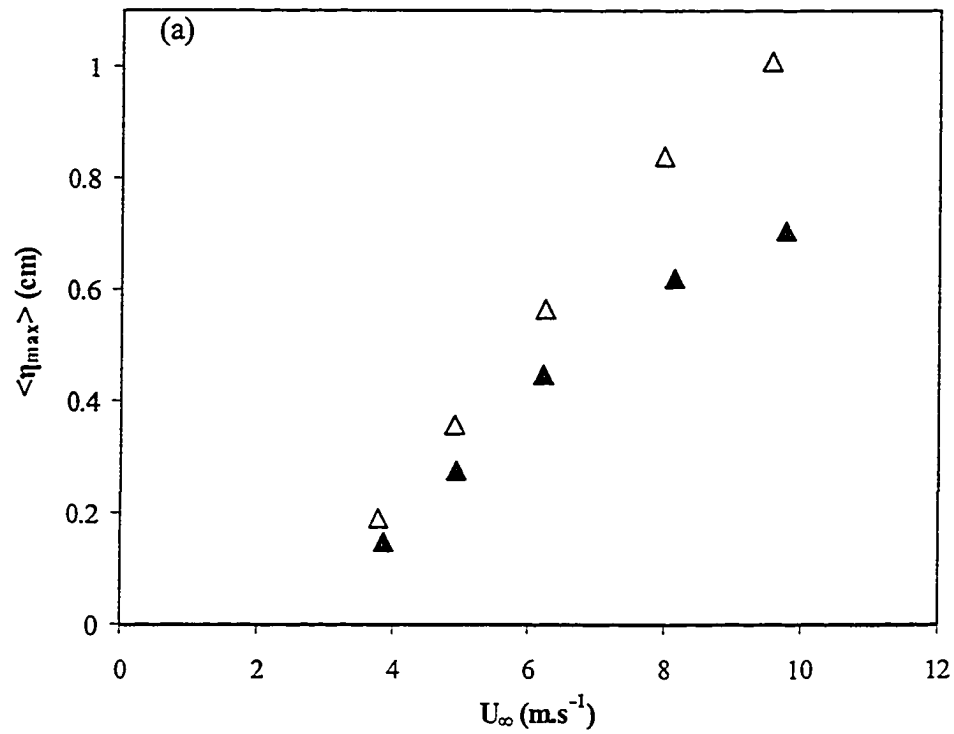


FIGURE 3.15: Plot of the maximum wave amplitude (η_{max}) versus wind speed. Δ , = Clean water surface; \blacktriangle , = surfactant-influenced water surface. (a) Microscale breaking waves. (b) Non-breaking waves.

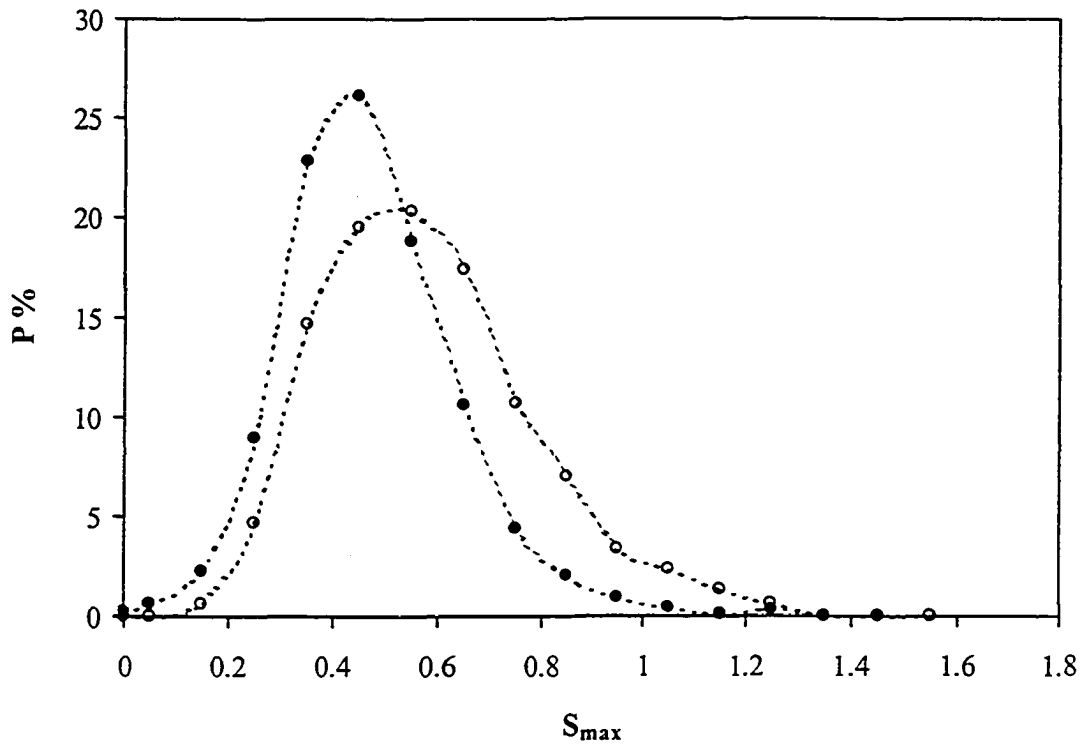


FIGURE 3.16: PDF's of the maximum wave slope (S_{max}) on the downwind face of the waves at a wind speed of 9.6 m.s^{-1} for a clean water surface. ○, = microscale breaking waves; ●, = non-breaking waves.

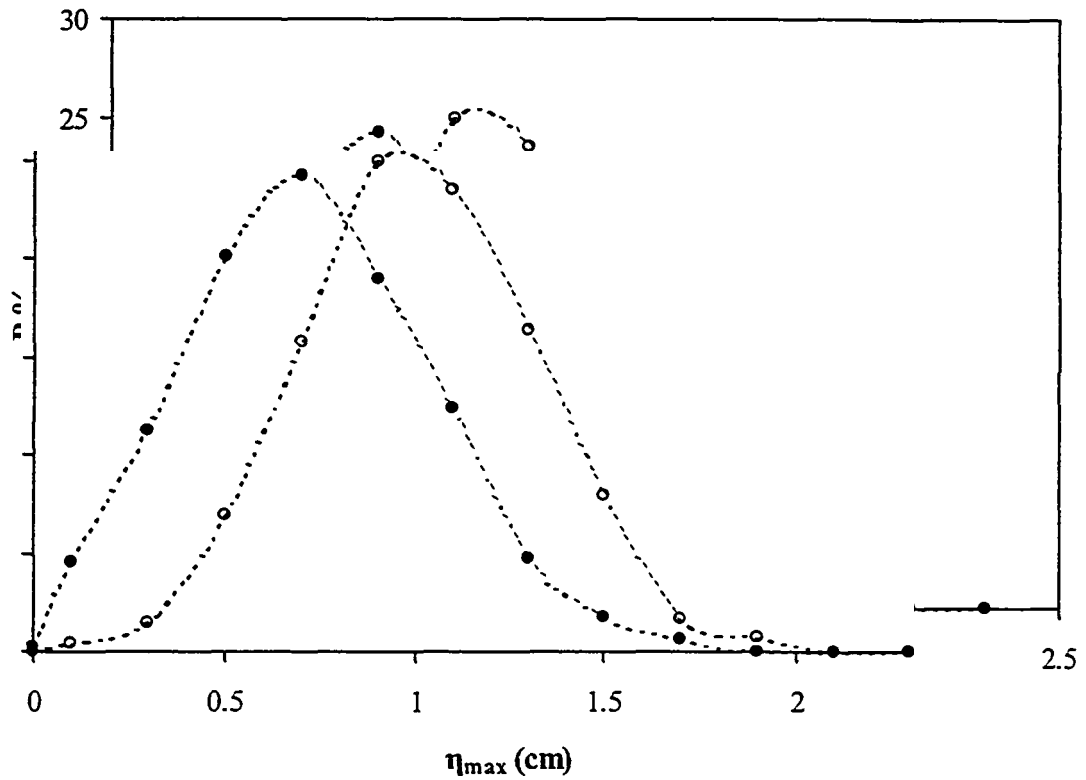


FIGURE 3.17: PDF's of the maximum wave amplitude (η_{max}) at a wind speed of 9.6 m.s^{-1} for a clean water surface. ○, = microscale breaking waves; ●, = non-breaking waves.

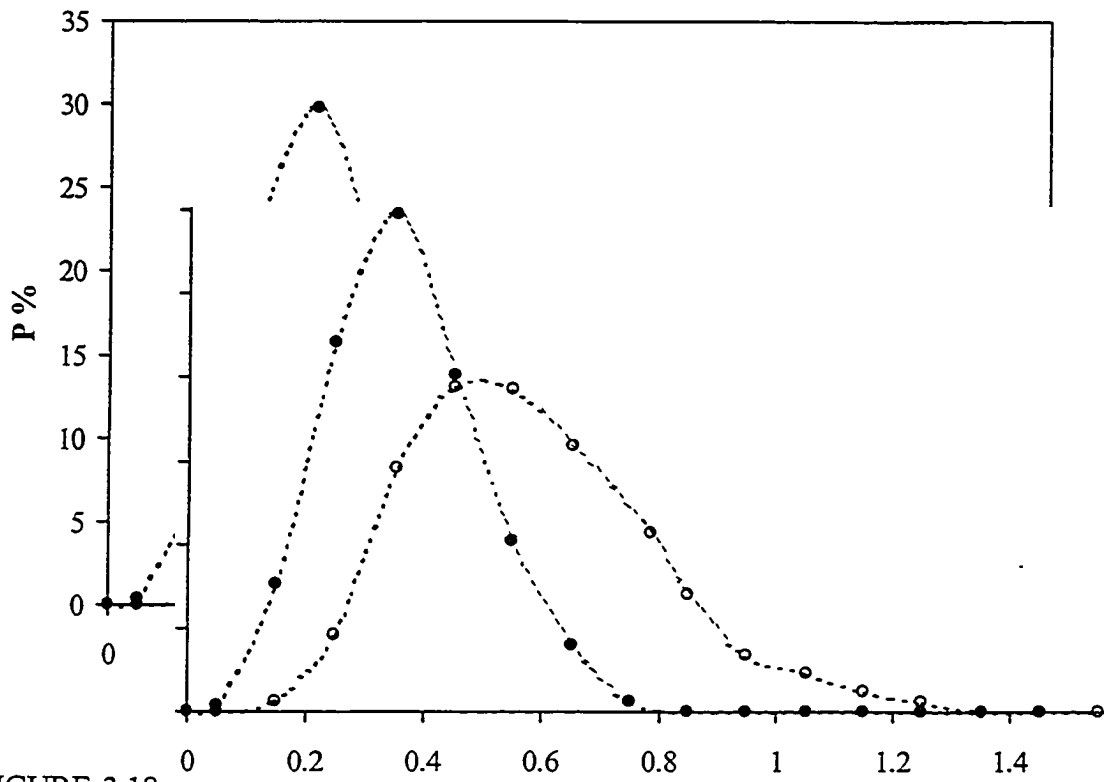


FIGURE 3.18:

the waves at a wind speed of $9.6 \text{ m}\cdot\text{s}^{-1}$ for microscale breaking waves. ○, = Clean water surface; ●, = surfactant-influenced water surface.

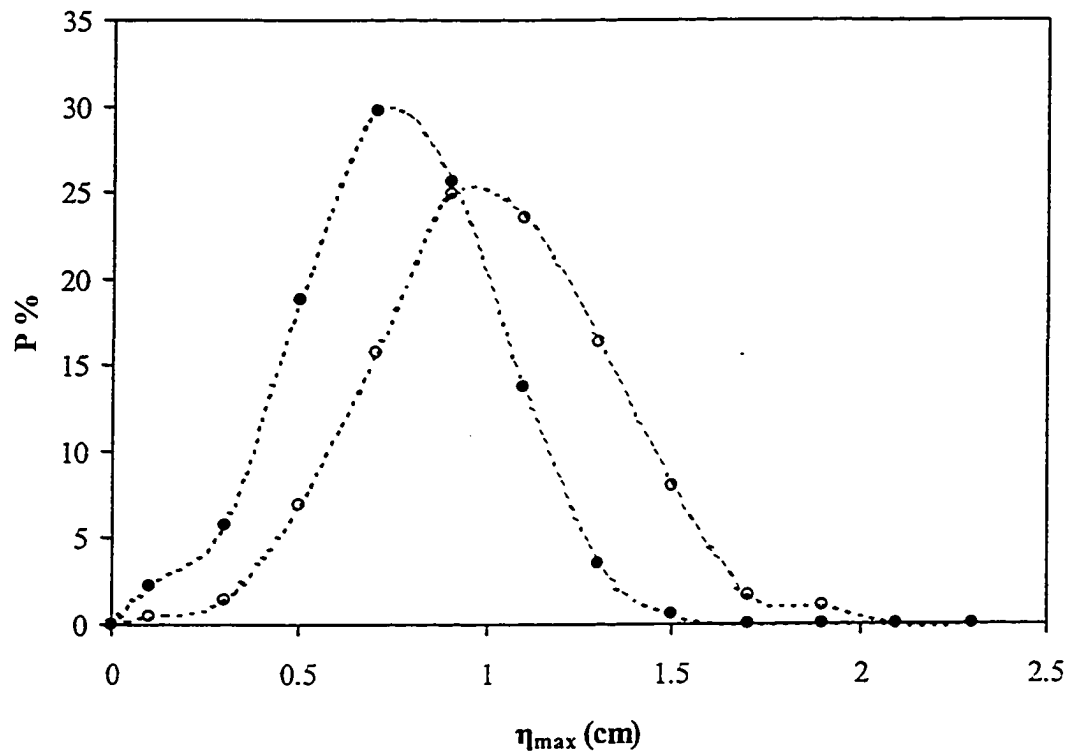


FIGURE 3.19: PDF's of the maximum wave amplitude (η_{max}) at a wind speed of $9.6 \text{ m}\cdot\text{s}^{-1}$ for microscale breaking waves. \circ , = Clean water surface; \bullet , = surfactant-influenced water surface.

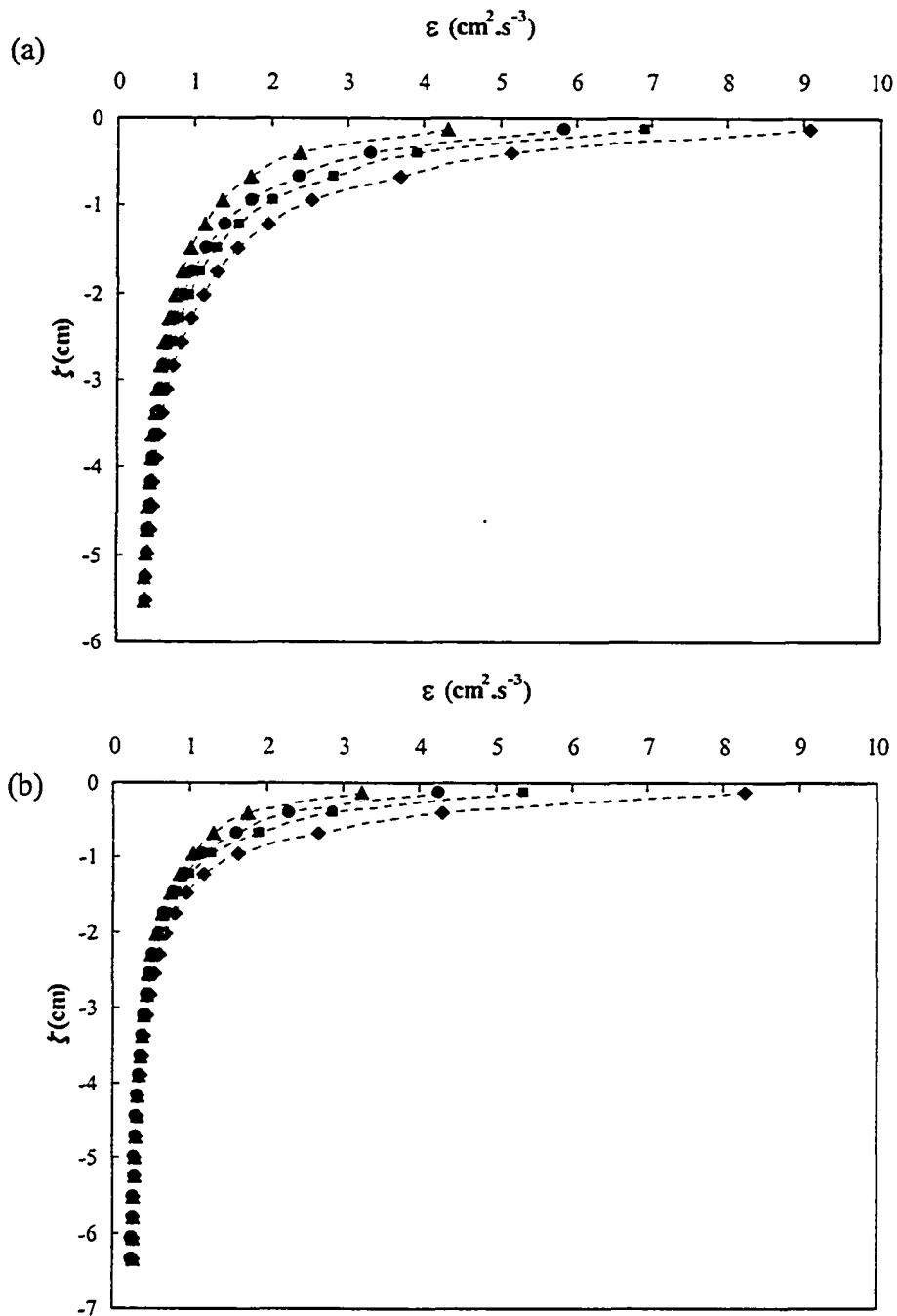


FIGURE 3.20: Vertical profiles of the rate of energy dissipation ε , versus ζ , the vertical coordinate in the wave following system at a wind speed of $9.6 \text{ m} \cdot \text{s}^{-1}$. Values are averaged over 10 minutes of data, \blacktriangle , = ε under non-breaking waves; \blacklozenge , = ε under microscale breaking waves; \blacksquare , = ε average for entire flow field (as in Figure 3.5); \bullet , = ε average for the background flow field (excluding breaking and non breaking waves). (a) Clean water surface. (b) Surfactant-influenced water surface.

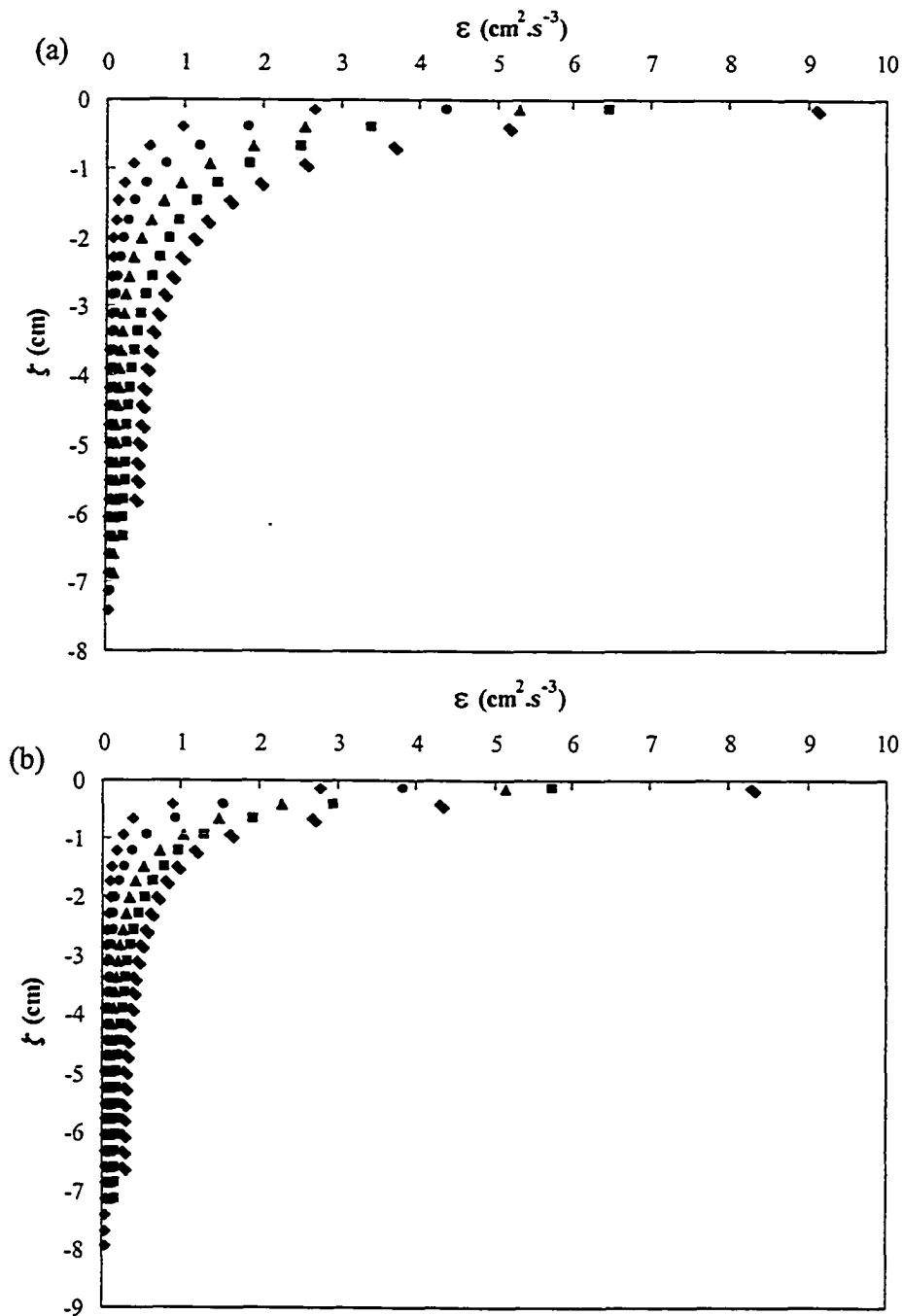


FIGURE 3.21: Vertical profiles of the rate of energy dissipation ε beneath microscale-breaking waves versus ζ , the vertical coordinate in the wave following system. Values are averaged over 10 minutes of data. (a) Clean water surface, (b) Surfactant-influenced water surface. \blacklozenge , = $3.8 \text{ m}\cdot\text{s}^{-1}$; \bullet , = $4.9 \text{ m}\cdot\text{s}^{-1}$; \blacktriangle , = $6.2 \text{ m}\cdot\text{s}^{-1}$; \blacksquare , = $8.0 \text{ m}\cdot\text{s}^{-1}$; \blacktriangledown , = $9.6 \text{ m}\cdot\text{s}^{-1}$.

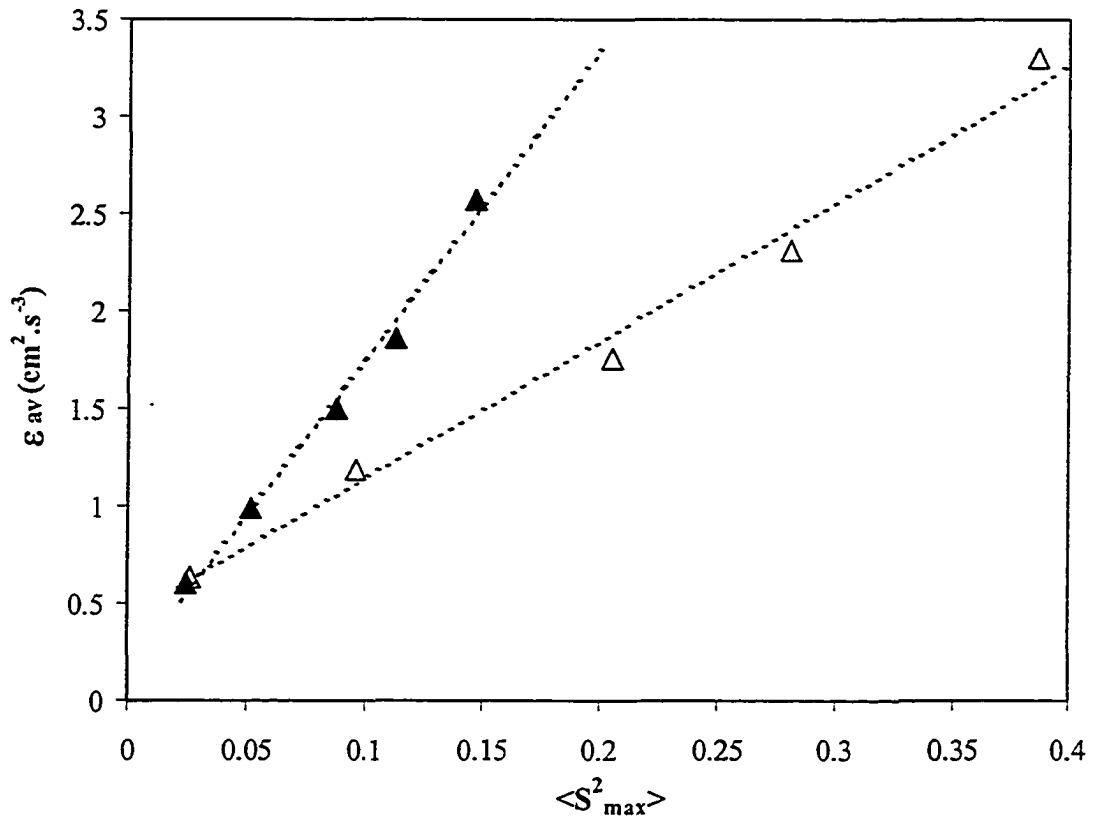


FIGURE 3.22: Plot of the mean square of the maximum wave slope on the downwind face of the waves, $\langle S^2_{max} \rangle$, versus the rate of energy dissipation, ϵ_{av} , averaged over top 2-cm layer. Both values are averaged over 10 minutes of data under microscale breaking waves only. Δ , = Clean water surface; \blacktriangle , = surfactant-influenced water surface.

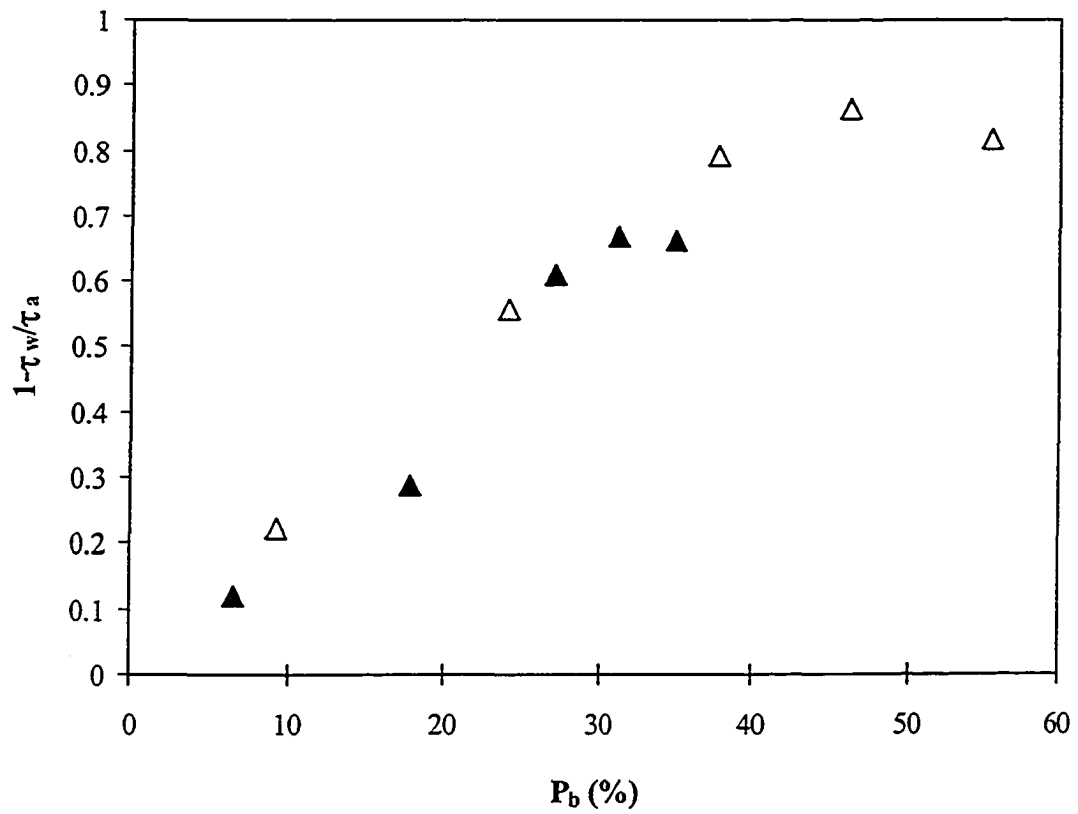


FIGURE 3.23: Plot of the fraction of the total momentum transferred to the wave field ($1 - \tau_w / \tau_a$) versus the percentage of microscale breaking waves P_b . Δ , = Clean water surface; \blacktriangle , = surfactant-influenced water surface.

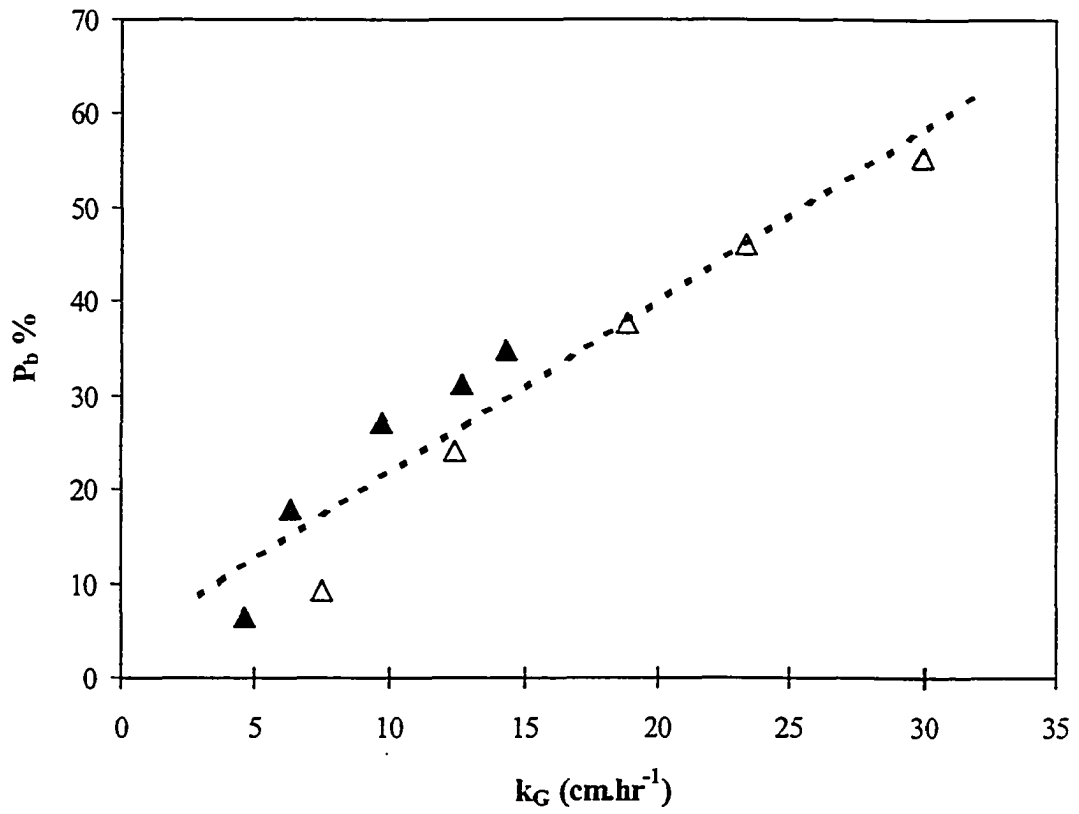


FIGURE 3.24: Plot of the bulk gas transfer velocity, k_G versus the percentage of microscale breaking waves P_b . Δ , = Clean water surface; \blacktriangle , = surfactant-influenced water surface. The dashed line represents a linear least squares regression for all the data points at both water surface conditions.

Chapter 4

Coherent Structures and Air-water Gas Transfer

4.1 Introduction

The detection of both the size and location of vortices is very important when studying the hydrodynamic characteristics of the aqueous boundary layer. The definition of a vortex has been widely discussed and a variety of mathematical and physical vortex definitions have been proposed (Pemberton et al 2002). One of the most specific definitions is that a vortex is the rotating motion of a considerably large mass of material particles around a general center (Lugt 1983). Coherent structures identified in terms of vorticity as a connected bulky turbulent fluid mass with instantaneous phase correlated vorticity over its spatial extent (Hussain 1986). Coherent structures are usually associated with regions of concentrated vorticity and sometimes they are defined as organized vortical structures (Camussi 2002). One of the most challenging features in the study of turbulent boundary layers, turbulent shear flows and turbulent mixing is the analysis and characteristics of coherent structures. They contribute to mass, momentum and heat transfer and to advection and mixing phenomena, hence they play an important role in many aspects of practical life.

A large body of literature has been devoted to the advancement of suitable methodologies to identify coherent structures and to detect their characteristics (Bonnet et al. 1998). Coherent structures are generally embedded in a random flow field and their detection will be based on when and where they are present. Separating coherent structures from the background turbulence is an important and challenging task. Several

detection methods are available but they are dependant on the exact definition used in each method to detect these structures. Also, they are dependent on the desired information, which is a fraction of the available experimental and numerical capabilities. Camussi (2002) explained four methodologies used to extract coherent structures from DPIV data: Galileian or Reynolds decomposition; direct analysis of the vorticity vector field; analysis of the velocity gradient tensor evaluated locally; and large eddy filtering simulation. In addition, he proposed and validated a wavelet-based technique. Bonnet *et al.* (1998) evaluated different coherent structure detection techniques and found that there was a qualitative and quantitative consistency between these techniques.

For wind-driven waves, fluxes of gas, heat, and momentum through the air-sea interface are mainly governed by the structure of the flow in the turbulent boundary layers above and below the interface. A number of wind wave laboratory studies have reported the existence of organized structures or bursts above and below the interface. In their experiment investigating the turbulent boundary layer over wind waves, Kawamura and Toba (1988) observed a high shear layer due to airflow separation. Furthermore, they observed the creation of organized motions on the windward face of the wave where the airflow reattaches. Banner and Melville (1976) observed airflow separation near the forward face of the wave during wave breaking only. They explained that the incidence of airflow separation involves a stagnation point on the interface and that this corresponds to the beginning of wave breaking.

Komori *et al.* (1993) used a hot-wire anemometer to measure flow velocities in the air above wind waves and a laser Doppler velocimetry (LDV) to measure flow velocities in the water below the wind waves. They observed waterside eddies created at

the same place where an organized airside motion was created on the windward face of the wave. They suggested that strong shear generated by the organized airside motions induced these eddies in the water.

Gas transfer across the air-water interface directly influences many processes in the natural environment and as a result it is of a great importance (Liss 1973). At the interface there are boundary layers in the air and water that may be considered as four layers positioned in series. The uppermost layer is the turbulent air, the second layer is the airside concentration boundary layer that is of the order of 1 mm, the third layer is the waterside concentration boundary layer which is also of the order of 1 mm and the lowest layer is the well mixed bulk water flow beneath the interface (Schwarzenbach *et al.* 1993). Gas transfer across the air-water interface occurs through molecular diffusion. Specifically, the turbulent eddies on both sides of the interface transmit parcels of fluid containing gases to their corresponding boundary layers where the actual transfer of gas takes place.

Gas flux F is expressed as the product of a gas transfer velocity, k_G , and the air-water concentration difference across the concentration boundary layers,

$$F = k_G \Delta c. \quad [4.1]$$

The gas transfer velocity characterizes the resistance to gas exchange across the air-water interface and the air-water concentration difference is the driving potential (Schwarzenbach *et al.* 1993). Accordingly, the air and water concentration boundary layers control the gas transfer across the air-water interface. Csanady (1990) stated that the thickness of these boundary layers is directly related to the properties of the near-surface turbulence and molecular diffusivity. Consequently, decreasing the thickness of

either of these boundary layers through any process (e.g. temporal variations, presence of surface-active materials, changes in surface boundary conditions, etc.) will change the air-water gas transfer rate. Chu and Jirka (1995) concluded that the fluxes of important environmental gases like oxygen and carbon dioxide are controlled by the near-surface turbulence generated in the water by turbulent shear and the molecular diffusivity of these gases. All scales of wave breaking generate near-surface turbulence and this turbulence has been proposed as an important mechanism that controls the air-water gas transfer rate (Jessup *et al.* 1997).

Surface renewal has been proposed as an explanation for the turbulent motions that govern air-water gas transfer in the waterside (Higbie 1935; Asher and Pankow 1991; Komori *et al.* 1993). Turbulent eddies near the interface continuously renew the water surface by bringing water parcels from deeper in the water column to the surface and in this manner the surface renewal takes place. The surface renewal model is the most physically realistic model for predicting air-water gas transfer velocities (Zappa *et al.* 2001). Using the surface renewal model, the gas transfer velocity k_G , is given by

$$k_G = C_l \sqrt{\frac{D}{\tau}} \quad [4.2]$$

where, D is the molecular diffusivity of the gas in the liquid and τ is the characteristic timescale of the surface renewal or the mean lifetime of a water parcel at the surface and C_l is a constant. Recently, the turbulent characteristics of the flow have been used to estimate the characteristic timescale τ of surface renewal. For example, Fortescue and Pearson (1967) used the integral turbulent length scale and the root mean square turbulent velocities to estimate τ . Lamont and Scott (1970) assumed that τ was equal to the

Kolmogorov time scale and Komori *et al.* (1993) used the occurrence frequency of eddies to calculate τ .

Komori *et al.* (1993) carried out an experiment in a wind-wave tank and measured the bulk air-water gas transfer velocity directly. They also estimated the gas transfer velocity using the surface renewal model. They found that the air-water gas transfer velocity was correlated with the frequency of appearance of surface renewal eddies. The gas transfer velocities obtained from their direct measurements were smaller than the values predicted using the surface renewal model by approximately a factor of three. Nonetheless, they concluded that the surface renewal model could be used to estimate the gas transfer velocity through the air-water interface. Similarly, Lamont and Scott (1970) found that gas transfer velocities values obtained from direct gas flux measurements were 2.5 times smaller than those predicted using the surface renewal model.

In a wind wave tank, Zappa *et al.* (2004) estimated the local transfer velocities inside and outside the wakes produced by microscale-breaking waves. They reported that the transfer velocity was enhanced by an average factor of 3.5 inside the wakes and that this enhancement was due to the near-surface turbulence and vortices produced by microscale-breaking waves. Siddiqui *et al.* (2004) investigated the near-surface flow beneath microscale-breaking waves in a wind wave tank experiment. They suggested that the near-surface flow could be categorized into two areas with different characteristics; energetic areas that are occupied by coherent structures and quiescent areas that are void of coherent structures. They used the surface renewal model to estimate the gas transfer velocity in these two areas and predicted that the gas transfer velocity in the energetic regions was 2.8 times larger than in the quiescent regions.

Additionally, they reported that 60% of the total air-water gas flux occurred through the energetic regions and that the rate of turbulent kinetic energy dissipation was approximately 2.5 times higher in the energetic regions compared to the quiescent regions. Moreover, they concluded that the bulk of the surface renewal was caused by microscale-breaking waves.

In this chapter, the effect of the presence of a surfactant on the characteristics of coherent structures generated beneath the air-water interface is discussed. In addition, using the characteristics of coherent structures, the gas transfer velocity is predicted using the surface renewal model for both water surface conditions.

4.2 Near-Surface Vorticity

It has been shown in chapter 3 that microscale-breaking waves generate strong vortices behind their leading edge and that no strong vortices are generated beneath non-breaking waves. Figure 4.1 shows a series of vorticity plots, with a time separation between each of them of 1/15 sec, that illustrate the creation and progression of the coherent structures generated beneath the crest of a microscale-breaking wave, at a wind speed of $9.6 \text{ m}\cdot\text{s}^{-1}$. In figure 4.1(a), a number of vortices and coherent structures that were generated by a previous breaker are visible. A vortex (labeled A) located at the front of the leading edge of an incoming microscale-breaking wave has just entered the field of view. The leading edge of the microscale-breaking wave has crossed approximately 1/3 of the DPIV field of view in Figure 4.1(b). It can be seen that there is a group of strong vortices behind the leading edge of the breaker. Vortex A is still located at the leading edge and an additional two vortices labeled B and C are also

appeared in Figure 4.1(b). In Figure 4.1(c) the breaker's leading edge has crossed approximately three quarters of the DPIV field of view. A number of strong vortices including the ones labeled A, B and C are visible in Figure 4.1(c) and another vortex labeled D can be seen on the windward face. In Figure 4.1(d), the forward face of this wave has traveled downwind of the field of view and the entire windward face of the wave is within the field of view. In this figure, more vortices are visible along the windward face of the wave. The vortices labeled A and B have been advected out of the field of view by the current in the aqueous boundary layer. However, the vortices labeled C and D are still visible in Figure 4.1 (d). The movement and evolution of vortices shown in Figure 4.1 is due to the combined effect of the current in the aqueous boundary layer and the wave orbital motion. It is noteworthy that these near-surface strong vortices were created immediately behind the leading edge of the breaker and that they typically extended from the leading edge on the leeward face to the windward face of the wave.

4.3 Coherent Structures Identification Technique

Coherent structures first must be identified using an objective criterion before their role in controlling air-water heat and gas transfer rates can be investigated. In this study, a scheme similar to the one developed by Siddiqui *et al.* (2004) that uses a vorticity threshold was used to identify coherent structures. Hussain and Hayakawa (1987) proposed that coherent structures should be identified by applying a vorticity threshold to a smoothed vorticity field and that the local maximum mean shear S_M is the logical choice for specifying the vorticity threshold value. The maximum mean shear, S_M is identified as the maximum time-averaged mean velocity gradient $\overline{(\partial u / \partial z)}_{max}$. They

concluded that the threshold level ω_T should be in the range of $2S_M$ to $3S_M$. The maximum local value of S_M in this study was found to be 1.6 s^{-1} at the lowest wind speed ($3.8 \text{ m}\cdot\text{s}^{-1}$) and 2.4 s^{-1} at the highest wind speed ($9.6 \text{ m}\cdot\text{s}^{-1}$). The characteristics of the detected coherent structures were compared using three different values of ω_T , to determine the sensitivity of the detection scheme to the value of the threshold. The three different values of ω_T , were 3.2 , 4.8 and 6.4 s^{-1} and these correspond to $2S_M$, $3S_M$ and $4S_M$ at the lowest wind speed. It was found that, as ω_T was increased by 1.6 s^{-1} (one times S_M), the vorticity of the detected coherent structures increased on average by approximately 19%, the average size of the detected coherent structures decreased on average by approximately 10% and the number of the detected coherent structures decreased on average by approximately 30%. This analysis demonstrated that the size and vorticity of the coherent structures were relatively insensitive to the threshold but that, the number of coherent structures is relatively sensitive to the threshold.

The vorticity threshold ω_T value was chosen to be 4.8 s^{-1} and it was kept constant for all wind speeds and both water surface conditions. This vorticity threshold ω_T value corresponds to $3S_M$ at the lowest wind speed and to $2S_M$ at the highest wind speed and, therefore, it falls within the range recommended by Hussain and Hayakawa (1987). This vorticity threshold was applied at all the grid points of the instantaneous vorticity fields computed from the instantaneous DPIV velocities. All adjacent grid points with vorticity values larger than the threshold, ω_T , were defined as being part of a coherent structure. The threshold value was applied to both positive and negative vorticity values so that both counter clockwise and clockwise vortices would be detected.

The mean and root-mean-square (RMS) of the absolute value of the vorticity were found to be 1.4 s^{-1} and 4.0 s^{-1} , for a clean water surface and 1.2 s^{-1} and 3.8 s^{-1} , for a surfactant-influenced water surface respectively, at the lowest wind speed of $3.8 \text{ m}\cdot\text{s}^{-1}$. The main objective here was to identify coherent structures or vortices that were considerably stronger than the background vorticity. The chosen vorticity threshold, ω_T , value of 4.8 s^{-1} guarantees that the identified structures have vorticity values larger than the background vorticity at the lowest wind speed.

The two dimensional instantaneous velocity and vorticity data obtained from the DPIV analysis were spaced 24 pixels (approximately 2.6 mm) in the horizontal and vertical directions. Figure 4.2 shows an example of coherent structures detected after applying the vorticity threshold scheme with this spatial resolution for an instantaneous vorticity field at a wind speed of $9.6 \text{ m}\cdot\text{s}^{-1}$. It is evident that the shapes of these coherent structures are quite angular and physically unrealistic with this spatial resolution. Siddiqui *et al.* (2004) found that interpolating the raw vorticity data onto a finer grid resulted in smoother and more physically realistic coherent structures. Furthermore, they found that, the basic shape, position and size of the structures were not changed significantly by the interpolation. Therefore, in order to smooth the edges of the detected coherent structures, the spatial resolution of the vorticity data was increased by interpolating the raw vorticity data.

To ensure that interpolating the vorticity data did not significantly alter the properties of the detected coherent structures, the following analysis was carried out. The spatial resolution of the vorticity data was increased by interpolating the vorticity data by factors of 2, 3, 4, 12 and 24, respectively using a bi-cubic interpolation scheme. It was

found that interpolating by factors of 2 and 3 did not smooth the coherent structure shapes adequately. But, interpolating by factors of 4, 12 and 24 produced relatively smooth coherent structure shapes and smooth PDF's of the coherent structure characteristics. There were no significant differences between the results obtained when interpolating by a factor of 4 and by factors of 12 and 24. Therefore, the vorticity data was interpolated by a factor of 4 and this increased the spatial resolution to 0.65 mm. After interpolating the vorticity data using the bi-cubic interpolation scheme, the vorticity threshold was then applied to these higher resolution vorticity fields. All grid points that had counterclockwise vorticity $\omega > \omega_T$ or clockwise vorticity $\omega < -\omega_T$ were identified as coherent structures.

Hussain and Hayakawa (1987) suggested that a threshold should be applied to the size of the detected structures. This is to ensure that one or two grid points with vorticity magnitudes exceeding the threshold do not get detected as coherent structures. Therefore, the detection algorithm rejected detected coherent structures that occupied less than four original grid points (i.e. minimum area 48 by 48 pixels² or 5.2 by 5.2 mm²). This ensures that all detected coherent structures have an equivalent diameter greater than 5.9 mm.

The sequence followed by the detection scheme was as follows: (i) the vorticity data was interpolated by a factor of 4; (ii) grid points that have vorticity value $|\omega| > \omega_T$ were identified, (iii) contiguous regions where $|\omega| > \omega_T$ that occupied less than four original grid points are discarded, and (iv) the remaining regions with $|\omega| > \omega_T$ are identified as coherent structures. After detecting the coherent structures, the maximum vorticity, area, perimeter, top width and the centroid coordinates of each coherent

structure were computed and stored. Figure 4.3(a) shows the contour lines of an instantaneous vorticity field beneath the crest of a microscale-breaking wave at a wind speed of $9.6 \text{ m}\cdot\text{s}^{-1}$. The coherent structures detected after applying the vorticity threshold scheme to the corresponding vorticity data are shown plotted in Figure 4.3(b). It can be seen that there are small vortices that have an absolute value larger than ω_T (4.8 s^{-1}) in Figure 4.3 (a) and that they are not detected as coherent structures in Figure 4.3(b) because they don't occupy four grid points. Comparing Figure 4.2 and Figure 4.3(b), it can be seen that the coherent structures obtained by interpolating by a factor of 4 have relatively smooth rounded edges and that the interpolation did not change the position or size of these structures.

The coherent structures shown in Figure 4.3(b) tend to have complex shapes and only a small number of them have approximately circular shapes. Therefore, the equivalent diameter, defined as the diameter of a circular structure that has an equal area to the coherent structure was used to compare the size of these complex structures. Therefore, in the following sections, the nominal size of each coherent structure, λ , was set equal to its equivalent diameter.

4.4 Characteristics of Coherent Structures

The primary characteristics of a coherent structure are its nominal size, λ , and its maximum vorticity, ω_{max} . First a comparison will be shown for the nominal size, λ , results obtained without interpolation and from interpolating the spatial resolution by factors of 4 and 24. Figure 4.4(a) shows the PDF of λ of coherent structures obtained with no interpolation and when interpolating by a factor of 4 at the highest wind speed of

9.6 m·s⁻¹. It can be seen that the distributions have the same shape but they are not identical. The PDF of the interpolated data is shifted slightly to the right. In other words, interpolating by a factor of 4 produces slightly larger coherent structures. The average values of the nominal size, $\langle \lambda \rangle$, were on average 7% larger when interpolating by a factor of 4 not only at this wind speed but at all wind speeds. This difference is considerably small with the good resolution obtained in terms of having rounded and realistic coherent structures.

Figure 4.4(b) compares the PDF's of λ , obtained from interpolating by factors of 4 and 24 at the highest wind speed of 9.6 m·s⁻¹. These PDF's show that there are a few more structures detected at λ value of 13 mm when interpolating by a factor of 4 than by a factor of 24. But it can be seen that the two PDF's are very similar at the two spatial resolutions. The average values of the nominal size, $\langle \lambda \rangle$, were obtained at these two spatial resolutions for different wind speeds and the average difference was always less than 5% at the same wind speed. These results demonstrate that interpolating by a factor of 4 gives essentially the same results as interpolating by a factor of 24 and in addition, interpolating by only a factor of 4 is computationally efficient.

In Figures 4.5(a)&(b), the PDF's of λ are plotted at wind speeds of 3.8 m·s⁻¹, 6.2 m·s⁻¹ and 9.6 m·s⁻¹ for clean and surfactant-influenced water surfaces, respectively. There is a sharp cutoff in the PDF's at 6mm and that is because the detection scheme discarded coherent structures with nominal sizes $\lambda < 5.9$ mm. All the distributions shown in Figure 4.5 have the same peak (mode) at λ value of 8 mm and that is probably related to setting a threshold of 5.9 mm for the nominal size of the coherent structures. These peaks at 8 mm indicate that the most frequently detected coherent structures have a size

of 8 mm for all wind speed and both water surface conditions. Also in Figure 4.5, it is evident that as the wind speed increases, the PDF's are shifted to the right and the distributions became more skewed. Specifically, as the wind speed increases from 3.8 to 9.6 m·s⁻¹, the 95th percentile of the λ distribution increased by 55% and 29% for clean and surfactant-influenced water surfaces, respectively. It is important to mention that there are undoubtedly structures smaller in size than 6 mm that were not detected. This of course is due to the finite spatial resolution of the DPIV data and to the requirement that a coherent structure occupies at least 4 DPIV grid points.

In Figures 4.6(a)&(b) the PDF's of the maximum vorticity, ω_{max} are plotted at the same wind speeds for clean and surfactant-influenced water surfaces, respectively. Since the vorticity threshold was set to 4.8 s⁻¹ in the detection scheme, there is a sharp cutoff in the PDF's at approximately ± 4.8 s⁻¹ (note that the ω_{max} bin size is 1.0 s⁻¹ in the PDF's in Figure 4.6). The trend in both figures shows that at the lowest wind speed, the number of coherent structures that have negative vorticity compared to the ones that have positive vorticity is small. As the wind speed increased the number of coherent structures that have negative vorticity increases and the number of coherent structures that have positive vorticity decreases. Therefore, the PDF's of positive ω_{max} are decreasing in amplitude and PDF's of negative ω_{max} are increasing in amplitude. In fact, the increase in the number of negative vorticity coherent structures with the increase of the wind speed is due to an increase in the mean shear, $\overline{(\partial u / \partial \zeta)}$ and to an increase in microscale-breaking waves. In other words, the mean shear $\overline{(\partial u / \partial \zeta)}$ is always positive, hence at low wind speeds, most of the vortices are positive. But, at higher wind speeds, microscale-breaking waves generate coherent structures with positive and negative vorticity and this

broadens the entire PDF. It is noteworthy that, the exact shape of the PDF of ω_{max} depends on the chosen vorticity threshold value. For example, the PDF's in Figures 4.6(a)&(b) all have the same the peak (mode) at ω_{max} value of 8 s^{-1} for positive structures and -8 s^{-1} for negative structures. Note that trends in the PDF's are the same for both water surface conditions.

The total kinetic energy of each coherent structure was calculated using the corresponding DPIV velocity data, by summing the contribution from all the grid points that the structure occupied. The nominal size λ of each structure can be used to compute the wavenumber $k = 2\pi/\lambda$. Consequently, distributions of total kinetic energy versus the wavenumber were produced at all wind speeds and for both water surface conditions. At a given wind speed, the total kinetic energy in a certain wavenumber bin was calculated by summing the kinetic energy of all the coherent structures that lie within that range of wavenumbers. Figures 4.7(a)&(b) show the distributions of the total kinetic energy of the coherent structures versus the wavenumber at wind speeds of 3.8 , 6.2 and $9.6 \text{ m}\cdot\text{s}^{-1}$ for clean and surfactant-influenced water surfaces, respectively. There is a cutoff on the right side of the distributions at a wavenumber of $1064 \text{ rad}\cdot\text{m}^{-1}$, which corresponds to λ of 5.9 mm . Figure 4.7 shows that as the wind speed increases, the total kinetic energy increases and that the appearance of larger coherent structures (i.e. lower wavenumbers) shifts the distributions to the left. Specifically, Figure 4.7 shows that the most energetic coherent structures (i.e. the peak of the distribution) occurred at wavenumbers of approximately $860 \text{ rad}\cdot\text{m}^{-1}$ at the lowest wind speed and $350 \text{ rad}\cdot\text{m}^{-1}$ at the highest wind speed. The corresponding λ values are 7.3 and 17.9 mm , thus it can be concluded that the most energetic coherent structures were detected at all wind speeds and both water

surface conditions. Figure 4.7 also shows that the total kinetic energy decreased with increasing wavenumber and followed a slope of approximately $-5/3$ for coherent structures that have wavenumbers larger than the most energetic ones. Following a slope of $-5/3$ is expected, as the plots shown in Figure 4.7 are equivalent to wavenumber energy spectra.

Values of the wavenumbers, k_{me} and nominal sizes, λ_{me} of the most energetic coherent structures are tabulated in table 4.1 for all wind speeds and both water surface conditions. It can be seen that, the most energetic coherent structures under a clean water surface have larger wavenumbers or smaller sizes than under the surfactant-influenced water surface. Specifically, as the wind speed increased from 3.8 to 9.6 m·s⁻¹, λ_{me} increased from 7.3 to 15 mm or by a factor of 2.05 under clean water surfaces and from 8.7 to 18 mm or by a factor of 2.3 under surfactant-influenced water surfaces. The presence of a surfactant increased the size of the energetic structures on average by 16%.

Figure 4.8 compares plots of the total kinetic energy versus wavenumber for clean and surfactant-influenced water surfaces at the highest wind speed. This comparison shows that for coherent structures smaller than the most energetic one (larger wavenumbers), the total kinetic energy is larger in clean water surface. However, for coherent structures larger than the most energetic one (smaller wavenumbers), the total kinetic energy is larger in surfactant-influenced water surfaces. The surfactant causes the kinetic energy to shift to lower wavenumbers.

Figure 4.9 is a plot of the average nominal size, $\langle\lambda\rangle$, versus wind speed for both water surface conditions. It can be seen that as the wind speed increased from 3.8 to 9.6 m·s⁻¹, $\langle\lambda\rangle$ increased from 8 to 10.2 mm or 27% under clean water surface and from 8 to

9.5 mm or 19% under surfactant-influenced water surface. The presence of a surfactant decreased the average nominal size, $\langle \lambda \rangle$ by 5%. The average maximum vorticity of the coherent structures, $\langle \omega_{max} \rangle$, is plotted as a function of wind speed in Figure 4.10 for both water surface conditions. This plot shows that $\langle \omega_{max} \rangle$ increased from 12.9 to 15.2 s^{-1} or 8% under clean water surfaces and from 12.7 to 14.4 s^{-1} or 13 % under surfactant-influenced water surfaces as the wind speed increased from 3.8 to 9.6 $m \cdot s^{-1}$. The surfactant reduces $\langle \omega_{max} \rangle$ by an average factor of 4%.

Figure 4.11 shows the occurrence frequency of coherent structures, f_{CS} , which is the number of detected coherent structures per unit time per unit area, plotted as a function of wind speed for both water surface conditions. As the wind speed increased from 3.8 to 9.6 $m \cdot s^{-1}$, Figure 4.11 shows that f_{CS} increased by approximately a factor of ten under clean water surfaces and by approximately a factor of nine under surfactant-influenced water surfaces. Moreover, surfactants reduced the frequency of occurrence of coherent structures by an average factor of approximately 20%. It is evident from Figures 4.9, 4.10 and 4.11, that the impact of a surfactant on the coherent structure properties ($\langle \lambda \rangle$, $\langle \omega_{max} \rangle$ and f_{CS}) becomes more significant as the wind speed increases.

It is useful to compare the results presented in Figures 4.9, 4.10 and 4.11 with those were reported by Siddiqui *et al.* (2004). Their detection scheme is similar to the scheme used in this study but there are several significant differences. Note that Siddiqui *et al.* (2004) reported results for clean water surfaces only and that the novel aspect of this study is that we compared the characteristics of coherent structures under clean and surfactant-influenced water surfaces. Siddiqui *et al.* (2004) used a threshold for the nominal size $\lambda = 4.3$ mm based on their criterion that a coherent structure must occupy a

minimum of two of the DPIV grid points. Hence, they reported values of $\langle \lambda \rangle$ that are significantly smaller than the values shown in Figure 4.9 and table 4.1. For example, their range of $\langle \lambda \rangle$ was from 5.7 mm to 6.5 mm and our range was from 8 mm to 10.2 mm at comparable wind speeds. The fact that they allowed smaller coherent structures to be detected increased the total number of detected coherent considerably. Their values of f_{CS} ranged from 2 to 6.4 compared to our range of 0.32 to 3.3 at comparable wind speeds. In addition, they used a vorticity threshold value $\omega_T = 6 \text{ s}^{-1}$ and applied this threshold to the absolute values of the interpolated vorticity data; hence they didn't differentiate between coherent structures that have positive and negative vorticity. Consequently, their values of $\langle \omega_{max} \rangle$ were in the range of 15.2 s^{-1} to 19.0 s^{-1} , which is larger than the values shown in Figure 4.10 and table 4.1 that ranged between 12.9 s^{-1} and 15.2 s^{-1} at comparable wind speeds. These differences between the two detection schemes explain the discrepancies in the two sets of results.

4.5 Air-Water Gas Transfer

4.5.1 Surface Renewal Model

This section will discuss the prediction of the air-water gas transfer velocity using the surface renewal model based on the characteristics of the detected coherent structures. Equation [4.2] shows how the gas transfer velocity can be estimated using a surface renewal model. In the literature, a number of practical ideas have been presented on how to estimate the actual values of the characteristic timescale of surface renewal τ . Asher and Pankow (1991) argued that τ should be defined as a statistical parameter related to the surface element lifetimes. Based on this idea, Siddiqui *et al.* (2004) developed a

method for predicting the time scale of surface renewal using the properties of the coherent structures. Their technique is adapted and used here to estimate the gas transfer velocities.

Siddiqui *et al.* (2004) assumed that the time needed for a particular eddy to renew the surface is inversely proportional to its rate of rotation or its angular velocity. Hence, the angular velocity of an eddy, Ω , is used to estimate the characteristic timescale of surface renewal τ . Specifically, the value of the maximum absolute vorticity (ω_{max}) is used to calculate Ω . The angular velocity equals half of the vorticity and hence, the characteristic timescale τ was defined as,

$$\tau = C_2 \left(\frac{1}{\Omega} \right) = C_2 \left(\frac{1}{(\omega_{max} / 2)} \right) \quad [4.3]$$

where, C_2 is a constant with a physical interpretation. If τ is the time it would take for an eddy to complete one revolution, then $C_2 = 2\pi$. On the other hand, if τ corresponds to the time it would take for an eddy to rotate one radian or approximately 60° , then $C_2 = 1$.

Siddiqui *et al.* (2004) defined the areas that coherent structures occupy near the water surface as energetic areas. The areas that have vorticity weaker than the vorticity threshold value are not occupied by coherent structures and are defined as quiescent areas. Accordingly, at any time, the air-water interface can be divided into these two types of areas. Then, the total gas transfer velocity, k_G can be expressed as a weighted average given by,

$$k_G = \Phi k_e + (1 - \Phi) k_q \quad [4.4]$$

where, k_e is the mean gas transfer velocity inside the energetic areas, k_q is the mean gas transfer velocity inside the quiescent areas, Φ is the fraction of the surface occupied by

energetic areas, $(1 - \Phi)$ is the fraction of the surface occupied by quiescent areas. This approach is analogous to Zappa *et al.* (2004), as they estimated the air-water heat transfer velocity as the weighted average of the transfer velocity that occurs inside wakes produced by microscale breaking waves and the transfer velocity that occurs outside these wakes.

Coherent structures located close to the air-water interface are actually the most effective at renewing the surface and they control the transfer rate inside the energetic areas. Figure 4.9 shows that the average size of the coherent structures ranged from approximately 8 to 10 mm. Figure 4.5 shows that the largest size of the coherent structures was approximately 20 mm. For that reason, coherent structures whose centroids were positioned within the top 1.0 cm layer of water are the only ones included when estimating the gas transfer velocities in the energetic areas.

The surface area renewed by one coherent structure, or the fraction of the surface occupied by this structure, is proportional to the nominal size of this coherent structure. Assuming that the top width of each coherent structure equals T , the mean value of T of all the coherent structures at each wind speed is defined as T_m . The transverse width of the coherent structures perpendicular to the direction of flow will be assumed to be equal to $C_3 T_m$ where C_3 is a constant. Thus, the total surface area renewed by all the coherent structures A_{cs} , is computed as,

$$A_{cs} = C_3 T_m \sum_{i=1}^{N_{cs}} T_i \quad [4.5]$$

where, N_{cs} is the total number of coherent structures in the top 1 cm and the sum is the total top width of all the coherent structures detected within the top 1 cm layer of water.

Assuming the total surface area, A_t , that the coherent structures could occupy, has a transverse width perpendicular to the wind direction equals to $C_3 T_m$ then,

$$A_t = C_3 T_m L N_f \quad [4.6]$$

where, L is the length of the DPIV field of view (10.2 cm) and N_f is the total number of analyzed vorticity fields. Therefore, the fraction of the surface occupied by energetic areas Φ , is simply given by,

$$\Phi = \frac{A_{cs}}{A_t} = \frac{\sum_{i=1}^{N_{cs}} T_i}{L N_f} \quad [4.7]$$

Siddiqui *et al.* (2004) argued that assuming that surface renewal is occurring continuously in both the energetic and quiescent areas, is not correct. Specifically, they argued that it was reasonable to assume that surface renewal was occurring 100% of the time inside the energetic areas because these regions were occupied by coherent structures all the time. But, it is not reasonable to assume that surface renewal occurs continuously in the quiescent areas. Siddiqui *et al.* (2004) argued that making an estimate of the fraction of time that near-surface eddies were strong enough to produce surface renewal in the quiescent areas would account for the intermittent nature of the surface renewal in these areas. It was shown in Figure 4.11 that the frequency of occurrence of coherent structures increased by a factor of ten from the lowest to the highest wind speed. Siddiqui *et al.* (2004) assumed that the frequency of occurrence of weaker eddies in the quiescent areas is comparable to the frequency of occurrence of the coherent structures detected in the energetic areas. Then, following Siddiqui *et al.* (2004), the fraction of time that surface renewal is occurring in the quiescent areas γ , can be estimated from,

$$\gamma_i = (f_{CS}) / (f_{CS})_{max} \quad [4.8]$$

where, $(f_{CS})_{max}$ is the frequency of occurrence of coherent structures at the highest wind speed of $9.6 \text{ m}\cdot\text{s}^{-1}$, and f_{CS} is the frequency of occurrence of coherent structures at a given wind speed. Note that equation [4.8] predicts $\gamma_i = 1$ at the highest wind speed. This means that we are assuming that surface renewal occurs 100% of the time in the quiescent areas at this wind speed. Using this idea, the total gas transfer velocity k_G is now given by,

$$k_G = \Phi k_e + \gamma_i (1 - \Phi) k_q. \quad [4.9]$$

The air-water interface may behave as either a free or rigid surface depending upon the cleanliness of the interface and, the difference can be justified using the surface renewal model (Zappa *et al.* 1999). This behavior can be expressed as,

$$k_G \sim S_c^{-n} \quad [4.10]$$

where, S_c is the Schmidt number and the exponent n is an empirical constant that depends on the eddy-diffusivity transport in the turbulent boundary layers (Deacon 1977, Coantic 1986 and Jähne *et al.* 1987). The differences in the Schmidt number dependence of k_G produced by the rigid and free surface boundary conditions has important implication for water surface cleanliness. For clean water surfaces, the tangential flow produces convergence and divergence zones and the surface behaves as a free surface and in that case, k_G is proportional to $D^{1/2}$ or $n = 1/2$, which is consistent with equation [4.2] for the surface renewal model (Deacon 1977). However, a surfactant-influenced interface changes the free surface boundary condition and suppresses near-surface turbulence. The surface stress may be too weak to overcome the restoring forces of the surfactant film and the surface behaves similar to a smooth rigid wall. Deacon (1977) found that in this case,

k_G is proportional to $D^{2/3}$ for smooth rigid walls and hence $n = 2/3$. In addition, Coantic (1986), Jähne *et al.* (1987) and Zappa *et al.* (1999) have confirmed experimentally that $n \approx 2/3$ for surfactant-influenced water surfaces. The Schmidt number S_c is the ratio between the kinematic viscosity ν and the molecular diffusivity D and accordingly, equation [4.2] can be expressed in terms of S_c as,

$$k_G = C_1 \nu^{1/2} \tau^{-1/2} S_c^{-n}. \quad [4.11]$$

The air-water gas transfer velocity for each coherent structure whose centroid was located within the top 1.0 cm layer was calculated using equations [4.3] and [4.11]. The constants C_1 and C_2 were both set equal to one and the Schmidt number S_c , was set equal to 600 (the Schmidt number of CO_2 in water at 20°C). The gas transfer velocities in clean water were calculated using $S_c^{-1/2}$ and in the surfactant-influenced water using $S_c^{-2/3}$. The air-water gas transfer velocity inside the energetic areas, k_e , was computed by taking the mean of all the individual values of air-water gas transfer velocity of each coherent structure. This is similar to Danckwerts (1970) who concluded that the exposure times of all fluid elements must be considered to estimate the average transfer rate even though these exposure times vary. This approach was used to estimate the value of k_e , at all wind speeds for both water surface conditions.

The near-surface flow in the quiescent areas is characterized by a relatively weak background vorticity because strong vorticity was associated with the coherent structures inside the energetic areas. So following Siddiqui *et al.* (2004), it was assumed that the quiescent surface areas were renewed by the weak background vorticity. The mean value of the absolute vorticity in the top 1 cm layer in the quiescent areas $\langle \omega_b \rangle$ was used to estimate the timescale of surface renewal in these areas. These mean values of vorticity

were then used in equations [4.3] and [4.11] to calculate the time scale of surface renewal and the gas transfer velocity in the quiescent areas.

4.5.2 Air-Water Gas Transfer Results

To measure the bulk gas transfer velocity, the water was supersaturated with Helium and SF₆. The concentrations of both gases were sampled throughout the experiments every 10 minutes over a period of 4 hours at two different stations, one at each end of the tank (Atmane *et al.* 2004). The transfer velocity of each gas was computed from the decrease in concentration with time (Asher *et al.* 1996).

The average values of the transfer velocity inside the energetic areas k_e , the air-water gas transfer velocity inside the quiescent areas k_q , the fraction of the surface occupied by energetic areas Φ , the fraction of time that surface renewal is occurring in the quiescent areas γ , the total predicted air-water gas transfer velocity k_G , and the measured bulk air-water gas transfer velocity k_G , are shown tabulated in table 4.2 at all wind speeds for both water surface conditions.

The data in table 4.2 shows that as the wind speed increased from 3.8 to 9.6 m·s⁻¹; values of k_e increased by approximately 12% from 34.3 to 38.3 cm·hr⁻¹ for clean water surfaces and by approximately 10% from 15.7 to 17.2 cm·hr⁻¹ for surfactant-influenced water surfaces. The average values of ω_{max} increased by 18% and 13% in clean and surfactant-influenced water, respectively and this was reflected in the increase of k_e in the energetic regions (see Figure 4.9). The estimates of k_e did not vary much with wind speed because of the small variations in $\langle\omega_{max}\rangle$ (see Figure 4.10). For the same increase in wind speed, k_q increased by approximately 24% from 12.7 to 15.8 cm·hr⁻¹ for clean

water surfaces and by approximately 21% from 5.7 to 7.0 cm-hr⁻¹ for surfactant-influenced water surfaces.

The ratio of k_e / k_q varied from 2.4 to 2.7 with an average value of 2.5 for both water surface conditions. This is consistent with Siddiqui *et al.* (2004) who found that the transfer velocities inside the energetic areas were on average 2.8 times larger than the transfer velocities inside the quiescent areas. Also Zappa *et al.* (2004) reported that the air-water heat transfer velocity inside the wakes produced by microscale-breaking waves was on-average 3.5 times higher than outside the wakes.

The tabulated values of the fraction of the surface occupied by energetic areas Φ , in table 4.2 ranged from approximately 0.1 to 0.47 and from 0.09 to 0.42 for clean and surfactant-influenced water surfaces, respectively as the wind speed increased from 3.8 m·s⁻¹ to 9.6 m·s⁻¹. This is reasonable since surface renewal by water parcels should increase when the wind speed increases, hence Φ increases. It is noteworthy that at the highest wind speed, approximately 50% of the surface is renewed in clean water. The fraction of time that surface renewal is occurring in the quiescent areas, γ_i , varied from 0.3 to 1.0 and from 0.2 to 1.0 for the same range of wind speed under clean and surfactant-influenced water surfaces, respectively.

The gas flux across the energetic areas is proportional to Φk_e , the gas flux across the quiescent areas is proportional to $\gamma_i(1 - \Phi) k_q$ and the total predicted gas flux is proportional to k_G . The ratio $\Phi k_e / k_G$ is an estimate of the fraction of the gas flux that occurred across the energetic areas. Specifically, this ratio is a measure of the contribution of the coherent structures inside the energetic regions to the total gas flux. This ratio ranged between 0.5 and 0.68 with an average value of approximately 0.59 for

clean water surfaces and between 0.51 and 0.64 with an average value of approximately 0.57 for surfactant-influenced water surfaces. These results mean that over the entire wind speed range, on average ~60% of the total gas transfer occurred across the energetic areas. Siddiqui *et al.* (2004) also found that 60% of the total gas transfer occurred across the energetic regions.

The tabulated values of the gas transfer velocity k_G in table 4.2 show that as the wind speed increased from 3.8 to 9.6 m·s⁻¹ the predicted k_G increased by approximately a factor of 4 from 6.6 to 26.3 cm·hr⁻¹ for clean water surfaces and by approximately a factor of 4.9 from 2.3 to 11.3 cm·hr⁻¹ for surfactant-influenced water surfaces. Table 4.2 shows that, for the same increase in wind speed, the measured k_G increased by factors of 4 and 3.1 for both clean and surfactant-influenced water surfaces, respectively (As previously shown in Chapter3). It is evident that both the predicted and measured k_G are a strong function of the wind speed while k_e and k_q are weak functions of the wind speed (as discussed previously). It is noteworthy that the presence of a surfactant reduced the predicted k_G values by approximately 46% and the measured k_G values by approximately 55%.

The properties of the coherent structures only varied slightly with wind speed. However, as the wind speed increased from 3.8 to 9.6 m·s⁻¹, the frequency of occurrence increased by a factor of 10 and the fraction of the surface occupied by coherent structures, Φ increased by approximately a factor of 5. It was the large increases in f_{CS} and Φ that caused the large change in the predicted values of k_G .

Figures 4.12(a)&(b) show comparisons between the measured bulk gas transfer velocities and the predicted total gas transfer velocities k_G , as a function of wind speed

for clean and surfactant-influenced water surfaces, respectively. It is evident from these figures that the predicted values are slightly less than the measured values but the trends of the predicted and measured values are similar. The predicted values are on average 17% and 35% less than the measured values for clean and surfactant-influenced water surfaces, respectively. In fact, this is relatively close agreement, compared to Scott (1970), Komori *et al.* (1993) and Siddiqui *et al.* (2004) who found that measured gas transfer velocities were 2.5, 3 and 1.5 times larger, respectively than those predicted using the surface renewal model. They all found that the surface renewal model overestimated k_G whereas in this study the gas transfer velocities were underestimated by approximately 25%. The implementation of the surface renewal model in this study is similar to Siddiqui *et al.* (2004), but they overestimated the gas transfer velocities by 50%. One of the main reasons for this inconsistency is the fact that they estimated Φ differently. Also, their average values for λ , ω_{max} and f_{CS} were different as explained earlier and this would also help explaining the differences in k_G .

One possible reason for the differences between the predicted and measured gas transfer velocities is the values of C_1 and C_2 . The value of these constants was arbitrarily assumed to be 1.0. Setting $C_2 = 1$, corresponds to the assumption that surface renewal happens once a coherent structure located near the air-water interface has rotated through an angle of approximately 60° . Changing the value of either or both of these constants could produce closer agreement between the measured and predicted gas transfer velocities. For example, setting $C_1 = 1.25$ and keeping $C_2 = 1.0$ increases the value of k_G by a factor of 25%. Previous studies used considerably different values of the constant

C_I , for example, Higbie (1935), Danckwerts (1970) and Komori *et al.* (1993) assumed C_I to be equal to $2/\sqrt{\pi}$, $1/\sqrt{\pi}$ and 0.34 respectively.

Figure 4.13 shows a plot of the measured values of k_G versus Φ for both water surface conditions. It is clear that there is a strong linear relation between them in both cases. The correlation coefficients were found to be 0.99 and 0.98 for clean and surfactant-influenced water surfaces. This strong correlation supports the conclusion that regardless of surface cleanliness, the gas transfer occurs mainly across the energetic areas where the coherent structures are renewing the surface. Siddiqui *et al.* (2004) reported a similar correlation coefficient of 0.96 and concluded that microscale-breaking waves were responsible for the majority of the surface renewal.

It may seem obvious that the detected coherent structures are associated with microscale-breaking waves. However, it is quite likely that some of the coherent structures are not related directly with microscale-breaking waves. Non-breaking waves and shear generated turbulence may generate eddies that renew the surface as well. Siddiqui *et al.* (2004) argued that it was impossible to differentiate with certainty the coherent structures that were generated by microscale wave breaking, non-breaking waves or shear generated turbulences. Nonetheless, they suggested that microscale-breaking waves were probably the primary source of the coherent structures and hence the mechanism controlling surface renewal and air-water gas transfer. To investigate this issue, a plot of the percentage of wave breaking P_b , and Φ is shown in Figure 4.14 for both water surface conditions. It is evident that there is a clear trend between the two parameters, that is, as the wave breaking increases, the fraction of the surface renewed increases. For the first four points in the figure that correspond to wind speeds less than 5

$\text{m}\cdot\text{s}^{-1}$, there is a linear relationship between P_b , and Φ regardless of the surface cleanliness. As the breaking percentage increases to approximately 25%, the fraction of the surface that is renewed increases slowly to 0.15. For the highest three wind speeds for each water surface condition, there is still a linear relationship between P_b , and Φ but Φ increases much more rapidly. These results support the argument that microscale-breaking waves are the main source of the surface renewal that drives air-water gas transfer.

4.6 Conclusions

In this chapter, results from a wind-wave tank experiment investigating the characteristics of coherent structures beneath clean and surfactant-influenced water surfaces and their influence on air-water gas transfer have been presented. A vorticity based detection scheme adapted from Siddiqui *et al.* (2004) was described and used to detect coherent structures. A surface renewal model was used to predict the air-water gas transfer velocities based on the characteristics of the detected coherent structures. Also, the model accounted for the presence of surfactants by taking into account their effect on the free surface boundary conditions (the power n of Schmidt number).

The results showed that the average nominal size and maximum vorticity of the coherent structures did not change significantly as the wind speed increased or with the presence of surfactants. As the wind speed increased from 3.8 to 9.6 $\text{m}\cdot\text{s}^{-1}$, the average nominal size increased by 27% and 19% for clean and surfactant-influenced water surfaces, respectively. The surfactant reduced the average nominal size by approximately 5%. Similarly, for the same increase in wind speed, the average maximum vorticity

increased by 8% for clean water surfaces and 13% for surfactant-influenced water. The surfactant reduced the average maximum vorticity by approximately 4%.

The coherent structures properties that changed significantly with the increase in wind speed and the presence of surfactants were the size of the most energetic coherent structures and the frequency of occurrence of coherent structures. The nominal size of the most energetic coherent structures increased from 7.3 to 15 mm and from 8.7 to 18 mm as the wind speed increased from 3.8 to 9.6 m·s⁻¹ for clean and surfactant-influenced water surfaces, respectively. The surfactant increased the nominal size of the most energetic coherent structures by approximately 16%. For the same increase in wind speed, the frequency of occurrence of coherent structures increased by a factor of ~10 for both clean and surfactant-influenced water surfaces and the presence of a surfactant reduced the frequency of occurrence of coherent structures by approximately 20%.

The surface renewal model underestimated the values of the gas transfer velocity by approximately 25%, which is in relatively close agreement compared to previous studies. The gas transfer velocity inside the energetic regions was found to be approximately 2.5 times larger than the gas transfer velocity in the quiescent regions for both water surface conditions. The model predicted that approximately 60% of the total gas flux occurred across the surface of the energetic regions at all wind speeds for both water surface conditions. The fraction of the water surface renewed by coherent structures and the frequency of occurrence of coherent structures are sensitive to the increase in the wind speed or the presence of surfactants. Therefore, they are the most effective parameters in predicting total air-water gas transfer velocities. The fraction of the water surface renewed by coherent structures increased by a factor of approximately 5 as the wind

speed increased from 3.8 to 9.6 m·s⁻¹ for both water surface conditions. It was found that the fraction of the water surface renewed by coherent structures was correlated with the percentage of microscale-breaking waves, which supports the hypothesis that microscale-breaking drives the majority of the surface renewal and hence controls the air-water gas transfer rate.

Clean water surfaces					
Wind Speed (m.s^{-1})	3.79	4.89	6.23	7.99	9.53
k_{me} (rad.m^{-1})	860	720	620	480	420
λ_{me} (mm)	7.31	8.73	10.13	13.09	14.96
$\langle \lambda \rangle$ (mm)	8.08	8.48	8.90	9.57	10.15
$\langle \omega_{max} \rangle$ (s^{-1})	12.90	13.44	13.79	14.42	15.20
f_{CS} ($\text{s}^{-1}\text{cm}^{-2}$)	0.32	0.63	1.16	2.15	3.25

Surfactant Influenced water surfaces					
Wind Speed (m.s^{-1})	3.87	4.91	6.21	8.15	9.75
k_{me} (rad.m^{-1})	720	620	570	420	350
λ_{me} (mm)	8.73	10.13	11.02	14.96	17.95
$\langle \lambda \rangle$ (mm)	8.02	8.23	8.6	9.09	9.52
$\langle \omega_{max} \rangle$ (s^{-1})	12.73	13.14	13.48	13.83	14.36
f_{CS} ($\text{s}^{-1}\text{cm}^{-2}$)	0.26	0.52	0.98	1.64	2.34

Table 4.1: Summary of the characteristics of coherent structures for both water surface conditions. k_{me} is the wavenumber of the most energetic coherent structures, λ_{me} is the nominal size the most energetic coherent structures, $\langle \lambda \rangle$ is the average nominal size of the coherent structures, $\langle \omega_{max} \rangle$ is the average maximum vorticity of coherent structures and f_{CS} is the frequency of occurrence of coherent structures or the number of coherent structures per cm^2 per second.

Clean water surfaces					
Wind Speed ($m.s^{-1}$)	3.79	4.89	6.23	7.99	9.53
k_e ($cm.hr^{-1}$)	34.31	35.09	35.95	36.47	38.33
k_q ($cm.hr^{-1}$)	12.69	13.63	14.89	15.16	15.83
k_e/k_q	2.70	2.57	2.41	2.41	2.42
Φ	0.10	0.14	0.23	0.36	0.47
γ_t	0.28	0.36	0.52	0.79	1.00
Φk_e ($cm hr^{-1}$)	3.30	5.05	8.22	13.17	17.90
$\gamma_t (1-\Phi) k_q$ ($cm hr^{-1}$)	3.26	4.21	5.95	7.62	8.43
k_G ($cm.hr^{-1}$) predicted	6.56	9.26	14.17	20.79	26.33
k_G ($cm.hr^{-1}$) measured	7.49	12.39	17.81	23.33	29.92
$\Phi k_e / k_G$	0.50	0.55	0.58	0.63	0.68

Surfactant Influenced water surfaces					
Wind Speed ($m.s^{-1}$)	3.87	4.91	6.21	8.15	9.75
k_e ($cm.hr^{-1}$)	15.70	15.86	16.04	16.53	17.23
k_q ($cm.hr^{-1}$)	5.76	6.13	6.55	6.77	6.99
k_e/k_q	2.73	2.59	2.45	2.44	2.47
Φ	0.09	0.12	0.19	0.32	0.42
γ_t	0.18	0.34	0.57	0.87	1.00
Φk_e ($cm hr^{-1}$)	1.35	1.92	3.12	5.27	7.21
$\gamma_t (1-\Phi) k_q$ ($cm hr^{-1}$)	0.93	1.85	3.00	4.01	4.07
k_G ($cm.hr^{-1}$) predicted	2.27	3.77	6.13	9.28	11.27
k_G ($cm.hr^{-1}$) measured	4.58	6.34	9.76	12.60	14.30
$\Phi k_e / k_G$	0.59	0.51	0.51	0.57	0.64

Table 4.2: Summary of air-water gas transfer results for both water surfaces conditions. k_e is the air-water gas transfer velocity inside the energetic areas, k_q is the air-water gas transfer velocity inside the quiescent areas, Φ is the fraction of the surface occupied by energetic areas, γ_t is the fraction of time that surface renewal is occurring in the quiescent areas, and k_G is the total air-water gas transfer velocity. Both the predicted and measured k_G were referenced to $S_e = 600$ for both water conditions.

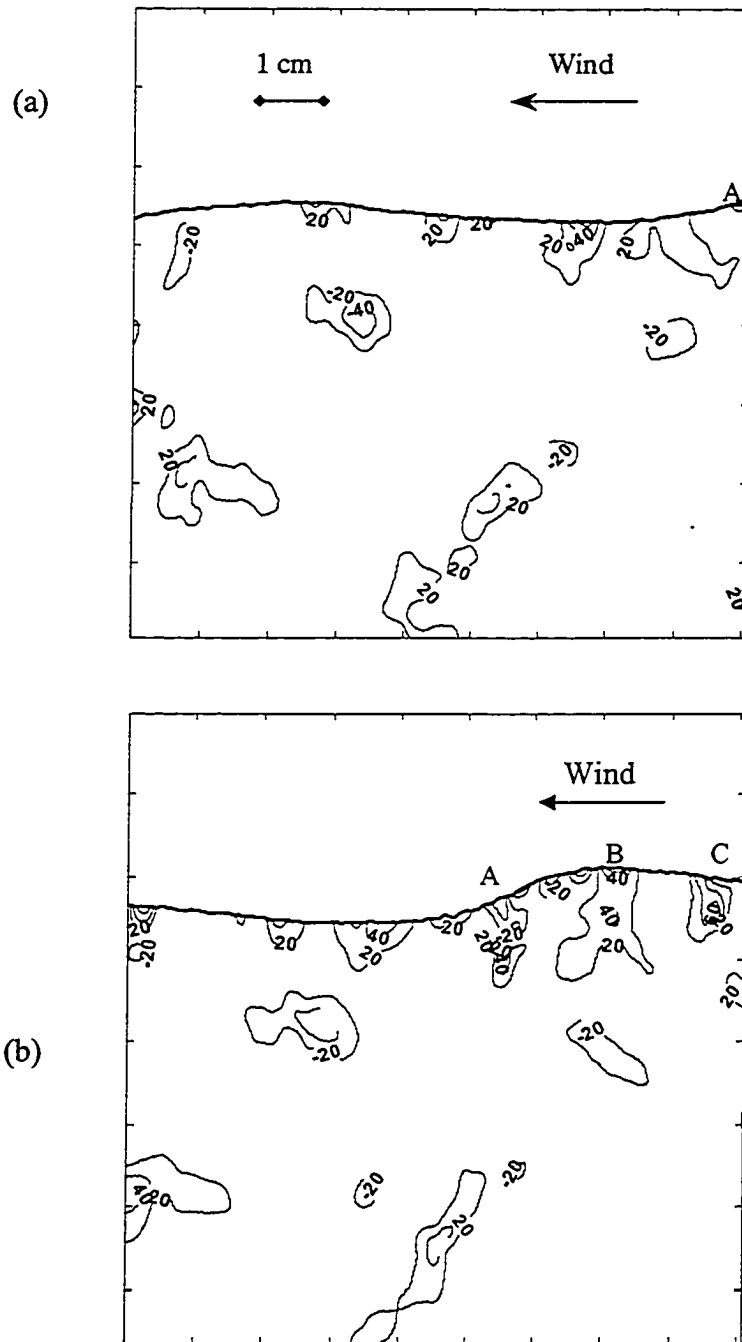


FIGURE 4.1(a-d): A sequence of four DPIV instantaneous vorticity contour plots at a wind speed of $9.6 \text{ m}\cdot\text{s}^{-1}$. The time separation between each vorticity field is $1/15 \text{ sec}$. The dimensions of the DPIV field of view are $9.2 \text{ cm} \times 9.2 \text{ cm}$. Positive vorticity ($\text{rad}\cdot\text{s}^{-1}$) contours correspond to vorticity and negative contours correspond to clockwise vorticity.

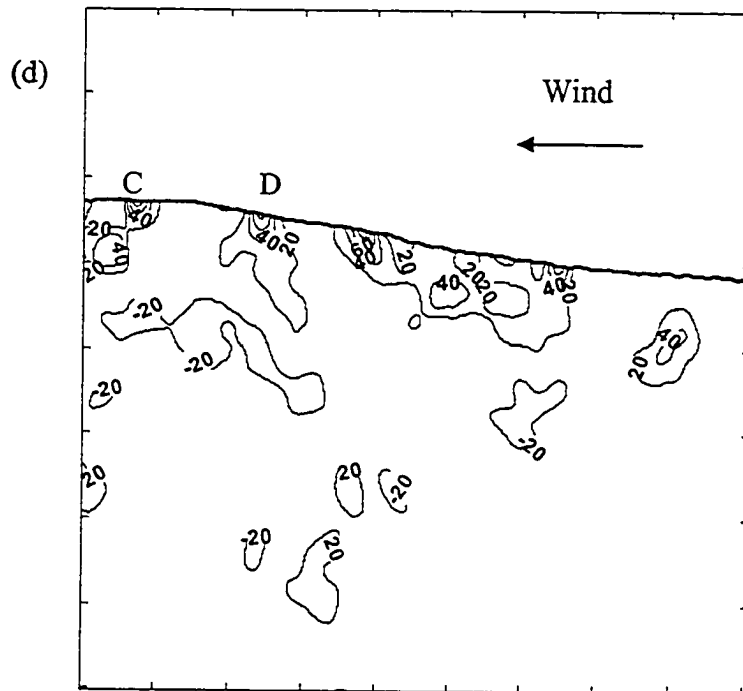
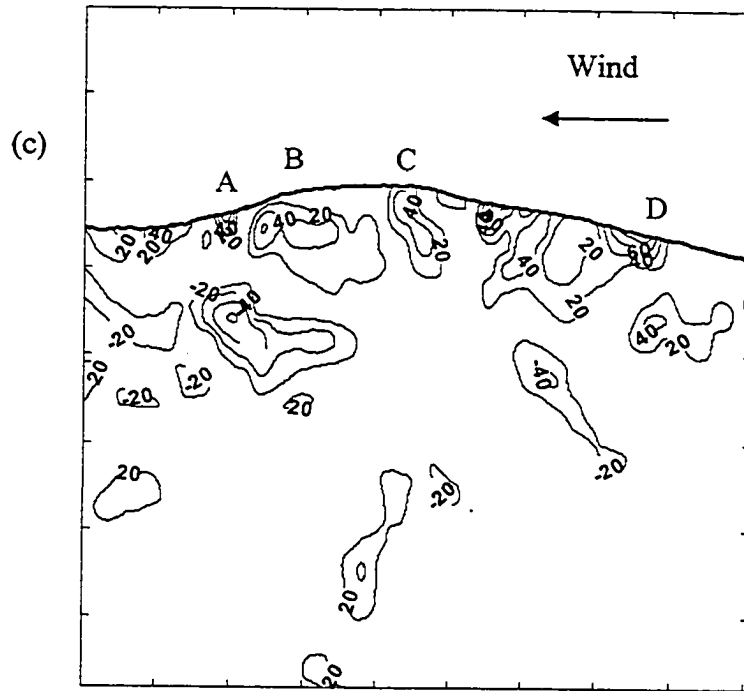


FIGURE 4.1: (continued)

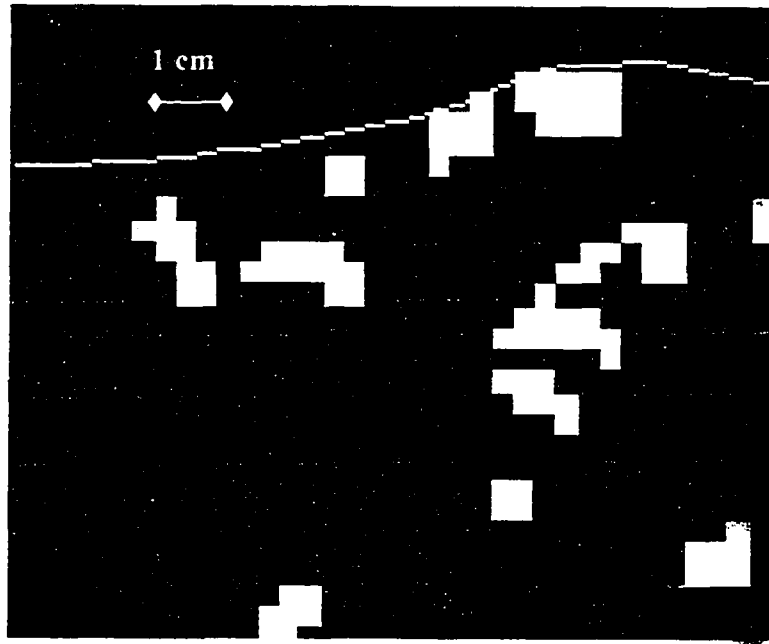


FIGURE 4.2: Plot showing the coherent structures identified by applying the vorticity threshold to the raw instantaneous vorticity field (i.e. no interpolation) at a wind speed of $9.6 \text{ m}\cdot\text{s}^{-1}$.

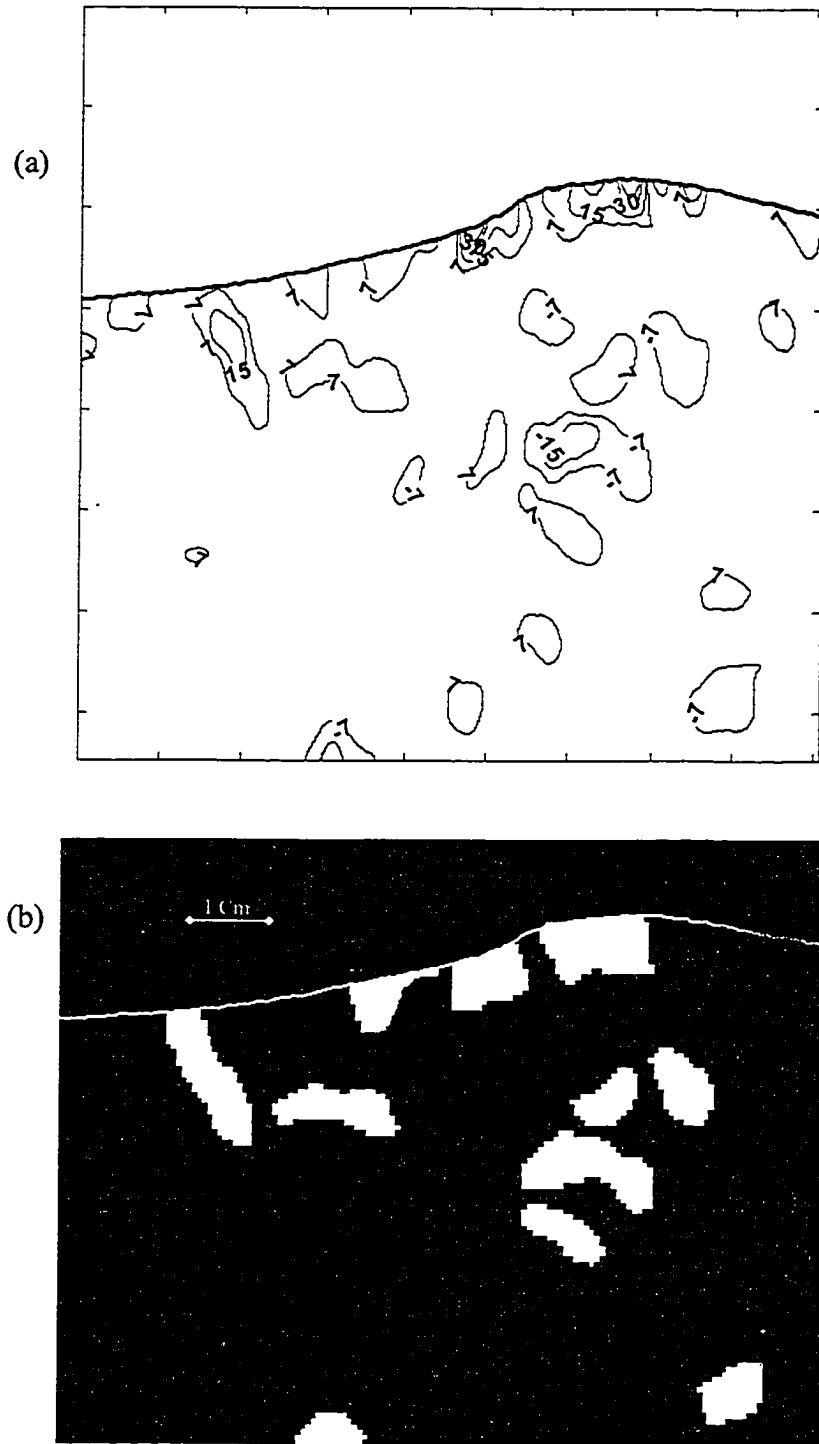


FIGURE 4.3: (a) Contours of the instantaneous vorticity beneath the crest of a microscale-breaking wave at a wind speed of $9.6 \text{ m}\cdot\text{s}^{-1}$. (b) Plot showing the coherent structures identified by applying the vorticity threshold on the instantaneous vorticity field shown in panel (a). Vorticity data was interpolated by a factor of 4.

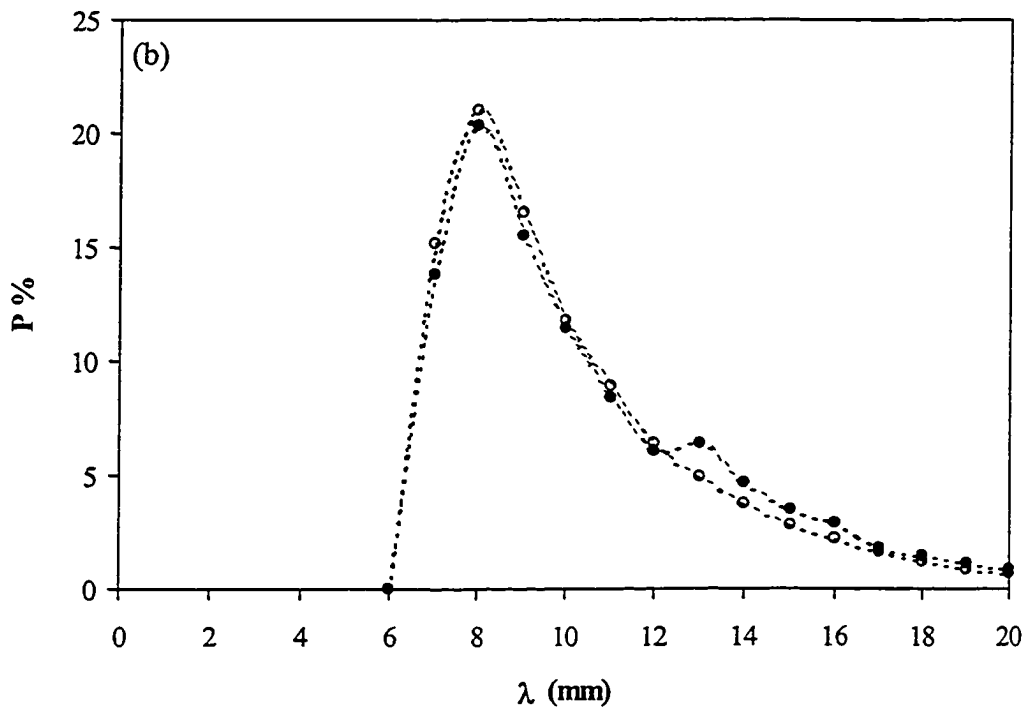
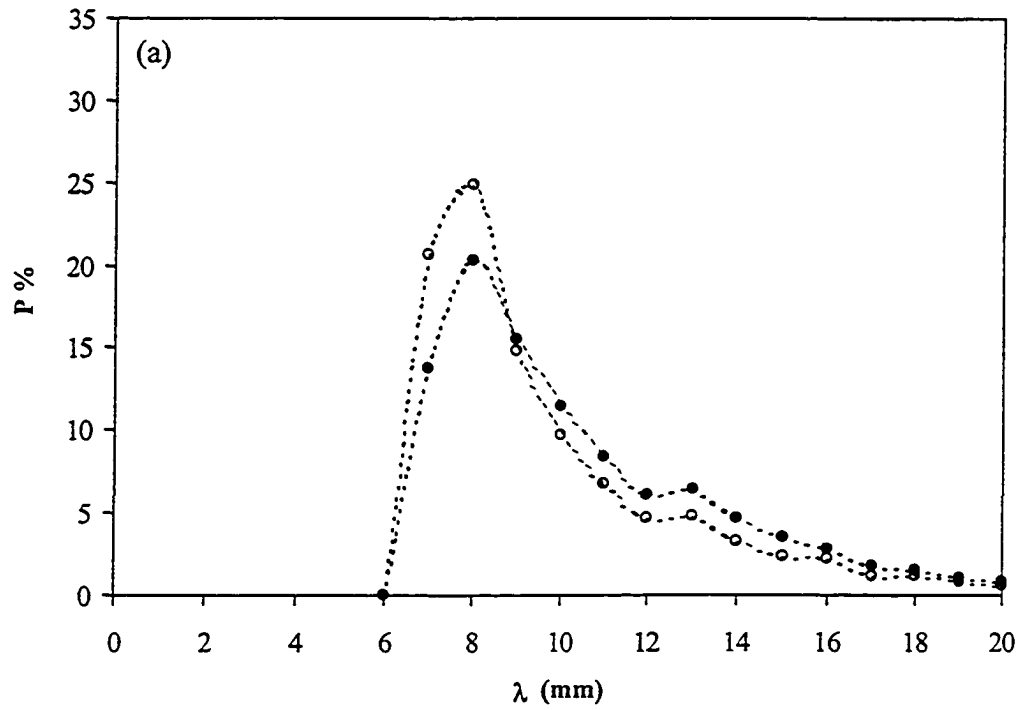


FIGURE 4.4: Probability density function (PDF) of λ , the nominal size of the coherent structures at wind speed of $3.8 \text{ m}\cdot\text{s}^{-1}$, (a) \circ , = no interpolation, \bullet , = interpolating by a factor of 4. (b) \circ , = interpolating by a factor of 24, \bullet , = interpolating by a factor of 4.

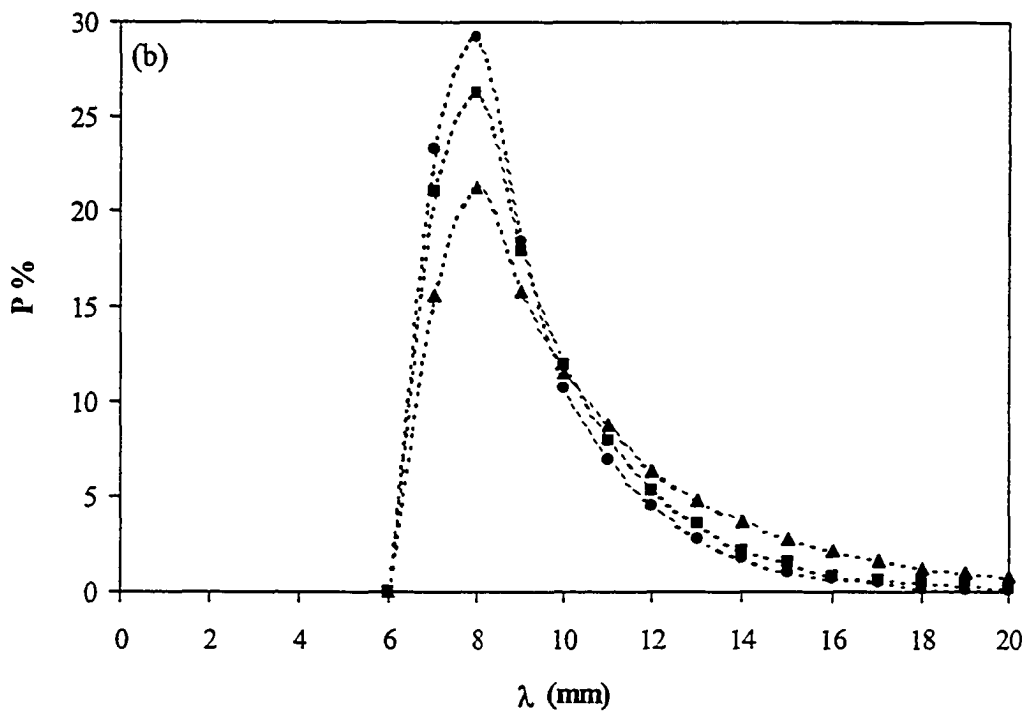
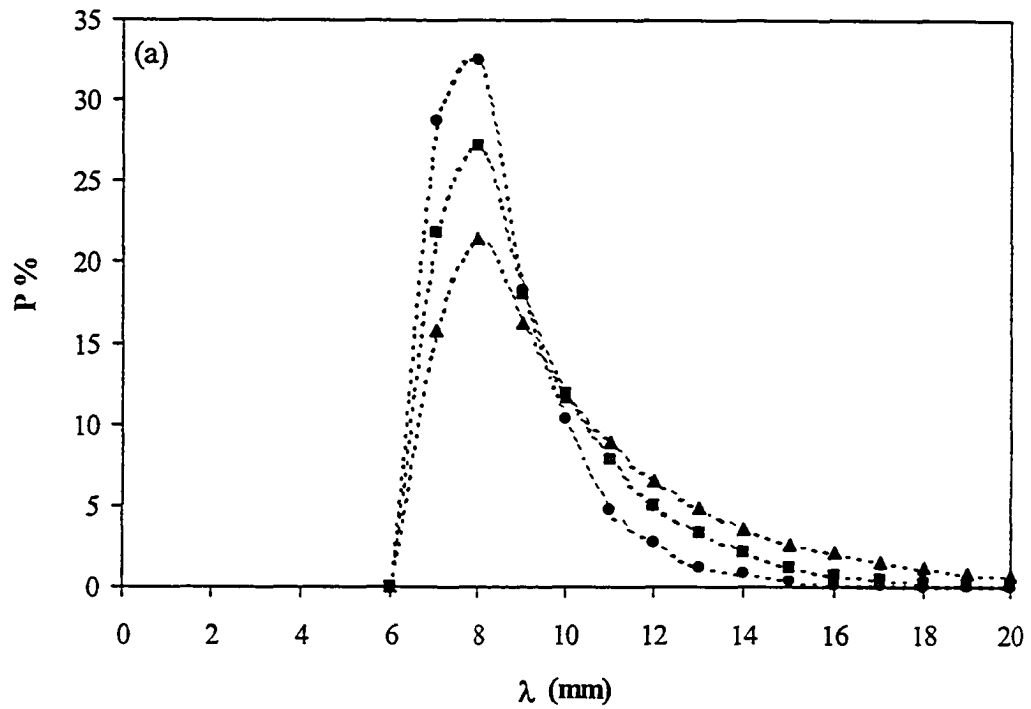


FIGURE 4.5: Probability density function (PDF) of λ , the nominal size of the coherent structures for different wind speeds obtained by interpolating by a factor of 4. (a) PDF's for clean water surfaces, (b) PDF's for surfactant-influenced water surfaces. \bullet , = $3.8 \text{ m}\cdot\text{s}^{-1}$; \blacksquare , = $6.2 \text{ m}\cdot\text{s}^{-1}$; \blacktriangle , = $9.6 \text{ m}\cdot\text{s}^{-1}$.

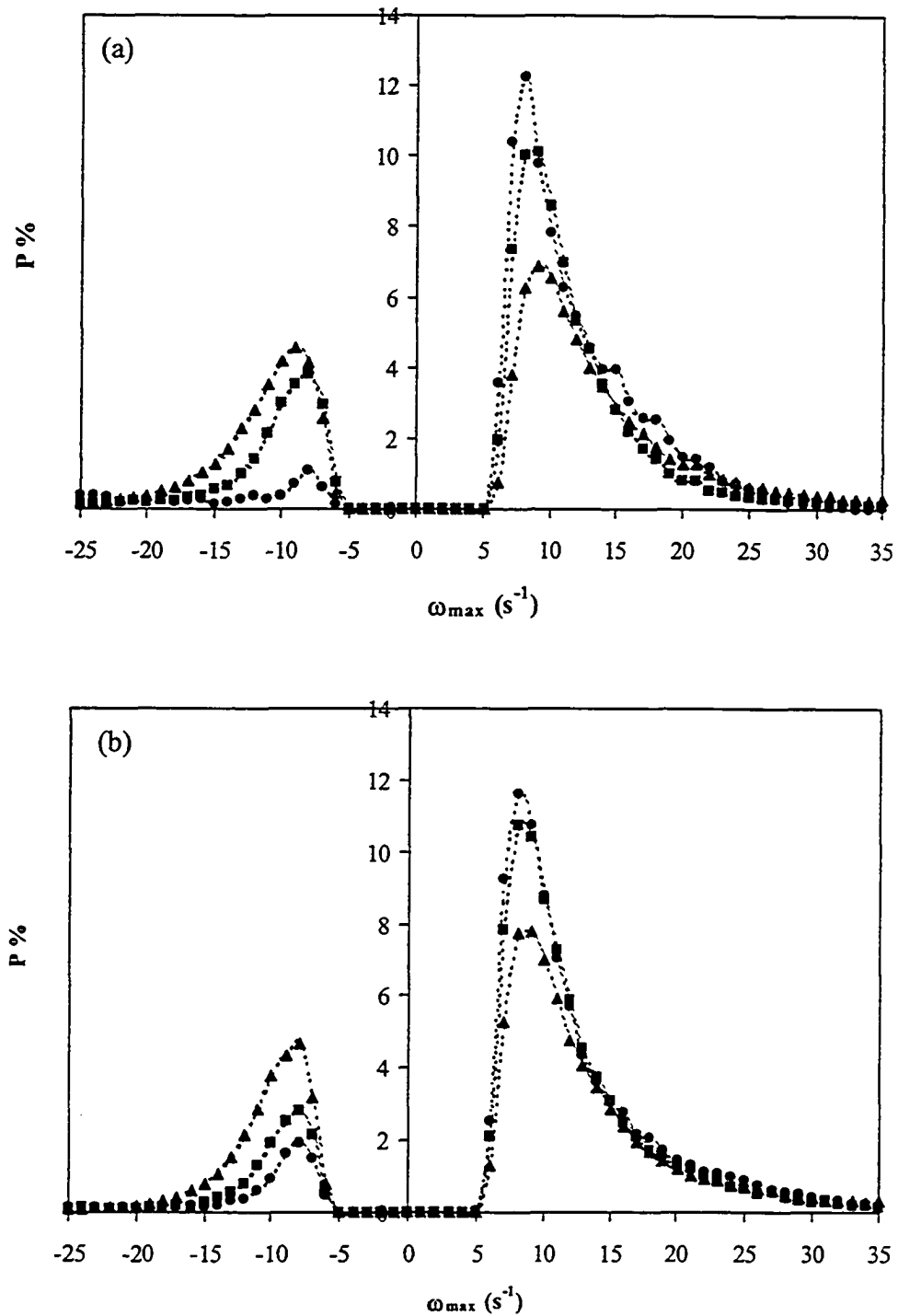


FIGURE 4.6: Probability density function (PDF) of ω_{max} , the maximum vorticity of the coherent structures at different wind speeds, positive values are the counter clockwise vortices and negative values are the clockwise vortices. (a) PDF's for clean water surfaces, (b) PDF's for surfactant-influenced water surfaces. \bullet , = $3.8 \text{ m}\cdot\text{s}^{-1}$; \blacksquare , = $6.2 \text{ m}\cdot\text{s}^{-1}$; \blacktriangle , = $9.6 \text{ m}\cdot\text{s}^{-1}$.

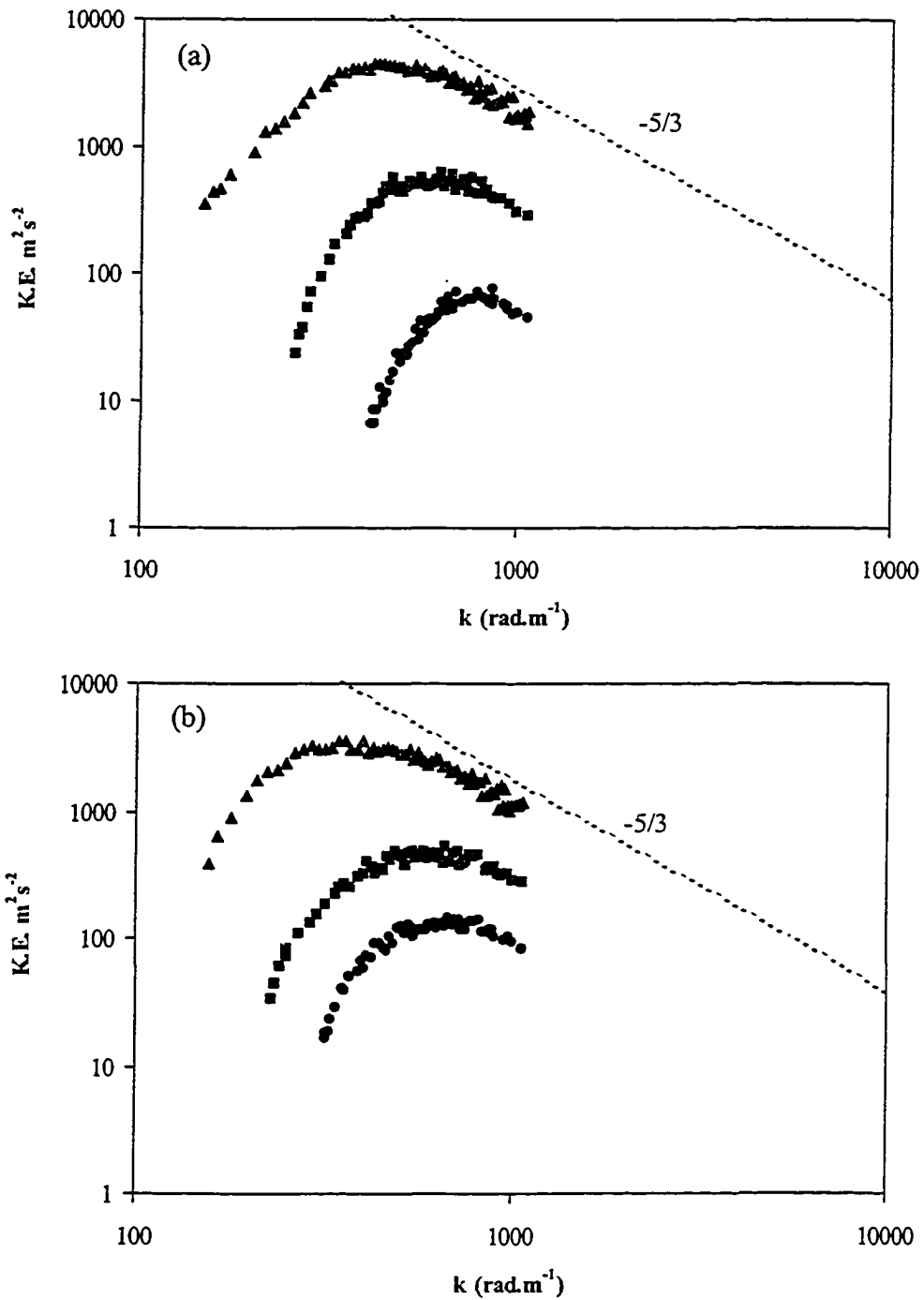


FIGURE 4.7: The total kinetic energy of coherent structures versus wavenumber ($k=2\pi/\lambda$) at different wind speeds. The wavenumber bin size equals 10 rad.m^{-1} and the values are summed over 10 minutes of data. (a) For clean water surfaces, (b) for surfactant-influenced water surfaces. \bullet , = 3.8 m.s^{-1} ; \blacksquare , = 6.2 m.s^{-1} ; \blacktriangle , = 9.6 m.s^{-1} .

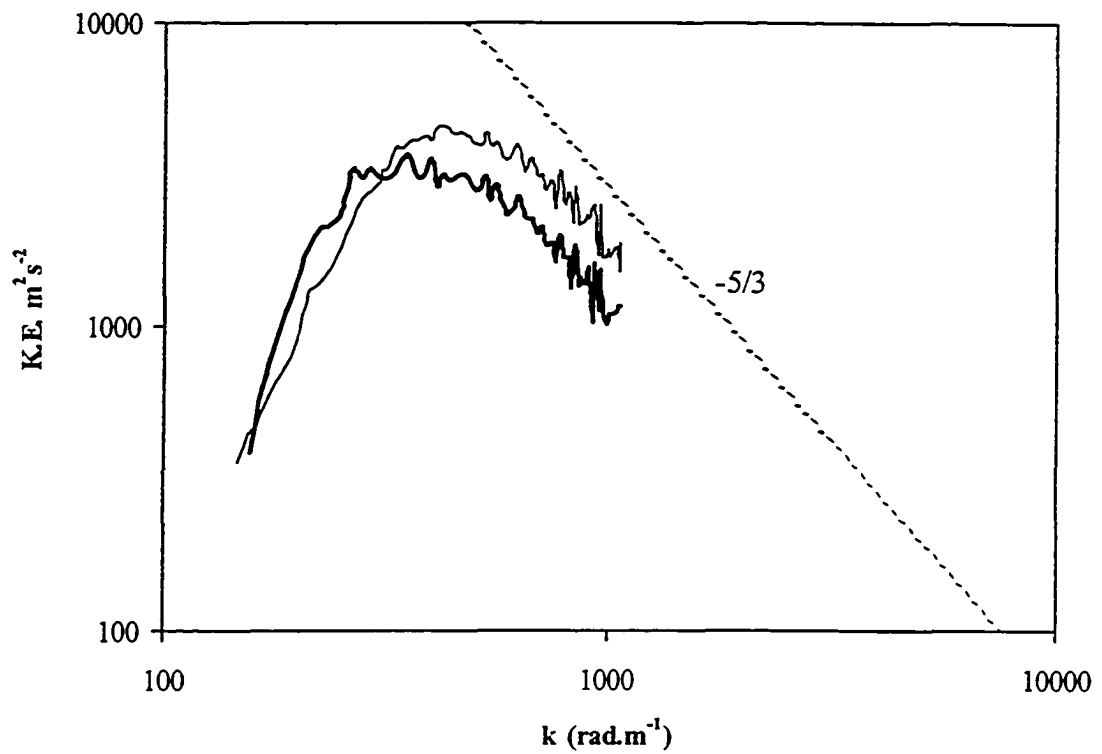


FIGURE 4.8: Comparison between the total kinetic energy of coherent structures versus wavenumber ($k=2\pi/\lambda$) at a wind speed of 9.6 m.s^{-1} . The wavenumber bin size equals 10 rad.m^{-1} and the values are summed over 10 minutes of data. Regular solid line is for a clean water surface and the bold solid line is for a surfactant-influenced water surface.

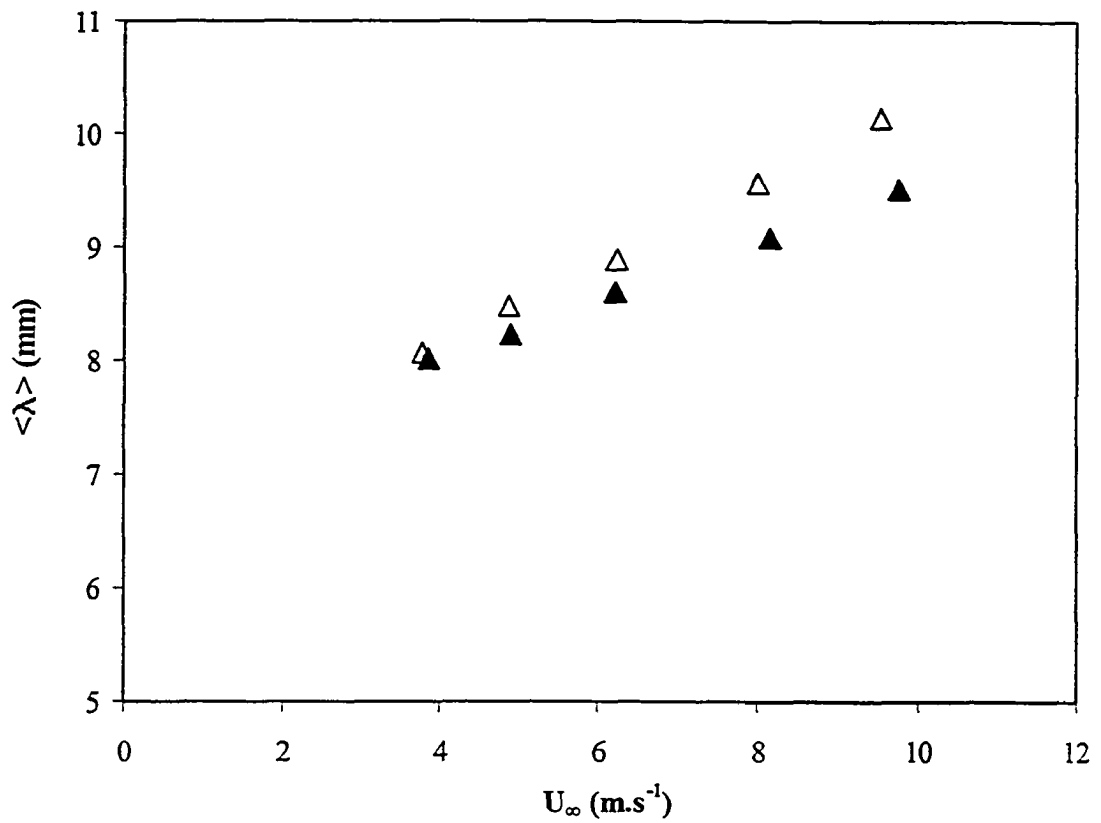


FIGURE 4.9: Plot of the average length scale, $\langle \lambda \rangle$ of the coherent structures as a function of wind speed. The values are averaged over 10 minutes of data. Δ , = Clean water surfaces; \blacktriangle , = surfactant-influenced water surfaces.

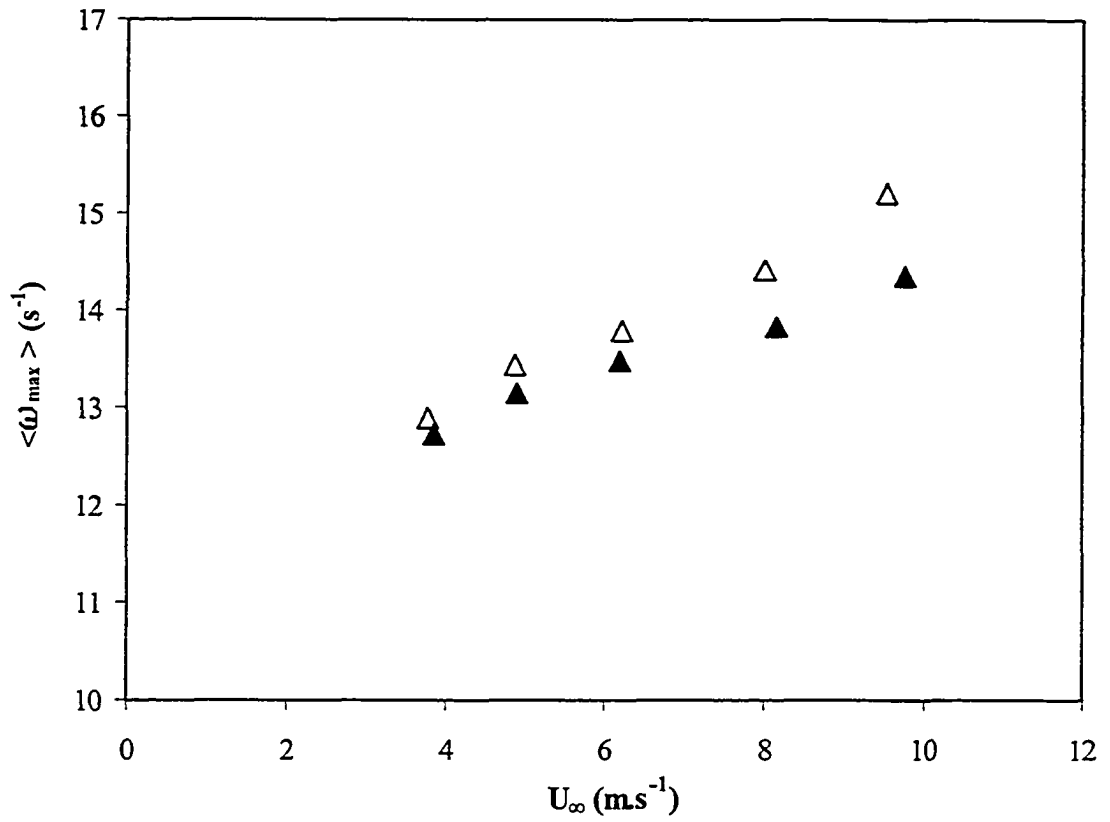


FIGURE 4.10: Plot of the average maximum vorticity, $\langle \omega_{max} \rangle$ of the coherent structures as a function of wind speed. The values are averaged over 10 minutes of data. Δ , = Clean water surfaces; \blacktriangle , = surfactant-influenced water surfaces.

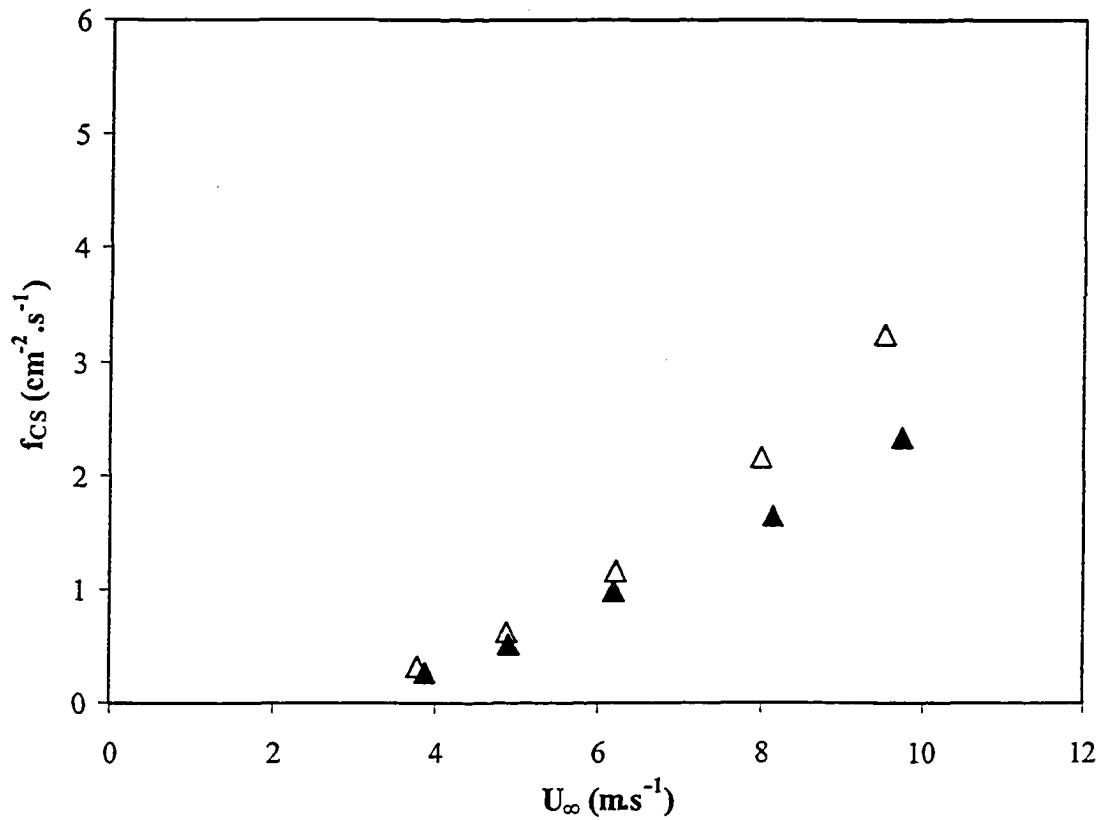


FIGURE 4.11: The frequency of occurrence of coherent structures, f_{CS} , defined as the number of coherent structures identified per second per cm^2 plotted versus wind speed. The values are averaged over 10 minutes of data. Δ , = Clean water surfaces; \blacktriangle , = surfactant-influenced water surfaces.

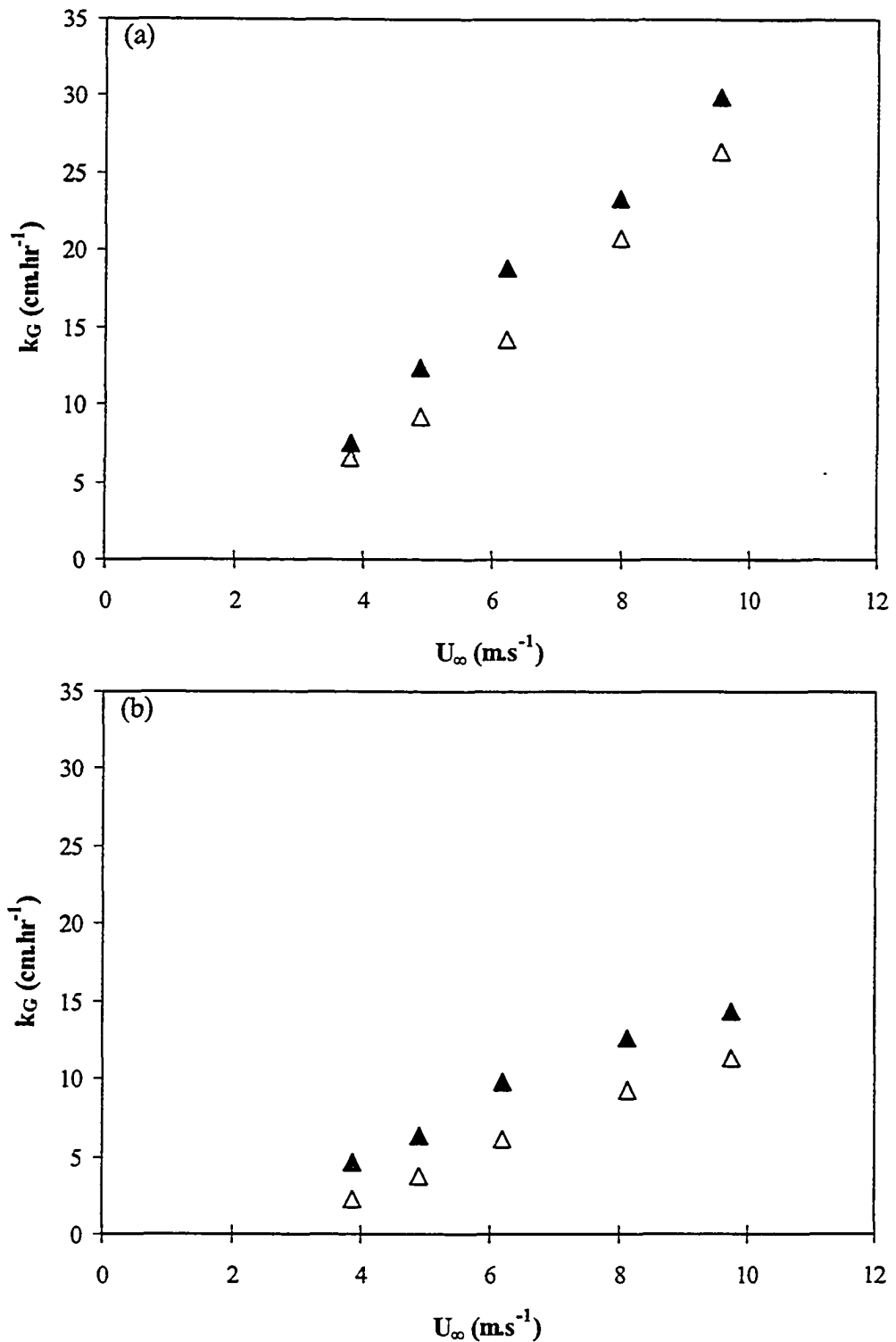


FIGURE 4.12: The total air-water gas transfer velocity, k_G scaled to a Schmidt number of 600, versus wind speed. (a) For clean water surfaces, (b) for surfactant-influenced water surfaces. Δ , = k_G , predicted using surface renewal model; \blacktriangle , = k_G , measured bulk values.

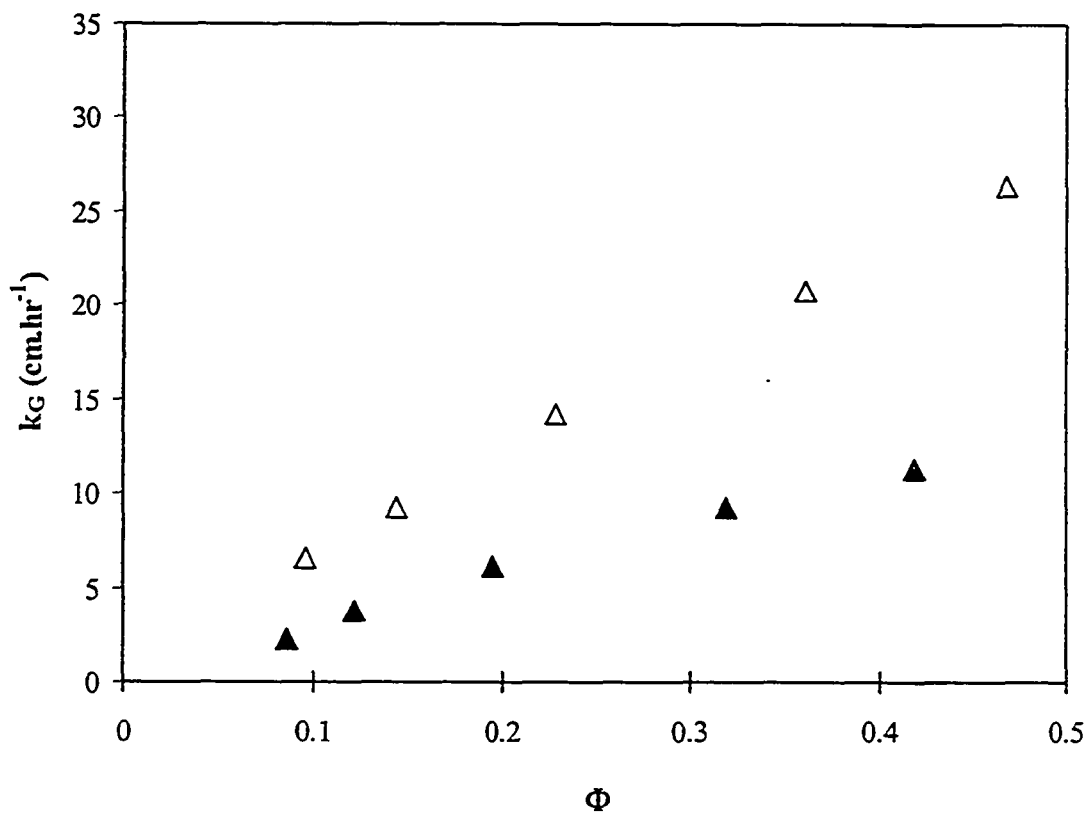


FIGURE 4.13: Measured bulk gas transfer velocity, k_G normalized to a Schmidt number of 600 versus Φ , the fraction of the surface area renewed by eddies. Δ , = Clean water surfaces; \blacktriangle , = surfactant-influenced water surfaces.

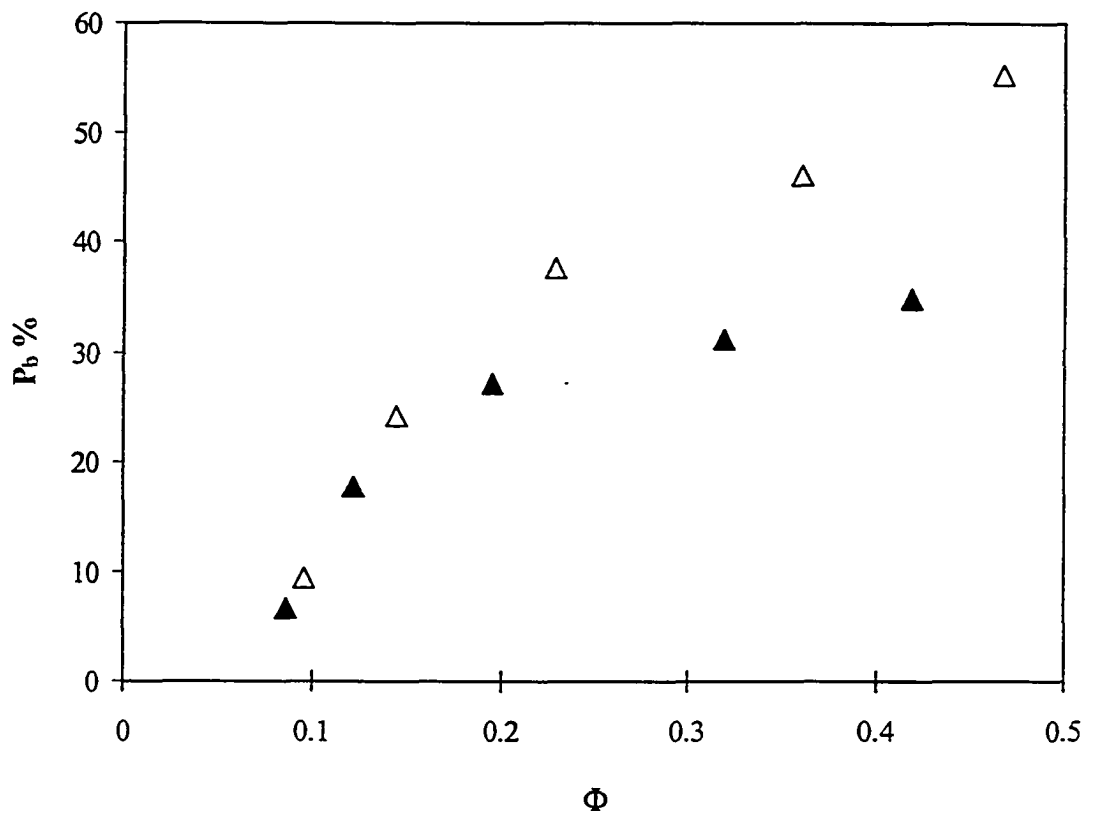


FIGURE 4.14: P_b , the percentage of microscale-breaking waves versus Φ , the fraction of the surface area renewed by eddies. Δ , = Clean water surfaces; \blacktriangle , = surfactant-influenced water surfaces.

Chapter 5

Conclusions and Recommendations

5.1 Summary and Conclusions

Previous laboratory wind wave experiments have demonstrated the importance of microscale wave breaking in controlling the flux of gas, heat and momentum and enhancing the near-surface turbulence. Surface-active materials present naturally in seas and also adventitiously in laboratory wind-wave tanks have a significant effect on free surface behavior and hence on the rate of gas transfer, the propagation characteristics of waves and the near-surface turbulence. This thesis reports on a series of laboratory experiments to investigate the effect of surfactants on the properties of the aqueous boundary layer beneath a wind driven air-water interface, the properties of microscale-breaking waves, the characteristics of coherent structures and the air-water gas transfer rates. The most novel aspect of this study is the comparisons between clean and surfactant-influenced water surfaces. A summary of the most significant conclusions derived from these investigations is presented below.

The presence of a surfactant caused the boundary layer on both sides of the air-water interface to become smoother. The flow in the aqueous boundary layer was found to be in the transition regime at all wind speeds for both water surface conditions. Surfactants reduced the roughness length on average by 20% and increased the friction velocity by 20% in the aqueous boundary layer. The airside shear stress was reduced by an average of 22% and the waterside shear stress increased by an average of 36% in the presence of a surfactant. The fraction of the total momentum transferred to the aqueous

boundary layer decreased from 0.8 to 0.2 for clean water surfaces and from 0.9 to 0.3 for surfactant-influenced water surfaces as the wind speed increased from 3.8 to 9.8 m·s⁻¹. A strong negative correlation was observed between the fraction of the total momentum transferred to the aqueous boundary layer and the mean square wave slope irrespective of the water surface cleanliness.

The ratio of the rate of dissipation of turbulent kinetic energy in surfactant-influenced water, to that in clean water decreased from 1.0 to 0.70 as the wind speed increased from 3.8 to 9.6 m·s⁻¹. Surfactants reduced the depth of the near-surface layer of enhanced turbulence on average by 35%. The thickness of this layer varied from 1.5 to 3.5 cm and from 1.2 to 2.5 cm for clean and surfactant-influenced water surfaces, respectively, as the wind speed increased from 3.8 to 9.6 m·s⁻¹.

Surfactants reduced the percentage of wave breaking by approximately one third. The percentage of breaking waves increased from 9% to 55% and from 7% to 35% for clean and surfactant-influenced water surfaces, respectively as the wind speed increased. The presence of a surfactant altered the geometric properties of both microscale-breaking waves and non-breaking waves. The surfactant reduced the wave amplitude and the maximum wave slope on the forward face of the waves by 25% and 28%, respectively, for breaking waves and 22% and 19%, respectively, for non-breaking waves. The maximum mean square wave slope on the downwind face of breaking waves, and the depth averaged rate of energy dissipation beneath the crests of breaking waves were found to be strongly correlated. A strong correlation was observed between the fraction of the total momentum transferred to the wave field and the percentage of breaking waves irrespective of the water surface cleanliness.

Surfactants did not change the average size and vorticity of the coherent structures significantly. The average nominal size decreased by ~5% and the average maximum vorticity by ~4% in the presence of a surfactant. However, the surfactant increased the size of the most energetic coherent structures by ~16% and reduced the frequency of occurrence of coherent structures by ~20%. The frequency of occurrence of coherent structures increased by a factor of ~10 for both clean and surfactant-influenced water surfaces as the wind speed increased from 3.8 to 9.6 m·s⁻¹.

The surfactant reduced the measured bulk gas transfer velocities by approximately 55% and the gas transfer velocities were found to be strongly correlated with the mean square wave slope irrespective of water surface cleanliness. A surface renewal model was used to predict the gas transfer velocities using the characteristics of the detected coherent structures. The surface renewal model underestimated the values of the gas transfer velocity by approximately 25%. Also, it predicted that approximately 60% of the total gas flux occurred across the surface of the energetic regions at all wind speeds for both water surface conditions. The gas transfer velocity inside the energetic regions was found to be approximately 2.5 times larger than the gas transfer velocity in the quiescent regions for both water surface conditions. The predicted gas transfer velocities were found to be most sensitive to variations in the fraction of the water surface renewed by coherent structures and the frequency of occurrence of coherent structures.

These combined results can be used to draw the following conclusions. These conclusions put a description of the sequence of events that occurs when the wind speed increases over a water surface. As the wind speed increases, the fraction of the total momentum transferred to the aqueous boundary layer decreases while at the same time

the fraction transferred to the wave field increases and consequently both the wave amplitude and slope increase. As the fraction of the total momentum transferred to the wave field increases so does the percentage of microscale-breaking waves. This increase in microscale wave breaking causes a corresponding increase in both the intensity and areal extent of the near-surface turbulence. This explains the observed linear correlation between the gas transfer velocity and the mean square wave slope. That is, it is the increase in the intensity and areal extent of the near-surface turbulence that causes the air-water gas transfer velocity to increase. The results predicted using the surface renewal model and the properties of the coherent structures support this conclusion. When the wind speed increased, the percentage of microscale-breaking waves increased and both the frequency of occurrence of coherent structures and the fraction of the water surface renewed by coherent structures increased dramatically. These dramatic increases were responsible for the increases observed in the gas transfer velocity.

The effect of a surfactant can be summarized quite simply. When a surfactant is present, the water surface is smoother and as a result the fraction of the total momentum transferred to the wave field decreases. Accordingly, there is less microscale wave breaking, less near-surface turbulence and the gas transfer velocity is lower.

5.2 Recommendations for Future Work

This thesis presented results that have significantly improved our understanding of the characteristics of the flow beneath microscale-breaking waves, the behavior of the aqueous boundary layer and the significance of surfactants in air-sea interactions. One of the fundamental issues that remains to be addressed is to investigate the evolution of

longer waves. This would require DPIV and profile measurements with larger fields of view. Having larger fields of view will help also to investigate how far the turbulent wakes produced by longer microscale-breaking wave are extended and what is the relative significance of these long breaking waves compared to the short ones.

Additional study of the pathways of momentum transfer at the air-water interface is also recommended. This thesis focused exclusively on the very young waves that occur at short fetches but future studies should include measurements at longer fetches. Field studies that include open ocean measurements would be particularly valuable. In addition, the strong correlation observed between the fraction of the total momentum transferred to the aqueous boundary layer and the mean square wave slope, could be verified through these experiments.

Another important step would be to carry out experiments similar to the experiments described in this thesis but with significantly higher resolution DPIV and profile measurements. Measurements with higher temporal and spatial resolutions would be advantageous for several reasons. One is that it would allow the behavior of the parasitic capillary waves that appear on the forward faces of microscale breaking waves to be studied. These waves are extremely small and higher spatial resolution measurements would enable their role in generating near-surface turbulence and enhancing air-water gas transfer to be studied. Higher spatial resolution measurements would also be important for studies of the coherent structures. Smaller size coherent structures would be resolved and their significance could then be investigated. Detecting a larger size range of coherent structure would lead to better detection of the most

energetic sizes, which can be used in surface renewal models to predict gas transfer velocities at the air-water interface.

Accurate numerical models of the microscale wave breaking phenomenon would be particularly valuable. This is because laboratory measurements of microscale-breaking waves are so challenging and field measurements have been too daunting a task up to now. Numerical models could be applied with different combinations of scales, theoretical models, and boundary conditions. The results presented in this thesis could be used to validate and calibrate numerical models.

References

- Agrawal, Y. C., Terray, E. A., Donelan, M. A., Hwang, P. A., Williams III, A. J., Drennan, W. M., Kahma, K. K. and Kitaigorodskii S. A. (1992) "Enhanced Dissipation of Kinetic Energy beneath Surface Waves". *Nature*, Vol. 359, pp. 219-220.
- Agüí, J. C. and Jiménez, J. (1987) "On the Performance of Particle Tracking". *Journal of Fluid Mechanics*, Vol. 185, pp. 447-468.
- Asher, W. E. and Pankow, J. F. (1991) "Prediction of Gas/Water Mass Transport Coefficients by a Surface Renewal Model". *Environmental Science Technology*, Vol. 25, pp.1294-1300.
- Asher, W.E., Karle, L.M., Higgins B.J., Farley P.J., Monahan E.C. and Leifer I.S. (1996) "The Influence of Bubble Plumes on Air-Seawater Gas Transfer Velocities". *Journal of Geophysical Research*, Vol. 101, pp. 12027-12041.
- Atmane, M. A., Asher, W. E. and Jessup, A. T. (2004) "On the Use of the Active Infrared Technique to Infer Heat and Gas Transfer Velocities at the Air-Water Free Surface". *Journal of Geophysical Research*, Vol. 109(C8), C08S14, pp.1-15.
- Banner, M. L. and Melville, W. K. (1976) "On the Separation of Air Flow over Water Waves". *Journal of Fluid Mechanics*, Vol. 77, pp. 825-842.
- Banner, M. L. and Peirson W. L. (1998) "Tangential Stresses beneath Wind-Driven Air-Water Interface". *Journal of Fluid Mechanics*, Vol. 364, pp.115-145.
- Banner, M. L. and Peregrine, D. H. (1993) "Wave Breaking in Deep Water". *Annual Review of Fluid Mechanics*, Vol. 25, pp. 373-397.
- Banner, M. L. & Phillips, O. M. (1974) "On the Incipient Breaking of Small Scale Waves". *Journal of Fluid Mechanics*, Vol. 65, pp. 647-656.

- Benilov, A. Y., Kouznetsov O. A. and Panin G. N. (1974) "On The Analysis of Wind-Induced Disturbances in the Atmospheric Turbulent Surface Layer". *Boundary Layer Meteorology*, Vol. 6, pp. 269-285.
- Bock, E.J., Hara, T., Frew, N.M. and McGillis, W.R. (1999) "Relationship Between Air-Sea Gas Transfer and Short Wind Waves". *Journal of Geophysical Research*, Vol. 104, pp. 25821-25831.
- Bonnet, J. P., Delville, J., Glauser, M. N., Antonia, R. A., Bisset, D. K., Cole, D. R., Fiedler, H. E., Garem, J. H., Hilberg, D., Jeong, J., Kevlahan, N. K. R., Ukeiley, L. S. and Vincendeau, E. (1998) "Collaborative Testing of Eddy Structure Identification Methods in Free Turbulent Shear Flows". *Experiments in Fluids*, Vol. 25, pp. 197-225.
- Bourassa, M.A. (2000) "Shear Stress Model for the Aqueous Boundary Layer Near the Air-Sea Interface". *Journal of Geophysical Research*, Vol. 105(C1), pp. 1167-1176.
- Brocchini, M. and Peregrine, D.H. (2001a) "The Dynamics of Strong Turbulence at Free Surfaces. Part 1: Description". *Journal of Fluid Mechanics*, Vol. 449, pp. 225-254.
- Brocchini, M. and Peregrine, D.H. (2001b) "The Dynamics of Strong Turbulence at Free Surfaces. Part 2: Free Surface Boundary Conditions". *Journal of Fluid Mechanics*, Vol. 449, pp. 255-290.
- Bye, J. A. T. (1988) "The Coupling of Wave Drift and Wind Velocity Profiles". *Journal of Marine Research*, Vol. 46, pp. 457-472.
- Bye, J. A. T. (1967) "The Wave-Drift Current". *Journal of Marine Research*, Vol. 25, pp. 95-102.
- Camussi, R. (2002) "Coherent Structure Identification From Wavelet Analysis of Particle Image Velocimetry Data". *Experiments in Fluids*, Vol. 32, pp. 76-86.

- Cane, M. A., Clement, A. C., Kaplan, A., Kushnir, Y., Pozdnyakov, D., Seager, R., Zebiak, S. E. and Murtugudde, R. (1997) "Twentieth-Century Sea Surface Temperature Trends". *Science*, Vol. 275, pp. 957–960.
- Ceniceros, H. D. (2003) "The Effects of Surfactants on the Formation and Evolution of Capillary Waves". *Physics of Fluids*, Vol. 13(1), pp. 245-256.
- Charnock, H. (1955) "Wind Stress on a Water Surface". *Quarterly Journal of the Royal Meteorological Society*, Vol. 81, pp. 639–640.
- Chen, G., Kharif, C., Zaleski, S. and Li, J. (1999) "Two Dimensional Navier Stokes Simulation of Breaking Waves". *Physics of Fluids*, Vol. 11 (1), pp. 121-131.
- Cheng, Z., and Mitsuyasu, H. (1992) "Laboratory Studies on the Surface Drift Current Induced by Wind and Swell". *Journal of Fluid Mechanics*, Vol. 243, pp. 247-259.
- Cheung, T. K. and Street, R. L. (1988) "The Turbulent Layer in the Water at an Air-Water Interface". *Journal of Fluid Mechanics*, Vol. 194, pp. 133-151.
- Chu, C. R. and Jirka, G. H. (1995) "Reaeration in Combined Wind Stream Driven Flows". *Air-Water Gas Transfer*, Edited by Jähne, B. and Monahan, E. C., AEON Verlag & studio, Hanau, Germany, pp. 79-88.
- Coantic, M. (1986) "A Model of Gas Transfer Across Air Water Interfaces With Capillary Waves". *Journal of Geophysical Research*, Vol. 91(C3), pp. 3925-3943.
- Cowen, E. A. and Monismith, S. G. (1997) "A Hybrid Digital Particle Tracking Velocimetry Technique". *Experiments in Fluids*, Vol. 22, pp. 199-211.
- Craig, P.D. (1996) "Velocity Profiles and Surface Roughness Under Breaking Waves". *Journal of Geophysical Research*, Vol. 101, 1265-1277.
- Craig, P.D. and Banner, M.L. (1994) "Modeling Wave-Enhanced Turbulence in the Ocean Surface Layer". *Journal of Physical Oceanography*, Vol. 24, pp. 2546-2559.

- Csanady, G.T. (1990) "The Role of Breaking Wavelets in Air-Sea Gas Transfer". *Journal of Geophysical Research*, Vol. 95, pp. 749-759.
- Csanady, G. T. (2001) *Air-Sea Interaction, Laws and Mechanisms*. Cambridge University Press.
- Dabiri, D. and Gharib, M. (1997) "Experimental Investigation of the Vorticity Generation Within a Spilling Water Wave". *Journal of Fluid Mechanics*, Vol. 330, pp. 113-139.
- Danckwerts, P. V. (1970) *Gas-Liquid Reactions*. McGraw-Hill.
- Deacon, E. L. (1977) "Gas Transfer to and Across an Air-Water Interface". *Tellus*, Vol. 29, pp. 363-374.
- Donelan, M.A. (1990) "Air-Sea Interaction. The Sea": *Ocean Engineering Science*, Vol. 9, Edited by Leméhauté, B. and Hanes, D., John Wiley and Sons, Inc., New York, pp. 239-292.
- Doron, P., Bertuccioli, L., Katz, J. and Osborn T. R. (2001) "Turbulence Characteristics and Dissipation Estimates in the Coastal Ocean Bottom Boundary Layer From PIV Data". *Journal of Physical Oceanography*, Vol. 31, pp. 2108-2134.
- Drennan, W.M., Donelan, M. A., Terray E.A. and Katsaros, K. B. (1996) "Oceanic Turbulence Dissipation Measurements in Swade". *Journal of Physical Oceanography*, Vol. 26, pp. 808-815.
- Elkamash, M.K. and Loewen, M.R. (2004) "Air-Sea Gas Transfer and Turbulence for Clean and Surfactant Contaminated Surfaces", *Proceedings of the 1st Water and environment Specialty Conference, 32nd Annual Conference*, Canadian Society for Civil Engineering, Saskatoon, Saskatchewan, Canada, 10 pages CD-Rom.
- Fincham, A. and Delerce, G. (2000) "Advanced Optimization of Correlation Imaging Velocity Algorithms". *Experiments in Fluids*, Supplement, pp. S13-S22.

- Fincham, A. and Spedding, G. R. (1997) "Low Cost, High Resolution DPIV for Measurement of Turbulent Fluid Flow". *Experiments in Fluids*, Vol. 23, pp. 449-462.
- Fortescue, G. E. and Pearson, J. R. A. (1967) "On Gas Absorption into a Turbulent Fluid". *Chemical Engineering Science*, Vol. 22, pp. 1163-1176.
- Frew, N. M., Bock, E. J., McGillis, W. R., Karachintsev, A. V., Hara, T., Münsterer, T. and Jähne, B. (1995), "Variation of Air-Water Gas Transfer with Wind Stress and Surface Viscoelasticity". *Air-Water Gas Transfer*, Edited by Jähne, B. and Monahan, E. C., AEON Verlag & studio, Hanau, Germany, pp. 529-541.
- Frew, N. M., Bock, E. J., Schimpf, U., Hara, T., Haußecker, H., Edson, J. B., McGillis, W. R., Nelson, R. K., McKenna, S. P., Uz, B. M. and Jähne, B. (2004) "Air-Sea Gas Transfer: Its Dependence on Wind Stress, Small-Scale Roughness, and Surface Films". *Journal of Geophysical Research*, Vol. 109, C08S17, pp. 1-23.
- Higbie, R. (1935) "The Rate of Absorption of a Pure Gas into a Still Liquid During Short Periods of Exposure". *AICHE Journal*, Vol. 31, pp. 365-389.
- Hinze, J. O. (1975) *Turbulence*. McGraw Hill.
- Holthuijsen, L. H. and Herbers, T. H. C. (1986) "Statistics of Breaking Waves Observed as Whitecaps and the Open Sea". *Journal of Physical Oceanography*, Vol. 16, pp. 290-297.
- Hsu, C.T., Wu, H.Y., Hsu, E.Y. and Street, R. L. (1982) "Momentum and Energy Transfer in Wind Generation of Waves". *Journal of Physical Oceanography*, Vol. 12, pp. 929-951.
- Hsu, C.T., Hsu, E. Y. and Street, R. L. (1981) "On the Structure of Turbulent Flow Over a Progressive Water Wave: Theory and Experiment in a Transformed, Wave-Following Coordinate System". *Journal of Fluid Mechanics*, Vol. 105, pp. 87-117.

- Hussain, A. K. M. (1986) "Coherent Structures and Turbulence". *Journal of Fluid Mechanics*, Vol. 173, pp. 303-355.
- Hussain, A. K. M. F. and Hayakawa, M. (1987) "Eduction of Large-Scale Organized Structures in a Turbulent Plane Wake". *Journal of Fluid Mechanics*, Vol. 180, pp. 193-229.
- Jähne, B. and Haußecker, H. (1998) "Air Water Gas Exchange". *Annual Review of Fluid Mechanics*, Vol. 30, pp. 443-468.
- Jähne, B., Munnich, K. O., Bosinger, R., Dutzi, A., Huber, W. and Libner, P. (1987) "On the Parameters Influencing Air-Water Gas Exchange". *Journal of Geophysical Research*, Vol. 92, pp. 1937-1949.
- Jessup, A. T., Zappa, C. J. and Yeh, H. (1997) "Defining and Quantifying Microscale Wave Breaking with Infrared Imagery". *Journal of Geophysical Research*, Vol. 102, pp. 23145-23153.
- Kawamura, H. and Toba, Y. (1988) "Ordered Motion in the Turbulent Boundary Layer Over Wind Waves". *Journal of Fluid Mechanics*, Vol. 197, pp. 105-138.
- Komori, S., Nagaosa, R. and Murakami, Y. (1993) "Turbulence Structure and Mass Transfer across a Sheared Air-Water Interface in Wind-Driven Turbulence". *Journal of Fluid Mechanics*, Vol. 249, pp. 161-183.
- Kundu, P. K. and Cohen, I. M. (2002) *Fluid Mechanics*, Academic Press.
- Lamont, J. C. and Scott, D. S. (1970) "An Eddy Cell Model of Mass Transfer into the Surface of a Turbulent Liquid". *AICHE Journal*, Vol. 16, pp.512-519.
- Lang, A.W., and Gharib, M. (2000) "Experimental Study of the Wake Behind a Surface Piercing Cylinder for a Clean and Contaminated Free Surface". *Journal of Fluid Mechanics*, Vol. 402, pp.109-136.

- Liss, P. S. (1973) "Processes of Gas Exchange across an Air-Water Interface". *Deep Sea Research*, Vol. 20, pp. 221-238.
- Loewen M. R. and Siddiqui M. H, (2005) "Detecting Microscale Breaking Waves". *Submitted to the Journal of Measurement Science and Technology*.
- Longuet-Higgins, M. S. (1992) "Capillary Rollers and Bores". *Journal of Fluid Mechanics*, Vol. 240, pp.659-679.
- Lugt, H. J. (1983) *Vortex Flow in Nature and Technology*, 1st Edition. New York: John Wiley & Sons.
- Mass, J. T., Milgram, J. H. (1998) "Dynamic Behavior of Natural Sea Surfactant Films". *Journal of Geophysical Research*, Vol. 103, pp. 15695-15715.
- Melville, W. K. (1996) "The Role of Surface-Wave Breaking in Air-Sea Interaction". *Annual Review of Fluid Mechanics*, Vol. 28, pp. 279-321.
- Melville, W. K., Veron, F. and White C. J. (2002) "The Velocity Field under Breaking Waves: Coherent Structures and Turbulence". *Journal of Fluid Mechanics*, Vol. 54, pp. 203-233.
- Miles, J. W. (1965) "A Note on The Interaction Between Surface Waves and Wind Profiles". *Journal of Fluid Mechanics*, Vol. 22, pp. 823-827.
- Mitsuyasu, H. (1985) "A Note on The Momentum Transfer from Wind to Waves". *Journal of Geophysical Research*, Vol. 90(C2), pp. 3343-3345.
- Okuda, K. 1982 "Internal Flow Structures of Short Wind Waves, I, On the Internal Vorticity Structures". *Journal of the Oceanographical Society of Japan*, Vol. 38, pp. 28-42.

- Pemberton, R. J., Turnock, S. R., Dodd, T. J. and Rogers, E. (2002) "A Novel Method for Identifying Vortical Structures". *Journal of Fluids and Structures*, Vol. 16(8), pp. 1051-1057.
- Peirson, W. L. (1997) "Measurements of Surface Velocities and Shear at a Wavy Air-Water Interface Using Particle Image Velocimetry". *Experiments in Fluids*, Vol. 23, pp. 427-437.
- Peirson, W. L. and Banner, M. L. (2003) "Aqueous Surface Layer Flows Induced by Microscale Breaking Wind Waves". *Journal of Fluid Mechanics*, Vol. 479, pp. 1-38.
- Rapp, R. J. and Melville, W. K. (1990) "Laboratory Measurements of Deep-Water Breaking Waves". *Philosophical Transactions of the Royal Society of London, Series A*, Vol. 331, pp. 735-800.
- Saylor, J. R., Szeri, A. J., Foulks, G. P. (2000) "Measurement of Surfactant Properties Using a Circular Capillary Wave Field". *Experiments in Fluids*, Vol. 29, pp. 509-518.
- Schlichting, H. T. and Gersten, K. (2000) *Boundary Layer Theory*, McGraw-Hill.
- Schwarzenbach, R. P., Gschwend, P. M. and Imboden, D. M. (1993) *Environmental Organic Chemistry*, John Wiley & Sons, Inc.
- Siddiqui, M. H. K. (2002) "Laboratory Measurements of the Flow beneath Microscale Breaking Waves". *Ph.D. Thesis*, Department Of Mechanical and Industrial Engineering, University of Toronto.
- Siddiqui M. H, and Loewen M. R. (2005) "Characteristics of the Wind Drift Layer and Microscale Breaking Waves". *Submitted to the Journal of Fluid Mechanics*.
- Siddiqui, M. K., Loewen, M. R., Asher, W. E. and Jessup, A. T. (2004) "Coherent Structures beneath Wind Waves and Their Influence on Air-Water Gas Transfer". *Journal of Geophysical Research*, Vol. 109(C3), C03024, pp. 1-14.

- Siddiqui, M. H. K., Loewen, M. R., Richardson, C., Asher, W. E. and Jessup, A. T. (2001) "Simultaneous Particle Image Velocimetry and Infrared Imagery of Microscale Breaking Waves". *Physics of Fluids*, Vol. 13, pp. 1891-1903.
- Snyder, R. L., Dobson, F. W., Elliot, J. A. and Long, R. B. (1981) "Array Measurements of Atmospheric Pressure Fluctuations above Gravity Waves". *Journal of Fluid Mechanics*, Vol. 102, pp.1-59.
- Soloviev, A. V., Vershinsky, N. V. and Bezverchinii, V. A. (1988) "Small-Scale Turbulence Measurements in the Thin Surface Layer of the Ocean". *Deep Sea Research*, Vol. 35, pp. 1859-1874.
- Teixeira, M. A. C., and Belcher, S.E. (2000) "Dissipation of Shear-Free Turbulence near Boundaries". *Journal of Fluid Mechanics*, Vol. 422, pp. 167-191.
- Tennekes, H. and Lumley, J. L. (1972) *A First Course in Turbulence*, MIT Press.
- Terray, E. A., Donelan, M. A., Agrawal, Y. C., Drennan, W. M., Kahama, K. K., Williams III, A. J., Hwang, P. A. and Kitaigorodskii, S. A. (1996) "Estimates of Kinetic Energy Dissipation under Breaking Waves". *Journal of Physical Oceanography*, Vol. 26, pp. 792-807.
- Thais, L. and Magnaudet, J. (1996) "Turbulent Structure beneath Surface Gravity Waves Sheared by the Wind". *Journal of Fluid Mechanics*, Vol. 328, pp. 313-344.
- Uz, B. M., Donelan, M. A., Hara, T. and Bock, E. J. (2002) "Laboratory Studies of the Effect of Short Wind Waves on Wind Stress". *Boundary Layer Meteorology*, Vol. 102, pp. 301-331.
- Veron, F. and Melville, W. K. (1999) "Pulse-to-Pulse Coherent Doppler Measurements of Waves and Turbulence". *Journal of Atmospheric and Oceanic Technology*, Vol. 16, pp. 1580-1597.

- Veron, F. and Melville, W. K. (2001) "Experiments on the Stability and Transition of Wind-Driven Water Surfaces". *Journal of Fluid Mechanics*, Vol. 446, pp. 25-65.
- Wu, J. (1968) "Laboratory Studies of Wind-Wave Interaction". *Journal of Fluid Mechanics*, Vol. 34, pp. 91-112.
- Wu, J. (1975) "Wind-Induced Drift Currents". *Journal of Fluid Mechanics*, Vol. 68, pp. 49-70.
- Yeh, H. H. (1995) "Free Surface Dynamics". *Advances in Coastal and Ocean Engineering*, Editor Liu, P. L., World Scientific, pp. 1-74.
- Zappa, C. J. (1999) "Microscale Wave Breaking and Its Effect on Air-Water Gas Transfer Using Infrared Imagery". *Ph.D. Thesis*, Applied Physics Laboratory, University Of Washington, Seattle.
- Zappa, C. J., Asher, W. E. and Jessup, A. T. (2001) "Microscale Wave Breaking and Air-Water Gas Transfer". *Journal of Geophysical Research*, Vol. 106, pp. 9385-9391.
- Zappa, C. J., Asher, W. E., Jessup, A. T., Klinke, J. K. and Long, S. R. (2004) "Microbreaking and the Enhancement of Air-Water Gas Transfer Velocities". *Journal of Geophysical Research*, Vol. 109(C8), C08S16, pp. 1-18.
- Zhang, X. and Harrison, S. (2004) "A Laboratory Observation of the Surface Temperature and Velocity Distributions on a Wavy and Windy Air-Water Interface". *Physics of Fluids*, Vol. 16(1), pp. L5-L8.

Appendix A

Error Analysis

A.1. Errors in the DPIV measurements

Cowen and Monismith (1997) reported that the total error in the DPIV measurements is the sum of the errors due to particle diameter, dynamic range, particle density, out of plane motion, gradient, dynamic range, peak locking and AGW interpolation. We used the results of Cowen and Monismith (1997) to estimate the error in our PIV data since they used a similar cross correlation algorithm and the same AGW interpolator in their analysis. We found that the velocity gradients are the largest in the top 1 cm layer at the highest wind speed of $9.6 \text{ m}\cdot\text{s}^{-1}$, so we expected the largest error to occur there. The procedure to estimate the error in the DPIV measurements is described below.

Table A.1 presents the mean and the standard deviation of the displacement in the streamwise and vertical directions obtained from the raw DPIV data without correction or interpolation. The mean and the standard deviation of the largest velocity gradients in the streamwise and vertical directions are also tabulated in table A.1. The errors due to velocity gradients were estimated by summing of the mean and the standard deviation of the velocity gradients (i.e. this gives an error estimate calculated using a gradient that is one standard deviation greater than the mean). Figure 5(e) in Cowen and Monismith (1997) was used to estimate the errors due to velocity gradients. The total error is the sum of the mean and root mean square (RMS) errors. The gradients in the streamwise

and vertical directions are approximately 7% and 4%, respectively. Hence the errors due to velocity gradients are,

$$\varepsilon_{u/l} = 0.24 \text{ pixels (corresponds to 7\% gradients)} \quad [\text{A.1}]$$

$$\varepsilon_{w/l} = 0.12 \text{ pixels (corresponds to 4\% gradients)} \quad [\text{A.2}]$$

where, $\varepsilon_{u/l}$ and $\varepsilon_{w/l}$ are the errors associated with the streamwise and vertical velocities, respectively. These estimated errors due to velocity gradients account for all the errors associated with variations in particle diameter, dynamic range, particle density, out of plane motion, gradient and dynamic range (Cowen and Monismith 1997).

The errors due to the AGW interpolation and peak locking were estimated from Figure 5(f) in Cowen and Monismith (1997) and were found to be 0.08 pixels for both the streamwise and vertical directions. Therefore, the total errors in the DPIV measurements were,

$$\varepsilon_u = \sqrt{(0.24)^2 + (0.08)^2} = 0.253 \text{ pixels} \quad [\text{A.3}]$$

$$\varepsilon_w = \sqrt{(0.12)^2 + (0.08)^2} = 0.144 \text{ pixels} \quad [\text{A.4}]$$

Thus, the resultant error, ε_r due to both u and w will be:

$$\varepsilon_r = \sqrt{\varepsilon_u^2 + \varepsilon_w^2} = 0.291 \text{ pixels} \quad [\text{A.5}]$$

The resultant velocity R is:

$$R = \sqrt{(\bar{u} + \sigma_u)^2 + (\bar{w} + \sigma_w)^2} = 11.64 \text{ pixels} \quad [\text{A.6}]$$

Therefore, the percentage of error in the DPIV velocity estimates is:

$$\% \text{ error} = 0.38/11.64 = 2.5\% \quad [\text{A.7}]$$

The errors in the vorticity would be twice the errors in the velocity, so the percentage error in the vorticity computation is approximately 5.0%. It is noteworthy that at lower wind speeds and further below the water surface the gradients are smaller and hence the errors will be smaller. So this estimated error is the maximum error associated with the DPIV velocity measurements in this study.

A.2. Errors in Wave Properties.

A.2.1 Errors in Significant Wave Height (H_s)

The maximum error in the wave height was calculated at the highest wind speed of $9.6 \text{ m}\cdot\text{s}^{-1}$. The mean significant wave height, H_s , was 1.2 cm and the standard deviation was 0.08 cm. The standard error of the mean is defined as the standard deviation divided by the square root of the number of sample points. The number of samples used to obtain the mean and the standard deviation of the significant wave height was 740. So the relative standard error of the mean is,

$$\varepsilon_{HS} = \frac{\sigma_{HS}}{H_{sm} \sqrt{N_s}} = 0.25 \% \quad [\text{A.8}]$$

where, ε_{HS} is the normalized error in the significant wave height, H_{sm} is the mean value of the significant wave height, σ_{HS} is the standard deviation of the significant wave height and N_s is the number of samples.

A.2.2 Errors in Lagrangian surface drift velocity (U_{SL})

The maximum random error in the Lagrangian surface drift velocity wave height was calculated for the highest wind speed of $9.6 \text{ m}\cdot\text{s}^{-1}$. The Lagrangian surface drift

velocity, U_{SL} was $25.48 \text{ cm}\cdot\text{s}^{-1}$, the standard deviation was $10.5 \text{ cm}\cdot\text{s}^{-1}$ and the number of samples was 300. So the normalized standard error of the mean was found to be 2.5%, which is the random error. The bias error was found to be on average 10%, which resulted from using different averaging times when tracking the heated patch. Hence, the total error in the Lagrangian surface drift velocity was estimated to be,

$$\varepsilon_{U_S} = \sqrt{(2.5)^2 + (10)^2} = 10.37\% \quad [\text{A.9}]$$

where, ε_{U_S} is the normalized error in the Lagrangian surface drift velocity.

A.2.3 Errors in the Airside Friction Velocity (u_{*a})

Vertical velocity profiles of the mean horizontal wind followed a semi-logarithmic velocity distributions expressed as (as discussed in chapter 2),

$$U(z) = \frac{u_{*a}}{\kappa} \ln\left(\frac{z}{z_{oa}}\right) \quad [\text{A.10}]$$

where $U(z)$ is the mean wind velocity, u_{*a} is the airside friction velocity, κ is the Von Karman constant ($\kappa = 0.4$), z is the vertical height above the interface (positive upwards) and z_{oa} is the airside roughness length. The airside friction velocity, u_{*a} and the roughness length, z_{oa} were obtained by performing a linear regression between $U(z)$ and $\ln(z)$. Hence equation [A.10] can be written as

$$U(z) = \frac{u_{*a}}{\kappa} \ln(z) - \frac{u_{*a}}{\kappa} \ln(z_{oa}) \quad [\text{A.11}]$$

Equation [A.11] is a linear equation of the form of $Y = aX + b$, where $Y = U(z)$, $a = \frac{u_{*a}}{\kappa}$,

$X = \ln(z)$ and $b = -\frac{u_{*a}}{\kappa} \ln(z_{oa})$. Fitting a regression line to equation [A.11] using the

least squares method will give the value of the slope a and the intercept b . The 95% confidence limits for a and b were estimated and resulted in a maximum relative error in a and b of 2.6% and 1.5%, respectively. Hence the maximum relative error in the airside friction velocity, u_{*a} is 2.6 % using the least square method.

Also, vertical velocity profiles of the mean horizontal wind were sampled repeatedly four times at a wind speed of $11 \text{ m}\cdot\text{s}^{-1}$. The airside friction velocity, u_{*a} was calculated for each repeat and then the mean and the standard deviation values were calculated and gave a normalized error of 5.3%.

A.2.4 Errors in the Airside roughness length (z_{oa})

Based on an error of 5.3 % in u_{*a} and maximum relative error in b of 1.5% (as discussed above), equation [A.11] was used to estimate the relative error in z_{oa} and it was found to be $\pm 13\%$.

A.2.5 Errors in the Waterside Friction Velocity (u_{*w})

The mean stream wise velocity profile can typically be expressed as a velocity defect law (as discussed in chapter 2),

$$\frac{U_s - \bar{u}(\zeta)}{u_{*w}} = \frac{1}{k} \ln\left(\frac{\zeta}{z_{ow}}\right) + C_r \quad [\text{A.12}]$$

To perform a least square method to equation [A.12] it will be written in the form of,

$$\bar{u}(\zeta) = -\frac{u_{*w}}{k} \ln(\zeta) + \frac{u_{*w}}{k} \ln(z_{ow}) - C_r + U_s \quad [\text{A.13}]$$

Similarly, equation [A.13] is a linear equation of the form of $Y = aX + b$, where $Y = \bar{u}(\zeta)$, $a = -\frac{u_{*w}}{k}$, $X = \ln(\zeta)$, and $b = \frac{u_{*w}}{k} \ln(z_{ow}) - C_r + U_s$. The values of the slope a

and the intercept b were obtained by fitting a regression line to equation [A.13] using the least squares method. The 95% confidence limits for a and b were estimated and resulted in a maximum relative error in a and b of 0.5% and 0.37%, respectively. So, the maximum relative error in the waterside friction velocity, u_{*w} is 0.5% using the least squares method.

It is noteworthy that the least square method described above were applied to the mean velocity profile that came from averaging 10 minutes of instantaneous velocity data. Values of u_{*w} were also calculated using 10 mean velocity profiles that came from averaging 1 minute of instantaneous velocity data at different wind speeds. The relative error varies between $\pm 2\%$ and $\pm 20\%$ at the different wind speeds. The standard deviation was found to be 7% at a wind speed of $6.2 \text{ m}\cdot\text{s}^{-1}$ and 10% at a wind speed of $9.6 \text{ m}\cdot\text{s}^{-1}$. Hence the maximum error in the waterside friction velocity, u_{*w} is 10% and the standard error of the mean is 3.2%.

As described in chapter 2, the mean velocity data were fitted to equation [A.12] for non-dimensional depths $\zeta^+ > 100$ to obtain accurate estimates of u_{*w} in the logarithmic layer. The average value of the correlation coefficient for the least squares fit to equation [A.12] was 0.99 and the minimum number of velocity data points within the logarithmic layer (i.e. $\zeta^+ > 100$) was 22. The slope was observed to be smaller when the least squares fit to equation [A.12] applied to $\zeta^+ < 100$. This indicated that a buffer layer or a roughness sublayer existed at smaller values of ζ^+ . To validate the analysis used to estimate u_{*w} in the logarithmic layer, values of u_{*w} were also estimated from the viscous shear stress just below the interface. The comparison between u_{*w} values showed a percentage difference less than 10% at all wind speeds. This close agreement provides

convincing evidence that fitting equation [A.12] in the logarithmic layer as described above produced accurate estimates of u_{*w} .

A.2.6 Errors in the Waterside roughness length (z_{ow})

The relative error in z_{ow} was calculated using equation [A.13] using the maximum relative error in b of 0.37%, (as discussed above), a relative error in U_s of 10.37% and a relative error in u_{*w} of 10%. The relative error in z_{ow} was found to be 50%. The main reason for this rather large error is that z_{ow} is very sensitive to any variations or errors in U_s (as discussed in chapter 2).

\bar{u}	σ_u	\bar{w}	σ_w	$\overline{\frac{\partial u}{\partial z}}$	$\left[\frac{\partial u}{\partial z}\right]_\sigma$	$\overline{\frac{\partial w}{\partial x}}$	$\left[\frac{\partial w}{\partial x}\right]_\sigma$
5.8	4.9	0.022	4.55	0.0162	0.056	0.0016	0.04

Table A.1: The values of \bar{u} , mean streamwise displacement; σ_u , the standard deviation of the streamwise displacement; \bar{w} , mean vertical displacement; σ_w , the standard deviation of the vertical displacement; $\overline{\frac{\partial u}{\partial z}}$, mean streamwise velocity gradient; $\left[\frac{\partial u}{\partial z}\right]_\sigma$, standard deviation of the streamwise velocity gradient; $\overline{\frac{\partial w}{\partial x}}$, mean vertical velocity gradient; $\left[\frac{\partial w}{\partial x}\right]_\sigma$, standard deviation of the vertical velocity gradient, computed within the top 1 cm layer of water at a wind speed of $9.6 \text{ m}\cdot\text{s}^{-1}$, all values are in pixels.

Appendix B

This appendix contains equations and tables that were not considered necessary for the main body of the thesis but included for completeness.

B.1. Parseval's Theorem

As shown in Chapter 2, the one-dimensional wave number spectrum defined as

$$\Phi(k,t) = \frac{1}{2\pi} \int_{-\infty}^{+\infty} R(r,t) e^{-ikr} dr \quad [\text{B.1}]$$

where, $R(r,t)$ is the longitudinal spatial correlation given by

$$R(r,t) = \overline{u_1(x_1,t)u_1(x_1+r,t)} \quad \text{B.2}$$

where, $u_1(x_1,t)$ is the instantaneous stream wise component of the velocity and the over bar denotes spatial averaging. The wave number spectrum defined by equation [B.1] is normalized such that Parseval's theorem is satisfied:

$$\int_0^{\infty} \Phi(k,t) dk = \overline{u_1(x_1,t)^2}. \quad [\text{B.3}]$$

where $\overline{u_1(x_1,t)^2}$ is the variance of the instantaneous stream wise component of the velocity.

B.2. Wind Sensor Calibration Equation

Wind speeds were measured during every run at a sample rate of 100 Hz using an A/D board. A wind sensor (OMEGA FMA-905-V) with an output voltage range 0-5 Volts was used to measure the wind velocity profile above the interface. The output

voltage values were converted to wind speed values according to the sensor's calibration equation, which is:

$$U_{\infty} = 5.07 * V \quad [\text{B.4}]$$

Where, U_{∞} is the wind speed in ($\text{m}\cdot\text{s}^{-1}$) and V is the voltage in volts.

B.3. Tables of Experimental Parameters

The following tables list the experimental parameters for the runs carried out for this study. Table B.1 lists the following parameters: the run name, the water surface condition, the rotary speed of the centrifugal fan that is installed on the upstream end of the tank to produce wind, the wind speed, the relative humidity, the bulk air temperature, the bulk water temperature, dt the separation time between PIV image pairs in milliseconds, and the CO_2 laser pulse rate. Table B.2 shows the directory name and the type of image files in each directory for each hard disk; PIV image files are for the DPIV images of the flow field; collocation image files are for the collocation unit described in Chapter 2 to scale the PIV images and to collocate field of view in the PIV, profile and IR images; and the still water images are for the images of the water surface before the wind blowing to orient the surface wave profile in both the PIV and profile images. Table 3.3 shows the same data shown in table 3.2 but for the profile and IR images.

Run Name	Surface Condition	Fan Speed RPM	Wind Speed m.s ⁻¹	Relative Humidity %	T _{air} °C	T _{water} °C	dt ms	CO ₂ Rate sec
C1	Clean	1600	9.47	58.21	24.15	23.80	6	0.5
C2	Clean	1000	6.23	61.21	22.84	22.63	13	1
C3	Clean	600	3.88	59.92	21.85	21.60	20	2
C4	Clean	1300	7.99	50.25	24.50	22.65	8	1
C5	Clean	800	4.89	47.18	24.04	24.53	15	1
C6	Clean	600	3.79	56.21	23.28	23.46	20	2
C7	Clean	1300	8.05	46.30	26.47	25.26	8	1
C8	Clean	1600	9.53	40.90	27.97	26.14	9	0.5

Run Name	Surface Condition	Fan Speed RPM	Wind Speed m.s ⁻¹	Relative Humidity %	T _{air} °C	T _{water} °C	dt ms	CO ₂ Rate sec
D1	Surfactant	1600	9.75	48.56	26.58	24.01	6	1
D2	Surfactant	800	4.91	52.92	24.95	26.50	15	1
D3	Surfactant	1300	8.15	50.61	26.15	26.23	8	1
D4	Surfactant	600	3.87	59.24	23.50	24.49	20	2
D5	Surfactant	1000	6.27	56.30	26.32	25.11	13	1
D6	Surfactant	1600	9.66	51.93	28.01	26.01	6	1
D7	Surfactant	1300	8.15	55.62	25.95	24.47	8	1
D8	Surfactant	1000	6.21	52.52	27.13	26.85	13	1

Table B.1: Experimental parameters

Hard Disk PIV 1 & 2				
Run Name	Directory Name	PIV files	Collocation Files	Still water Files
C1	C1_piv_0823	X	X	X
C2	C2_piv_0823	X	as C1	X
C3	C3_piv_0824	X	X	X

Hard Disk PIV 3 & 4				
Run Name	Directory Name	PIV files	Collocation Files	Still water Files
C4	C5_piv_0824	X	as C3	X
C5	C4_piv_0824	X	as C3	X

Hard Disk PIV 5 & 6				
Run Name	Directory Name	PIV files	Collocation Files	Still water Files
C6	C6_piv_0826	X	X	X
C7	C7_piv_0826	X	as C6	X
C8	C8_piv_0826	X	as C6	X

Hard Disk PIV 7 & 8				
Run Name	Directory Name	PIV files	Collocation Files	Still water Files
D1	D1_piv_0827	X	X	X
D2	D2_piv_0827	X	X	X
D3	D3_piv_0827	X	as D2	X

Hard Disk PIV 9 & 10				
Run Name	Directory Name	PIV files	Collocation Files	Still water Files
D4	D4_piv_0828	X	X	X
D5	D5_piv_0828	X	X	X

Hard Disk PIV 11 & 12				
Run Name	Directory Name	PIV files	Collocation Files	Still water Files
D6	D6_piv_0828	X	as D5	X
D7	D7_piv_0829	X	X	X
D8	D8_piv_0829	X	X	X

Table B.2: Contents of PIV hard disks of the PIV data.

Hard Disk PRF 1 & 2					
Run Name	Directory Name	Profile files	IR files	Collocation Files	Still water Files
C1	Run-C1	X	X	X	X
C2	Run-C2	X	X	as C1	X
C3	Run-C3	X	X	X	X
C4	Run-C4	X	X	as C3	X
C5	Run-C5	X	X	as C3	X

Hard Disk PRF 3 & 4					
Run Name	Directory Name	Profile files	IR files	Collocation Files	Still water Files
C6	Run-C6	X	X	X	X
C7	Run-C7	X	X	as C6	X

Hard Disk PRF 5 & 6					
Run Name	Directory Name	Profile files	IR files	Collocation Files	Still water Files
C8	Run-C8	X	X	as C6	X
D1	Run-D1	X	X	X	X
D2	Run-D2	X	X	X	X
D3	Run-D3	X	X	as D2	X
D4	Run-D4	X	X	X	X

Hard Disk PRF 7 & 8					
Run Name	Directory Name	Profile files	IR files	Collocation Files	Still water Files
D5	Run-D5	X	X	X	X
D6	Run-D6	X	X	as D5	X
D7	Run-D7	X	X	X	X
D8	Run-D8	X	X	X	X

Table B.3: Contents of PRF hard disks of the surface profile and IR data. X indicates files are located in this directory. Other notations, “as C1” means that these files are located in C1 directory.